TECHNICAL UNIVERSITY OF LIBEREC
Faculty of Mechanical Engineering

Digital Holographic Interferometry for Temperature Field Measurements in Flowing Gases and Liquids

Dissertation Thesis

Study programme:	P2302 Machines and Equipment
Study branch:	Machine and Equipment Design
Author:	**Ing. Gramoz Cubreli**
Thesis Supervisor:	doc. Ing. Petra Dančová, Ph.D. Department of Power Engineering Equipment

Liberec 2022

Declaration

I hereby certify, I, myself, have written my dissertation as an original and primary work using the literature listed below and consulting it with my thesis supervisor and my thesis counsellor.

I acknowledge that my dissertation is fully governed by Act No. 121/2000 Coll., the Copyright Act, in particular Article 60 – School Work.

I acknowledge that the Technical University of Liberec does not infringe my copyrights by using my dissertation for internal purposes of the Technical University of Liberec.

I am aware of my obligation to inform the Technical University of Liberec on having used or granted license to use the results of my dissertation; in such a case the Technical University of Liberec may require reimbursement of the costs incurred for creating the result up to their actual amount.

At the same time, I honestly declare that the text of the printed version of my dissertation is identical with the text of the electronic version uploaded into the IS/STAG.

I acknowledge that the Technical University of Liberec will make my dissertation public in accordance with paragraph 47b of Act No. 111/1998 Coll., on Higher Education Institutions and on Amendment to Other Acts (the Higher Education Act), as amended.

I am aware of the consequences which may under the Higher Education Act result from a breach of this declaration.

January 25, 2022 Ing. Gramoz Cubreli

Acknowledgments

The number of people whom I would like to thank for helping me during all this time while I was conducting my Ph.D. at the Technical University of Liberec is endless, but I would like to specially thank the following ones:

- My supervisor **doc. Ing. Petra Dančová, Ph.D.** for her help and support;
- My tutor (specialist supervisor) **Ing. Pavel Psota, Ph.D.** for his tremendous help, guidance and kindness throughout the whole process;
- My supervisor during my first three years of studies, **prof. Ing. Tomáš Vít, Ph.D.**;
- My dear colleagues and friends **Ahmad Kouta**, **Anas Elbargthi**, **Shehab Attila, Shehab Hassan, Jan Rýdlo and many others** for their support and advices;
- **The Ministry of Education, Sport and Health of Czechia and the Czech Embassy in Prishtina (Republic of Kosovo)** for the scholarship and this amazing lifetime experience;
- Last but not least **my parents**, without whom all of this wouldn't have been possible!

Annotation

This Ph.D. dissertation introduces and elaborates the optical technique known as Digital Holographic Interferometry (DHI) in the field of applied fluid mechanics for the purpose of investigating the properties and visualization of flowing gases and liquids.

The work deals mostly with the general aspects of using digital holographic interferometry as the main technique of investigation, deepening in some of its technical aspects for data treatment and visualization. It gradually present the evolving process of studying different forms of temperature fields, based on the distribution of its refractive index, starting with simple 2D distribution toward 3D distribution that is treated with tomographic approach. It brings to light main concepts and possibilities of using this technique for the field of fluid mechanics.

Apart the general theoretical background introduced in the beginning of this thesis, each chapter contains an introduction to some more theoretical and technical aspects of the optical setup and data treatment that are needed for a better and full understanding of the process of capturing, treating and presenting the data. General conclusions are drawn at the end of each chapter.

Throughout our work, we have achieved a deviation below tenths of degree Celsius between the temperature registered from the thermocouples, *ANSYS* simulations and the one measured by the optical technique for the case of heat measurements in water, falling within 5% of error margin for the case of a 2D temperature field. For the case of a 3D temperature field from a pulsatile jet with water as its working fluid, we estimated that the relative uncertainty of the temperature field measurement near the orifice is below 5%, compared to the relative uncertainty increasing up to 15% further from the orifice. We also achieved an increase of the range of measurement for the case of two-wavelength digital holographic interferometry.

Each investigation is accompanied with a whole-field picture of visualizing the temperature and other important properties of the fluid/gas under study, which is one of the main advantages of this optical technique.

Keywords: Digital holographic interferometry; temperature fields; spatial-carrier; Fourier Transform, convection; water; pulsatile jets; tomography.

Anotace

Tato Ph.D. disertační práce pojednává o optické metodě známé jako digitální holografická interferometrie (DHI) v oblasti aplikované mechaniky tekutin za účelem zkoumání vlastností a vizualizace proudících plynů a kapalin.

Práce se zabývá především obecnými aspekty použití digitální holografické interferometrie jako hlavní analytické techniky, přičemž prohlubuje některé její technické aspekty v oblasti zpracování a vizualizaci dat. Postupně popisuje proces studia různých forem teplotních polí založených na rozložení jejich indexu lomu, počínaje jednoduchým 2D rozložením až po složitější 3D rozložení, které je řešeno tomografickým přístupem. Tato práce také přibližuje hlavní pojmy a možnosti využití této metody v oblasti mechaniky tekutin.

Kromě popsané obecné teorie dané problematiky na začátku této práce, obsahuje každá kapitola úvod k některým teoretičtějším a techničtějším aspektům optického nastavení a zpracování dat, které jsou potřebné pro lepší a plné pochopení procesu snímání, zpracování a prezentace dat. Na konci každé kapitoly jsou uvedeny obecné závěry.

Při meření teploty ve vodě jsme dosáhli shody mezi teplotou měřenou termočlánky, simulací v prostředí *ANSYS* a teplotou naměřenou vyvinutou optickou technikou v rámci desetiny celsia, což je odchylka spadající do 5% chybové tolerance. To bylo v případě 2D teplotního pole. V případě zkoumání 3D teplotního pole pulzujícího trysky s vodou jako pracovní tekutinou jsme odhadli, že relativní nejistota měření teplotního pole v blízkosti ústí trysky je menší než 5%, ve vzdálenějších místech pak dosahuje 15%. Bylo dosaženo zvýšení rozsahu měření dvouvlnové digitální holografické interefrometrie.

Jednotlivé pasáže jsou doprovázeny obrázky vizualizací teplotních polí a jiných důležitých vlastností podstatných při výzkumu tekutin, což je jedna z hlavních výhod dané metody optické analýzy.

Klíčová slova: Digitální holografická interferometrie; teplotní pole; prostorový-nosič (spatial-carrier); Fourierovy trasformace; konvekce/proudění; voda; pulzní trysky; tomografie.

Content

List of figures

Motivation and objectives of the dissertation thesis

This thesis presents real-time interferometric measurements and visualization of dynamic phenomena in flowing transparent gases and liquids. It focuses on digital holographic interferometry as an optical technique for temperature field measurements and visualization. Air is investigated as the flowing gas while water as the flowing liquid.

Owing to the wide range of applications of optical techniques, in research and industry, notably in applied fluid mechanics, the investigation and understanding of phenomena developing unobstructed from the viewer within their natural course and the lack of such studies for the case of flowing gases and liquids were the principle motives that made this research happen.

The aim of this research was the investigation via optical ways of the imaging of temperature fields, unobstructed from their normal flow, with high precision and high spatial resolution, in real time for different applications falling in the field of applied fluids mechanics for mechanical engineering. But, this doesn't limit the vast number of possible applications and use in other multidisciplinary fields that this technique has, as can be read in *Chapter 5*.

The principle aims set for the course of this research were:

- To introduce main properties and understanding of light and the digital holographic interferometric technique in a comprehensive way;
- To compile an extensive literature review on applications of digital holographic interferometry in different fields, specifically in the study of gases, liquids and possibly solids;
- To perform initial research on liquids to assert the viability of the chosen optical technique;
- To validate initial results through CFD calculations;
- To explore the possibility of extending the range of measurement through the use of a two-wavelength off-axis optical configuration for air temperature fields;
- To study temperature fields generated by pulsatile jets in water.

This thesis is mainly experimental in its nature of investigation.

With the theoretical corpus, literature review, rich graphical representation of results for each designated chapter and the achieved results, we bring an interesting research in the field of optics and its application in applied fluid mechanics.

Summary

The dissertation thesis is divided into 10 chapters.

Chapter one, as a start is a short dive into the history of light, highlighting key moments and personalities that shed light onto phenomena related to light, its nature and its applications.
Chapter two brings to light key properties of light with an expanded mathematical foundation.
Chapter three outlines holography and its fundamentals, which are essential to this thesis.
Chapter four gives a short introduction to the concept of heat and some properties.
Chapter five contains an extensive literature review on applications of optical techniques (mostly digital holographic interferometry) on measurements in air, liquids and solids, from older and recent articles, thus pointing obvious advances made in data acquisition, processing and presentation.
Chapter six deals with temperature measurements and visualization of heat generated from a metal-rod heater placed in a water tank.
Chapter seven validates numerically, through simulations by *ANSYS,* the results obtained in chapter six.
Chapter eight focuses on two-wavelength measurements in air, providing an extended range of unambiguous measurements. Three different study cases are considered.
Chapter nine investigates temperature fields generated by a synthetic pulsatile jet, operating with water.
Chapter ten provides general conclusions to this dissertation thesis.

Apart theoretical introduction of each chapter, relevant information on the optical setup, used material, technique, Fourier domain information, errors and conclusions are drawn in all relevant chapters.

1. History of light

Through legends, myths and fragments (as quotations or paraphrases) passed down in written form since the dawn of humanity, knowledge was attributed to have a divine origin. With the birth of first major civilizations around 5 000 BC around river flows (Euphrates, Nile, Indus and Yellow River), knowledge gathering, classification and passing down from generation to generation the technological advents was a necessity to solve major problems that were reoccurring and needed better solutions.[1-4]

Describing light and explaining its nature has been a quest since antiquity. Light has been assigned in many cultures the symbol of enlightenment, salvation and purity. Understanding human vision and the way it works were one of the primary steps into understanding light. In Ancient Egypt people believed that the day was an outcome from the opening of the eye of Raa (The Sun God), while night fell when He closed his eyes.[5–7]

In Ancient Greece, Greeks disposed of knowledge that was already gathered and considered advanced for the time. Their knowledge came from Mesopotamia and Egypt mainly, knowledge which was up to some point systemized and considered advanced.[1]
Democritus (460-370BC) believed that the air between the eye and the objected was contracted, and this contracted air contained the details that were transferred to the eye. Epicurus's opinion (342-270 BC) was that atoms flow continuously between the object and the eye. Plato (428-328 BC) on the other hand said that light was consisted of rays that were emitted by the eye.[2,3,8–10]
In the work *"Republic"* of Plato, the apparent bending of object when they are partly submerged in water can be found mentioned. Optical elements and technology date since the antiquity and some have survived till our days. Mirrors were made of polished copper, bronze and later in a copper alloy rich in tin. Some of these mirrors were found in Egypt, near the Pyramid of Sesostris II (1900 B.C.).[11]
On the other hand, some other authors and philosopher gave more developed opinion. Euclid (300BC) wrote a book called *"Elements"* which explains light through geometry[3]. Claudius Ptolemy (90-168 AD) wrote a book called *"Optics"* in which he discussed theories about vision, reflection etc. and conducted various experiments.[2,8]

Philosophy and sciences were an important part of the Islamic Golden Age. Arabs surpassed the Greeks in the field of optics[1]. Abu Yusef Yaqoub ibn Ishaq Al-Kindi (800-873) wrote a book called *"De Aspectibus"* which had a great influence in optics in the Western and Islamic world during the Middle Ages[3]. Ibn Sina (980-1037) rejected the notion of visual fire, according to which, when the eye opens it sends light to the objects so they can be seen. The theory of visual fire was a theory supported by Euclid in Ancient Greece. Even if the credits of the discovery of the Law of Refraction are attributed to Willebrord Snellius (1580-1626), there are evidences that it was discovered much earlier by Abu Sad Al Alla Ibn Sahl (940-1000). He wrote a book *"On burning mirrors and lenses"* where he talked about elliptical and parabolic burning mirrors. A scientist named Abu Ali al-Hasan ibn al-Hasan ibn al-Haytham (965-1040), known as Alhazen, wrote a book titled *"Kitab al-Manzir" (''Book of optics'')*[2] which remained the most influential book of optics until the book of Newton *"Opticks"* in 1704. He was considered the greatest authority in Europe for several centuries[1,10]. He demonstrated that light doesn't have its source in the eye[6], but rather in light sources. He proved this by an experiment with two lanterns and a pinhole. He was the first one to invent the pinhole camera (that Kepler called it "*camera obscura"* in the 17th century) and is the source of the theory of parabolic and spherical mirrors and how the eye functions.[1–3,8–12]

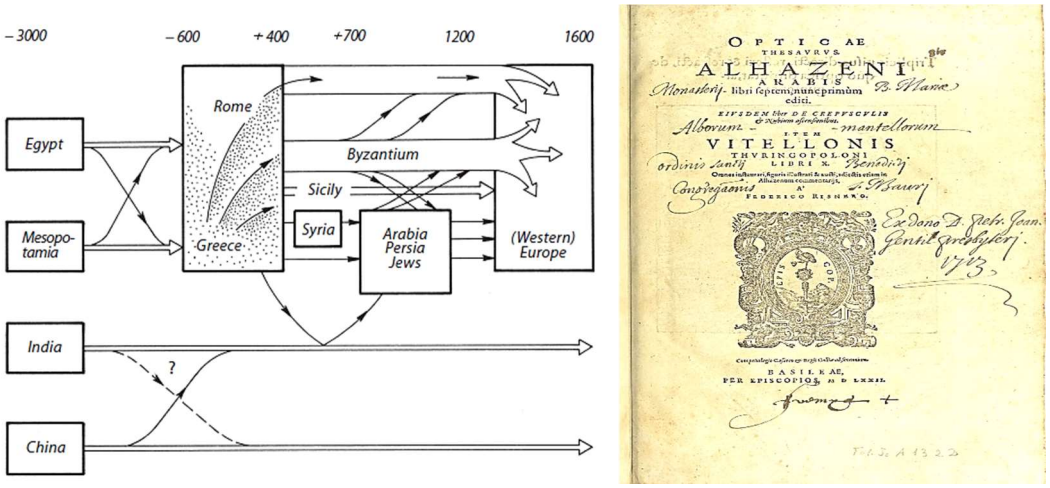

a) b)

Fig.1.1. *a) Schematic representation of the path by which the ancient cultural legacy was transmitted to Europe[1] and b) cover page of "Book of Optics'' from Alhazen.*[13]

In the 13th century, Europe was using most texts of optics coming from the Arab world.[12]

Johannes Kepler (1571-1630) is an important person in the history of science and light. His interests in optics have originated when he observed a solar eclipse on July 10th, 1600, with the *camera obscura*. He stated that they eye has an aperture, same as in the camera. He published his work in 1604.[3,8]

René Descartes (1590-1650) was a French mathematician and philosopher which contributed in optics with his book *"Dioptrics"*, published in 1637 that dealt with the nature of light and laws of optics. While Snellius didn't publish his work while he was alive, Descartes did so. He published it around 15 years after the death of Snellius and it seems that Descartes discovered the same law independently. This is the reason why in France and in some countries it is known as *The Law of Descartes-Snellius*.[1,3,6,8,12]
"La Dioptrique" has the more practical goal of showing how to construct good lenses. This book is divided into two parts: vision, including the structure of the eye, and the law of refraction.[1]

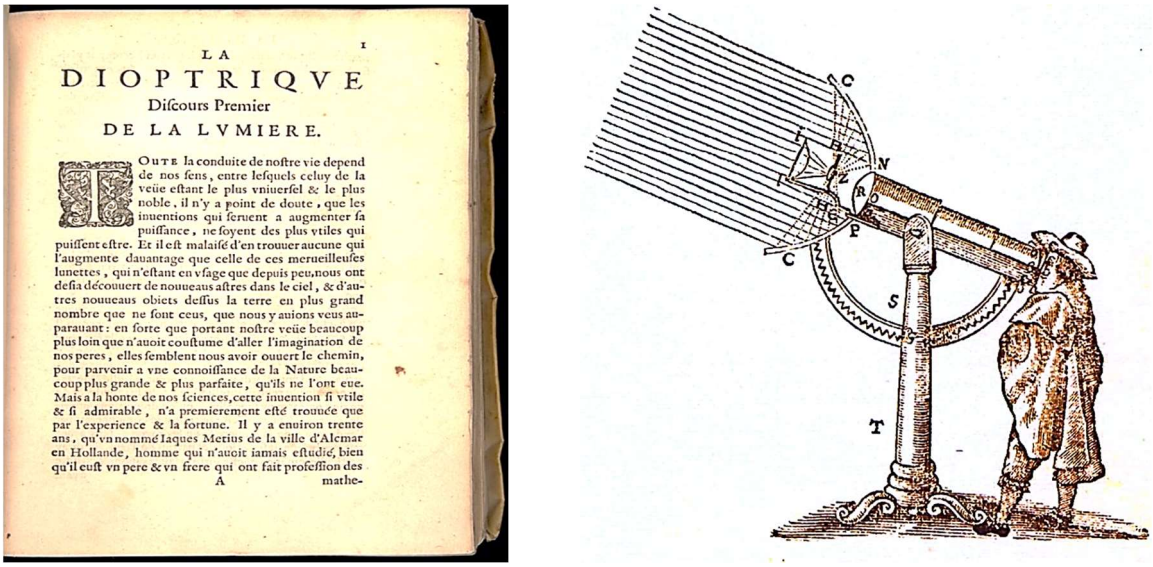

a) b)

Fig.1.2. *a) First page of "La dioptrique" by René Descartes and b) the depiction of his compound telescope*.[14]

The debate on the nature of light started since the antiquity and was more prominent since the 17th century between the advocates of the corpuscular theory (Newton) and those advocating a wave-like nature (Hooke, Huygens).[6,15]
Fermat (1601-1675) contributed in optics by demonstrating *Snell's Law* using the principle of the least time, based on the conviction that all processes in nature proceed in the most economical way[1,8]**.** He opposed to Descartes' assumptions, stating that a denser material would present greater resistance for light to propagate in it, thus decreasing the speed of light[1,6].[3,9]

Newton (1642-1727) remains one of the biggest scientist of all time. He contributed in optics by showing that the color is a property of light, he showed that light coming from the sun consists of all colors, proved that white light is consisted of all colors, contributed in creating a reflective telescope etc. and promoted a corpuscular theory of light.[3,6,8,9,16]
Newton was interested in colors since he noticed that one of the annoying flaws of telescope is a color edge around the image. He also worked with Icelandic spar crystal (Icelandic: *silfurberg,* lit. *silver-rock*) which exhibits birefringence[1].

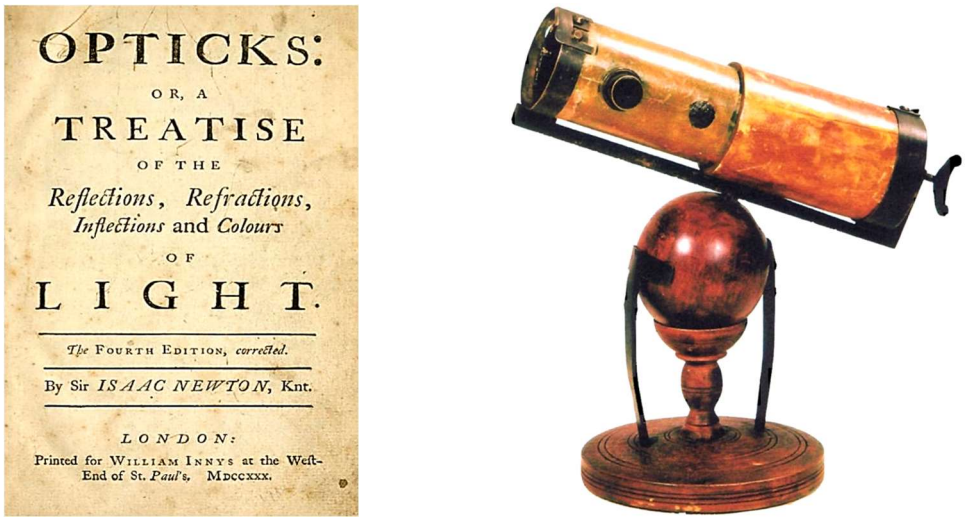

a) b)

Fig.1.3. *a) Cover of Newton's book "Opticks'' published in 1730*[17] *and b) a replica of the first reflecting telescope made by Newton and shown to the Royal Society in 1668.*[18]

Huygens (1629-1695) contributed to the science of light with the wave nature of light, published in the *"Traité de la lumière"* in 1690. He considered that light has a wave nature and propagates the same as sound waves, through a medium called ether, and advocated for a finite, nevertheless high speed of light. *The Law of Huygens* discovered and formulated by him bears his name and it states that every point on a wavefront can be considered as a new source.[3,4,6,8–10]
Huygens concluded that light effectively slowed down when entering dense media[11]. Huygens didn't start his formulations out of philosophical principles, rather from physical principles. Huygens published his book after the death of Hooke since Hooke was strongly against his findings.[1]

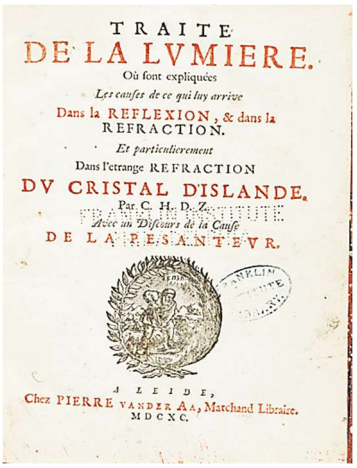
TRAITE
DE LA LVMIERE.
Où sont expliquées
Les causes de ce qui luy arrive
Dans la REFLEXION, & dans la
REFRACTION.
Et particulierement
Dans l'etrange REFRACTION
DV CRISTAL D'ISLANDE.
Par C. H. D. Z.
Avec un Discours de la Cause
DE LA PESANTEVR.
A LEIDE,
Chez PIERRE VANDER AA, Marchand Libraire.
M D C X C.

Fig.1.4. *Cover of "Traité de la lumière", written by Huygens.*[19]

Young (1773-1829) was the one to demonstrate the wave nature of light with its double-slit experiment. With his experiment, he was able to calculate the wavelength of up to 7 colors. His experiment presents the basics of light interference, which is the core effect that is studied in this thesis. He was the first one to state that light is made of periodic waves and understood the importance of coherence.[1,8,16] His discovery pointing a wave-like nature of light received little recognition and remained mostly as an individual research program. It was not until Fresnel rediscovered it in 1815 and offered a similar theory to Young's that it would get acceptance from others. Young was initially trained as a medical doctor, from where he developed his interest in studying vision. He spoke 13 languages at the age of 14. [3,4,9,12,15,20,21]

Fresnel (1788-1827) contributed with his experiments on diffraction. He showed his work in a competition organized by the French Academy of Science, where Laplace and Poisson where two of the three-member committee. At his time, the corpuscular theory of light was well known and supported by other scientists, notably this committee. But, after Poisson challenged Fresnel's theory with a simple question through an experimental demonstration, Fresnel demonstrated that his theory was valid and overcame the challenge of Poisson by proving that the supposition made according to his theory was correct. This way, he won the contest. The experiment was related to the presence of a bright spot in the shadow of a disc that was illuminated, and the bright spot is named as *the Poisson spot*, sometimes *the Aragon spot* or even *the Fresnel spot*. After this, Fresnel's theory was used to explain the polarization of light and its properties. He was the first to obtain circular polarized light, and said that light was a transverse wave, a fact he proved later.[3,6,8,9,21]
He started as a civil engineer building roads in southern France as a chemistry lover and had basic knowledge of physics. His scientific career lasted less than 10 years since he died of tuberculosis. [3,9,12,21]

Polarization was given its name by Malus, stating that natural light upon being reflected at a certain angle behaves like one of the rays exiting a double-refracting crystal.[1,3,12]

The connection between light and electricity was already being discussed in the middle of the 19th century. Maxwell (1831-1879) was the first one to explain light as a combination of mutually perpendicular electric and magnetic fields propagating in the direction that was normal to both of them, in 1865. The first one to prove that light was an electromagnetic wave was Hertz (1857-1894) in 1888.[3,6,8]

Maxwell was an admirer of Faraday and formulated mathematically his discoveries, even though Faraday's concept of force lines wasn't well understood by others. Both of them were very close and worked together.[1]

Gustav Kirchhoff (1824-1887) formulated *The Theory of Black Body Radiation* in 1859 without knowing the research done by Stewart in the same field.[8]

In 1881 and then 1887, Michelson and Morley conducted the same interferometric experiment few times to determine the speed of light and to challenge the existence of aether and aether wind, and their results were shocking and thought to be erroneous. The experiment was redone by many other scientists with better apparatus, to result the same. The result was that the speed of light was always the same and that aether doesn't exist. This experiment was of great importance to the formation of the theory of relativity. [1,9,12]

The 19th century was a century of great contribution in all aspects of physics. With the formulation of *The Second Law of Thermodynamics* and the irreversible concept, for the first time the direction of process was set, contrary to the laws of classical mechanics. The establishment of probability theory and statistical methods opened up a new era in physics.[1]

On December 15th, 1900, Max Planck (1858-1947) was the one who presented a valid radiation formula that covered the whole frequency spectrum. The constant $\hbar$ carries his name as *Planck's constant*. Planck's finding started a new era of thinking in physics. He demonstrated that the energy of radiation was directly proportional to the frequency, and not the amplitude as a classical physicist would expect, and that energy was quantized.[8]

Albert Einstein (1879-1955) was the one that revolutionized the way how we see physics and how we understand how our world works. He used Planck's hypothesis when he published his paper on the photoelectric effect in 1905, which basically reintroduced the particle nature of light, not the same way Newton saw it, in a corpuscular way, but rather as discreetness in energy. Einstein introduced the concept of photon, revolutionized physics and gave birth to quantum physics and theory of relativity.[7–9]

The Theory of Special Relativity was formulated in 1905 by Einstein. In 1915, he published a paper where he described gravity as a geometric property of space and time. Einstein's idea of gravity was conflicting with the Newton's already accepted idea. The experiment on the bending of light determined Einstein's theory as the precise one. In 1911, Einstein obtained a value of $0.87\ [arc\ sec]$ bending angle for light grazing the Sun. This is a value that, Johann Georg von Soldner (1804) also obtained a hundred years ago based on the corpuscular nature of light of Newton. But, when Einstein added to this the effect of general theory of relativity, the valued went to $1.83\ [arc\ sec]$, which he published on November 18, 1915. According to Newton's theory, all objects with finite speed passing by a massive object will experience bending. The bending of light and its angle should be independent of the mass of the particle consisting light, thus considering that light had a corpuscular nature, and according to Newton it should and did bend.[8]
On May 29, 1929, a solar eclipse took place in Africa, in the Principe Islands. Sir Arthur Eddington (1882-1944) went there on an expedition to measure the bending on light from stars by the gravitational force of the sun, in order to compare with both values obtained from Newton and Einstein. The values he measured reveled that Einstein had right. This made Einstein famous.[8]

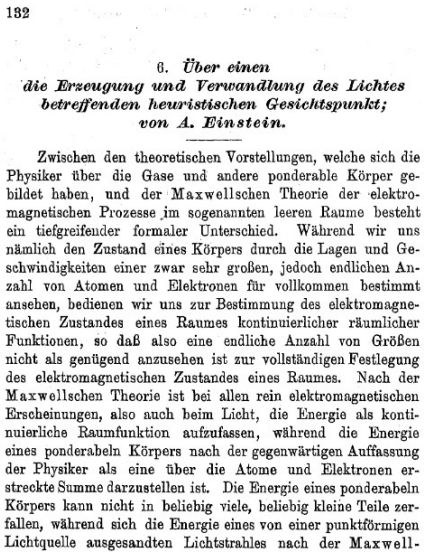

132

6. *Über einen die Erzeugung und Verwandlung des Lichtes betreffenden heuristischen Gesichtspunkt; von A. Einstein.*

Zwischen den theoretischen Vorstellungen, welche sich die Physiker über die Gase und andere ponderable Körper gebildet haben, und der Maxwellschen Theorie der elektromagnetischen Prozesse im sogenannten leeren Raume besteht ein tiefgreifender formaler Unterschied. Während wir uns nämlich den Zustand eines Körpers durch die Lagen und Geschwindigkeiten einer zwar sehr großen, jedoch endlichen Anzahl von Atomen und Elektronen für vollkommen bestimmt ansehen, bedienen wir uns zur Bestimmung des elektromagnetischen Zustandes eines Raumes kontinuierlicher räumlicher Funktionen, so daß also eine endliche Anzahl von Größen nicht als genügend anzusehen ist zur vollständigen Festlegung des elektromagnetischen Zustandes eines Raumes. Nach der Maxwellschen Theorie ist bei allen rein elektromagnetischen Erscheinungen, also auch beim Licht, die Energie als kontinuierliche Raumfunktion aufzufassen, während die Energie eines ponderabeln Körpers nach der gegenwärtigen Auffassung der Physiker als eine über die Atome und Elektronen erstreckte Summe darzustellen ist. Die Energie eines ponderabeln Körpers kann nicht in beliebig viele, beliebig kleine Teile zerfallen, während sich die Energie eines von einer punktförmigen Lichtquelle ausgesandten Lichtstrahles nach der Maxwell-

Fig.1.5. *Einstein's article "On a Heuristic Viewpoint Concerning the Production and Transformation of Light" with the explanation of the photoelectric effect.*[22]

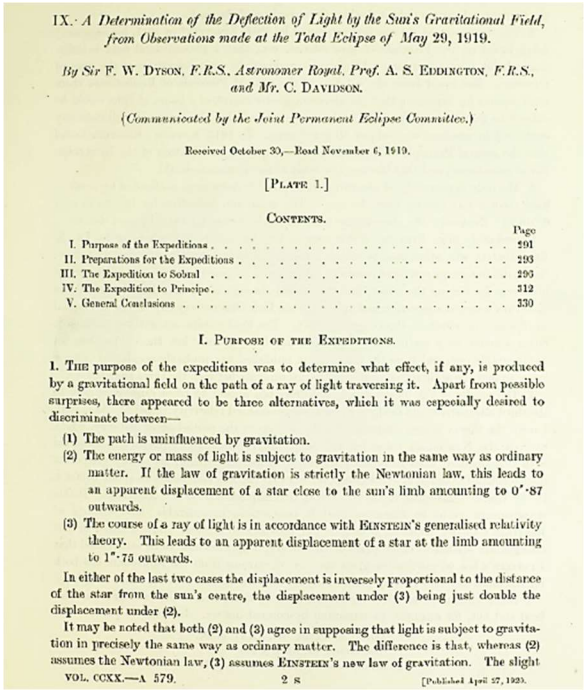

IX. *A Determination of the Deflection of Light by the Sun's Gravitational Field, from Observations made at the Total Eclipse of May 29, 1919.*

By Sir F. W. Dyson, *F.R.S., Astronomer Royal, Prof.* A. S. Eddington, *F.R.S., and Mr.* C. Davidson.

(Communicated by the Joint Permanent Eclipse Committee.)

Received October 30,—Read November 6, 1919.

[Plate 1.]

Contents.

I. Purpose of the Expeditions.

1. The purpose of the expeditions was to determine what effect, if any, is produced by a gravitational field on the path of a ray of light traversing it. Apart from possible surprises, there appeared to be three alternatives, which it was especially desired to discriminate between—

(1) The path is uninfluenced by gravitation.

(2) The energy or mass of light is subject to gravitation in the same way as ordinary matter. If the law of gravitation is strictly the Newtonian law, this leads to an apparent displacement of a star close to the sun's limb amounting to 0″·87 outwards.

(3) The course of a ray of light is in accordance with Einstein's generalised relativity theory. This leads to an apparent displacement of a star at the limb amounting to 1″·75 outwards.

In either of the last two cases the displacement is inversely proportional to the distance of the star from the sun's centre, the displacement under (3) being just double the displacement under (2).

It may be noted that both (2) and (3) agree in supposing that light is subject to gravitation in precisely the same way as ordinary matter. The difference is that, whereas (2) assumes the Newtonian law, (3) assumes Einstein's new law of gravitation. The slight

Fig.1.6. *First page of the publication of results from the solar eclipse of May 29,1919 by Sir Arthur Eddington.*[23]

All discoveries in the first quarter of the 20th century made this probably the most revolutionary time of the development of physics. Discoveries from Planck, Einstein and Niels Bohr changed the conventional way we understand physics and quantum physics was born. Werner Heisenberg, Max Born, Paul Dirac and Edwin Schrodinger gave a huge contribution in developing this new branch of physics that explained the sub-atomic effects and the effects that happen at speeds comparable to the speed of light, which Newtonian physics couldn't. The wave-particle duality of light gained more and more support and was

established. Interference was explained by the wave nature of light, while the excitation of an atom upon shining with a light and the absorption of the photon required a particle nature of light.[8]

In 1927, Paul Adrien Dirac (1902-1982) put together the wave and corpuscular nature of light into a single theory.[8]

Years after followed with the theory of spontaneous emission, demonstration of the theory of Casimir about mutual attraction by two conducting plate in vacuum in 1947, the discovery of laser in 1950 as a source of coherent light and the first pulsed laser operation was demonstrated by Theodore Maiman (1927-2007) in ruby in 1960 and the first cw (continuous wave) laser was built the same year by Ali Javan. Following times opened the era of a new discipline in physics, quantum optics.[6,8]

2. Properties of light

The nature of light was not fully understood until the 19th century. Before that, the particle nature of light was predominantly seen as the true nature of it, even though in some situations this theory couldn't justify some effects in nature (see *Chapter 1*). Our understanding of the surrounding world and light in particular has been influenced on the development of quantum physics.

Light is an electromagnetic, transverse propagating wave with a speed of $c_0 = \frac{1}{\sqrt{\varepsilon_0 \mu_0}} \approx 299\,792\,458 \left[\frac{m}{s}\right] \approx 3 \cdot 10^8 \left[\frac{m}{s}\right]$ in vacuum, where the free space permittivity is given by $\varepsilon_0 = 8.85 \cdot 10^{-1} \left[\frac{F}{m}\right]$ and the free space permeability by $\mu_0 = 4\pi \cdot 10^{-7} \left[\frac{H}{m}\right]$. Light is made of photons, that are zero mass particles. Light wave is made of the electrical field $\vec{E}(x, y, z, t)$ and the magnetic field $\vec{B}(x, y, z, t)$, where x, y, z are the spatial coordinates and t is the time. After generation, light moves independently from its source and the electric and magnetic fields that consist light generate each other indefinitely.

2.1. Waves

A propagating wave is represented mathematically in the form of a harmonic wave $\psi(x,t) = Acos(\omega t - kx)$, which is a solution of the Maxwell's equations. The wave has its period t, frequency f, angular frequency ω, wave number k, speed of propagation v, intensity I, phase φ, power P and energy E.

2.1.1. Harmonic waves

A harmonic wave is said to be a wave of a sine or cosine form. Their importance arises by the fact that any wave shape can be obtained by superimposing various harmonic waves. A wave is said to be monochromatic, if it is represented by a wave having a harmonic time dependency.

Since the electric and magnetic components are time dependent in the wave equation and show a harmonic variation, then one form of the solution of the wave equation is considered to be the harmonic wave. The harmonic time dependency is stored inside the angular frequency.

Generally, it can be mathematically expressed with[21]:

$$\psi(x,t) = Acos(\omega t \pm kx) \tag{2.1}$$

or,

$$\psi(\vec{r}) = A(\vec{r})cos\big(2\pi\vartheta \pm \varphi(\vec{r})\big) \tag{2.2}$$

, when it isn't dependent of time, where the amplitude $A(\vec{r})$ and the phase $\varphi(\vec{r})$ are dependent of the position, given by the vector position $\vec{r}$.

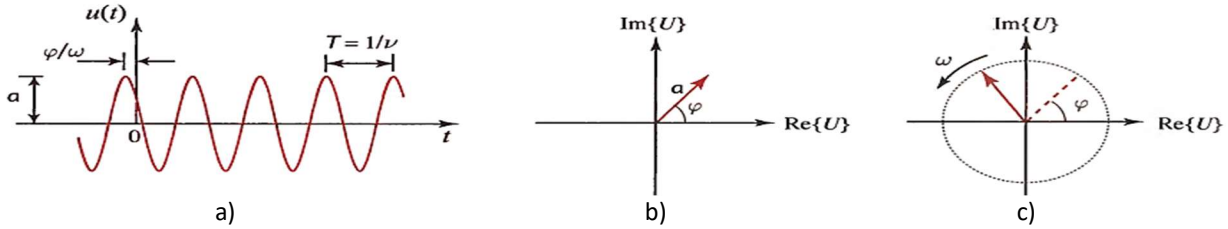

a) b) c)

Fig.2.1. *Representation of a harmonic monochromatic wave at a fixed position r with its components b) and c).*[24]

For calculation purposes, it is very desirable to express the wavefunction as a complex function[24]:

$$\psi(x,y,z,t) = A(x,y,z)\cdot e^{j\{\omega t+\varphi(x,y,z)\}} \tag{2.3}$$

$$\text{or } \psi(\vec{r},t) = A(\vec{r})\cdot e^{j\{\omega t+\varphi(\vec{r})\}} \tag{2.4}$$

$$\text{with } Re\{\psi(\vec{r},t)\} = \frac{1}{2}[\psi(\vec{r},t)+\psi^*(\vec{r},t)] \tag{2.5}$$

The complex wavefunction is entirely described by $\psi(\vec{r},t)$[24]. Rewriting the above equation yields[24]:

$$\psi(\vec{r},t) = \psi(\vec{r})\cdot e^{j\omega t} \tag{2.6}$$

$$\text{, with } \psi(\vec{r}) = A(\vec{r})\cdot e^{j\varphi(\vec{r})} \tag{2.7}$$

named as the complex amplitude[24]. This then yields[24]:

$$Re\{\psi(\vec{r},t)\} = Re\{\psi(\vec{r})\cdot e^{j\omega t}\} = \frac{1}{2}\left[\psi(\vec{r})\cdot e^{j\omega t}+\psi^*(\vec{r})\cdot e^{-j\omega t}\right] \tag{2.8}$$

By substituting the above equation into the wave equation, an equation known as the Helmholtz equation is obtained[24]:

$$\nabla^2\psi + k^2\,\psi = 0 \tag{2.9}$$

From the equation above, it holds that: $|\psi(\vec{r})| = A(\vec{r})$ and $arg\{\psi(\vec{r})\} = \varphi(\vec{r})$

Harmonic waves traveling along the x axis can be mathematically represented in different ways. For example[11]:

$$\psi(x,t) = Acos(\omega t \pm kx) \tag{2.10}$$

$$\psi(x,t) = Acos[k(vt \pm x)] \tag{2.11}$$

$$\psi(x,t) = Acos\left[2\pi\left(\frac{t}{\tau}\pm\frac{x}{\lambda}\right)\right] \tag{2.12}$$

$$\psi(x,t) = Acos\left[2\pi\vartheta\left(t\pm\frac{x}{v}\right)\right] \tag{2.13}$$

2.1.2. Transverse waves

Let us have a monochromatic electromagnetic wave described in free space by[11]:

$$\vec{E}(\vec{r}) = \vec{E}_0 e^{-j\vec{k}\cdot\vec{r}} \tag{2.14}$$

$$\vec{H}(\vec{r}) = \vec{H}_0 e^{-j\vec{k}\cdot\vec{r}} \tag{2.15}$$

Involving the Maxwell's equations, the following equations are obtained[11]:

$$\vec{k}\times\vec{H}_0 = -\omega\epsilon\vec{E}_0 \tag{2.16}$$

$$\vec{k}\times\vec{E}_0 = \omega\mu\vec{H}_0 \tag{2.17}$$

From *eq.(2.16)* and *eq.(2.17)*, it can be concluded that $\vec{k}$, $\vec{E}$ and $\vec{H}$ are all mutually orthogonal. The very fact that $\vec{E}$ and $\vec{H}$ lie on the same plane, which is normal to $\vec{k}$, makes this wave to be called a transverse electromagnetic wave. Alternatively, if it is considered that the wave is propagating in the z direction,

$\vec{E}$ is constant over each of an infinite set of planes perpendicular to the direction of propagation, since the electric field $\vec{E}$ is a solution of the equation[11]:

$$\nabla^2\vec{E} = \mu_0\varepsilon_0\frac{\partial^2\vec{E}}{\partial t^2} \tag{2.18}$$

, which represents one of the Maxwell's equation for free space after some mathematical treatment.

Since $\vec{E} = \vec{E}(z,t)$, then the previous equation becomes[11]:

$$\frac{\partial E_z}{\partial z} = 0 \tag{2.19}$$

From this equation it can be understood that, if there is a component on the direction of propagation, it won't vary with z. So, for any time, E_z is constant, and this is impossible if the wave travels on the z direction. The other option coming from the equation above is the case of $E_z = 0$, which means that the wave has no electric field component in the direction of propagation. The electric field in this case is transverse. In such case, it can be decided to set the electrical field parallel to the x axis. In this case, from the Maxwell's equation, it follows that[11]:

$$\frac{\partial\vec{E}_x}{\partial z} - \frac{\partial\vec{E}_z}{\partial x} = -\frac{\partial\vec{B}_y}{\partial t} \tag{2.20}$$

Since the electric field is parallel to the x axis, then a component on the z axis doesn't exist. This leads to[11]:

$$\frac{\partial\vec{E}_x}{\partial z} = -\frac{\partial\vec{B}_y}{\partial t} \tag{2.21}$$

It is clear that $\vec{B}$ can only have a component along the y axis. From this it can be concluded that, in free space, electromagnetic waves are transverse waves. In real materials this is not the case, since materials can have free charges or can be dissipative. Since here the case is dealt with harmonic waves, the following can be written[11]:

$$\vec{E} = \vec{x}\cdot B_x(z,t) \tag{2.22}$$

$$\vec{B} = \vec{y}\cdot B_y(z,t) \tag{2.23}$$

$$E_x(z,t) = E_{0x}\cos\left(\omega\left(t - \frac{z}{c}\right) + \varepsilon\right) \tag{2.24}$$

$$\frac{\partial E_x(z,t)}{\partial z} = \frac{E_{0x}\omega}{c}\sin\left(\omega\left(t - \frac{z}{c}\right) + \varepsilon\right) \tag{2.25}$$

Then it holds that[11]:

$$B_y(z,t) = -\int\frac{\partial E_x(z,t)}{\partial z}dt = -\frac{E_{0x}\omega}{c}\int\sin\left(\omega\left(t - \frac{z}{c}\right) + \varepsilon\right)dt = \frac{1}{c}E_x(z,t) \tag{2.26}$$

From the fact that B_y and E_x only differ for a scalar, it can be seen that they are in phase for any point. It can also be seen that they are perpendicular to each other at any point.[11]

2.1.3. Plane waves

Plane waves are waves that have planar wavefronts that stretch ideally to infinity on both sides and are represented mathematically by the function[24]:

$$\psi(\vec{r}) = A \cdot e^{-j\vec{k}\cdot\vec{r}} \tag{2.27}$$

, where $\vec{k}\cdot\vec{r} = k_x \cdot \vec{x} + k_y \cdot \vec{y} + k_z \cdot \vec{z}$ and $\vec{k}$ is the wavevector, while A is a complex constant. The phase in this case is $arg\{\psi(\vec{r})\} = arg\{A\} - \vec{k}\cdot\vec{r}$. The equation $\vec{k}\cdot\vec{r} = arg\{A\} + 2\pi m$ where m is an integer, describes the set of parallel planes which are perpendicular to the wavevector $\vec{k}$. If our direction of propagation would be parallel to the z axis, then[24]:

$$\psi(\vec{r}) = A \cdot e^{-jk\cdot z} \tag{2.28}$$

and $Re\{\psi(\vec{r},t)\} = |A|\cos(2\pi\vartheta t - kz + arg\{A\})$. (2.29)

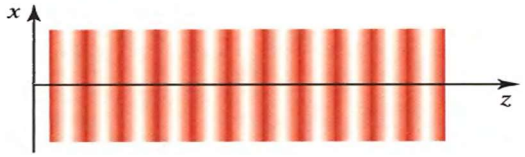

Fig.2.2. *Representation of the wavefronts from a plane wave.*[24]

2.1.4. Wave equation

Light propagates in different mediums with different speeds. Wave propagation in free space can be described in 1D by the differential wave equation[11,21]:

$$\frac{\partial^2\psi(x,t)}{\partial x^2} = \frac{1}{v^2}\cdot\frac{\partial^2\psi(x,t)}{\partial t^2} \tag{2.30}$$

, where $\psi(x,t)$ represents the profile (disturbance profile) of the wave, v is the wave speed, x is the space coordinate while t is the time. In 3D, the differential wave equation is[11]:

$$\nabla^2\psi(x,y,z,t) = \frac{1}{v^2}\cdot\frac{\partial^2\psi(x,y,z,t)}{\partial t^2} \tag{2.31}$$

The wave equation is similar to the above mentioned one, only $c = v$ must be applied. This equation is a must in order to satisfy Maxwell's equation described later and can be derived from them. This equation combines wave optics with the electromagnetic theory through the relation $c_0 = \frac{1}{\sqrt{\varepsilon_0\mu_0}}$.

2.2. Maxwell's equations

That the light had a wave nature, an electromagnetic nature to be precise, was made evident from Maxwell's equations in the late 1800s. The dual nature of light is evidenced by the fact that it propagates in a wave fashion through space and yet displays particle like behavior during emission and absorption[11]. Maxwell showed that the same laws that govern electromagnetics are the same ones that govern electromagnetic waves, hence they describe light propagation. Maxell's equation can be found in different forms[11,24,25].

Integral form of Maxwell's equations in the absence of magnetic or polarizable media

$$\oint \vec{E} \cdot d\vec{s} = \frac{q}{\varepsilon_0} \quad (Gauss'Law\ for\ electricty) \tag{2.32}$$

$$\oint \vec{B} \cdot d\vec{s} = 0 \quad (Gauss'Law\ for\ magnetism) \tag{2.33}$$

$$\oint \vec{E} \cdot d\vec{s} = -\frac{d}{dt}\phi_B \quad (Faraday's\ Law\ of\ induction) \tag{2.34}$$

$$\oint \vec{B} \cdot d\vec{s} = \mu_0 j + \frac{1}{c^2} \cdot \frac{\partial}{\partial t} \int \vec{E} \cdot d\vec{A} \quad (Ampère's\ Law) \tag{2.35}$$

Differential form of Maxwell's equations in the absence of magnetic or polarizable media

$$\vec{\nabla} \cdot \vec{E} = \frac{q}{\varepsilon_0} = 4\pi k\rho \quad (Gauss'Law\ for\ electricity) \tag{2.36}$$

$$\vec{\nabla} \cdot \vec{B} = 0 \quad (Gauss'Law\ for\ magnetism) \tag{2.37}$$

$$\vec{\nabla}\, x\vec{E} = -\frac{\partial}{\partial t}\vec{B} \quad (Faraday's\ Law\ of\ induction) \tag{2.38}$$

$$\vec{\nabla} x \vec{B} = \frac{4\pi k}{c^2}\vec{J} + \frac{1}{c^2} \cdot \frac{\partial}{\partial t}\vec{E} = \frac{\vec{J}}{\varepsilon_0 c^2} + \frac{1}{c^2} \cdot \frac{\partial}{\partial t}\vec{E} = \mu_0 \vec{J} + \frac{1}{c^2} \cdot \frac{\partial}{\partial t}\vec{E} \quad (Ampère's\ Law) \tag{2.39}$$

, where $k = \frac{1}{4\pi\varepsilon_0}$ and $c^2 = \frac{1}{\varepsilon_0 \mu_0}$.

Differential form of Maxwell's equations with magnetic and/or polarizable media

$$\vec{\nabla} \cdot \vec{D} = \rho, (Gauss'Law\ for\ electricity) \tag{2.40}$$

, where $\vec{D} = \varepsilon_0 \vec{E} + \vec{P}$ is used for the general case, $\vec{D} = \varepsilon_0 \vec{E}$ is for the free space and $\vec{D} = \varepsilon \vec{E}$ is used for an isotropic media.

$$\vec{\nabla} \cdot \vec{B} = 0 \quad (Gauss'Law\ for\ magnetism) \tag{2.41}$$

$$\vec{\nabla} x \vec{E} = -\frac{\partial}{\partial t}\vec{B} \quad (Faraday's\ Law\ of\ induction) \tag{2.42}$$

, where $\vec{B} = \mu_0(\vec{H} + \vec{M})$ for the general case, $\vec{B} = \mu_0 \vec{H}$ for free space and $\vec{B} = \mu \vec{H}$ for an isotropic linear magnetic medium.

$$\vec{\nabla} x \vec{H} = \vec{J} + \frac{\partial}{\partial t}\vec{D} \quad (Ampère's\ Law) \tag{2.43}$$

2.3. Intensity and power

For a monochromatic wave, it holds that: $I(\vec{r}) = |\psi(\vec{r})|^2$. As it can be seen, the intensity of a monochromatic wave doesn't vary with time. This comes from $\psi(\vec{r}) = A(\vec{r})cos\big(2\pi\vartheta \pm \varphi(\vec{r})\big)$ inserted into the following equation[11,21,24]:

$$\begin{aligned}\big\{Re\{\psi(\vec{r},t)\}\big\}^2 &= \left\{\frac{1}{2}[\psi(\vec{r},t) + \psi^*(\vec{r},t)]\right\}^2 = \\ &= \left\{\frac{1}{2}\big[A(\vec{r},t)cos\big(2\pi\vartheta \pm \varphi(\vec{r},t)\big) + A(\vec{r},t)cos\big(2\pi\vartheta \pm \varphi(\vec{r},t)\big)\big]\right\}^2 = \\ &= \big\{A(\vec{r}) * \cos\big(2\pi\vartheta \pm \varphi(\vec{r})\big)\big\}^2 = \frac{A(\vec{r})^2}{2}\end{aligned} \tag{2.44}$$

Which yields the following if averaging for longer than $\frac{1}{\vartheta}$ is done:

$$2 * \big\{Re\{\psi(\vec{r},t)\}\big\}^2 = \{\psi(\vec{r},t)\}^2 = I(\vec{r},t) \tag{2.45}$$

Or it can be expressed simply as $I(\vec{r},t) = 2 \cdot \langle \nabla^2 \psi(\vec{r},t) \rangle \ \left[\frac{W}{cm^2}\right]$ (2.46)

The optical power is then[24]:

$$P(t) = \int_S I(\vec{r},t) d\vec{s} \ [W] \tag{2.47}$$

, while the optical energy is[24]: (2.48)

$$E_{Energy}(t) = \int_t P(t) dt \ [J]$$

2.4. Superposition principle

The superposition principle is one of the most fundamental yet most important property of waves, in this case of light.

If two waves are described by[11,21]:

$$\nabla^2 \psi_1(x,y,z,t) = \frac{1}{v^2} \cdot \frac{\partial^2 \psi_1(x,y,z,t)}{\partial t^2} \tag{2.49}$$

$$\nabla^2 \psi_2(x,y,z,t) = \frac{1}{v^2} \cdot \frac{\partial^2 \psi_2(x,y,z,t)}{\partial t^2} \tag{2.50}$$

, if $\psi_1$and ψ_2 are solutions of the Maxwell's equation, then $\psi_1 + \psi_2$ is also a solution and is given by[11,21]:

$$\nabla^2 [\psi_1(x,y,z,t) + \psi_2(x,y,z,t)] = \frac{1}{v^2} \cdot \frac{\partial^2 [\psi_1(x,y,z,t) + \psi_2(x,y,z,t)]}{\partial t^2} \tag{2.51}$$

This means that the resulting disturbance is the algebraic sum of the individual constituent waves at that location. Depending on the fact if the waves are in phase or out of phase, another property which is a result of the superposition principle, which is the constructive or destructive interference will manifest.

2.5. Polarization

The characteristic vector of light determines its propagation in different media and its transmission, reflection and refraction when it passes through boundaries between different media.

Light's polarization determines the behavior of the electrical field vector $\vec{E}(x,y,z,t)$ and its development with time. The vector of polarization lies in a plane perpendicular to the direction of propagation.[24]

Let us have a monochromatic plane wave with angular frequency ω travelling in the z direction with velocity c. The electric field $\vec{E}(x,y,z,t)$ that lies in the $x-y$ plane can be described by[24]:

$$\vec{E}(x,y,z,t) = \vec{E}(z,t) = Re\left\{\vec{A}\cdot e^{j\omega\left(t-\frac{z}{c}\right)}\right\} \tag{2.52}$$

, where $\vec{A} = \tilde{A}_x\cdot\vec{x}+\tilde{A}_y\cdot\vec{y} = A_x e^{j\varphi_x}\cdot\vec{x} + A_y e^{j\varphi_y}\cdot\vec{y}$ represents the complex envelope and the $\tilde{}$ symbol represents complex components.

To make the writing simpler, a vector of the form $\vec{r} = r_x\cdot\vec{x}+r_y\cdot\vec{y}+r_z\cdot\vec{z}$ is used instead of writing the set of coordinates (x,y,z,t), hence $\vec{E}(x,y,z,t) = \vec{E}(\vec{r},t)$.

Ideally, depending on the case, the electric and magnetic field vectors oscillate with the same frequency, but this isn't always the case. Both of the electric and magnetic field vectors can oscillate independently from each other, leading to different kinds of polarization.

The real and imaginary part of a complex electric field vector do not represent any physical significance, they are just written so for mathematical convenience.

2.5.1. Elliptical polarization

Since the wave travels in the z direction, then[24]:

$$\begin{aligned}\vec{E}(\vec{r},t) = \vec{E}(z,t) = E_x\cdot\vec{x} + E_y\cdot\vec{y} = Re\left\{\left[A_x e^{j\varphi_x}\cdot\vec{x} + A_y e^{j\varphi_y}\cdot\vec{y}\right]\cdot e^{j\omega\left(t-\frac{z}{c}\right)}\right\} = \\ = Re\left\{\left[A_x e^{j\left\{\varphi_x+\omega\left(t-\frac{z}{c}\right)\right\}}\cdot\vec{x} + A_y e^{j\left\{\varphi_y+\omega\left(t-\frac{z}{c}\right)\right\}}\cdot\vec{y}\right]\right\} = \\ = A_x cos\left[\omega\left(t-\frac{z}{c}\right)+\varphi_x\right]\cdot\vec{x} + A_y cos\left[\omega\left(t-\frac{z}{c}\right)+\varphi_y\right]\cdot\vec{y}\end{aligned} \tag{2.53}$$

By separating each component, then[24]:

$$E_x = A_x cos\left[\omega\left(t-\frac{z}{c}\right)+\varphi_x\right] \tag{2.54}$$

$$E_y = A_y cos\left[\omega\left(t-\frac{z}{c}\right)+\varphi_y\right] \tag{2.55}$$

These two equations are the parametric equations of the ellipse[26]:

$$\frac{E_x^2}{A_x^2}+\frac{E_y^2}{A_y^2}-2\frac{E_x E_y}{A_x A_y}\cos(\varphi_x-\varphi_y) = sin^2(\varphi_x-\varphi_y) \tag{2.56}$$

The orientation and shape of the ellipse will determine its polarization. If the z coordinate is frozen, the electric field vector will rotate elliptically on the $x-y$ plane. If time t is frozen, it will rotate forming a helix through an elliptical cylinder in space.

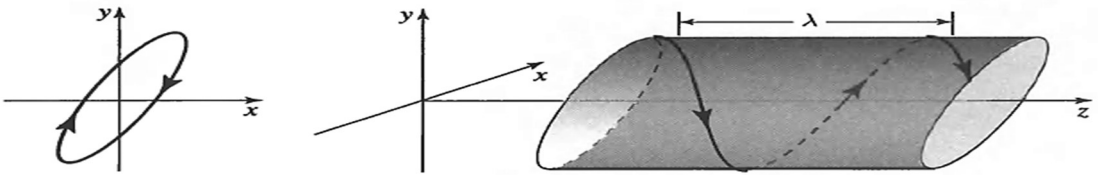

a) b)

Fig.2.3. *Representation of a circular polarization: a) movement of the electric field vector and b) spatial representation of the envelope that the electric field vector traces.*[24]

2.5.2. Linear polarization

If from *eq.(2.53)* $A_x = 0$, then the wave will be linearly polarized in the y direction. If $A_y = 0$ then the wave will be linearly polarized in the x direction. The wave will have a linear polarization also for the cases when the phase difference between the components of the electrical field will be shifted for $\varphi = 0$ and $\varphi = \pi$, from[21,25]:

$$E_x = A_x cos\left[\omega\left(t - \frac{z}{c}\right) + \varphi_x\right] = A_x cos\left[\omega\left(t - \frac{z}{c}\right)\right] \tag{2.57}$$

$$E_y = A_y cos\left[\omega\left(t - \frac{z}{c}\right) + \varphi_y\right] = A_y cos\left[\omega\left(t - \frac{z}{c}\right)\right] \tag{2.58}$$

$$\Rightarrow for\ \varphi = 0;\quad \frac{E_x}{E_y} = \frac{A_x}{A_y} \tag{2.59}$$

$$\Rightarrow for\ \varphi = \pi;\quad \frac{E_x}{E_y} = -\frac{A_x}{A_y} \tag{2.60}$$

, which both represent equations of a straight line. In this case it is said that the wave has a linear polarization. In general, the condition is $\varphi = m\pi\ (for\ m = \pm 1, \pm 2, \dots)$.

If $A_x = A_y$, then the linear behavior of the electric field will draw a plane, which is called the plane of polarization, which in this case will form an angle of $45°$ with both axes.[24]

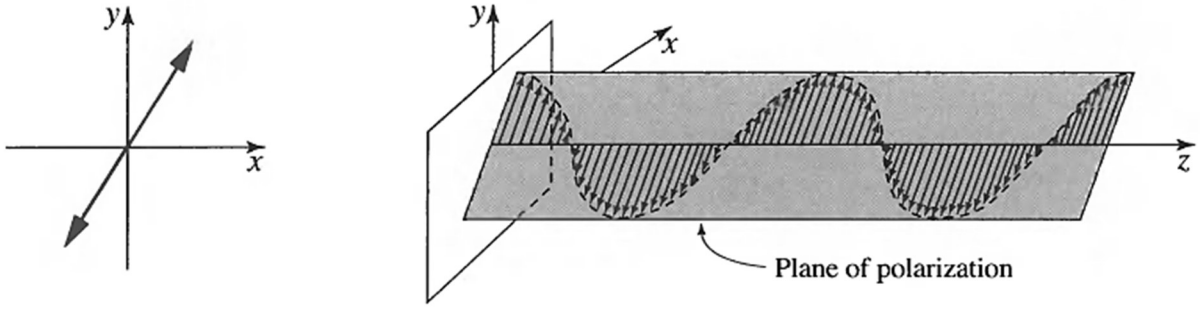

a) b)

Fig.2.4. *Representation of a linear polarization: a) movement of the electric field vector and b) spatial representation of plane that the electric field vector traces.*[24]

2.5.3. Circular polarization

For the cases when $\varphi = \pm\frac{\pi}{2}$ and $A_x = A_y = A_o$, the following stand[11,21,24–26]:

$$E_x = A_x cos\left[\omega\left(t - \frac{z}{c}\right) + \varphi_x\right] = A_0 cos\left[\omega\left(t - \frac{z}{c}\right) \pm 0\right] = A_0 cos\left[\omega\left(t - \frac{z}{c}\right)\right] \quad (2.61)$$

$$E_y = A_y cos\left[\omega\left(t - \frac{z}{c}\right) + \varphi_y\right] = A_0 cos\left[\omega\left(t - \frac{z}{c}\right) \mp \frac{\pi}{2}\right] = A_0 sin\left[\omega\left(t - \frac{z}{c}\right)\right] \quad (2.62)$$

$$\Rightarrow E_x^2 + E_y^2 = A_0^2 \quad (2.63)$$

, which represents the equation of a circle with radius A_0.

If z is frozen, the tip of the electrical field vector will rotate in space forming a circular cylinder. If $\varphi = +\frac{\pi}{2}$ it will rotate clockwise when viewed from the direction to where the wave is headed, and is said to be right circularly polarized. While if $\varphi = -\frac{\pi}{2}$ it will rotate counterclockwise and is said to be left circularly polarized. This way of denoting the circular polarization isn't always used, so it is necessarily to always doublecheck with the literature that was used, since different books of optics provide with one of the convention. The general condition is $\varphi = \pm\frac{\pi}{2} + 2m\pi\ (for\ m = 0, \pm1, \pm2, \dots)$.[24]

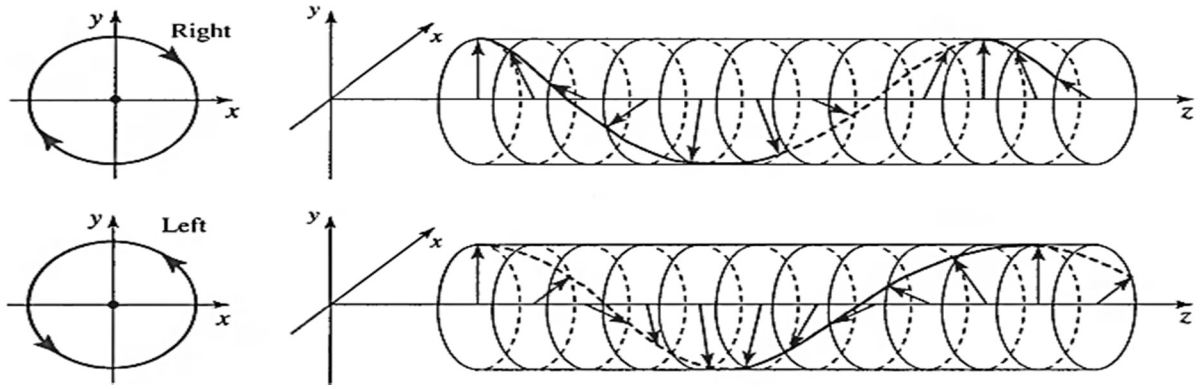

a) b)

Fig.2.5. *Representation of right and left circular polarization: a) movement of the electric field vector and b) spatial representation of the envelope that the electric field vector traces.*[24]

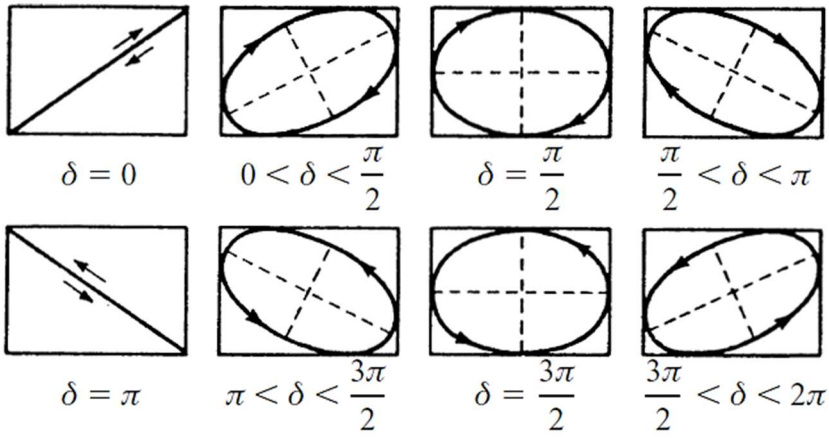

Fig.2.6. *Gradual changing from linear to elliptical polarization for both directions.*[25]

2.5.4. Unpolarized light

For the case when the light is not monochromatic, or if both electric and magnetic component don't oscillate always with the same frequency, it will result in the constant change of polarization. When different atoms emit at different frequencies, and atoms emit for $10^{-8}[s]$, we are unable to track this fast change of polarization, then in this case we speak about unpolarized light. This case causes the averaging of all effects of polarization.[11,27]

Birefringence, optical activity, anomalous refraction (Iceland's famous crystals) etc. are interesting effects of polarization. Absorption can vary with polarization as well. Substances that change the polarization of light passing through it are called polarizers.

2.6. Poynting vector

The flow of the electromagnetic power is described by the Poynting vector. During light propagation, the energy flow is shared equally between both the electric and magnetic fields of the wave. The direction of the Poynting vector doesn't have to be the same as the direction of propagation. The Poynting vector is perpendicular to $\vec{E}$ and $\vec{B}$ and energy flows along the direction of the Poynting vector. In general, the Poynting vector is simply given by[11]:

$$\vec{S} = \vec{E} \times \vec{B} \tag{2.64}$$

If the wave is described by an harmonic, linearly polarized plane wave travelling in the $\vec{k}$ direction in free space, where $\vec{E} = \vec{E}_0 \cos(\vec{k} \cdot \vec{r} - \omega t)$ and $\vec{B} = \vec{B}_0 \cos(\vec{k} \cdot \vec{r} - \omega t)$, where $\vec{E}_0 = E_0(\vec{r})$, $\vec{B}_0 = B_0(\vec{r})$, then the Poynting vector is given by[11]:

$$\vec{S} = c^2 \varepsilon_0 \vec{E}_0 \times \vec{B}_0 cos^2\left(\vec{k} \cdot \vec{r} - \omega t\right) = \frac{1}{\mu_0} \cdot \vec{E}_0 \times \vec{B}_0 \cdot cos^2\left(\vec{k} \cdot \vec{r} - \omega t\right) \tag{2.65}$$

$$\left|\vec{S}\right| = S = \left[\vec{E}_0 \perp \vec{B}_0 \forall \text{ t}\right] = \frac{1}{\mu_0} \underbrace{\left|\vec{E}_0 \times \vec{B}_0\right|}_{E_0 B_0} \cdot \underbrace{\left|cos^2\left(\vec{k} \cdot \vec{r} - \omega t\right)\right|}_{1} = \frac{1}{\mu_0} E_0 B_0 \tag{2.66}$$

Irradiance (or the optical density) is the average energy per unit area per unit time and is given through the time averaging of the Poynting vector[11]:

$$I = \langle S \rangle_T = \varepsilon_0 c \lim_{T \to \infty} \frac{1}{2T} \int_{-T}^{T} E^2 dt = \frac{c^2 \varepsilon_0}{2} \vec{E}_0 x \vec{B}_0 = \frac{c^2 \varepsilon_0}{2} E_0^2 = \varepsilon_0 c \langle E^2 \rangle_T = \frac{c}{\mu_0} \langle B^2 \rangle_T \tag{2.67}$$

, by using the relation $E = cB$. For a monochromatic wave, it holds that: $I(\vec{r}) = |\psi(\vec{r})|^2$. As it can be seen, the intensity of a monochromatic wave doesn't vary with time.

Since all the detectors (photodiodes, photoelectronic devices, photomultipliers, human eye and photoemulsions) react on the quadratic electrical intensity, they are often referred to as quadratic detectors. The physical justification of using a time averaged value comes from the fact that detectors aren't capable of following changes of intensity of light. This frequency of fluctuation is too high, hence the usage of the time averaged identity.[11]

In an isotropic, linear, nondispersive and homogenous material, the vectors $\vec{P}$ and $\vec{E}$ are parallel to each other and propagate in the same direction. The relation between both of them is[24]:

$$\vec{P} = \varepsilon_0 \chi \vec{E} \tag{2.68}$$

, where χ is the electric susceptibility. This leads to[24]:

$$\vec{D} = \varepsilon_0 \vec{E} + \vec{P} = \varepsilon_0 \vec{E}(1 + \chi) = \varepsilon \vec{E} \tag{2.69}$$

This implies that $\vec{D}$ and $\vec{E}$ are also parallel. This also leads to[24]:

$$\vec{B} = \mu \vec{H} \tag{2.70}$$

For a monochromatic planewave in an isotropic material, it stands that[21]:

$$\vec{S} = \vec{E} \times \vec{H} = \vec{E} \times \frac{\vec{B}}{\mu_0} = \vec{E} \times \frac{\vec{k} \times \vec{E}}{\mu_0 \omega_0} = \frac{E^2}{\mu_0 \omega_0} \vec{k} = \frac{\frac{u_{em}}{\varepsilon_0}}{\mu_0 \omega_0} \cdot \frac{\omega \vec{n}}{c} = \vec{n} \cdot u_{em} c \tag{2.71}$$

For an anisotropic media, the Poynting vector propagates at an angle θ_{aniso} from the wave vector. This implies that $\vec{D}$ will also propagate at the angle θ_{aniso} from $\vec{E}$, for which[21]:

$$\vec{k} \cdot \vec{S} = kScos(\theta_{aniso}) \tag{2.72}$$

$$\vec{k} \cdot \vec{S} = \vec{k} \cdot (\vec{E} \times \vec{H}) = \vec{E} \cdot (\vec{H} \times \vec{k}) = \vec{E} \omega \vec{D} = \omega u_{em} \tag{2.73}$$

$$\Rightarrow kScos(\theta_{aniso}) = \omega u_{em} \Rightarrow S = \frac{\omega u_{em}}{kcos(\theta_{aniso})} = \frac{u_{em}}{cos(\theta_{aniso})} \tag{2.74}$$

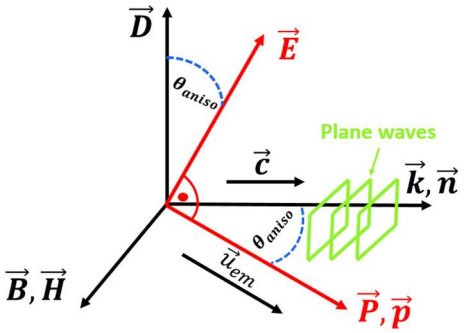

Fig.2.7. *Poynting vector and angle formation.*[21]

2.7. Interference

2.7.1. General

According to the superposition principle, the resultant electric-field intensity $\vec{E}$ is equal to the vector sum of each of the individual waves at that point in space. The optical interference is formulated somehow similar, defining it as the total irradiance from two or more waves coming from their individual interactions, which will deviate from the sum of the component irradiances[21]:

$$\vec{E} = \vec{E}_1 + \vec{E}_2 + \cdots + \vec{E}_n = \sum_{i=1}^{n} \vec{E}_i \tag{2.75}$$

Since lights varies fast in frequency, generally analyzing the interference through light's intensity will be easier. In order to generalize the analysis, let's consider that our light waves are monochromatic and of the same frequency, propagating in a homogenous medium. Here it is considered that the point of interference P is far enough from the sources, in order for the waves to be considered as planwaves and any split of the waves to be greater than their wavelength.

2.7.2. Interference of two waves

Let two waves be defined as the following[11]:

$$\vec{E}_1(\vec{r},t) = \vec{E}_{01}cos\left(\vec{k}_1 \cdot \vec{r} - \omega t + \varepsilon_1\right) \tag{2.76}$$

$$\vec{E}_2(\vec{r},t) = \vec{E}_{02}cos\left(\vec{k}_2 \cdot \vec{r} - \omega t + \varepsilon_2\right) \tag{2.77}$$

The irradiance from both waves is for simplicity[11]:

$$I = \langle S\rangle_T = \varepsilon_0 c\langle E^2\rangle_T = \varepsilon_0 c\langle \vec{E}\cdot\vec{E}\rangle_T = \varepsilon_0 c\langle\left(\vec{E}_1+\vec{E}_2\right)\cdot\left(\vec{E}_1+\vec{E}_2\right)\rangle_T \sim \langle\left(\vec{E}_1+\vec{E}_2\right)\cdot\left(\vec{E}_1+\vec{E}_2\right)\rangle_T \tag{2.78}$$

From this, the following can be written[11]:

$$\vec{E}^2 = \left(\vec{E}_1+\vec{E}_2\right)\cdot\left(\vec{E}_1+\vec{E}_2\right) = {\vec{E}_1}^2 + {\vec{E}_2}^2 + 2\vec{E}_1\vec{E}_2 \tag{2.79}$$

From this, using the above relation for $\langle E^2\rangle_T$ for each of the components, the following is obtained[11]:

$$I = I_1 + I_2 + I_{12} \tag{2.80}$$

Of particular interest is the last term of the equation. By further mathematical analysis, it results that[11]:

$$\begin{aligned}\langle\vec{E}_1\cdot\vec{E}_2\rangle_T = \langle\vec{E}_{01}\cdot\vec{E}_{02}\cdot\{&\cos\left(\vec{k}_1\cdot\vec{r}+\varepsilon_1\right)\cdot\cos(\omega t)+\sin\left(\vec{k}_1\cdot\vec{r}+\varepsilon_1\right)\cdot\sin(\omega t)\}\\ &\cdot\{\cos\left(\vec{k}_2\cdot\vec{r}+\varepsilon_2\right)\cdot\cos(\omega t)+\sin\left(\vec{k}_2\cdot\vec{r}+\varepsilon_2\right)\cdot\sin(\omega t)\}\rangle_T =\end{aligned} \tag{2.81}$$

$$\begin{aligned}= \langle\vec{E}_{01}\cdot\vec{E}_{02}\{&\cos\left(\vec{k}_1\cdot\vec{r}+\varepsilon_1\right)\cos\left(\vec{k}_2\cdot\vec{r}+\varepsilon_2\right)\cos^2(\omega t)\\ &+\cos\left(\vec{k}_1\cdot\vec{r}+\varepsilon_1\right)\sin\left(\vec{k}_2\cdot\vec{r}+\varepsilon_2\right)\sin(\omega t)\cos(\omega t)\\ &+\sin\left(\vec{k}_1\cdot\vec{r}+\varepsilon_1\right)\cos\left(\vec{k}_2\cdot\vec{r}+\varepsilon_2\right)\sin(\omega t)\cos(\omega t)\}\\ &+\sin\left(\vec{k}_1\cdot\vec{r}+\varepsilon_1\right)\sin\left(\vec{k}_2\cdot\vec{r}+\varepsilon_2\right)\sin^2(\omega t)\rangle_T\end{aligned}$$

Knowing that $\langle\cos^2(\omega t)\rangle_T = \langle\sin^2(\omega t)\rangle_T = \frac{1}{2}$ and $\langle\cos(\omega t)\sin(\omega t)\rangle_T = 0$ and rearranging, results in[11]:

$$\langle\vec{E}_1\cdot\vec{E}_2\rangle_T = \vec{E}_{01}\cdot\vec{E}_{02}\cdot\frac{1}{2}\cdot\cos\left(\vec{k}_1\cdot\vec{r}-\vec{k}_2\cdot\vec{r}+\varepsilon_1-\varepsilon_2\right) = \frac{1}{2}\vec{E}_{01}\vec{E}_{02}cos\theta \tag{2.82}$$

, where θ represents the phase difference between the two waves. This phase difference comes from different initial phase shift (if it exists) and the path length difference that arises while propagating. Thus[11]:

$$I_{12} = \langle\vec{E}_1\cdot\vec{E}_2\rangle_T = \frac{1}{2}\vec{E}_{01}\vec{E}_{02} \tag{2.83}$$

By taking in account that[11]:

$$I_1 = \langle\vec{E}_1\cdot\vec{E}_1\rangle_T = \frac{1}{2}E_{01}^2 \rightarrow E_{01} = \sqrt{2I_1} \tag{2.84}$$

$$I_2 = \langle\vec{E}_2\cdot\vec{E}_2\rangle_T = \frac{1}{2}E_{02}^2 \rightarrow E_{02} = \sqrt{2I_2} \tag{2.85}$$

It can now be written that[11]:

$$I = I_1 + I_2 + 2cos\theta\sqrt{I_1 I_2} \tag{2.86}$$

From the previous equation, the following cases are obtained[11]:

a) For $cos\theta = 1$, which means $\theta = 0, \pm 2\pi, 4\pi, \dots$, it contributes in a total constructive interference $I_{max} = I$.
b) For $0 < cos\theta < 1$, with out of phase waves, it contributes in constructive interference and $I_1 + I_2 < I < I_{max}$.
c) For $cos\theta = 0$ it results in $I = I_1 + I_2$.
d) For $-1 < cos\theta < 0$, destructive interference appears and $I_1 + I_2 > I > I_{min}$
e) For $cos\theta = -1$, which means $\theta = \pm\pi, \pm 3\pi, \dots$, it contributes in total destructive interference and $I_{min} = I_1 + I_2 - 2cos\theta\sqrt{I_1 I_2}$.

It can be seen that, if $\vec{E}_1 \perp \vec{E}_1$, then $I = I_1 + I_2$, because $I_{12} = 0$. If $\vec{E}_1 \parallel \vec{E}_1$ then $I = I_1 + I_2 + 2\sqrt{I_1 I_2}$. For the case that both waves' intensities are equal at the interference point, it can be written that $I_1 = I_2 = I_0$, thus having[11]:

$$I = 4I_0 cos^2\left(\frac{\theta}{2}\right) \tag{2.87}$$

The analysis could also be done with the exponential form, with phasors. If both complex waves are defined as[21]:

$$\vec{E}_1 = Re\left\{E_{01} e^{i\{\vec{k}_1 \cdot \vec{r} + \varepsilon_1\}} e^{-i\omega t}\right\} = Re\{\vec{\xi}_1 e^{-i\omega t}\} = Re\{\vec{\xi}_1\} cos(\omega t) + Im\{\vec{\xi}_1\} sin(\omega t) \tag{2.88}$$

$$\vec{E}_2 = Re\left\{E_{02} e^{i\{\vec{k}_2 \cdot \vec{r} + \varepsilon_2\}} e^{-i\omega t}\right\} = Re\{\vec{\xi}_2 e^{-i\omega t}\} = Re\{\vec{\xi}_2\} cos(\omega t) + Im\{\vec{\xi}_2\} sin(\omega t) \tag{2.89}$$

, then at the point of interference it can be written that[21]:

$$\vec{\xi} e^{-i\omega t} = (\vec{\xi}_1 + \vec{\xi}_2) e^{-i\omega t} \tag{2.90}$$

If it is taken in account that $\vec{k}_1$ and $\vec{k}_1$ form an angle θ_z with the direction of propagation (in this case assuming z axis) with $\vec{k}_1 = (ksin\theta_z, 0, kcos\theta_z), \vec{k}_2 = (-ksin\theta_z, 0, kcos\theta_z)$, the falling waves form an angle α at the interference point, and if it is considered that $E_{01} = E_{02} = E$ and $\varepsilon_1 = \varepsilon_2 = 0$, the following is obtained[21]:

$$\vec{\xi} = \vec{\xi}_1 + \vec{\xi}_2 = E\{e^{ikxsin\theta_z} e^{ikzcos\theta_z} + e^{-ikxsin\theta_z} e^{ikzcos\theta_z}\} = 2Ecos(kxsin\theta_z) e^{ikzcos\theta_z} \tag{2.91}$$

$$I = \langle \vec{E}^2 \rangle = \langle \left(Re\{\vec{\xi} e^{-i\omega t}\}\right)^2 \rangle = 2E^2 cos^2(kxsin\theta_z) = 4{I_0}^2 cos^2(kxsin\theta_z) \tag{2.92}$$

The spatial period of fringes is given as[21]:

$$\Lambda(\alpha) = \frac{\pi}{ksin\theta_z cos\alpha} = \frac{\lambda}{2sin\theta_z cos\alpha} \tag{2.93}$$

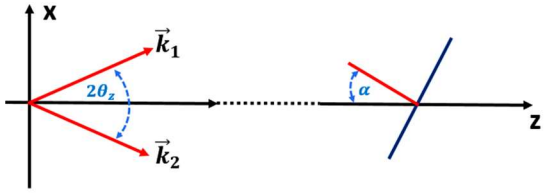

Fig.2.8. *Geometrical configuration of interfering rays.*[21]

2.7.3. Interference of three waves

For the case of three waves with $\vec{k}_1 = (ksin\theta_z, 0, kcos\theta_z), \vec{k}_2 = (0,0,k), \vec{k}_3 = (-ksin\theta_z, 0, kcos\theta_z)$, it can be written that[21]:

$$\vec{\xi} = \vec{\xi}_1 + \vec{\xi}_2 + \vec{\xi}_3 \approx E\big(1 + 2cos(kxsin\theta_z)\big)e^{ikz} \tag{2.94}$$

$$I \approx E^2\big(1 + 2cos(kxsin\theta_z)\big)^2 \tag{2.95}$$

2.7.4. Interference of *N* waves

For the case of N waves with $\vec{k}_m = \left(ksin\theta_z cos\left(\frac{2\pi m}{N}\right), ksin\theta_z sin\left(\frac{2\pi m}{N}\right), kcos\theta_z\right)$, it can simply be written that[21]:

$$I = \left|\vec{\xi}\right|^2 = \left|\sum_{m=1}^{N} \vec{\xi}_m\right|^2 \tag{2.96}$$

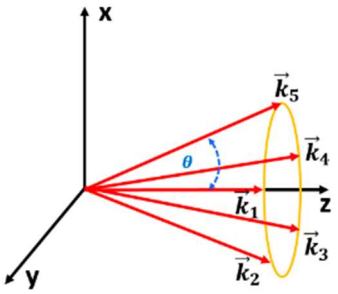

Fig.2.9. *Five plane waves' wavevectors and their angle* θ_z.[21]

2.7.5. Spherical waves and their interference

Let two spherical waves coming from two openings at a distance $d_{opening}$ from each other be defined as[11]:

$$\vec{E}_1(r_1, t) = \vec{E}_{01}(r_1)cos(k \cdot r_1 - \omega t + \varepsilon_1) = \vec{E}_{01}(r_1)e^{i\{k \cdot r_1 - \omega t + \varepsilon_1\}} \tag{2.97}$$

$$\vec{E}_2(r_2, t) = \vec{E}_{02}(r_2)cos(k \cdot r_2 - \omega t + \varepsilon_2) = \vec{E}_{02}(r_2)e^{i\{k \cdot r_2 - \omega t + \varepsilon_2\}} \tag{2.98}$$

Then the phase at the interference point, far from the source, is[11]:

$$\theta = k(r_1 - r_2) + (\varepsilon_1 - \varepsilon_2) \tag{2.99}$$

In the vicinity of the source, it is expected that the spatial average intensity to be constant and remain as $I = I_1 + I_2$, because $\langle I_{12}\rangle_{space} = \langle \vec{E}_{01}\vec{E}_{02}cos\theta\rangle = 0$, since depending on the position from point to point the flux density will be different.[11]

In regions where $d_{opening}$ is small compared to the measuring point (at r_1 or r_2), it can be assumed that $\vec{E}_{01}$ and $\vec{E}_{02}$ are constant for a small region. In this case, it can be considered that the intensity of the light at the interfering point is[11]:

$$I = 4I_0 cos^2\left(\frac{\theta}{2}\right) = 4I_0 cos^2\left(\frac{k(r_1 - r_2) + (\varepsilon_1 - \varepsilon_2)}{2}\right) \tag{2.100}$$

This is holds for the case when $\vec{E}_{01} = \vec{E}_{02}$ and $I_1 = I_2 = I_0$. In this case[11]:

$$a) \quad I = I_{max} \quad for \quad cos\left(\frac{k(r_1-r_2)+(\varepsilon_1-\varepsilon_2)}{2}\right) = 1 \rightarrow r_1 - r_2 = \frac{2\pi m+\varepsilon_2-\varepsilon_1}{k} \tag{2.101}$$

$$b) \quad I = I_{min} \quad for \quad cos\left(\frac{k(r_1-r_2)+(\varepsilon_1-\varepsilon_2)}{2}\right) = 0 \rightarrow r_1 - r_2 = \frac{\pi(2m+1)+\varepsilon_2-\varepsilon_1}{k} \tag{2.102}$$

The exponential form analysis would look like as the following[21]:

$$\vec{E}_1 = E_{01}e^{i\{k_1\cdot r-\omega t+\varepsilon_1\}} = E_{01}e^{i\{k_1\cdot r+\varepsilon_1\}}e^{-i\omega t} = \vec{\xi}_1 e^{-i\omega t} \tag{2.103}$$

$$\vec{E}_2 = E_{02}e^{i\{k_2\cdot r-\omega t+\varepsilon_2\}} = E_{02}e^{i\{k_2\cdot r+\varepsilon_2\}}e^{-i\omega t} = \vec{\xi}_2 e^{-i\omega t} \tag{2.104}$$

The parabolic approximation can be used to rewrite them as[21]:

$$\vec{\xi}_1 = E_{01}e^{i\{k_1\cdot r+\varepsilon_1\}} = [\varepsilon_1 = 0, E_{01} = E_{02} = E, k_1 = k] \approx Ee^{ikz+\frac{ik}{2z}\left\{\left(x+\frac{d_{opening}}{2}\right)^2+y^2\right\}} \tag{2.105}$$

$$\vec{\xi}_2 = E_{01}e^{i\{k_2\cdot r+\varepsilon_2\}} = [\varepsilon_2 = 0, E_{01} = E_{02} = E, k_2 = k] \approx Ee^{ikz+\frac{ik}{2z}\left\{\left(x-\frac{d_{opening}}{2}\right)^2+y^2\right\}} \tag{2.106}$$

The intensity will be[21]:

$$I = \left|\vec{E}_1 + \vec{E}_1\right|^2 = \left|\vec{\xi}_1 e^{-i\omega t} + \vec{\xi}_2 e^{-i\omega t}\right|^2 \tag{2.107}$$

$$I \sim \langle E^2\rangle_T = \langle\left(\vec{E}_1 + \vec{E}_2\right)\cdot\left(\vec{E}_1 + \vec{E}_2\right)\rangle_T = \langle\vec{E}_1{}^2\rangle_T + \langle\vec{E}_2{}^2\rangle_T + \langle 2\vec{E}_1\vec{E}_2\rangle_T = I_1 + I_2 + I_{12} \tag{2.108}$$

, where:

$$I_1 = \langle\vec{E}_1\cdot\vec{E}_1\rangle_T = \langle\vec{\xi}_1 e^{-i\omega t}\cdot\vec{\xi}_1 e^{-i\omega t}\rangle_T = \frac{1}{2}E_{01}^2 \tag{2.109}$$

$$I_2 = \langle\vec{E}_2\cdot\vec{E}_2\rangle_T = \langle\vec{\xi}_2 e^{-i\omega t}\cdot\vec{\xi}_2 e^{-i\omega t}\rangle_T = \frac{1}{2}E_{02}^2 \tag{2.110}$$

$$I_{12} = \langle 2\vec{\xi}_1 e^{-i\omega t}\vec{\xi}_2 e^{-i\omega t}\rangle_T = \tag{2.111}$$

$$= 2\langle E_{01}e^{ikz+\frac{ik}{2z}\left\{\left(x+\frac{d_{opening}}{2}\right)^2+y^2\right\}}e^{-i\omega t}\cdot E_{02}e^{ikz+\frac{ik}{2z}\left\{\left(x-\frac{d_{opening}}{2}\right)^2+y^2\right\}}e^{-i\omega}\rangle_T =$$

$$= E_{01}E_{02}\frac{1}{2}cos\left(kz+\frac{k}{2z}\left\{\left(x+\frac{d_{opening}}{2}\right)^2+y^2\right\} - kz+\frac{k}{2z}\left\{\left(x-\frac{d_{opening}}{2}\right)^2+y^2\right\}\right) =$$

$$= E_{01}E_{02}\frac{1}{2}cos\left(\frac{kxd}{z}\right)$$

Since $E_{01} = E_{02} = E$, it turns out that $I_1 = I_2 = I_0$, thus[21]:

$$I_{12} = E^2\frac{1}{2}cos\left(\frac{kxd}{z}\right) = 2I_0 cos\left(\frac{kxd}{z}\right) \tag{2.112}$$

$$I = I_0 + I_0 + E^2\frac{1}{2}cos\left(\frac{kxd}{z}\right) = 2I_0 + 2I_0 cos\left(\frac{kxd}{z}\right) = 4I_0 cos^2\left(\frac{kxd}{2z}\right) = 2E^2 cos^2\left(\frac{kxd}{2z}\right) \tag{2.113}$$

2.7.6. Optical path

Previously, it was assumed that the waves propagate in air, but in this thesis and in many real applications, the optical waves propagate in mediums with different refractive indices. Here, some light onto the effect of such media is shed. The phase difference between two waves, denoted as $\Delta\varphi$, can be expressed via the geometrical path of both waves by the relation[21]:

$$\Delta\varphi = k\Delta s = k_0 n\Delta s = k_0\Delta l \tag{2.114}$$

, where $k = \frac{\omega}{c}$ is the wave number in a specified media with index of refraction n and speed of light c, while $k_0 = \frac{\omega}{c_0}$ is in vaccum and speed of light c_0. From these, the following relation exists[21]:

$$n = \frac{k}{k_0} = \frac{c_0}{c} \tag{2.115}$$

The relation for the difference of optical paths is given by:

$$\Delta l = n\Delta s \tag{2.116}$$

In wave optics, the optical path is defined as[11,21]:

$$l = \int nds \tag{2.117}$$

The relation between the geometric path difference and the optical path difference is[21]:

$$\Delta\varphi = k_0\Delta l = \frac{2\pi}{\lambda}\Delta l \tag{2.118}$$

2.7.7. Coherence

If two lightbulbs are taken and the light projected in a screen is observed, no interference fringes will manifest, only a uniform brightness is seen, the intensity of which is equal to the sum of the intensities of each of them.[28]

For the case when the two beams that interfere have a significant difference in frequencies, this produces a rapid phase difference, thus making I_{12} to average toward zero when being detected and the total intensity to be equal to the sum of the intensities of each individual wave. To produce observable fringes, the two sources must emit light with their phases being somehow correlated. This correlation is called coherence and coherence can be defined as the ability of light to interfere.[28]

In case of a shift (constant shift), similar interference can be detected. Thus, the two sources must be coherent in space and in time. Interference happens with sources of a single wavelength. White light does partially interfere, but it doesn't produce a clear interference fringe pattern.[21]

2.7.7.1. Temporal coherence

Light is emitted by atoms. All these atoms emit light independently, with a specific quanta of energy (photons) of the time range of $10^{-8}[s]$, the amplitude of which fluctuates fast in time in a randome way, which means that the spectral width of this light will have a finite spectral band bigger than $10^8[Hz]$. Because of this, beams from two randomly light emitting sources won't produce interference. For this case it is said that these waves are not coherent. If I_1 and I_2 are the intensity of the light coming from respective sources, then the total intensity at some point can be written as $I = I_1 + I_2$.[21]

Each light source has atoms that emit wave trains of a definite length L_c. If in case the difference of the optical path of both waves interfering is greater than L_c, fringes will vanish. Thus, on the screen only a uniform intensity profile will be seen. The spatial extent to which this coherent oscillation of wave trains occurs is defined as the coherence length L_c. Temporal coherence depicts the correlation that a wave has with itself at different points in time. The shortest time interval for which the wave oscillates in a coherent sinusoidal form, is defined as the coherence time[21]:

$$\tau = \frac{L_c}{c} = \frac{c}{c\Delta\upsilon} = \frac{1}{\Delta\upsilon} = \left[\Delta\upsilon = \frac{\upsilon\Delta\lambda}{\lambda}\begin{cases}\frac{\Delta\omega}{\Delta k} = \frac{2\pi\Delta\upsilon}{2\pi\left|\Delta\left(\frac{1}{\lambda}\right)\right|} = \frac{\Delta\upsilon}{\frac{\Delta\lambda}{\lambda^2}} \\ \frac{\omega}{k} = \upsilon\lambda\end{cases}\right] = \frac{\lambda}{\upsilon\Delta\lambda} = [c = \lambda\upsilon] = \frac{\lambda^2}{c\Delta\lambda} \tag{2.119}$$

, where Δf is the finite spectral width. From this it can be said that the coherence length is a measure of the spectral width. The longer this interval, the greater the temporal coherence.

Most light emitting devices we face every day emit incoherent lights, for which the coherent length is of the range of micrometers. In those case, if we would really want to see any interference, the lengths of the interferometer arms would have to be of the same size. On the other hand, laser have coherence lengths that can extend up to few kilometers. But when a laser emits light, it emits light with more than one frequency around the frequency it is meant to. This causes the coherence length to decrease. Thus, selecting lasers as monochromatic as possible is the best solution. The best way to make sure that two waves are coherent is to obtain them through the same source.[21]

2.7.7.2. Effect of spectral broadening from interference

If light is not purely monochromatic, its spectra will contain other frequencies as well. This means that the contrast of interference will be less than the one coming from the pure monochromatic wave. If both interfering waves come from the same source, and the definition of the normalized spectra is used, it can be written that[21]:

$$I(\omega) = I_1(\omega) + I_2(\omega) + 2\sqrt{I_1(\omega)I_2(\omega)}\cos(\omega\tau) \tag{2.120}$$

,where (2.121)

$$I = \int_0^\infty I(\omega)d\omega\,; \quad I_1(\omega) = I_1 g(\omega); \quad I_2(\omega) = I_2 g(\omega); \quad \int_0^\infty g(\omega)d\omega = 1$$

This applies for the interference of waves with the same frequency. Since we talk about multiple frequencies, then all frequencies will have to be take in account, leading to[21]:

$$I = \int_0^\infty I(\omega)\, g(\omega)d\omega = \underbrace{\int_0^\infty I_1(\omega)g(\omega)d\omega}_{I_1} + \underbrace{\int_0^\infty I_2(\omega)g(\omega)d\omega}_{I_2} + \tag{2.122}$$

$$+ \int_0^\infty 2\sqrt{I_1(\omega)I_2(\omega)}\cos(\omega\tau)\, g(\omega)d\omega = I_1 + I_2 + 2\sqrt{I_1 I_2}\gamma(\tau)$$

Where the following is defined as the degree of temporal coherence[21]:

$$\gamma(\tau) = \int_0^\infty \cos(\omega\tau)\, g(\omega)d\omega \tag{2.123}$$

The phase difference can be expressed as follows:

$$\Delta\varphi = k\Delta l = \frac{\omega\Delta l}{c} = \omega\tau \tag{2.124}$$

If an interference experiment with white light (polychromatic) is performed, the individual monochromatic components won't be affected and the resulting interfering pattern will be given as the sum of each of the monochromatic interference pattern:[21]

$$I = \sum_k I(\omega_k) \tag{2.125}$$

Thus, when using white light for interference, only the zero-th order will be white, the rest will be broadened, hence blurred, to a range from violet to red. If there will be white strips or black ones, this is determined by the phase difference $\Delta\varphi = k\Delta l$ between both beams. In the case of white illumination with wider spectra $\Delta\omega$, its wave vector will differ by the value up to $\Delta k = \frac{\Delta\omega}{c}$, thus the coherence length will be[21]:

$$L_c = \frac{2\pi}{\Delta k} = \frac{2\pi}{\underbrace{\Delta\omega}_{\tau_c}} c = \frac{c}{\Delta\upsilon} = \frac{1}{\frac{\Delta\upsilon}{c}} = \frac{1}{\left|\Delta\left(\frac{1}{\lambda}\right)\right|} = \frac{\lambda^2}{\Delta\lambda} \tag{2.126}$$

, where τ_c is the temporal coherence.

When the geometric path difference Δl will be greater than the coherence length L_c, the interference fringe pattern won't be visible. From this, the coherence length depends also on the spectral sensitivity of the detector. If a spectral filter is placed in front of the detector, the interference will increase considerably and the coherence length will be longer.

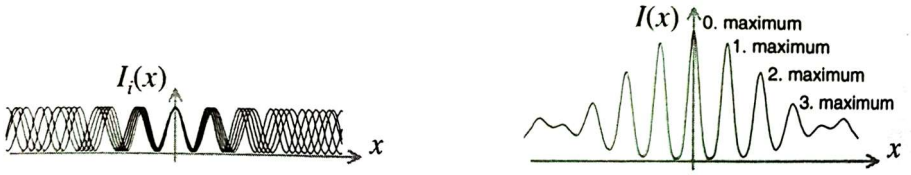

Fig.2.10. *a) Intensity distribution of five different monochromatic beams and b) the intensity profile of the interfering fringes that is formed.*[21]

2.7.7.3. Visibility of fringes

The visibility of interference fringes, which defines the contrast of the visibility of the fringes, is defined as[28]:

$$V = \frac{I_{max} - I_{min}}{I_{max} + I_{min}} = \frac{I_1 + I_2 + 2\sqrt{I_1 I_2} - \left(I_1 + I_2 - 2\sqrt{I_1 I_2}\right)}{I_1 + I_2 + 2\sqrt{I_1 I_2} + \left(I_1 + I_2 - 2\sqrt{I_1 I_2}\right)} = \frac{2\sqrt{I_1 I_2}}{I_1 + I_2} \tag{2.127}$$

Since we deal with finite coherence, it is important to introduce the complex self-coherence, defined as[28]:

$$\Gamma(\tau) = \langle E(t+\tau)E^*(\tau)\rangle = \lim_{T\to\infty}\frac{1}{2T}\int_{-T}^{T} E(t+\tau)E^*(\tau)dt \tag{2.128}$$

, which is basically the autocorrelation of E.

The definition of the normalized degree of coherence is[29]:

$$\gamma(\tau) = \frac{\Gamma(\tau)}{\Gamma(0)} \tag{2.129}$$

This implies that the intensity of two interfering waves is corrected to the form[28]:

$$I = I_1 + I_2 + 2|\gamma|\sqrt{I_1 I_2}cos\theta \tag{2.130}$$

, resulting in[28]:

$$V = \frac{I_{max} - I_{min}}{I_{max} + I_{min}} = \frac{2\sqrt{I_1 I_2}}{I_1 + I_2}|\gamma| \tag{2.131}$$

For the case when $I_1 = I_2 = I_0$, it turns out that $V = |\gamma|$. If a wave has ideally infinite coherence length, then $|\gamma| = 1$, if it is completely incoherent $|\gamma| = 0$ and for partial coherent light it holds that $0 < |\gamma| < 1$.

2.7.7.4. Spatial coherence

Spatial coherence describes the correlation of different parts of the same wavefront.[28]

Spatial coherence is explained via the Young's experiment. If a light source and a screen are placed, and between them an aperture that has two holes is placed, separated between them at a distance d_{sep}, under some conditions the effect of interference will be seen on the screen. Light passing by the appertures will act as a new source of wavefront and will superimpose on the screen, each one having maxima and minima interferences, since optical paths at different points on the screen are different for different point sources. Generally speaking, when taking multiple holes in account, all contributions from each one are compensated.

If the distance between holes surpasses a set limit distance d_{coher} (the coherence distance) the interference fringes vanish, so the compensation doesn't occur. Compared to temporal coherence, the spatial coherence depends on the geometry of the interferometer.[28]

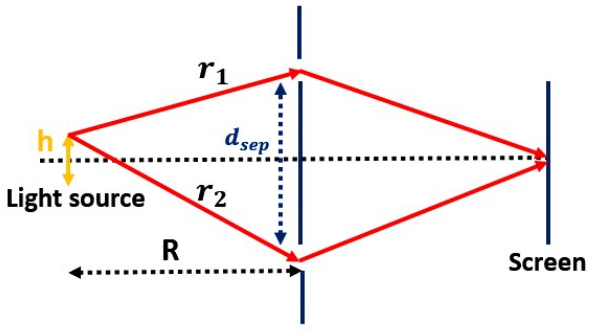

Fig.2.11.*Young's interferometer.*[28]

From the figure above[28]: (2.132)

$$r_2 - r_1 < \frac{\lambda}{2}$$

, where $r_1 = R^2 + \left(\frac{d-h}{2}\right)^2$ and $r_2 = R^2 + \left(\frac{d+h}{2}\right)^2$.

Finally[28]:

$$r_2 - r_1 \approx \frac{dh}{2R} < \frac{\lambda}{2} \tag{2.133}$$

The complex self-spatial coherence is given by[28]:

$$\Gamma(\vec{r}_1, \vec{r}_2, \tau) = \langle E(\vec{r}_1, t+\tau) E^*(\vec{r}_2, \tau) \rangle = \lim_{T\to\infty} \frac{1}{2T} \int_{-T}^{T} E(\vec{r}_1, t+\tau) E^*(\vec{r}_2, \tau) dt \tag{2.134}$$

, where $\vec{r}_1$ and $\vec{r}_2$ represent the spatial vectors of the holes. For partially coherent light, it holds that[28]:

$$I = I_1 + I_2 + 2\sqrt{I_1 I_2} \cdot Re\{\Gamma(\vec{r}_1, \vec{r}_2, \tau)\} \tag{2.135}$$

The normalized form is given by[28]:

$$\gamma(\vec{r}_1, \vec{r}_2, \tau) = \frac{\Gamma(\vec{r}_1, \vec{r}_2, \tau)}{\sqrt{\Gamma(\vec{r}_1, \vec{r}_1, 0)\Gamma(\vec{r}_2, \vec{r}_2, 0)}} \tag{2.136}$$

For the case when $\tau = 0$, it is called the complex degree of coherence.
Coherence is not a property of the source, but of the light wave.[29]

2.7.8. Interferometers

Similar to Young's experiment, the same mathematical and physical foundations apply to a number of other interferometers. The grouping of interferometers can be done depending on various parameters, such as amplitude-splitting interferometers, wavefront-splitting interferometers (Young's experiment) etc.

2.7.8.1. Michaelson's interferometer

Michaelson's interferometer is probably the most known of all. It is an amplitude splitting interferometer[11] and it is used to measure length at extreme accuracy. The typical optical configuration is shown in Fig.2.12. When the movable mirror is displaced by $\frac{\lambda}{2}$, all fringes will move, occupying position of fringes that were there before. If N is the number of fringes and they are being counted, then it can be written that the difference in length is[11,21]:

$$\Delta d = N\frac{\lambda}{2} \tag{2.137}$$

The phase difference is:

$$\Delta\varphi = k\Delta l = \frac{2\pi}{\lambda}\Delta l \tag{2.138}$$

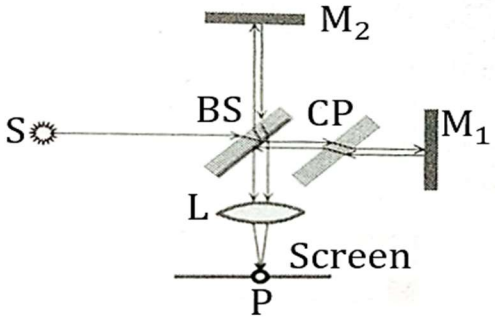

Fig.2.12. *Michaelson's interferometer and its components: laser source (S), beamsplitter (BS), compensating plate (CP), lens (L), focusing point (P) and mirrors (M_1, M_2).*[21]

2.7.8.2. Twyman-Green's interferometer

This kind of interferometer is obtained from a Michaelson interferometer by using a monochromatic source of light emitting a planewave, and a collimator. It uses a lens to focus the whole-field of view onto the camera. It is used in optical testing (lenses, optical prisms, surface shape testing).[11,21,30]

By distorting the front of the planewave, it is possible to determine defects of the lens. This can be nowadays done by computers, which can automatically generate a 3D model of the lens and perform necessary adjustment for the production/adjusting of the lenses. It is used in surface shape testing.

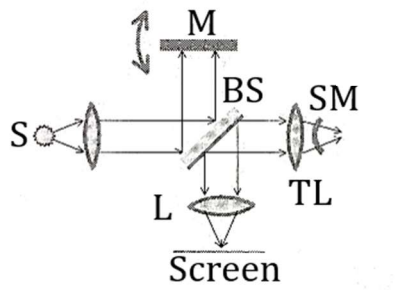

Fig.2.13. *Twyman-Green interferometer and its components for lens testing: laser source (S), beamsplitter (BS), testing lens (TL), spherical mirror (SM), mirror (M) and lens (L)***.**[21]

2.7.8.3. Mach-Zehnder's interferometer

It is an amplitude splitting interferometer. It contains two beam splitters. In this interferometer, the two ways resulting from the split travel on separate paths. The optical path difference can be created by tilting one of the beam splitters. The very fact that both arms are separated make this kind of interferometers suitable for many applications. A small downside of this kind of interferometer is that it is difficult to align. By placing an object that will create a difference in optical path, thus changing the pattern of fringes, different phenomena can be observed.[11,21]

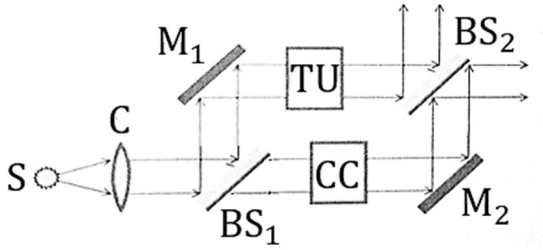

Fig.2.14. *Mach-Zehnder's interferometer and its components: laser source (S), collimator (C), beamsplitters (BS_1, BS_2), mirrors (M_1, M_2), testing unit (TU) and compensating cell (CC).*[21]

2.8. Diffraction

When light travels and its wavefront meets obstacles or aperture, it deviates from its rectilinear propagation (amplitude or phase alters), causing diffraction. Diffraction is the bending of light when it passes by edges of objects. Diffraction can be seen when lights passes through an aperture, bends, and forms a greater circle than the opening on a screen positioned further away, which contradicts our perception and assumption that light is in place where "it basically shouldn't''. The interfering pattern that is formed beyond the obstacle is called the diffraction pattern. Diffraction can mathematically be interpreted with different theories, but for the sake of simplicity and understanding, wave theory is used.

2.8.1. Huygens-Fresnel principle

Diffraction can be understood from the *Huygens-Fresnel principle*. According to *Huygens' Principle* published in 1678, every point in the opening aperture will act as a new wave source. This definition was refined by Fresnel in 1819. According to it, every point on a wavefront at a given moment can be regarded as a new source of spherical secondary wavelets, with the same frequency and is independent of the wavelength.[11,21,28,29]

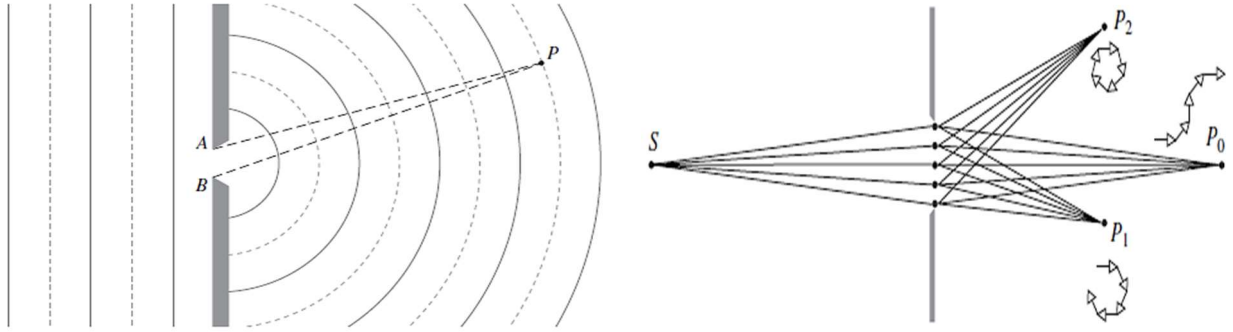

a) b)

Fig.2.15. *a) Classical wave picture and b) QED and probability amplitude for the diffraction at a small aperture.*[11]

If the wavelength of the laser is greater than the aperture, the waves will after the aperture spread in greater angles and interfere constructively. As smaller as the aperture gets, the more circular the waves diffracted from the aperture will be. For the opposite case, the waves will interfere constructively only in a small zone in front of the aperture, because the optical path difference in most of the points away from the centerline will make an average contribution of zero, hence destructively interfering. If the aperture is very small, optical path lengths passing through different points will have similar value, phasors will add up in a non-spiral way, increasing the amplitude of the intensity in that point.[11]

2.8.2. Fresnel diffraction

Calculating the Huygens-Fresnel diffraction is impossible for a finite aperture. In order to simplify the calculation, Fresnel's approximation is used. In this approximation, a spherical wave is approximated to a parabolic wave. In the Fresnel approximation, the distance from the source to the diffracting system or the distance from the diffracting system and point of observation are comparable with the size of the aperture. In other words, this is the near-field analysis. It uses the binomial expansion of the square root to approximate the oblique distance[29,31]:

$$r = \sqrt{(x-X)^2 + (y-Z)^2 + z^2} = z\sqrt{1 + \left(\frac{x-X}{z}\right)^2 + \left(\frac{y-Y}{z}\right)^2} = z\sqrt{1+\beta^2} \approx \tag{2.139}$$

$$\approx z\left(1 + \frac{1}{2}\beta^2 - \frac{1}{8}\beta^4 + \frac{1}{16}\beta^6 - \cdots\right) \approx z\left(1 + \frac{1}{2}\beta^2\right)$$

, where:

$$\beta = \sqrt{\left(\frac{x-X}{z}\right)^2 + \left(\frac{y-Y}{z}\right)^2} \tag{2.140}$$

Since the distance of the diffracting system and the observation point is large compared to the position of the observation point in the image plan and the ones in the aperture, then $r \approx z$ in the integral.

In order for this assumption to make sense, it is needed that $\beta \ll 1$. But this turn out to not be enough as a condition. In order for the neglected members to not contribute to the deviation of the phase of the parabolic wave from the spherical wave, it must further be required that the product of the wave vector k and the first neglected term $z\beta^4$ be much less than one, this means[29]:

$$\Delta\Phi \approx kz\frac{1}{8}\beta^4 \ll 1[rad] \tag{2.141}$$

$$\frac{2\pi}{\lambda}z\frac{1}{8}\left(\sqrt{\left(\frac{x-X}{z}\right)^2+\left(\frac{y-Y}{z}\right)^2}\right)^4 \ll 1 \quad \rightarrow \quad \{(x-X)^2+(y-Y)^2\}^2 \ll \frac{4\lambda}{\pi}z^3 \tag{2.142}$$

But in the case of digitally recorded holograms, it holds that[29]:

$$k\left(\frac{X^2+Y^2}{2z}\right) \ll 1 \quad \rightarrow \quad X^2+Y^2 \ll \frac{z\lambda}{\pi} \tag{2.143}$$

The condition can also appear in the form of[21]:

$$N\beta^2 = \frac{\beta^2 r^2{}_{apert.}}{\lambda z} \ll 1 \tag{2.144}$$

, where N is known as the Fresnel number and $r_{apert.}$ is the radius of the aperture, since $cos\beta \approx \beta \approx \frac{r_{apert.}}{z}$. Now, the *Huygens-Fresnel Principle* looks like[21]:

$$\xi(x,y) = \frac{ke^{ikz}}{2\pi iz}\int\limits_{Aperture} E_0(X,Y)e^{ik\frac{(x-X)^2+(y-Y)^2}{2z}}dS \tag{2.145}$$

2.8.2.1. Circular aperture

Let's define an aperture with radius $r_{apert.}$ on which a lightwave of the form E_0e^{ikz} travels in the z direction and the point of parabolic emission is at coordinates (X,Y), while the observation point is selected to be on the same axis as the one passing by the center of the aperture $(x=0, y=0)$ and taking that $E_0(X,Y) = E_0$ .Thus, the Huygens-Fresnel integral and intensity can be expressed as[21]:

$$\xi(0,0) = \frac{ke^{ikz}}{2\pi iz}E_0\int\limits_{Aperture}\underbrace{e^{ik\frac{x^2+y^2}{2z}}}_{1}\underbrace{e^{-ik\frac{xX+yY}{2z}}}_{1}e^{ik\frac{X^2+Y^2}{2z}}dS = \tag{2.146}$$

$$= \frac{ke^{ikz}}{2\pi iz}E_0\int\limits_{\rho=0}^{r_{apert.}}\int\limits_{\varphi=0}^{2\pi}e^{ik\frac{r_{apert.}^2}{2z}}\rho d\rho d\varphi = E_0e^{ikz}\left(1-e^{ik\frac{r_{apert.}^2}{2z}}\right)$$

$$I = |\xi(0,0)|^2 = 4E_0^2 sin^2\left(\frac{kr_{apert.}^2}{4z}\right) = 4E_0^2 sin^2\left(\frac{\pi r_{apert.}^2}{2\lambda z}\right) \tag{2.147}$$

2.8.3. Fraunhofer diffraction

In the Fraunhofer approximation, the observation point is far away, and is greater in comparison to the dimensions of the aperture. This will result in having the Fresnel number $N \ll 1$ so that in $z\left(1+\frac{1}{2}\beta^2\right)$ it can be written that[21]:

$$\Delta\theta \approx kz\frac{1}{2}\beta^2 = kz\frac{1}{2}\left(\left(\frac{x-X}{z}\right)^2+\left(\frac{y-Y}{z}\right)^2\right) = k\frac{X^2+Y^2}{2z} \approx k\frac{r_{apert.}^2}{2z} \approx \pi\frac{r_{apert.}^2}{\lambda z} \approx \pi N \tag{2.148}$$

$$\xi(x,y) = \frac{ke^{ikz}}{2\pi iz}\int\limits_{Aperture}\xi_0(X,Y)e^{ik\frac{(x-X)^2+(y-Y)^2}{2z}}dS = \tag{2.149}$$

$$= \frac{ke^{ikz}}{2\pi iz}\int\limits_{Aperture}\xi_0(X,Y)e^{ik\frac{x^2+y^2}{2z}}e^{-ik\frac{xX+yY}{2z}}\underbrace{e^{ik\frac{X^2+Y^2}{2z}}}_{1}dS =$$

$$= \frac{ke^{ikz}}{2\pi iz}e^{ik\frac{x^2+y^2}{2z}}\int\limits_{Aperture}\xi_0(X,Y)e^{-ik\frac{xX+y}{2z}}dS$$

, which represents a Fourier integral.

If a simplification would be needed, by neglecting the constant scaling and the complex exponent (which doesn't contribute in the intensity), it could be rewritten as[21]:

$$\xi(x,y) = \int\limits_{Aperture}\xi_0(X,Y)e^{-ik\frac{xX+yY}{2z}}dS \tag{2.150}$$

If further simplification would be required, by making use of the condition that $\beta \ll 1$, and since both α_x and α_y are very small since the measuring point is far away from the aperture, the following could be assumed:

$$sin\alpha_x \approx \alpha_x = \frac{x}{z} \quad sin\alpha_y \approx \alpha_y = \frac{y}{z} \tag{2.151}$$

Which leads to[21]:

$$\xi(\alpha_x,\alpha_y) = \int\limits_{Aperture}\xi_0(X,Y)e^{-ik(Xsin\alpha_x+Ysin\alpha_y)}dS \tag{2.152}$$

This represents the Fraunhofer approximation and is valid as long as $N \ll 1$ and $\beta \ll 1$.

2.8.3.1. Rectangular aperture

For a rectangular aperture, it can be written that[21]:

$$\xi(\alpha_x, \alpha_y) \approx \int_{-\frac{d_1}{2}}^{\frac{d_1}{2}} e^{-ikX sin\alpha_x} dX \int_{-\frac{d_2}{2}}^{\frac{d_2}{2}} e^{-ikY sin\alpha_y} dY \tag{2.153}$$

$$I = I_0 \left(\frac{sin\left(\frac{\pi d_1}{\lambda}\right) sin\left(\frac{\pi d_2}{\lambda}\right)}{\frac{\pi^2}{\lambda^2} d_1 d_2} \right)^2 = [\ \ I_0 = (d_1 d_2)^2\ \ ] = \left(\frac{sin\left(\frac{\pi d_1}{\lambda}\right) sin\left(\frac{\pi d_2}{\lambda}\right)}{\frac{\pi^2}{\lambda^2}} \right)^2 \tag{2.154}$$

The analysis can also be done differently. Let us suppose a configuration as in Fig.2.16., where a monochromatic plane wave propagates across the opening. According to the *Huygens-Fresnel Principle*, all points in the opening can be considered as a second source of waves. Since the elementary unit dS is smaller than the wavelength, all the contributions are in phase at point P, hence a constructive interference will occur. The intensity of the optical wave at point P, if a constant source strength in the entire opening is assumed, will be[11]:

$$d\vec{E} = \frac{K}{r} e^{i(\omega t - \vec{k}\vec{r})} d\vec{S} \tag{2.155}$$

, with $R = \sqrt{X^2 + Y^2 + Z^2}$ and $r = \sqrt{X^2 + (Y-y)^2 + (Z-z)^2} \approx R\left(1 - \frac{Yy+Zz}{R^2}\right)$. K is the strength of the secondary source and can be expressed as $K = \frac{k}{2\pi i} = \frac{1}{i\lambda}$, leading to[11]:

$$E = \frac{K}{R} e^{i(\omega t - kR)} \iint_{Apert.} e^{\frac{ik(Yy+Zz)}{R}} dS = \frac{K}{R} e^{i(\omega t - kR)} \int_{-\frac{b}{2}}^{\frac{b}{2}} e^{\frac{ikYy}{R}} dy \int_{-\frac{a}{2}}^{\frac{a}{2}} e^{\frac{ikZz}{R}} dz = \tag{2.156}$$

$$= \frac{K}{R} e^{i(\omega t - kR)} \frac{sin\left(\frac{kaZ}{2R}\right)}{\frac{kaZ}{2R}} \frac{sin\left(\frac{kbY}{2R}\right)}{\frac{kbY}{2R}}$$

$$I(Y,Z) = \langle (Re\{E\})^2 \rangle_T = I(Y=0, Z=0) \left(\frac{sin\left(\frac{kaZ}{2R}\right)}{\frac{kaZ}{2R}} \right)^2 \left(\frac{sin\left(\frac{kbY}{2R}\right)}{\frac{kbY}{2R}} \right)^2 \tag{2.157}$$

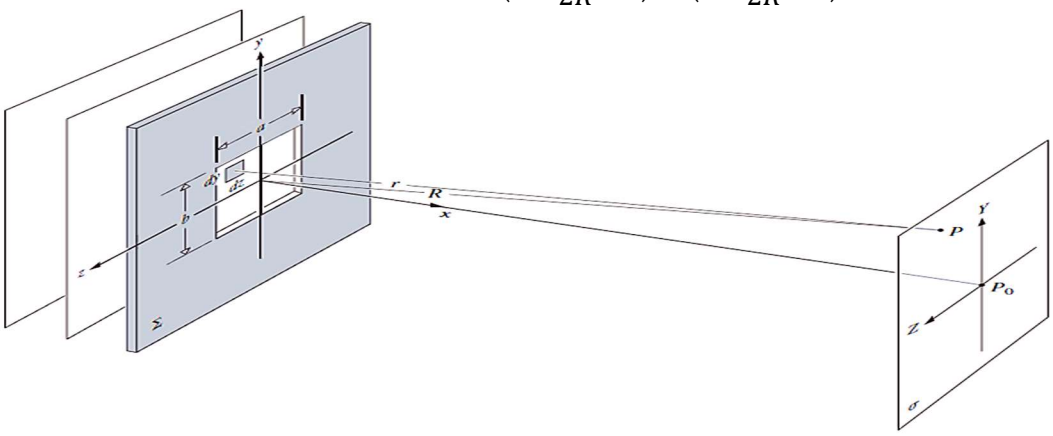

Fig.2.16. *Rectangular aperture.*[11]

2.8.3.2. Circular aperture

Because of the symmetry, $\alpha_x = 0$ and $\alpha_y = \beta$, it holds that[21]:

$$\xi \approx \int_{Apert.} e^{-ikYsin\beta} dX\, dY = \int_{\rho=0}^{r_{apert.}} \int_{\varphi=-\pi}^{\pi} e^{-ik\rho sin\varphi sin\beta}\, \rho d\rho d\varphi \tag{2.158}$$

Which leads to the Bessel function which is defined by[21]:

$$J_n(x) = \frac{1}{2\pi} \int_{-\pi}^{\pi} \cos(xsin\varphi - n\varphi)\, d\varphi \tag{2.159}$$

The intensity will thus be[21]:

$$I \approx I_0 \frac{4J_1^2(kr_{apert.}sin\varphi)}{\left(kr_{apert.}sin\varphi\right)^2} \tag{2.160}$$

Because of the symmetry, if the intensity is plotted, a tower-like shape corresponding to the central maximum of the function will be obtained. It is known as the Airy disk and is surrounded by a dark ring which corresponds to the first zero of the Bessel function in the formula.

The diameter of such shape is given by $d \approx 1.22 \frac{f\lambda}{d_{apert.}}$ when using a lens, since in that case $f \approx R$. From this the Rayleigh criterion for resolution is given by[21]:

$$\beta \approx 1.22 \frac{\lambda}{d_{apert.}} \tag{2.161}$$

This represents the minimum angle for which it is possible to distinguish between two overlapping shapes in the intensity profile.

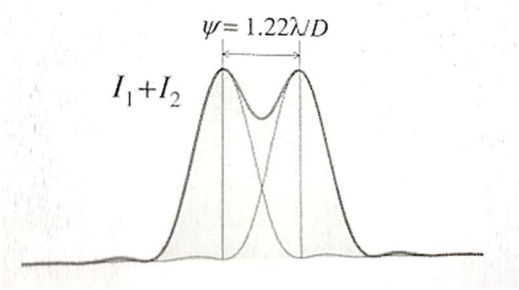

Fig.2.17. *Rayleigh criterion.*[21]

For a circular aperture, it holds that[11]:

$$E = \frac{K}{R} e^{i(\omega t - kR)} \int_{\rho=0}^{a} \int_{\phi=0}^{2\pi} e^{\frac{ik\rho q}{R}\cos(\phi-\varphi)}\, \rho d\rho d\phi = \frac{K}{R} e^{i(\omega t - kR)} 2\pi a^2 \frac{R}{kaq} J_1\left(\frac{kaq}{R}\right) \tag{2.162}$$

$$I(\theta) = \frac{K^2 S_{apert.}^2}{2R^2} \left(\frac{2J_1(kasin\theta)}{kasin\theta}\right)^2 \tag{2.163}$$

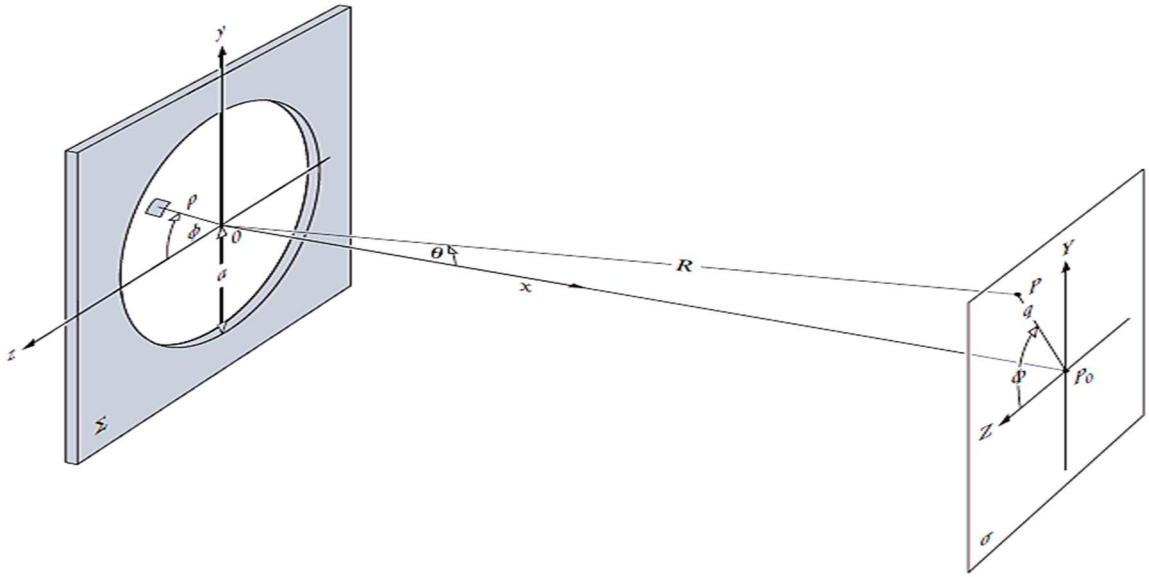

Fig.2.18. *Circular aperture.*[11]

In a general fashion, the Fresnel-Kirchhoff diffraction formula looks like[29]:

$$E = \frac{iE_0}{\lambda} \iint_{Apert.} \frac{e^{ik(r_{SP}+r_{PB})}}{r_{SP}r_{PB}} \left(\frac{\cos(\vec{r}_{SP},\vec{n}) - \cos(\vec{r}_{PB},\vec{n})}{2} \right) dxdy \tag{2.164}$$

For an observing point at infinity, and the source located at the center of the aperture, it can be written that[29]:

$$\cos(\vec{r}_{SP},\vec{n}) = 1 \; and \; \cos(\vec{r}_{PB},\vec{n}) = -\cos\theta \tag{2.165}$$

For sufficient distance of observation $\vec{r}_{PB} \parallel \vec{n}$, the term in the nominator in the bracket is 2, which yields[29]:

$$E = \frac{iE_0}{\lambda} \iint_{Apert.} \frac{e^{ik(r_{SP}+r_{PB})}}{r_{SP}r_{PB}} dxdy \tag{2.166}$$

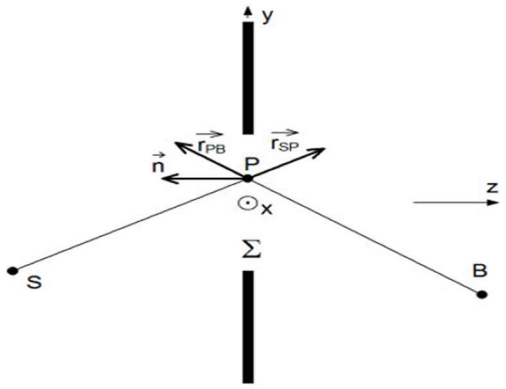

Fig.2.19. *Geometry for the Fresnel-Kirchhoff diffraction.*[29]

3. Holography

3.1. General

When shooting a photography, the viewer sees only a 2D representation of a 3D world. In classical photography, the 2D representation of the world is done from a perspective, which means that the third dimension, i.e. the depth, is lost. Hence the viewer cannot have the feeling of the depth when looking to a classical photography. A hologram is an image that offers the possibility of having the third dimension recorded and reproduced. This is simply done by using a reference light when recording the scene, and the same referencing light is used to reconstruct the image from the coded image in a hologram.[21]

A hologram is a coded image in the form of bright and dark fringes, obtained from the interference between the reference and object beam. Every single point of the hologram represents the interference from many points from the real scene that is being illuminated. Thus, every single point in a hologram contains information about the whole scene under illumination, unlike classical photography where every single point on the photography corresponds to a single point from the real scene. This is a tremendous advantage of holograms, since the original scenery can be reconstructed based on the information of only one spot. Holography was invented by Dennis Gabor in 1948.[11,26]

Classical photography records only the intensity of light that falls into the camera/plate, but holograms contain also the phase information. This comes from the fact that interference is sensitive to the phase of the reference and object beam.

What is recorded can be expressed as[21]:

$$\vec{E}_O = \vec{E}_{Obj}(\vec{r},t) = \vec{E}_{0Obj}cos\left(\vec{k}_1 \cdot \vec{r} - \omega t + \varepsilon_1\right) \tag{3.1}$$

$$\vec{E}_R = \vec{E}_{Ref}(\vec{r},t) = \vec{E}_{0R}cos\left(\vec{k}_2 \cdot \vec{r} - \omega t + \varepsilon_2\right) \tag{3.2}$$

$$I_{Hologram} \sim \left|\vec{E}_{Total}\right|^2 = E_{Total} \cdot E^*_{Total} = \left|\vec{E}_O\right|^2 + \left|\vec{E}_R\right|^2 + \vec{E}_O\vec{E}^*_R + \vec{E}_R\vec{E}^*_O \tag{3.3}$$

In order to obtain the object beam, the hologram must be illuminated with the reference beam, thus[21]:

$$\vec{E}_{Hologram} = \vec{E}_R\left|\vec{E}_O\right|^2 + \vec{E}_R\left|\vec{E}_R\right|^2 + \vec{E}_O\vec{E}^*_R\vec{E}_R + \left(\vec{E}_R\right)^2\vec{E}^*_O = \vec{E}_R(I_o + I_R) + \vec{E}_O I_R + \left(\vec{E}_R\right)^2\vec{E}^*_O \tag{3.4}$$

The first term from the left represent the reference beam modulated by I_o and I_R respectively. The second term represents our object beam multiplied by the intensity of the reference beam. For the case when the reference beam is uniform, the object beam can easily be recovered. The last member is proportional to the complex conjugate object beam $\vec{E}^*_O$, and thus gives a real image, which is made up of convergent waves.[21]

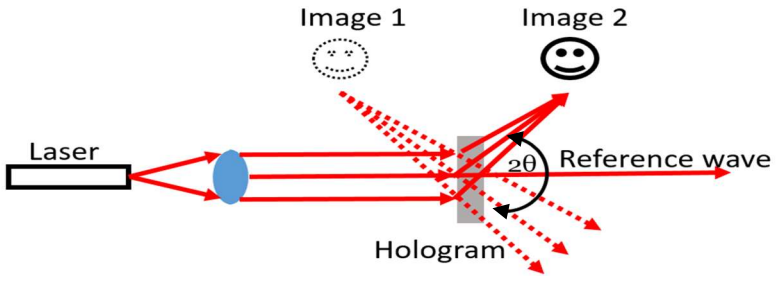

Fig.3.1. *Reconstruction of hologram.*[21]

Previously, holograms were recorded in photoemulssive plates, but the invention of CCD/CMOS camera and the progress of computer technology made it possible to shift entirely to cameras. The advantage of photoemulssive plates is that they had the possibility to record up to 1000 $[fringes/mm]$.[21]

When both the object and reference wave travel in parallel, we have an inline holographic setup. When introducing an angle between them, we speak of the off-axis holographic setup. The advantage of having an off-axis setup results from the fact that spectral components resulting from the object and referencing wave will be well separated in the frequency domain, which means they will propagate at different angles, resulting in an easier separation of the interference pattern for the purpose of reconstructing the object wave.

If θ is the angle between the object and reference wave, then[32]:

$$\vec{E}_{Hologram} = \vec{E}_R(I_o + I_R) + \vec{E}_O I_R e^{-jkxsin\theta} + \left(\vec{E}_R\right)^2 \vec{E}_O^* e^{jkxsin\theta} \tag{3.5}$$

The first term represents a plane wave travelling parallel to the alignment of the setup (parallel to the object beam). The second term reproduces a virtual image of the object wave at angle θ. The third term represents the real object wave reconstructed, with an angle of deflection $-\theta$. The zero diffraction order propagates on the same direction as $\vec{E}_R$.[32]

There are different kinds of holography, as Fourier-Transform holography, volume holography etc.

In the classical double exposure holographic technique, the same plate is used for two exposures: the first exposure is done by illuminating the object in its initial state with the reference beam and recording this on the plate. The second exposure is done by illuminating the object in its final state with the reference beam on the same plate. This will cause an interfering pattern to be registered on the plate from both exposures. After illuminating the plate with the reference beam, virtual images between the initial and finale state can be seen. However, nowadays cameras are used instead of plates. Cameras make possible to digitally record the holograms and manipulate them numerically for processing and reconstruction. This also enables the possibility of faster, real-time visualization of phenomena.

3.2. Generation of holograms

In digital holography, we use digital sensors to capture images. Illuminating the object in its initial state with the reference beam and in its final state can be expressed mathematically as[28]:

$$\vec{E}_{oi}(x,y) = E_{0i}(x,y)e^{-j\varphi(x,y)} \tag{3.6}$$

$$\vec{E}_{of}(x,y) = E_{0f}(x,y)e^{-j[\varphi(x,y)+\Delta\varphi(x,y)]} \tag{3.7}$$

, where the index i, f represent intial and finale state respectively. Here it was assumed that there is no change in the direction of propagation. If it is assumed that $E_{0i}(x,y) = E_{0f}(x,y) = E(x,y)$), then :

$$I(x,y) = \left|\vec{E}_{oi}(x,y) + \vec{E}_{of}(x,y)\right|^2 = 2E^2(x,y)[1 + cos\{\Delta\varphi(x,y)\}] \tag{3.8}$$

In a general form, this can be rewritten as[28,33]:

$$I(x,y) = A(x,y) + B(x,y)cos\{\Delta\varphi(x,y)\} \tag{3.9}$$

$A(x,y)$ and $B(x,y)$ depend from the coordinates in the interferogram. This mathematical equation describes the relation between the intensity of the interference and its phase. There are numerous techniques used to determine $A(x,y)$, $B(x,y)$ and $\Delta\varphi(x,y)$, since the cosine function is an even function and can cause ambiguity. Such techniques are phase-shifting holography with minimum of 3 interferograms recorded, Fourier Transform method etc.[28]

3.3. Recording

CCD (Charged Coupled Device) were invented in the '60s. They are mostly used for image acquisition. They are available in the form of line scan or area scan geometries. Usually they are built in the form of a rectangular matrix. There are three types of CCD architecture: full-frame device, frame-transfer device and interline transfer device and all of them are suitable for digital holography. Full-frame devices are more advantageous than the others since the exposure can be adjusted.[28] Nowadays most of the imaging devices have a CMOS (Complementary Metal-Oxide Semiconductor) sensor.

If the CCD array has $N \times M(x \times y)$ pixels with pixel to pixel distance of d_x and d_y in respective directions, assuming that it is dealt as a square matrix, gives $N = M = N_{pix}$ and $d_x = d_y = d_{pix}$.

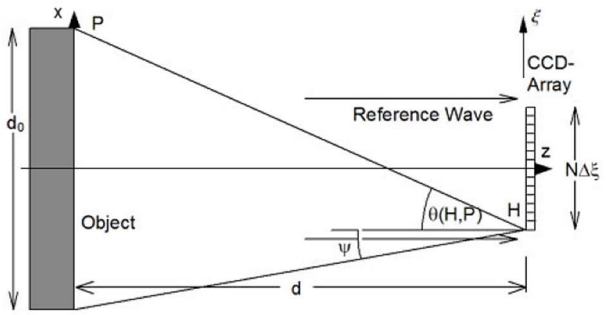

Fig.3.2. *Geometry for recording a digital Fresnel hologram.*[29]

If the angle θ is defined as the angle between the reference wave and object wave at any point, it can be written that the distance between two interference fringes that form the hologram is[21,29]:

$$\Lambda_{dist} = \frac{\lambda}{2sin\theta_z cos\alpha} = \frac{\lambda}{2sin\left(\frac{\theta}{2}\right)} \tag{3.10}$$

The Nyquist sampling theorem states that in order to faithfully reproduce a signal, it must be sampled at least as twice for its smallest cycle. This means that sampling must be done for more than two pixels, which means that two pixels must fit into the distance Λ_{dist}. The spatial frequency is given by $\frac{1}{\Lambda_{dist}} = f_{dist}$. Since θ is small, the approximation $sin\left(\frac{\theta}{2}\right) \approx \frac{\theta}{2}$ can be used. This leads to[29]:

$$\Lambda_{dist} > 2d_{pix} \rightarrow \theta < \frac{\lambda}{2d_{pix}} \tag{3.11}$$

This means that, CCD cameras can be used as long as θ is small enough to fulfill the sampling criteria. For those parts that don't work, the CCD camera can be positioned far away or by reducing the imaging angle.[29]

It can further be written that, by assuming that θ is small, $\theta \approx \tan(\theta)$, obtaining[29]:

$$\tan(\theta) = \frac{\frac{h}{2} + \frac{N_{pix} d_{pix}}{2}}{d} < \frac{\lambda}{2 d_{pix}} \tag{3.12}$$

which leads to the formula relating the maximum height of the object under investigation, its distance from the CCD camera and pixel size in order to fulfill the sampling theorem[29]:

$$h < \frac{\lambda d}{d_{pix}} - N_{pix} d_{pix} \tag{3.13}$$

When the object is too big, a negative lens can be used to reduce the image and fulfill the sampling theorem.

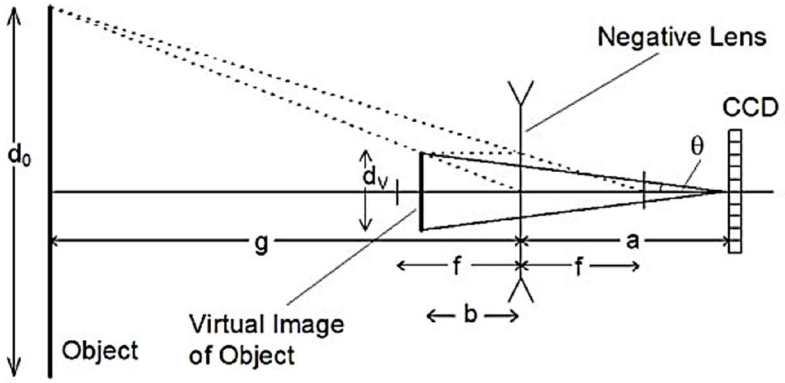

Fig.3.3. *Reduction of imaging angle.*[29]

Let us make of use of the following formulas[29]:

$$\frac{1}{f} = \frac{1}{g} - \frac{1}{b} \tag{3.14}$$

$$M_{magn} = \frac{h_v}{h} = \frac{-f}{g - f} \tag{3.15}$$

$$\tan(\theta) = \frac{h_v}{2(a + b)} \tag{3.16}$$

$$h_v = \frac{-hf}{g - f} \tag{3.17}$$

$$b = \frac{gf}{f - g} \tag{3.18}$$

From these, the distance of the lens from the CCD camera depending on the other parameters is obtained[29]:

$$a = \frac{-hf}{2\tan(\theta)\,(g - f)} + \frac{fg}{g - f} \tag{3.19}$$

The distance between the virtual image and the CCD is now $d_{V-CCD} = a + b$, which will be used for the reconstruction of the hologram.

3.4. Reconstruction by the Fresnel Approximation

As it was discussed before, the diffraction of light at an aperture is described by the Fresnel-Kirchhoff integral[28]:

$$\Gamma(x_a, y_a) = \frac{j}{\lambda} \int_{\infty}^{\infty} \int_{\infty}^{\infty} h(x,y) E_R(x,y) \frac{e^{-j\frac{2\pi}{\lambda}R}}{R} dxdy \tag{3.20}$$

, where:

$$R = \sqrt{(x-x_a)^2 + (y-y_a)^2 + d} = d\sqrt{1 + \left(\frac{x-x_a}{d}\right)^2 + \left(\frac{y-y_a}{d}\right)^2} \approx \tag{3.21}$$

$$\approx d\left(1 + \frac{1}{2}\left[\left(\frac{x-x_a}{d}\right)^2 + \left(\frac{y-y_a}{d}\right)^2\right]^2\right) = d + \frac{(x-x_a)^2}{2d} + \frac{(y-y_a)^2}{2d}$$

By using the conjugate reference beam, the real image can be reconstructed, so[28]:

$$\Gamma(x_a, y_a) = \tag{3.22}$$

$$= \frac{j}{\lambda} \int_{\infty}^{\infty} \int_{\infty}^{\infty} h(x,y) {E_R}^*(x,y) \frac{e^{-j\frac{2\pi}{\lambda}R}}{R} dxdy = [R \approx d] =$$

$$= \frac{j}{\lambda d} e^{-j\frac{2\pi}{\lambda}d} \int_{\infty}^{\infty} \int_{\infty}^{\infty} h(x,y) {E_R}^*(x,y) e^{-j\frac{\pi}{\lambda d}[(x-x_a)^2 + (y-y_a)^2]} dxdy =$$

$$= \frac{j}{\lambda d} e^{-j\frac{2\pi}{\lambda}d} e^{-j\frac{\pi}{\lambda d}[{x_a}^2 + {y_a}^2]} \int_{\infty}^{\infty} \int_{\infty}^{\infty} h(x,y) {E_R}^*(x,y) e^{-j\frac{\pi}{\lambda d}[x^2+y^2]} e^{j\frac{2\pi}{\lambda d}[x \cdot x_a + y \cdot y_a]} dxdy$$

This is known as the Fresnel approximation/transformation and makes it possible to reconstruct the beam in a plane behind the hologram.

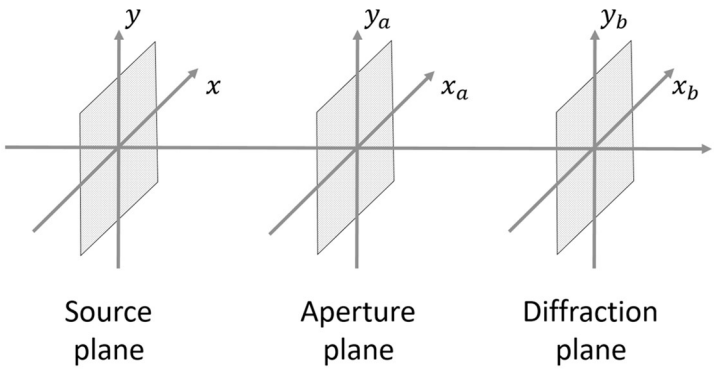

Fig.3.4. *Coordinate system for reconstruction.*[28]

The intensity and phase are calculated by:

$$I(x_a, y_a) = |\Gamma(x_a, y_a)|^2 \tag{3.23}$$

$$\varphi(x_a, y_a) = \arctan\left(\frac{Im\{\Gamma(x_a, y_a)\}}{Re\{\Gamma(x_a, y_a)\}}\right) \tag{3.24}$$

When reconstructing the virtual image, a lens can be introduced into the numerical reconstruction, and represents the eye of an observer looking at the numerically reconstructed hologram. This lens can be mathematically described by[28]:

$$L(x,y) = e^{j\frac{\pi}{f\lambda}(x^2+y^2)} \tag{3.25}$$

In order to compensate for the aberration caused by the lens, the reconstructed beam must be multiplied with[28]:

$$C_{comp}(x_b,y_b) = e^{j\frac{\pi}{f\lambda}(x_b^2+y_b^2)} \tag{3.26}$$

Then the reconstruction formula for a lens with focal distance $f = \frac{d}{2}$ with the Fresnel approximation is[28]:

$$\Gamma(x_b,y_b) = \frac{j}{\lambda} C_{comp}(x_b,y_b) \int_{\infty}^{\infty}\int_{\infty}^{\infty} h(x,y)E_R(x,y)L(x,y)\frac{e^{-j\frac{2\pi}{\lambda}R}}{R}dxdy \tag{3.27}$$

The complete formula to reconstruct the virtual image hence will be[28]:

$$\Gamma(x_b,y_b) = \tag{3.28}$$

$$= \frac{i}{\lambda d} e^{-j\frac{2\pi}{\lambda}d} e^{-j\frac{\pi}{\lambda d}[{x_b}^2+{y_b}^2]} C_{comp}(x_b,y_b) \int_{\infty}^{\infty}\int_{\infty}^{\infty} h(x,y)E_R(x,y)L(x,y)e^{-j\frac{\pi}{\lambda d}[x^2+y^2]} e^{j\frac{2\pi}{\lambda d}[x\cdot x_b+y\cdot y_b]}dxdy$$

$$= \frac{i}{\lambda d} e^{-j\frac{2\pi}{\lambda}d} e^{-j\frac{\pi}{\lambda d}[{x_b}^2+{y_b}^2]} \int_{\infty}^{\infty}\int_{\infty}^{\infty} h(x,y)E_R(x,y)e^{j\frac{\pi}{\lambda d}[x^2+y^2]} e^{j\frac{2\pi}{\lambda d}[x\cdot x_b+y\cdot y_b]}dxdy$$

In order to digitize, sampling must occur, thus the following substitutions will be used:

$$x_D = \frac{x_a}{\lambda d} \;\; and \; x_y = \frac{y_a}{\lambda d} \tag{3.29}$$

From these, the Fresnel approximation looks like[28]:

$$\Gamma(x_D,y_D) = \tag{3.30}$$

$$= \frac{j}{\lambda d} e^{-j\frac{2\pi}{\lambda}d} e^{-j\pi\lambda\;\;[{x_D}^2+{y_D}^2]} \int_{\infty}^{\infty}\int_{\infty}^{\infty} h(x,y){E_R}^*(x,y)e^{-j\frac{\pi}{\lambda d}[x^2+y^2]} e^{j2\pi[x\cdot x_D+y\cdot y_D]}dxdy$$

The 2D Fourier Transform and its inverse transform are defined as:

$$F(x_F,y_F) = \int_{-\infty}^{\infty}\int_{-\infty}^{\infty} f(x,y)e^{-j2\pi(x\cdot x_F+y\cdot y_F)}\,dxdy = F\{f(x,y)\} \tag{3.31}$$

$$f(x,f) = \int_{-\infty}^{\infty}\int_{-\infty}^{\infty} F(x_F,y_F)e^{j2\pi(x\cdot x_f+y\cdot y_f)}\,dx_F dy_F = F^{-1}\{f(x,y)\} \tag{3.32}$$

If the last equation is compared with the Fourier transform, it can be rewritten as[28]:

$$\Gamma(x_D, y_D) = \frac{j}{\lambda d} e^{-j\frac{2\pi}{\lambda}d} e^{-j\pi\lambda d[{x_D}^2+{y_D}^2]} \cdot F^{-1}\left\{h(x,y){E_R}^*(x,y)e^{-j\frac{\pi}{\lambda d}[x^2+y^2]}\right\} \tag{3.33}$$

Its discrete equivalent, for $M \times N$ points with steps of Δx and Δy, is given by[28]:

$$\Gamma(m,n) = \tag{3.34}$$

$$= \frac{j}{\lambda d} e^{-j\frac{2\pi}{\lambda}d} e^{-j\pi\lambda d[(m\cdot\Delta x_D)^2+(n\cdot\Delta y_D)^2]} \sum_{k=0}^{M-1}\sum_{l=0}^{N-1} h(k,l){E_R}^*(k,l)e^{-j\frac{\pi}{\lambda d}[(k\Delta x)^2+(l\Delta y)^2]} e^{j2\pi(k\Delta x\cdot m\Delta x_D + l\Delta y\cdot n\Delta y_D)}$$

, for $m = 0,1,\dots,M-1$ and $n = 0,1,\dots,N-1$.

Following relations exist:

$$\Delta x_D = \frac{1}{M\Delta x} \rightarrow \Delta x_a = \frac{\lambda d}{M\Delta x} \tag{3.35}$$

$$\Delta y_D = \frac{1}{N\Delta y} \rightarrow \Delta y_a = \frac{\lambda d}{N\Delta y} \tag{3.36}$$

From these, it can be written that[28]:

$$\Gamma(m,n) = \tag{3.37}$$

$$= \frac{j}{\lambda d} e^{-j\frac{2\pi}{\lambda}d} e^{-j\pi\lambda d\left[\left(\frac{m}{M\Delta x}\right)^2+\left(\frac{n}{N\Delta y}\right)^2\right]} \sum_{k=0}^{M-1}\sum_{l=0}^{N-1} h(k,l){E_R}^*(k,l)e^{-j\frac{\pi}{\lambda d}[(k\Delta x)^2+(l\Delta y)^2]} e^{j2\pi\left(\frac{km}{M}+\frac{ln}{N}\right)}$$

$$= \frac{j}{\lambda d} e^{-j\frac{2\pi}{\lambda}d} e^{-j\pi\lambda d\left[\left(\frac{m}{M\Delta x}\right)^2+\left(\frac{n}{N\Delta y}\right)^2\right]} \cdot F^{-1}\left\{h(k,l){E_R}^*(k,l)e^{-j\frac{\pi}{\lambda d}[(k\Delta x)^2+(l\Delta y)^2]}\right\}$$

This represents the discrete Fresnel transform.

Reconstructing with a virtual lens yields[28]:

$$\Gamma(m,n) = \tag{3.38}$$

$$= \frac{j}{\lambda d} e^{-j\frac{2\pi}{\lambda}d} e^{j\pi\lambda d\left[\left(\frac{m}{M\Delta x}\right)^2+\left(\frac{n}{N\Delta y}\right)^2\right]} \sum_{k=0}^{M-1}\sum_{l=0}^{N-1} h(k,l)E_R(k,l)e^{j\frac{\pi}{\lambda d}[(k\Delta x)^2+(l\Delta y)^2]} e^{j2\pi\left(\frac{km}{M}+\frac{ln}{N}\right)} =$$

$$= \frac{j}{\lambda d} e^{-j\frac{2\pi}{\lambda}d} e^{j\pi\lambda d\left[\left(\frac{m}{M\Delta x}\right)^2+\left(\frac{n}{N\Delta y}\right)^2\right]} \cdot F^{-1}\left\{h(k,l)E_R(k,l)e^{j\frac{\pi}{\lambda d}[(k\Delta x)^2+(l\Delta y)^2]}\right\}$$

The reason why Δx_D and Δx_y are dependent on the reconstruction distance d is because they correspond to the diffraction limited resolution of optical systems. Eventhough it might seem that for smaller pixels $\Delta x_D \times \Delta x_y$ a better resolution could be obtained, this is impossible, since the physical resolution is limited by the diffraction limit. If the camera sensor is to be considered as an aperture of the optical system $M\Delta x_D \times N\Delta x_y$, the Fresnel transformation represents the diffraction limit defined by this rectangular aperture. This means that the Fresnel transformation represents the ''natural scaling'' algorithm setting the resolution of the reconstructed image by a discrete Fresnel transform to always its physical limit.[32]

3.5. Measurement of refractive index

When the refractive index changes, it causes the change of the optical path of the rays that go through. This cause a variation of the phase according to the change of the refractive index. Mathematically, the relation is given by[29]:

$$\Delta\varphi(x,y) = \frac{2\pi}{\lambda}\int_{L_1}^{L_2}\Delta n(x,y,z)dz = \frac{2\pi}{\lambda}\int_{L_1}^{L_2}[n(x,y,z) - n_0]dz \tag{3.39}$$

, where n_0 is the refractive index of the medium under measurement at its initial state and $n(x,y,z)$ at its finale/perturbated state, L_1 and L_2 are the starting and ending point of the beam path inside the measuring unit . While light passes through the phase object, it integrates all the phase change along its path. This mathematical formula assumes linear propagation of light waves inside the medium of thickness L with no variation of its refractive index along the axis of propagation. If the refractive index doesn't vary in the direction of propagation, then[34]:

$$\Delta\varphi(x,y) = \frac{2\pi}{\lambda}\int_{L_1}^{L_2}\Delta n(x,y,z)dz = \frac{2\pi}{\lambda}\int_{L_1}^{L_2}[n(x,y,z) - n_0]dz = \frac{2\pi}{\lambda}L[n(x,y,z) - n_0] \tag{3.40}$$

The refractive index is linked to the density through the Lorentz-Lorenc equation[35]:

$$\frac{n^2-1}{n^2+2} = K\rho \xrightarrow{yields} n^2 = \frac{1+2\rho\frac{R_L}{M}}{1-\rho\frac{R_L}{M}} \tag{3.41}$$

, where K denotes the Gladstone-Dale constant, which is a property of gases and liquids and is mostly independent from the pressure and temperature, but slightly dependent on the chosen wavelength for measurement [34], M the molecular weight and R_L the molecular refractivity. For diluted gas $n \approx 1$, then the equation can be approximated to[35,36]:

$$n = 1 + \frac{3\rho R_L}{2M} = 1 + \frac{\rho R_G}{M} = 1 + K\rho \xrightarrow{yields} n - 1 = K\rho = \frac{KMP}{RT} \tag{3.42}$$

, where R_G is the Gladstone-Dale molecular refractivity and R is the universal gas constant $R = 8.3143\left[\frac{J}{Kmol}\right]$. The equation on above on the right represents the Gladstone-Dale equation. It is used for optical analysis of gases and liquids and their compositions. The relation between the change of refractive index of air Δn, the disturbed air length l and the number of interference fringes shift N is given by[37]:

$$N = \frac{l}{\lambda}\Delta n \tag{3.43}$$

For the case of axially-symmetric temperature fields, the relation is given by[38]:

$$\Delta\varphi(x,y) = \frac{4\pi}{\lambda}\int_{\infty}^{-\infty}\frac{r[n(x,y,z) - n_0]}{\sqrt{r^2 - x^2}}dr \tag{3.44}$$

, where r is the distance from the center of symmetry. The temperature change is calculated via[39]:

$$\Delta T = \frac{\Delta\varphi\lambda}{2\pi L\frac{dn}{dT}} \tag{3.45}$$

, where $\frac{dn}{dT}$ represents the change of refractive index with temperature.

3.6. Refractive index calculations

In order to perform the calculations, calculating the following values are an important part of the process. The atmospheric pressure is defined as $\mathrm{p}_0 = 101325[\mathrm{Pa}]$.

The formula to calculate the refractive index of air at $T = 15[°\mathrm{C}]$ and $\mathrm{p} = \mathrm{p}_0$ is[40]:

$$n_{air}(\lambda, T = 15[°\mathrm{C}], \mathrm{p}_0) = 1 + \frac{0.05792105}{238.0185 - \frac{1}{\lambda^2}} + \frac{0.00167917}{58.362 - \frac{1}{\lambda^2}} \tag{3.46}$$

$(According\ to\ Ciddor\ 1996\ for\ \lambda = 230[nm] - 1630[nm])$

The formula to calculate the refractive index of air at a certain temperature other than $T = 15[°\mathrm{C}]$ is:

$$n_{air}(\lambda, T, p) = 1 + \frac{n_{air}(\lambda, 15[°\mathrm{C}], 101325[\mathrm{Pa}]) - 1}{1 + 3.4785 \cdot 10^{-3}\left[\frac{1}{°\mathrm{C}}\right](T - 15[°\mathrm{C}])} \cdot \frac{p}{p_0} \tag{3.47}$$

The formula to calculate the change of refractive index of air with temperature is given by:

$$\frac{\mathrm{dn_{air}}}{\mathrm{dT}}(\lambda, \mathrm{T}, \mathrm{p}) = -0.00367 \cdot \frac{n_{air}(\lambda, T, p) - 1}{1 + 0.00367\left[\frac{1}{°\mathrm{C}}\right] \cdot T} \tag{3.48}$$

From these, the following are obtained[40]:

$$n_{air}(\lambda = 635[nm], T = 15[°\mathrm{C}], \mathrm{p}_0) = 1.000276505 \tag{3.49}$$

$(According\ to\ Ciddor\ 1996)$ [40]

$$n_{air}(\lambda = 780[nm], T = 15[°\mathrm{C}], \mathrm{p}_0) = 1.00027516 \tag{3.50}$$

$(According\ to\ Ciddor\ 1996)$ [40]

$$n_{air}(\lambda = 3415.862[nm], T = 15[°\mathrm{C}], \mathrm{p}_0) = 1.000272620 \tag{3.51}$$

$(According\ to\ Mathar\ 2007\ which\ covers\ the\ range\ \lambda = 2800[nm] - 4200[nm]\ )$ [41]

$$\frac{\mathrm{dn_{air}}}{\mathrm{dT}}(\lambda = 635[\mathrm{nm}], \mathrm{T} = 15[°\mathrm{C}], \mathrm{p} = \mathrm{p}_0) = -9.6182 \cdot 10^{-7}\left[\frac{1}{K}\right] \tag{3.52}$$

$$\frac{\mathrm{dn_{air}}}{\mathrm{dT}}(\lambda = 780[\mathrm{nm}], \mathrm{T} = 15[°\mathrm{C}], \mathrm{p} = \mathrm{p}_0) = -9.5715 \cdot 10^{-7}\left[\frac{1}{K}\right] \tag{3.53}$$

$$\frac{\mathrm{dn_{air}}}{\mathrm{dT}}(\lambda = 3415.862[\mathrm{nm}], \mathrm{T} = 15[°\mathrm{C}], \mathrm{p} = \mathrm{p}_0) = -9.4831 \cdot 10^{-7}\left[\frac{1}{K}\right] \tag{3.54}$$

Eventhough $\frac{\mathrm{dn_{air}}}{\mathrm{dT}}$ is slightly different for the three wavelengths, the small change won't affect the calculations. In order not to make the calculations more complicated, it was decided to take a constant value of $\frac{\mathrm{dn_{air}}}{\mathrm{dT}}$ for the three cases throughout the temperature change as given in[29]:

$$\frac{\mathrm{dn_{air}}}{\mathrm{dT}}(\lambda = 632.8[\mathrm{nm}], \mathrm{T} = 14.85[°\mathrm{C}], \mathrm{p} = 101325[\mathrm{Pa}]) = -9.617 \cdot 10^{-7}\left[\frac{1}{K}\right] \tag{3.55}$$

3.7. Phase unwrapping

Phase unwrapping is often needed to reconstruct the real continuous phase $\varphi(x, y)$ from it's wrapped counterpart $\varphi^w(x, y)$. When the phenomena under investigation surpasses the range of measurement defined by a single wavelength, or when the object is thicker than the laser wavelength used for research, the phase gets wrapped and suffers from 2π ambiguities. The range of measurement is directly connected to the wavelength. For smaller wavelength, the range decreases, while for longer wavelength it increases. Longer wavelengths produce fewer fringes, reducing the number of 2π ambiguities. Phase has a periodicity of 2π $[radians]$ and the phase of light can be expressed as a multiple of this 2π periodicity. The repetitive nature of light propagation as a wave in the form of a sinusoidal wave makes the range of clear unambiguous measurement to be limited to one cycle of repetition, i.e. one wavelength. In other words, the wrapping is a direct consequence of the 2π periodicity of the $arctan$ function used to extract the phase profile from the light that is being measured. During the phase unwrapping process, the absolute phase difference between points of measurement in time and space must be less than the value of π $[radians]$, for a better unwrapping. There are cases when the difference is much higher, causing multiple wrapping simultaneously. Care must be taken when dealing with such situations. For a much wider range of measurement, a two-wavelength technique can be used.

The original phase map can be expressed as:

$$\varphi(x, y) = \varphi^w(x, y) + 2\pi N(x, y) \tag{3.56}$$

, where N is an integer value describing the number of 2π jumps. Unwrapping can be done by scanning the phase profile and correcting for the jumps. In cases when the profile has emphasized noise level, this straightforward way of unwrapping might be not successful[34].

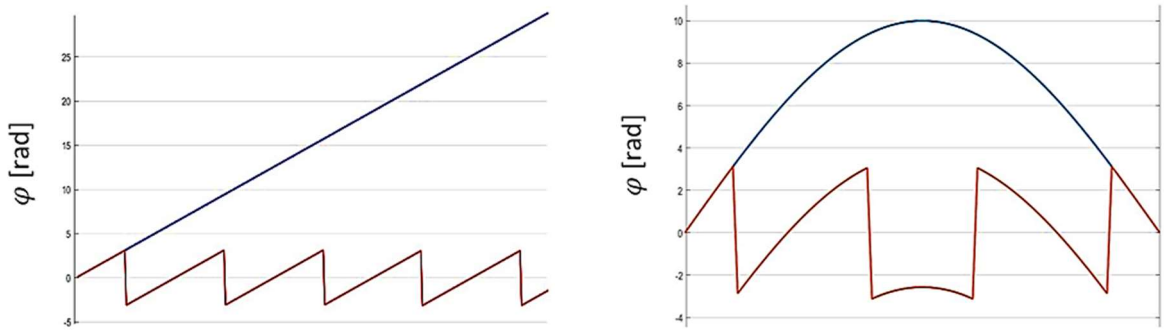

Fig.3.5. *Examples of wrapping and unwrapping.*

3.8. Applications of digital holographic interferometry

When a transparent/semitransparent body/material is put under optical investigation, by applying force into it or changing its refractive index by temperature, pressure, concentration etc. (in thin materials, gases or fluids), refractive index will change accordingly to these changes, causing changes in the optical path of travelling beams. Holographic interferometry measures these changes of optical path, returning useful data to interpret and visualize phenomena that caused such changes.

Digital holographic interferometry (DHI) is a non-invasive technique that is fast and can provide accurate date for the measurement of many physical parameters compared to conventional holography technique.

The whole process of recording the optical wavefront, storage, reconstruction and visualization is all done computer wise.[42]

DHI is a simple method, using simple structure, easy to operate, highly sensitive[43]. The main goal is to retrieve the phase function of a known fringe pattern, with the best accuracy, in order to determine changes that the system is undergoing. Main advantages of DHI are the sensitivity and the non-intrusive and non-contact character of the technique. The main disadvantage on the other hand is that the media under investigation must be transparent[44]**.**

DHI has been used for measuring different physical parameters, such as shape/deformation[45–47], temperature[48], vibration[49,50], strain[51] etc. Visualization of convection flow of transparent fluids [20,52,53] and the measurement of the temperature fields[52–54] have been reported.

Determining temperature distribution and heat flow is of immense importance in science and engineering[42]**.** Often, free and forced convection might be superimposed in many processes, making the investigation difficult. Knowledge of transport properties in liquid mixtures and changes in refractive indices is important for many applications in biochemical engineering, environment contamination etc. [55–60]. Thermal boundary layer development along a heated surface is found in many practical cases (in compact heat exchanger, oil coolers). It is very useful, in terms of investigation, analyzing and visualizing such processes of heat development with DHI as a potential and strong tool.

The 3D temperature field, Nusselt number of a thermally developing convection flow in the direction of the measuring beam of a holographic interferometer and its validity has been reported[61], standard interferometry by using the wavelet transform was used to study thermoconvective flow induced in a liquid sample[62], temperature measurements in laminar free convection flow of water using DHI was reported[42], temperature and physical structure measurements for liquid pool fire(n-decane) supported on water in rectangular Pyrex containers has also been reported[63,64]. Investigation of oscillatory heat transfer phenomena (acoustically driven flow) at high frequency using holographic interferometry, temperature distribution for physical situations that were characterized with periodic pressure variation were also conducted, where a new formula was introduced to link the temperature change with the pressure variation[65,66].

It is of great importance for applications to know the transport properties in liquid mixtures, which are difficult to be estimated using the kinetic theory since the coefficients may change sign depending on composition and temperature. In terms of concentrations, the determination of thermodifussion (Soret) coefficients and time-dependent evolution of the concentration field in water/ethanol and water/isopropanol mixtures by DHI have been reported[44]. Another method using holography technique by the effect of thermal diffusion forced Rayleigh scattering was used to determine the concentration of mixtures[67,68]. Small differences of refractive indices in solutions based on the effect of SPR (Surface Plasmon Resonance) and heterodyne interferometry with a sensitivity of at least $8.57 * 10^{-7}$were investigated in other institutions[43]. A modified Michelson interferometer was used to detect changes in volume of sample through phase transition for measuring the expansion of materials at the solid/liquid phase transition[69]. Measurement of the temperature and concentration dependencies of the refractive index of hen-egg-white lysozyme (HEWL) with a Mach-Zehnder interferometer was also reported[70].

4. Introduction to heat

This chapter introduces briefly the main concept of heat and some other important concepts that are related to the research conducted and presented in this thesis.

Heat flows constantly from our blood circulatory system to the air around us. From our body, the warmed air buoys off and warms the room where we are located. Heat transfer is present in everything and everywhere at some degree.[71]

4.1. Expressing heat in terms of thermodynamics

For a closed system, the *First Law of Thermodynamics* is expressed as[71]:

$$\dot{Q} = \dot{W} + \frac{dU}{dt} \quad \left[\frac{W}{m^2 K}\right] \tag{5.1}$$

, where $\dot{Q}$ is the heat transfer rate, $\dot{W}$ is the work transfer rate and $\frac{dU}{dt}$ is the change in time of the internal energy of the system.

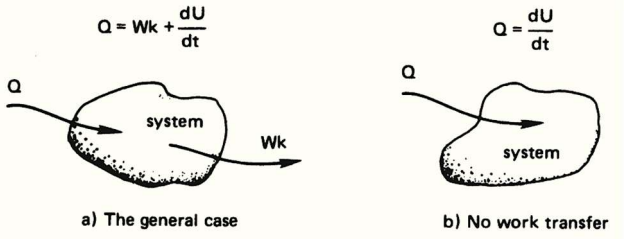

Fig.4.1. *The First Law of Thermodynamics for a closed system.*[71]

For the case when pdV is the only work happening, we have[71]:

$$\dot{Q} = p\frac{dV}{dt} + \frac{dU}{dt} \tag{5.2}$$

Depending on weather we have a constant volume process or constant pressure process, we have:

a) constant pressure process[71]:

$$\dot{Q} = \frac{dH}{dt} = mc_p\frac{dT}{dt} \tag{5.3}$$

b) constant volume process[71]:

$$\dot{Q} = \frac{dU}{dt} = mc_v\frac{dT}{dt} \tag{5.4}$$

, where $H\ [J]$ is the enthalpy, $c_p\ \left[\frac{J}{kgK}\right]$ the specific heat capacity for constant pressure, $c_v\ \left[\frac{J}{kgK}\right]$ specific heat capacity for constant volume, n is the number of moles of gas while for liquids it is replaced with the mass m. When the fluid under investigations is uncompressible, it turns out that[71]:

$$\dot{Q} = \frac{dU}{dt} = mc\frac{dT}{dt} \tag{5.5}$$

It is also important to remember that all real heat transfer processes that happen in nature generate entropy.

4.2. Modes of heat transfer

Heat transfer is the process of the displacement of thermal energy due to a spatial gradient of temperature. There are different types of heat transfer which are illustrated below.[72]

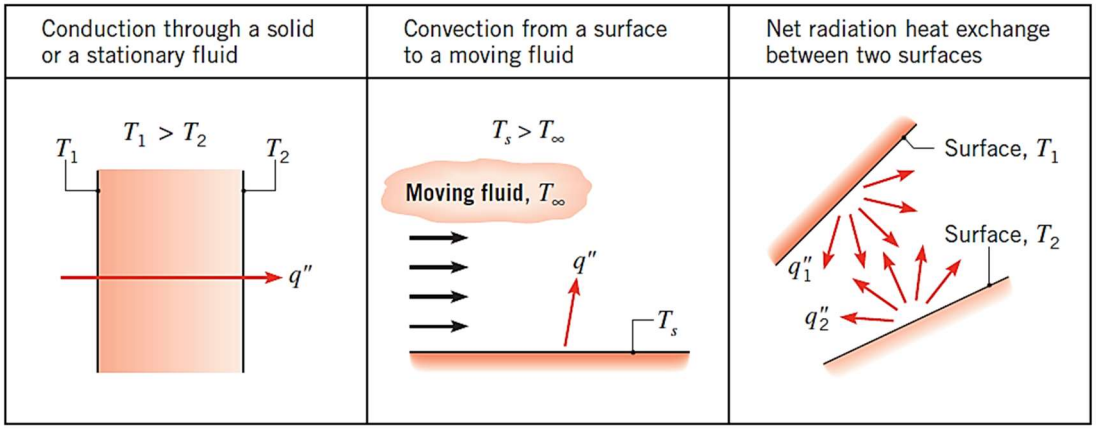

Fig.4.2. *Modes of heat transfer.*[72]

4.2.1. Heat conduction

Conduction is referred to the heat transfer in a medium (solid/liquid) or across two solids where a spatial temperature gradient exists.

Heat transfer in conduction occurs from particles that have more energy and transfer this energy to particles that have less energy. This means that this process happens at molecular level. In gases, the transfer of energy happens between molecules while in solids the process happens in lattice vibration at atomic levels, depending on the material, while in conductors free electrons also participate in this process.[72]

Fourier's Law states that: The heat flux q $\left[\frac{W}{m^2}\right]$, resulting from thermal conduction is proportional to the magnitude of the temperature gradient and opposite to it in sign which can be written as[72]:

$$q = -k\frac{dT}{dx} \quad \left[\frac{W}{m^2}\right] \tag{5.6}$$

, where k $\left[\frac{W}{mK}\right]$ is the thermal conductivity and $\frac{dT}{dx}$ $\left[\frac{K}{m}\right]$ the temperature gradient.

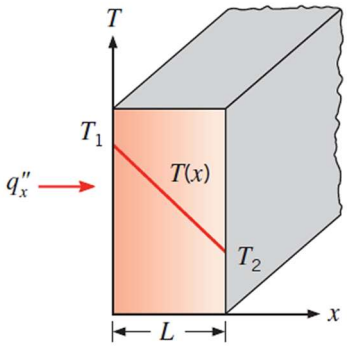

Fig.4.3. *Conduction through a slab.*[72]

For a simple case of one dimensional heat transfer by conduction, let's refer to Fig.4.3. If T_1 is the temperature of the environment on the left side of the slab, while the block represents a slab of a heat conducting material, and the right side is with lower temperature, then the temperature gradient may be expressed as[72]:

$$\frac{dT}{dx} = \frac{T_2 - T_1}{L} \tag{5.7}$$

and the heat flux is[72]:

$$q = k\frac{T_1 - T_2}{L} = k\frac{\Delta T}{L} \tag{5.8}$$

However, there is no way to decide which side the heat should flow, hence in one dimension analysis, the law takes the following form (where we already assign that q always flows from regions of high temperatures to the lower ones)[71]:

$$q = k\frac{\Delta T}{L} \tag{5.9}$$

In three dimensions, this law is written in the form[71]:

$$\vec{q} = -k\nabla T \tag{5.10}$$

, where:

$$\nabla T = \vec{x}\frac{\partial T}{\partial x} + \vec{y}\frac{\partial T}{\partial y} + \vec{z}\frac{\partial T}{\partial z} \tag{5.11}$$

Conduction heat flux increases with increasing thermal conductivity for a given temperature gradient. The thermal conductivity of material defers from material to material and from the state of the material. Solids have higher thermal conductivity than liquids, which have higher thermal conductivity than gases. In solids, which represent atoms arranged in structures called lattices, the thermal conduction happens mainly because of two phenomena, the free electrons that travel in the lattice structure and the lattice vibration waves.[72]

Thermal conductivity is expressed as[72]:

$$k = \frac{1}{3}C\bar{c}\lambda_{mfp}\left[\frac{W}{mk}\right] \tag{5.12}$$

, where C is the electron specific heat per unit volume, $\bar{c}$ is the mean electron velocity and λ_{mfp} is the mean electron free path.

Thermal conductivity is less effective in liquids because of the intermolecular spacing and for liquids it is expressed as[72]:

$$k \approx \frac{1}{3}c_v\rho\bar{c}\lambda_{mfp}\left[\frac{W}{mk}\right] \tag{5.13}$$

4.2.2. Heat convection

Convection is referred to heat transfer from a solid to a moving liquid with different temperature.

The process of convection involves heat transfer that comes from the random motion of molecules and by the bulk itself (motion of the fluid). Molecules that possess random motion get clustered in bigger groups and as such their individual energies superimpose. The bulk motion of the fluid and this superimposition create the total heat transfer.[72]

In the case of free convection, buoyancy forces induce the flow. This happens because of the density differences caused by the temperature gradient in the fluid. By being in contact with the hot surface, the fluid gets less dense and thus the buoyancy forces create a force that ascends the less dense fluid, which is then replaced with a much denser fluid, in other words a colder fluid.[72]

Free convection includes also latent heat exchange, which includes boiling and condensation.

Let us have a warm body and a cooling gas flowing around as illustrated in Fig.4. While the cooling gas passes by the warm body, one part of this cooling gas (a thin layer of it) will form a boundary layer around the warm body and conduct heat. This thin layer will be continuously substituted and taken away and mixed with the cool gas further away into the stream. This process of carrying heat is called convection. [71]

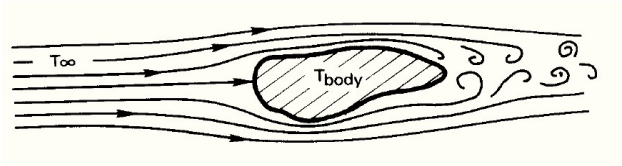

Fig.4.4. *Convection around a warm body*.[71]

The equation describing the process can be written as[71]:

$$q = \bar{h}(T_{body} - T_{\infty}) \tag{5.14}$$

, which is the steady state cooling law of Newton. $\bar{h}\ \left[\frac{W}{m^2}\right]$ is the average convection heat transfer coefficient and T_{∞} the temperature of the gas/fluid. This represents another simplification since $\bar{h}$ can depend on the temperature difference ΔT. In cases where the cooling fluid is forced to pass by the warm body and ΔT won't be large, $\bar{h}$ is independent of ΔT. This is called forced convection.[71]

In the case when fluid buoys up from a hot body or down from a cold one, we have the case of free (natural) convection.[71]

4.2.3. Radiation

Thermal radiation is referred to the heat that is emitted from bodies in the form of electromagnetic radiation. Such energy in most cases, compared to convection or conduction is neglected, because of its low magnitude. Radiation is taken in account when there is heat transfer processes that happen in high temperature.[71]

The reason why we warm up when we walk in the sun comes from this kind of heat transfer. This radiation takes place over a range of the electromagnetic spectrum. Depending on the wavelength, the transferred energy will be different. The model for perfect thermal radiation is the so called black body, which is a body that absorbs all the energy that falls into it but reflects nothing from it.[71]

4.3. Heat diffusion equation

When the temperature distribution is known and there is no bulk motion, the conduction heat flux can be computed at any point from *Fourier's law*. By taking a small control volume with infinitively small dimensions, taking in account that there might be an energy source E_g, that the medium can save some energy thus changing the internal energy E_{st}, specifying that no work is done on the system and only thermal forms of energy will be taken in account, then conduction heat rates at the opposite sides of the control volumes can be expressed as[72]:

$$q_{i+di} = q_i + \frac{\partial q_i}{\partial i} di \qquad i = x, y, z \tag{5.15}$$

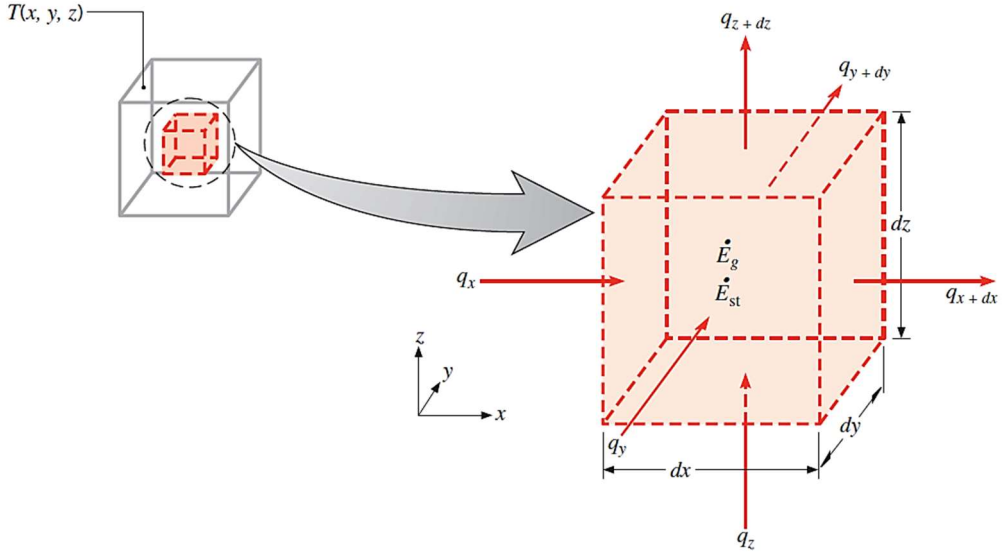

Fig.4.5. *Elementary control volume.*[72]

The general form of the heat equation is[72]:

$$\frac{\partial}{\partial x}\left(k\frac{\partial T}{\partial x}\right) + \frac{\partial}{\partial y}\left(k\frac{\partial T}{\partial y}\right) + \frac{\partial}{\partial z}\left(k\frac{\partial T}{\partial z}\right) + q = \rho c_p \frac{\partial T}{\partial t} \tag{5.16}$$

, where q $\left[\frac{W}{m^3}\right]$ is the rate at which energy is generated and the right part of the equation represent the internal energy stored by the medium. This equation provides the basic tool for heat conduction analysis and $T(x, y, z)$ can be obtained by solving it. If thermal conductivity is constant, the equation takes the form of[72]:

$$\frac{\partial^2 T}{\partial x^2} + \frac{\partial^2 T}{\partial y^2} + \frac{\partial^2 T}{\partial z^2} + \frac{q}{k} = \frac{1}{\alpha}\frac{\partial T}{\partial t} \tag{5.17}$$

, where α $\left[\frac{m^2}{s}\right]$ is the thermal diffusivity. In cylindrical coordinates it will look like[72]:

$$\frac{1}{r}\frac{\partial}{\partial r}\left(kr\frac{\partial T}{\partial r}\right) + \frac{1}{r^2}\frac{\partial}{\partial \phi}\left(k\frac{\partial T}{\partial \phi}\right) + \frac{\partial}{\partial z}\left(k\frac{\partial T}{\partial z}\right) + q = \rho c_p \frac{\partial T}{\partial t}$$

4.3.1. Boundary condition

Since the equation is of the first order in time (but it is of second order in spatial coordinates), one condition known as the initial condition must be specified.

The following shows three most common cases, given at the surface $x = 0[72]$:

1) The first case represents the case with a surface that maintains a constant temperature. It is known as the *Dirichlet condition*.
2) The second represents the case when a constant heat flux q_s exists at the surface and is expressed as:

$$q_x(0) = -k\frac{\partial T}{\partial x}\Big|_{x=0} = q_s \tag{5.18}$$

It is known as the *Neumann condition*.

3) The third represents the case that correspond to the existence of convection heating.

1. Constant surface temperature

$$T(0, t) = T_s \qquad (2.31)$$

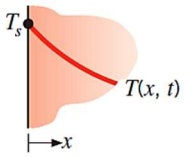

2. Constant surface heat flux
   (a) Finite heat flux

$$-k\frac{\partial T}{\partial x}\Big|_{x=0} = q_s'' \qquad (2.32)$$

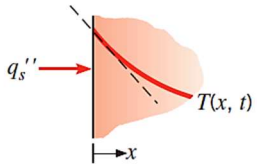

   (b) Adiabatic or insulated surface

$$\frac{\partial T}{\partial x}\Big|_{x=0} = 0 \qquad (2.33)$$

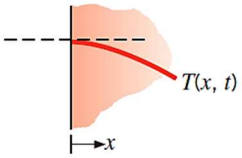

3. Convection surface condition

$$-k\frac{\partial T}{\partial x}\Big|_{x=0} = h[T_\infty - T(0, t)] \qquad (2.34)$$

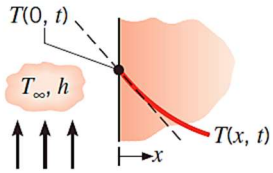

Fig.4.6. *Boundary conditions at the surface.*[72]

4.3.2. Heat generated by a cylinder source

Let us take in consideration a heat generator of a cylindrical shape, that has in it wires that carry current. The heat that is generated within it should be equal to the rate at which heat is transmitted to the sorroundings. The heat equation from the cylindrical form in this case takes the form of[72]:

$$\frac{1}{r}\frac{d}{dr}\left(r\frac{dT}{dr}\right) + \frac{q}{k} = 0 \tag{5.19}$$

, for which the solution is[72]:

$$T(r) = -\frac{q}{4k}r^2 + C_1 \ln r + C_2 \tag{5.20}$$

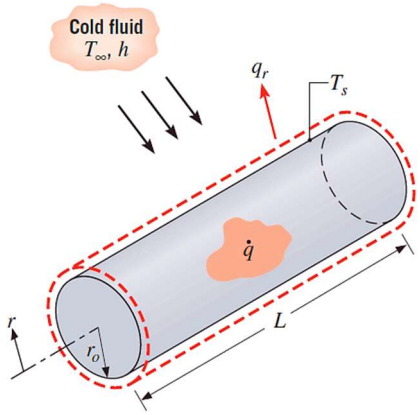

Fig.4.7. *Conduction from a cylindrical heater.*[72]

By applying both the first and second initial conditions the followings hold[72]:

$$\left.\frac{dT}{dr}\right|_{r=0} = 0 \tag{5.21}$$

$$\text{and} \quad T(r_0) = T_s \tag{5.22}$$

Because of symmetry we obtain $C_1 = 0$.

For $r = r_0$ from the boundary condition, it results that[72]:

$$C_2 = T_s + \frac{q}{4k}r_0^2 \tag{5.23}$$

Therefore[72]:

$$T(r) = \frac{qr_0^2}{4k}\left(1 - \frac{r^2}{r_0^2}\right) + T_s \tag{5.24}$$

4.3.3. Free convection

Free convection plays a significant role in electronic devices, in the determination of heat losses, air conditioning in buildings etc.

Fluid motion is due to buoyancy forces within the fluid, which causes convection currents. The temperature gradient which is present will cause a density gradient, and combined with the gravitational forces, the movement of mass will occur. With increasing temperature, the density of fluids and gases generally decreases.[72]

In the case when the heating plate is horizontally placed, the buoyancy force has two components, one parallel and one normal to the surface. This will cause a decrease of buoyancy forces parallel to the plate, hence a decrease of the fluid velocities along the plate. In the case of horizontal plate, the buoyancy force is exclusively normal to the surface.[72]

4.3.4. Horizontal cylinder

For an isothermal cylinder, Morgan has suggested the following relation[72]:

$$\overline{Nu}_D = \frac{\bar{h}D}{k} = CRa_D^n \tag{5.25}$$

, where C is a constant, values of which are shown in the table below and Ra_D^n the Rayleigh number at power of n for the characteristic diameter D of the cylindrical heater.

Ra_D	C	n
10^{-10}–10^{-2}	0.675	0.058
10^{-2}–10^{2}	1.02	0.148
10^{2}–10^{4}	0.850	0.188
10^{4}–10^{7}	0.480	0.250
10^{7}–10^{12}	0.125	0.333

Fig.4.8. *Constants for free convection on a horizontal cylinder.*[72]

This correlation gives the average Nusselt number of the isothermal cylinder, which is influenced by the development of the boundary layer. This creates the shape of the plum that ascends from the cylinder and is shown in the following figure.

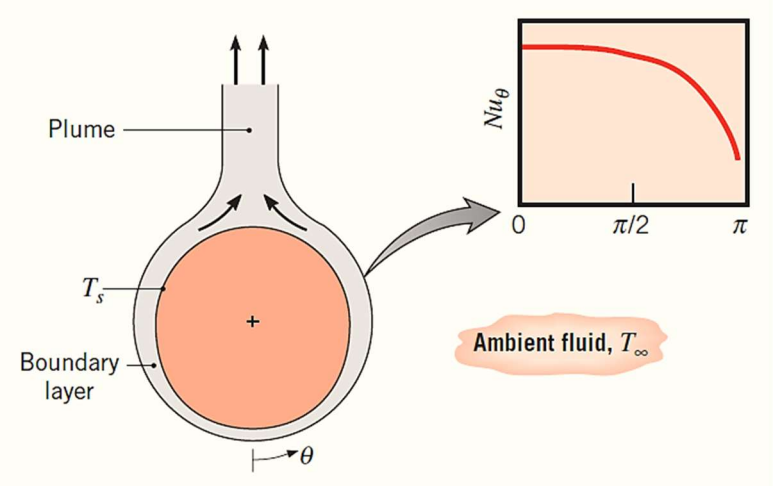

Fig.4.9. *Development of boundary layer and the distribution of the Nusselt number.*[72]

The influence of the Nusselt number starts at angle $\theta = 0[rad]$ to $\theta = \pi[rad]$. If the flow remains laminar over the entire surface, the Nusselt number is characterized by a maximum for $\theta = 0[rad]$ and decays with a monotical trend with increasing θ.[72]

5. Literature review

This chapter is dedicated to a general compilation of recent and older research works on the topic of using digital holographic interferometry for the study of liquids, gases and solids in the form of an extensive literature review. It aims at shedding light to mostly recent developments, the evolution and possibilities of applying optical techniques for diverse forms of application, not only to fluid mechanics but far beyond. Since this dissertation is focused on studying and visualizing temperature fields in flowing gases and liquids, most of the presented works are from the area of applied fluid mechanics, but not only restricted to it.

5.1. Introduction

Holography is an optical technique that provides the possibility to record phase objects. Interference fringes formed by the combination of the reference wave and the object wave give access to information coded in it. If any change of the optical path length happens, it will be reflected on the interference fringe through the change of phase, which can come as a consequence of temperature gradient, concentration gradient, movement or vibrations etc.

Holography was invented by Dennis Gabor in 1948.[11,21]

Measurement by holographic interferometry started more than 40 years ago. Holographic interferometry enables to perform interference between objects separated in time instead of interference between objects separated in space as in classical interferometry.[20]

Digital holographic interferometry has replaced classical interferometric holography by using modern equipment for capturing holograms (CCD or CMOS camera) and uses computers to process all data and to reconstruct numerically the diffraction of the reference beam, which eliminates the time consuming steps of developing photographic plates and enables fast and easy access to the phase.

Digital holographic interferometry is used in scientific research as well as in industry. It can be used to visualize temperature fields in periodical fluids, complex fluids, in fast moving fluids with high temperature, diffusion coefficients[20] via real-time evolution of concentration, in combustion processes by the measurement of temperature and temperature profile of flame, diffusion (interdiffusion, diffusion through a meniscus), the Soret effect, convection, dissolution, in designing air conditioning units, heat transfer units, thermal energy storage systems, machines, industrial processes, to study thermal properties of phase-change materials and to predict the thermal behavior of a liquid (by only using a pixel), optimization of aircraft structures, etc.[20,36,37,73–78]

Digital holographic interferometry can also be used in painting conservation and restoration[79,80],the analysis of standing soundwaves[81], thermal stress monitoring[82], in digital microscopy[83], in the study of plasma densities[84], and for the characterization of optical waveguides[85].

This technique delivers high spatial and temporal resolution of the distribution of the refractive index, in real time, and the advance in data acquisition, data processing and the high-speed computers make this technique very powerful and attractive. Its disadvantages are the small size of the sensor chips and smaller resolution, smaller than the photographic plates, which implies that smaller objects can be investigated.

We can highlight two advantages of holographic interferometry over classical interferometry[20,34,86]:

1) The ability to measure diffuse reflecting surfaces of objects;
2) Its differential character, meaning that the classical condition of having two arms of the interferometric setup optically equal is no longer required, implying also that experiments can be done without super precision and the need of high quality optical elements. Worth mentioning is the fact that, in digital holographic interferometry, two or more waves can be compared, thus a series of holograms can be used, averaged to eliminate random fluctuation and used for reconstruction, a possibility that didn't exist before .

Digital holographic interferometry can be used where other techniques fail to attain certain accuracy and in experiments where the normal flow of the fluid/gas shouldn't be interrupted. Because digital holographic interferometry is a non-contact optical method, it is a very suitable technique for measurements, and with the help of processing devices, it is useful to visualize temperature fields.

Another advantage of the technique is the fact that imperfections of the beam path won't influence the shape of the interference field. Worth mentioning, as well, the direct retrieval of the interference phase from the holograms obtained digitally is a benefit.[28]

Therefore, it is an excellent technique to detect small changes of refractive index, density, pressure and temperature.

More extensive details on the theory and the practical setup of holographic interferometry (and others) can be found in the papers with the following referencing number[28,61,87–91].

5.2. Digital holographic interferometry for air

5.2.1. Visualizing temperature fields using digital holographic interferometry

Digital holographic interferometry has a wide range of application in temperature field visualization in fluid mechanics. Here, unsteady temperature field visualization, generated by a heated pulsed jet, was object of the study. Jets are used for heating/cooling applications, among others. The air comes out from the jet by pushing hot air from the nozzle through an orifice.

In order to compare the accuracy of results, measurements were performed using two techniques, digital holographic interferometry as the non-contact optical method, and constant-current anemometry technique, as the point temperature measurement method which is in contact with the hot air. Due to the fact that phase change in such experiment is very low, a double-sensitive interferometric setup, allowing light to pass twice through the region of interest, was employed to obtain faithful results. The possibility of reconstructing a 3D visualization of the temperature field exists as well, using tomographic approach. However, a disadvantage for this kind of setup is the light efficiency. Other interferometric setups can be used for such experiment, such as the Twyman-Green interferometer[86].

A problem arising during such measurements is the frequency at which the phenomenon repeats itself and the possibility to capture and visualize such temperature fields. Since the process is periodical, it can be synchronized with the camera, i.e. the jet is synchronized with the camera. Such synchronization is crucial for the experiment to work as it should and to obtain faithful data.

The setup employed is shown in Fig.5.1. Light passes twice through the phase object, and most of the light is lost while passing through the beam splitter, hence the light efficiency problem.

Important identity to be calculated is the phase change captured in each hologram. The intensity and phase distributions are defined as in *eq.(3.23)* and *eq.(3.24).*

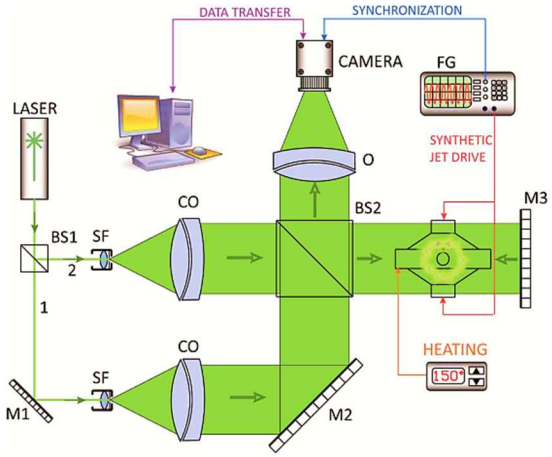

Fig.5.1. *Setup for digital holographic interferometry with double sensitivity used for air temperature field measurement.*[73]

At first, a reference hologram was captured a priori to the beginning of the experiment. The rest of the holograms were captured in synchronization with the jet. Randomness was eliminated by averaging the phase, from a series of holograms captured at the same exact point in time in the period, since the phenomenon is periodical. Phase unwrapping was done by simple modulo of 2π.

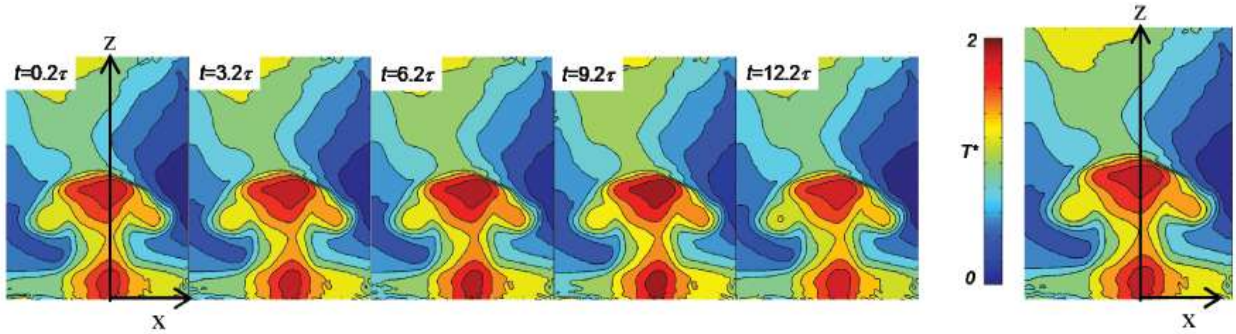

Fig.5.2. *Phase averaging example.*[92]

The refractive index is linked to the density through the Lorentz-Lorenc equation as in *eq(3.41)* and the Gladstone-Dale equation in *eq.(3.42)*.

While the light passes through the object, it integrates all the phase change along its path. The relation between the phase and the refractive index along the path is given by *eq.(3.39).*

Temperature of air reached $T = 150[°C]$ during measurements. Temperature was calculated by similar formula as in *eq.(5.2).*

The comparison of data obtain by digital holographic interferometry and constant current anemometry is shown in Fig.5.3.

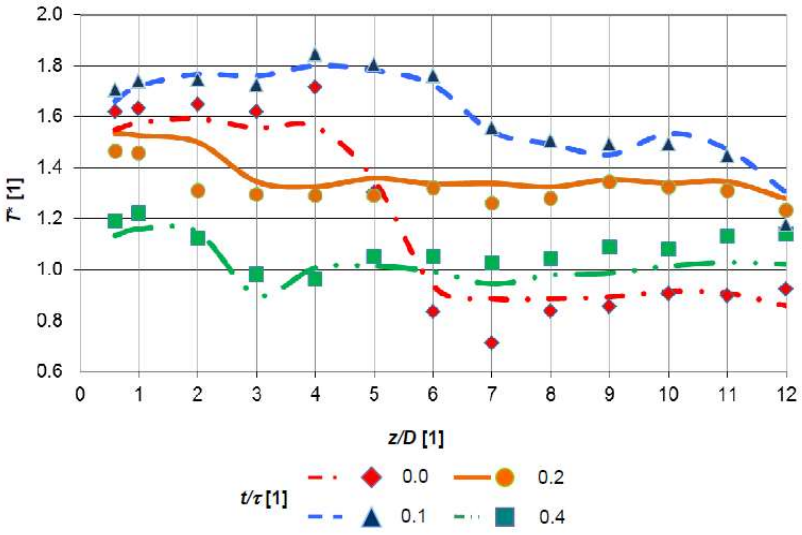

Fig.5.3. *Temperature comparison between digital holographic interferometry (solid line) and hot wire anemometry by constant current anemometry. τ is the time period of the jet.*[92]

From the data of the graph in Fig.5.3., it can be seen that the digital holographic technique shows more accurate results[92], without disturbing the normal flow of the air from the nozzle. The only limitation of this technique is the frequency of the CCD camera that is used.

A slight problem can result from the phase averaging that occurs in the direction of propagation of light, but this can be partially overcome by using the Abel transformation while digitally processing the data.[92]

Other examples of temperature measurements are shown in Fig.5.3. and Fig.5.4.

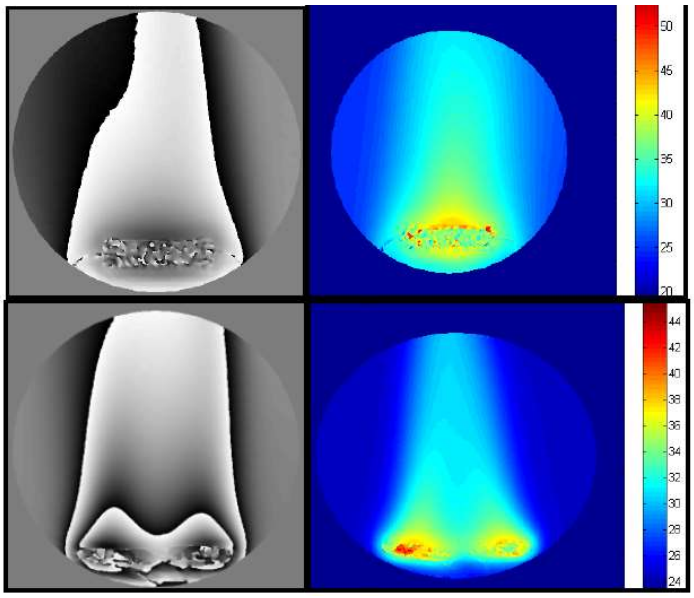

Fig.5.4. *Reconstructed interference phase distribution and corresponding temperature fields of a resistive spiral heated by the electric current with a Mach-Zehnder interferometer (single exposure path).*[34]

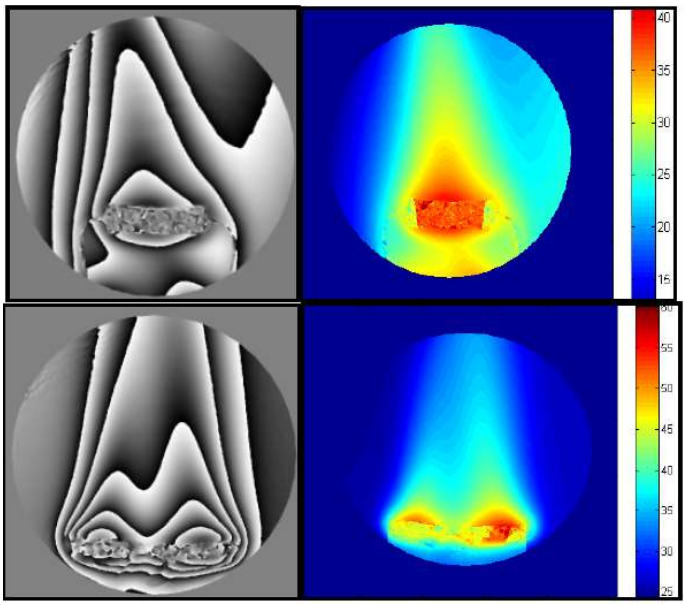

Fig.5.5. *Reconstructed interference phase distribution and corresponding temperature fields of a resistive spiral heated by the electric current with a Twyman - Green interferometer (double exposure path).[*34]

More details on the experiment represented above and other similar experiments can be found in [34],[86] and [93].

Overall, the disadvantages of the constant-current anemometry are that, it disturbs the air flow and temperature field, needs some correction when making simultaneous measurements of the temperature and the velocity fields, and is a time consuming technique since it requires also equal conditions during the whole experiments for all periods of measurements. Another important limitation of the constant-current anemometry technique is its limitation to up to $3[kHz]$.[92]

5.2.2. Measuring air temperature using laser interferometry

Plasma's temperature, density, intensity and refractive index are of importance in laser-induced plasma and laser material interaction[37]. Plasma changes happen in very short period of time, in a very small region. The aim of this experiment was to detect air temperature changes in laser-induced plasma using interferometry. Because these changes are very small, holographic interferometry was used to overcome difficulties presented when using ordinary temperature measurement techniques using thermocouples for this type of experiments. The plasma is generated at the focal distance.[37]

It was reported that, due to insufficient contact of the thermocouple with the material at the focal region, measurement with thermocouple caused problems ***(Takaki et al., 2001)***. One of the main problem was the huge gradient of temperature in the holder of the material, which is why a non-contact optical method was needed in order to determine the temperature field.

This experiment was performed using the simplest interferometer setup, the Michelson interferometer. The change in temperature was extracted by the shifting of interference fringes.

The relation between the change of refractive index of air $\Delta n = n - n_i$ (n_i is the refractive index of air at its initial value, while n is the final value), the change of optical length ΔL, the disturbed air length l, the number of interference fringes shift N is given by:

$$N = \frac{\Delta L}{\lambda} = \frac{l}{\lambda}\Delta n \tag{5.1.}$$

The temperature was estimated from the following equation:

$$T = \frac{PR_G T_i d}{N\lambda R_0 T_i + R_G P_i d} \tag{5.2.}$$

, where, P_i represent the initial pressure, P the final pressure, R_G the Gladstone-Dale molecular refractivity, T_i the initial temperature in Kelvin and R_0 the general gas constant.

Simple schematic view of the setup is shown in Fig.5.6.

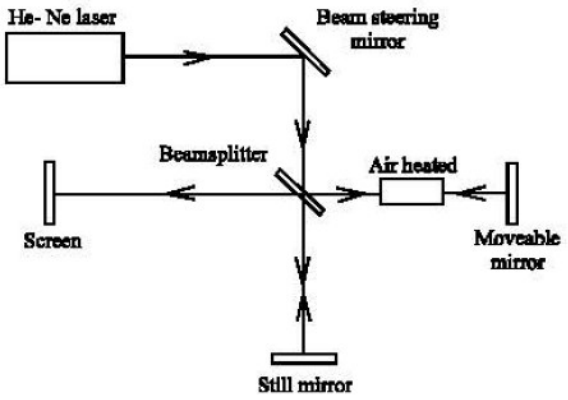

Fig.5.6. *Schematic view of the Michelson interferometer.*[37]

Air on one of the arms was heated from $293[K]$ to $593[K]$. A thermocouple was also inserted in the region of interest as a matter of comparison of data acquired by digital holographic interferometry and its accuracy. A ND:YAG laser with pulse duration of $8[ns]$ was used.

When both waves from the arms fall into the camera's surface, they interfere, creating a pattern of bright and dark fringes that are almost parallel. When heat is generated, some disturbance in one arm will occur, which will be reflected by a shift of fringe pattern, caused by a change of the optical path of the laser beam. Phototransistors were used to detect the number of fringe shifts, apart just using a camera to record the interference fringes shift.

This experiment showed that air temperature measurements are possible using a simple Michelson interferometer. It shows that plasma temperature measurements are possible when being pulse induced. Also these findings were in accordance with values obtained by thermocouples.[37]

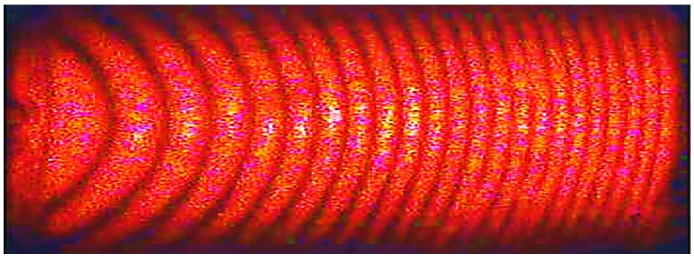

Fig.5.7. *Interference pattern of both waves coming from the arms of the interferometer (without heating).*[37]

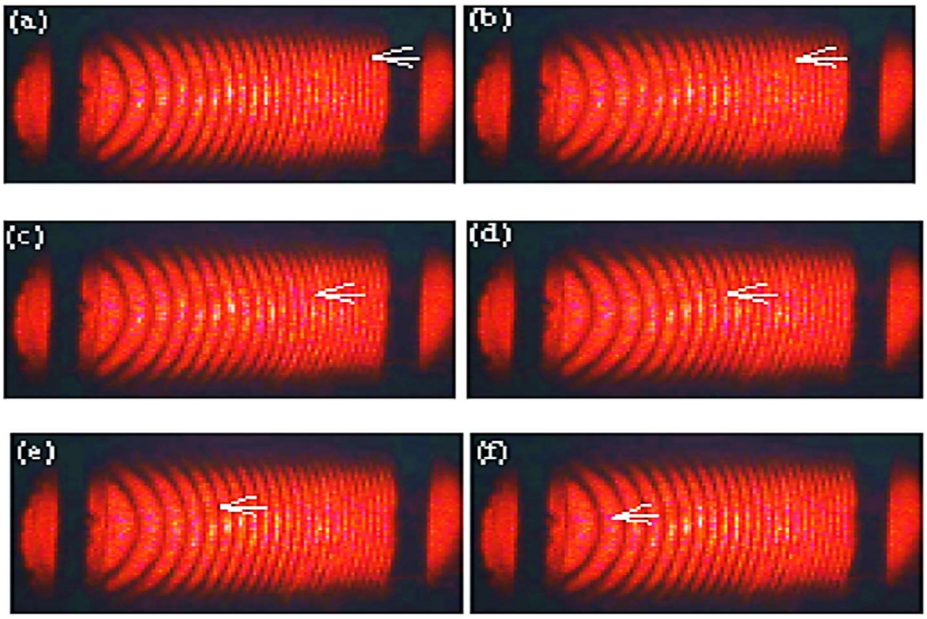

Fig.5.8. *Observation of plasma formation in one of the arm of the interferometer taken in different time after heating process started: a) 0.04[s], b) 0.08[s], c) 0.12[s], d) 0.16[s], e) 0.20[s] and f) 0.24[s].*[37]

5.2.3. Temperature measurement of axisymmetric flames

The aim of this experiment was to demonstrate the measuring of gaseous' flame temperature and temperature profile using digital holographic interferometry, to be more correct, lensless Fourier transform digital holographic interferometry. This experiment was performed by using the flame of a candle as the axisymmetric object. The main procedure here was to calculate the phase difference between two holograms taken at two different times. Holograms were electronically recorded, numerically reconstructed and the results were on real time.

In order to have a good distribution of the intensity of light, diffused illumination was used. This brought also some other benefits[74]:

1) Nearly uniform irradiance of light over the electronic sensor;
2) Elimination of noise coming from dust and scratches on optical elements;
3) The sensor received higher frequencies, i.e. information from the whole object.

The scheme of the optical setup is shown in Fig.5.9. The whole process of capturing and processing the images recorded by the CCD camera is schematically represented by Fig.5.10. in the form of a chart.

The first hologram was captured when the candle wasn't lighted on, as a reference. Other holograms were taken at regular intervals, at the most stable position of the flame, and at a phase difference smaller than $2\pi[rad]$. A phase unwrapping was performed by using the Goldstein method, thus converting the discontinuous phase distribution into a continuous one. The reason behind the sharp fringes from the reconstructed phase difference map is the path length difference which is smaller than the coherence length of the laser. The spacing between successive fringes indicates the difference in the refractive index between the locations inside the flame, while the color gradient (white to black) corresponds to the refractive index gradient.[74]

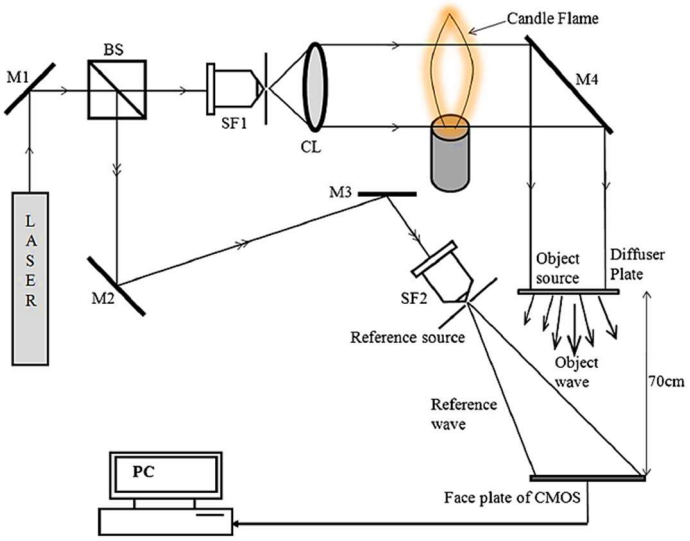

Fig.5.9. *Setup used for measuring candle's temperature and its temperature profile.*[74]

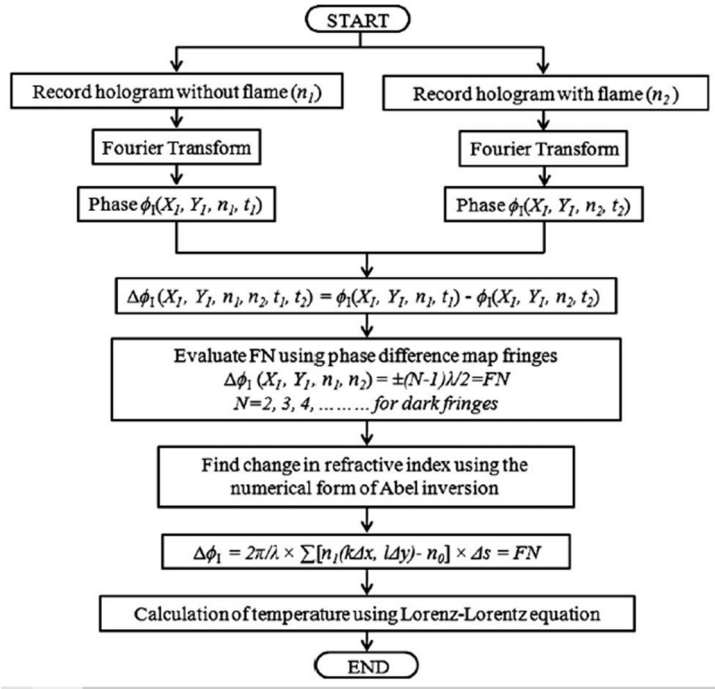

Fig.5.10. *Flow chart of the experiment*.[74]

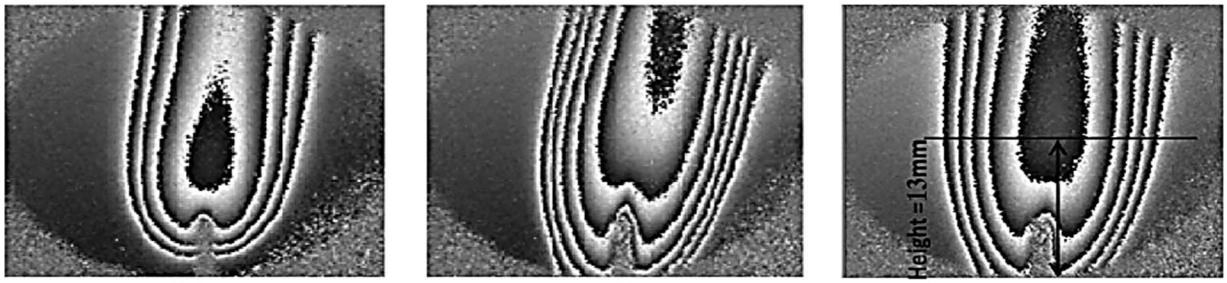

Fig.5.11. *Reconstructed flame (phase difference map) of the candle taken at different times.*[74]

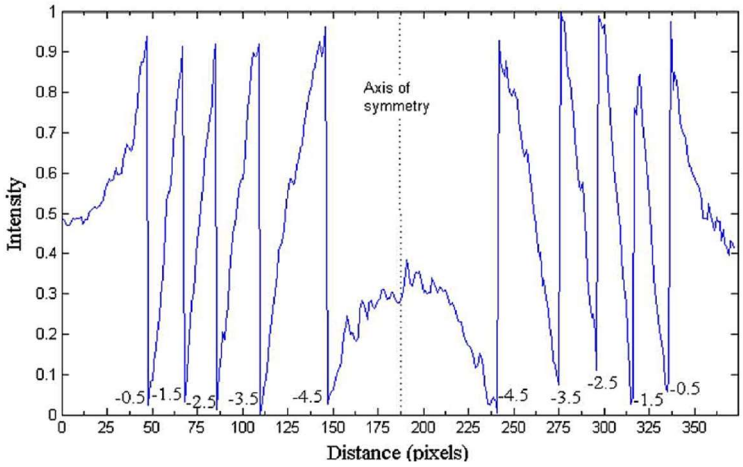

a)

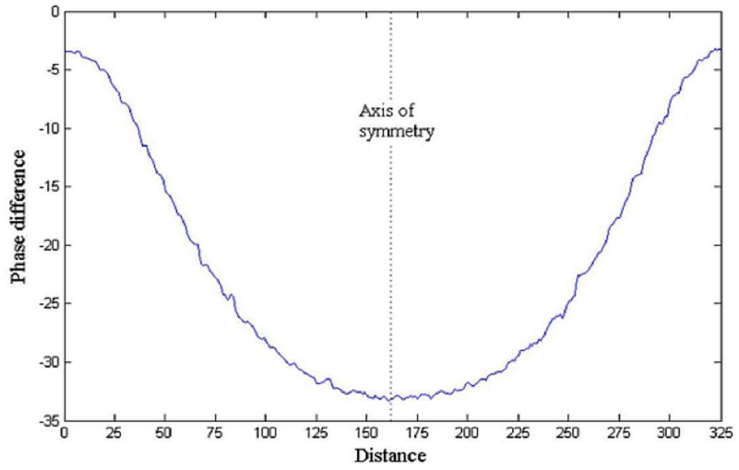

b)

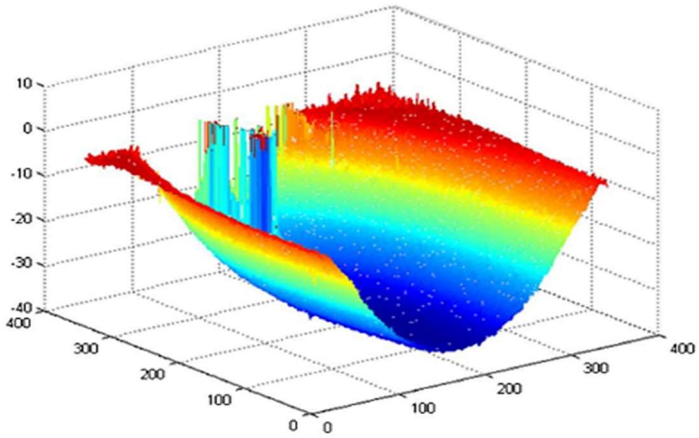

c)

Fig.5.12. *a) Line profile of the phase difference map, b) unwrapped phase map profile and c) 3D phase profile, of the flame at height of 13[mm].*[74]

Fig.5.12. shows the radial profile of the wrapped phase difference and b) its continuous distribution of the phase difference (unwrapped) in an axial plane at a height of $13[mm]$, while c) shows the 3D profile phase profile.[74]

The candle's wick is the reason behind the discontinuity in the unwrapped phase map profile at $x = 200$ and $y = 400$ where the phase is equal to 0, hence the phase difference cannot be calculated, while the rest represents the region around the wick inside the flame, yielding to a negative phase difference profile.[74]

From the obtained data and calculation, the temperature distribution is shown in Fig.5.13.

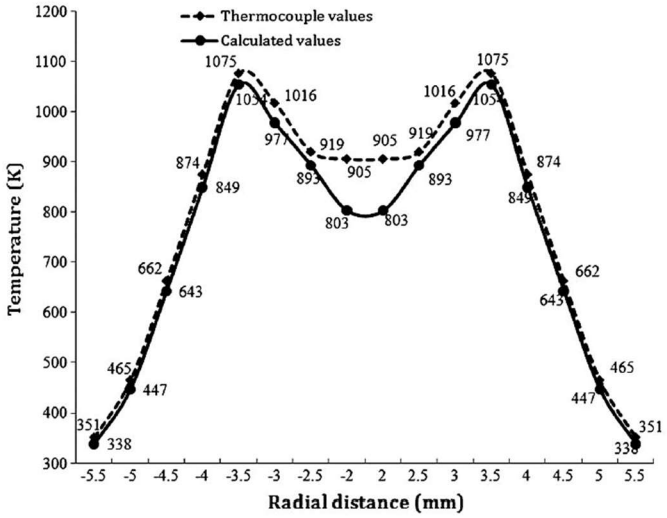

Fig.5.13. *Temperature profile versus radial distance of the candle flame at height of 13[mm].*[74]

To calculate such temperature distribution, the Lorenz-Lorentz equation was used:

$$T = \frac{T_0}{\left(\frac{n - n_0}{n_0}\right)\left(\frac{3PA + 2RT_0}{3PA}\right) + 1} \tag{5.3.}$$

, where T_0 is the temperature at the reference condition at which the refractive index is n_0, P is the atmospheric pressure, R is the gas constant and A is the molar refractivity of air.

This experiment demonstrated that digital holographic interferometry is a conveyable, accurate, fast and powerful technique for the measurement of the temperature of flames.

The accuracy could be enhanced by using a pulse laser.[74]

5.2.4. Temperature measurements in premixed flames with different structures

The aim of this experiment was to determine the flame structure and the temperature profile of different flames with different structure and the comparison of data obtained with thermocouples. It also investigates the effect of composition change in the reconstruction of the temperature profile. Flames under investigation are laminar, axisymmetric, premixed propane-air flames.

One of the advantage of interferometric holography is the possibility to make measurements using not top high quality optical elements.

It is already known that fuel-lean flame compared to fuel-rich flame have simpler flame structure[75]. Measurements with flame requires high temporal and spatial resolution since they can vary significantly. 99% pure propane was used in this experiment. The optical setup used for this experiment is shown in Fig.5.14. He-Ne laser of wavelength $\lambda = 632.8[nm]$ was used.

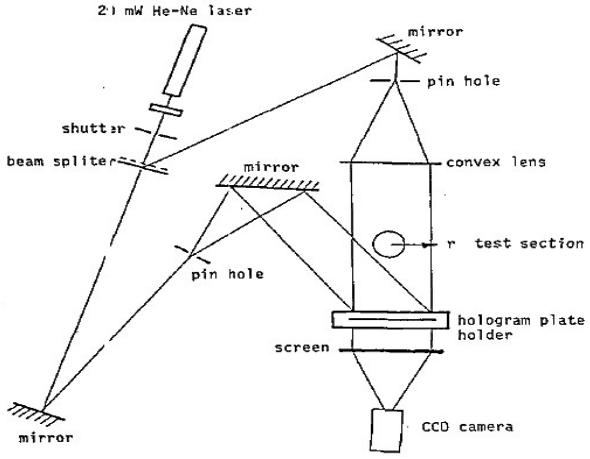

Fig.5.14. *Optical setup.*[75]

Double exposure was proposed in this experiment, due to the fact that, for the lean-flame case a $10[Hz]$ in frequency motion oscillation was noticed, while the same happened for the rich-flame but in regions that were higher from the flame tip (compared with the lean-flame case).[75] Measurements were also performed using thermocouples, which were mounted in a 2D traversing gear in order to perform measurements through the flame. The fringe counter technique that was used to determine the distribution of the fringe number and the fringe pattern for both flames are shown in Fig.5.15.

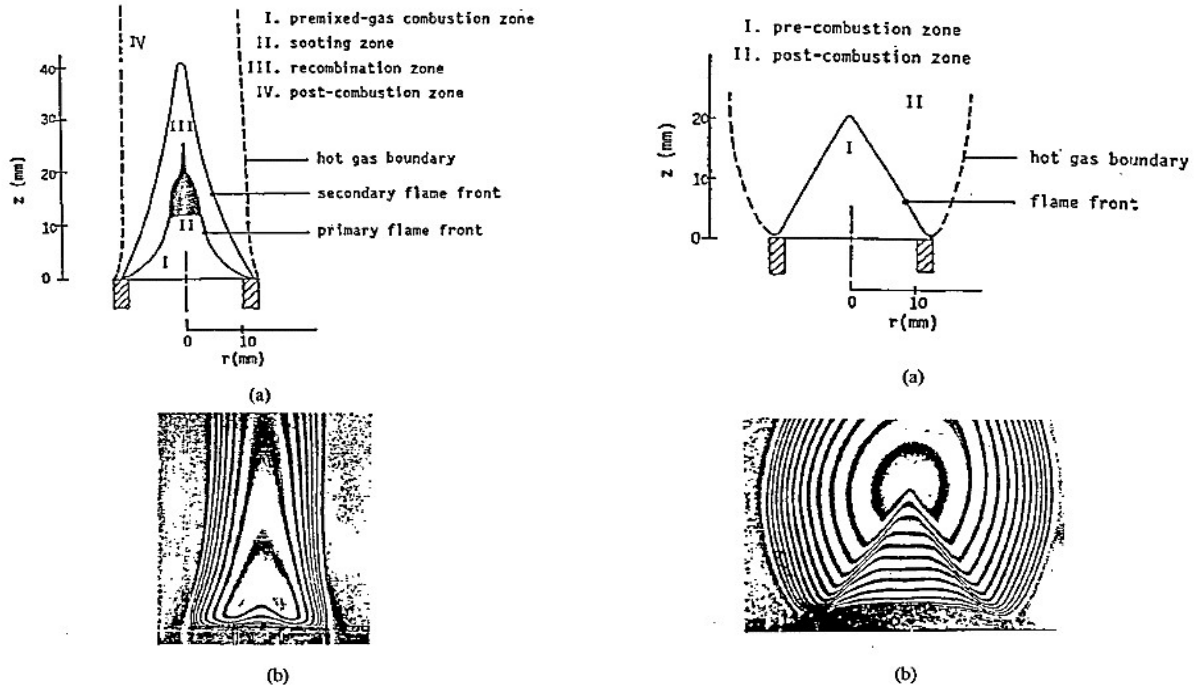

Fig.5.15. *Scheme of flames (a) and their fringe patterns (b): left fuel-rich flame, right fuel-lean flame.*[75]

It can be seen from the fringe patterns in Fig.5.15. that both flames are almost axisymmetric.

Since the species composition distribution wasn't measured here, simplified calculations that were suggested by Weinber were used. The equation that was used was[75]:

$$n(r) - 1 = K(r)\rho(r) \tag{5.4.}$$

, where $n(r), K(r)$and $\rho(r)$ are functions of the fringe number distribution, calculated using the Abel inversion. It was concluded that the composition change affects only the rich flame interferometric reconstruction. By using the ideal gas law, the temperature distribution can be obtained.[75]

It was also noted that the Gladstone-Dale shows significant variation for the rich-fuel case.[94]

Thermocouple temperature measurements were used for comparison. Three different distribution of R_L were used for reconstruction:

1) T_1 – Linear interpolation of R_L values at the axis (R_L of the reactants) and at the hot gas boundary (R_L of the products);
2) T_2 – Uniform R_L distribution using R_L of the products;
3) T_3 – Uniform R_L distribution using R_L of the reactants;

Results are shown in Fig.5.16. at the axial positions of $2[mm]$ and $12[mm]$.

In general, the accordance between both techniques is satisfactory for the fuel-lean flame. But this cannot be said for the fuel-rich flame as shown in Fig.5.17.[75]

From Fig.5.16. and Fig.5.17., it was shown that the rich-flame has a much more complex flame structure, thus, it was concluded that this implies that the change of composition cannot be neglected and has to be taken in account for the reconstruction of the temperature with interferometric holography. This implies that a uniform or linear R_L can't be used for the rich flame case but can be used for the lean-flame case. Thus, further studies are needed for the complex flame structure.[75]

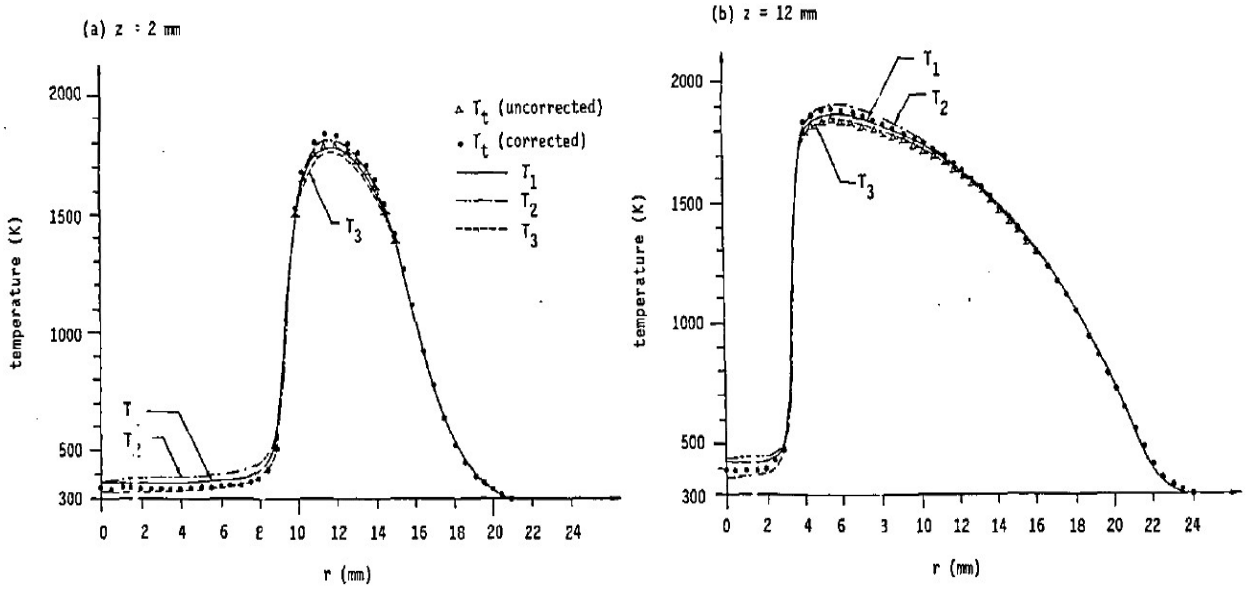

Fig.5.16. *Comparison of temperature measurement between holographic interferometry and thermocouple measurements for fuel-lean flame at a)* $z = 2[mm]$ *and b)* $z = 12[mm]$.[75]

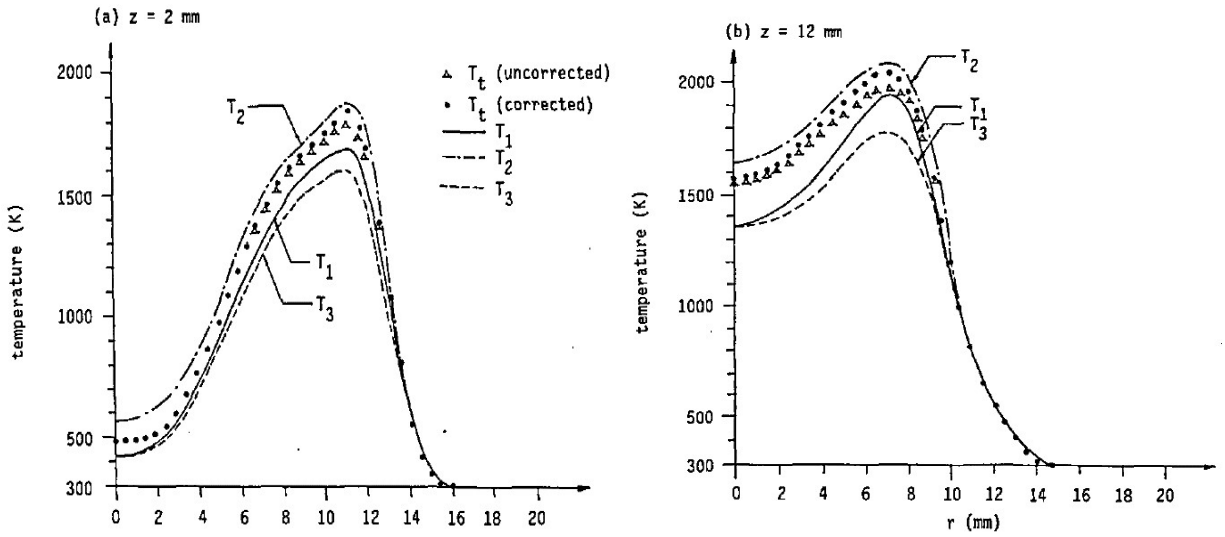

Fig.5.17. *Comparison of temperature measurement between holographic interferometry and thermocouple measurements for fuel-rich flame a)* $z = 2[mm]$ *and b)* $z = 12[mm]$.[75]

5.2.5. Measurement of asymmetrical temperature field and tomographic reconstruction

The aim of this experiment was to visualize the periodic asymmetrical temperature field of hot air coming out from a synthetic jet. The experiment is similar to the first experiment described in *section-5.2.1.* A Twyman-Green setup with double sensitivity was used. The setup is shown in Fig.5.18. In this experiment, a synthetic jet with a $9[mm]$ orifice was used. It is based on the similar idea of synchronizing the camera with the jet. The examination of an asymmetric temperature field requires a large number of different points of measurements in order to be used as a tomographic approach. But, since the phenomenon is periodic, there is no need to use as many sensors. This can be simplified using a camera and a rotational stage. The process of acquiring the image is the same as in the first described experiment. The Radon-transform and its inverse transform were used for the image processing of the holograms. The 3D image was reconstructed numerically as stacked plane slices of the whole temperature field.[76]

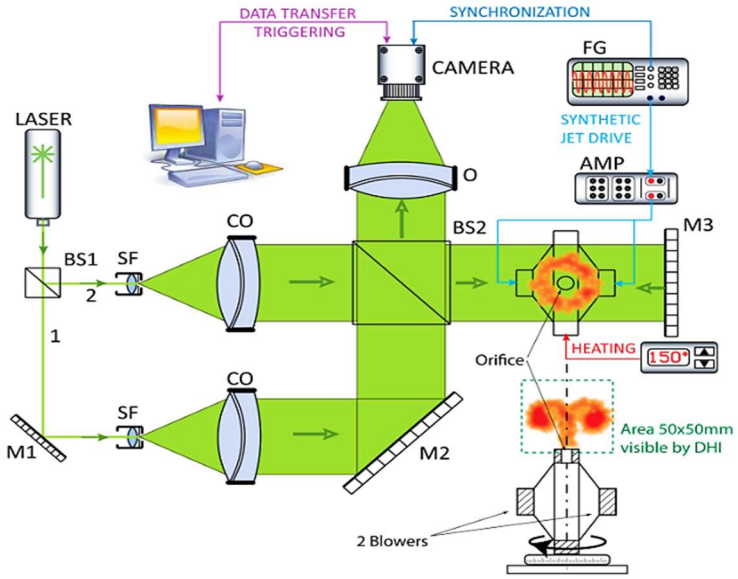

Fig.5.18. *Setup used to visualize the 3D profile of an asymmetric temperature profile.*[76]

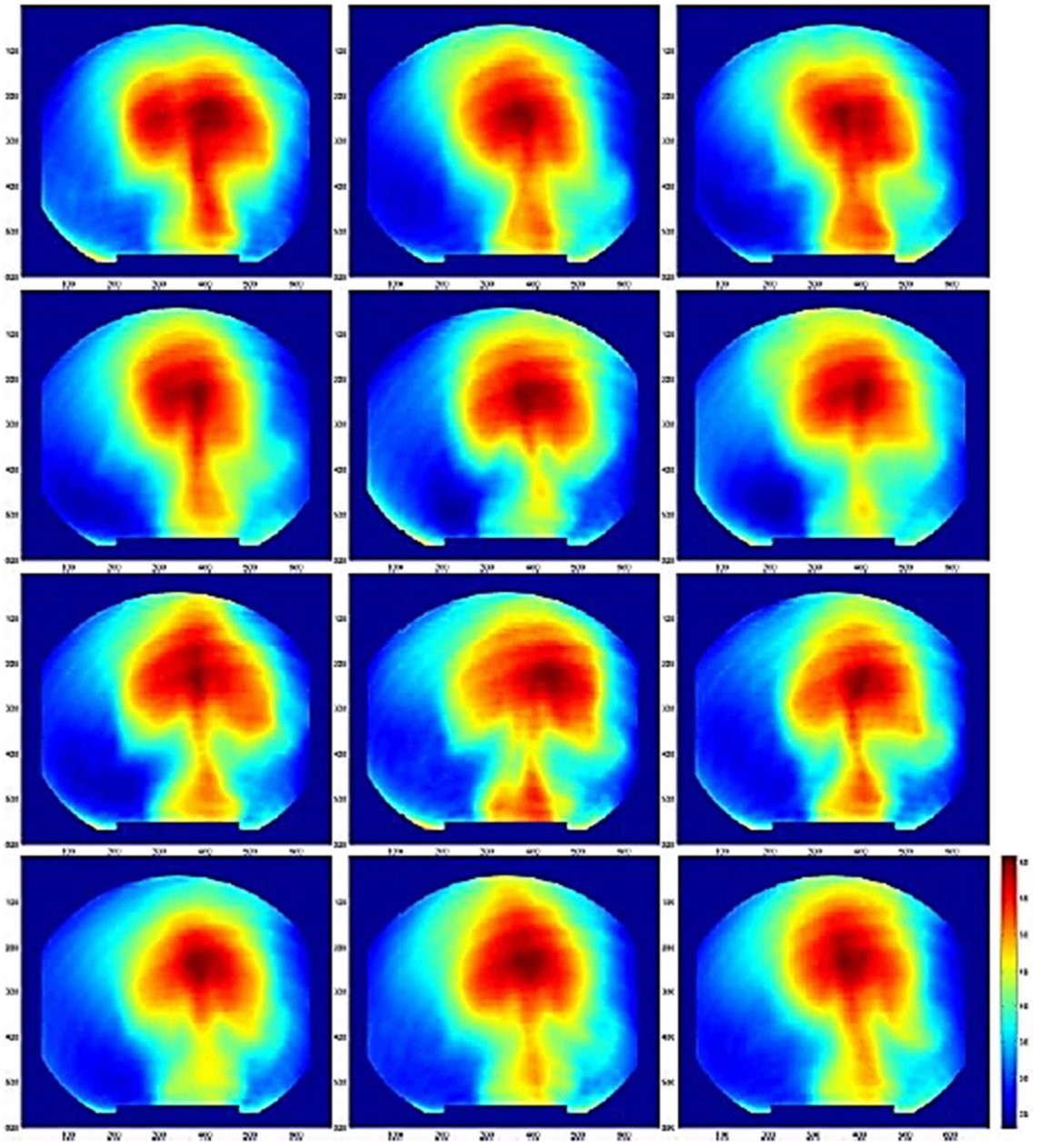

Fig.5.19. *Image taken at different time but on the same phase, each with a 16[ms] delay and an angle of 50[°]*.[76]

As said, during the reconstruction, all phase fields corresponding to the same angle were averaged (see Fig.5.19.). The reconstruction of the 2D plane slices was realized by the method of filtered back-projection. These slices were stacked together afterwards to form the 3D temperature profile.[76]

Fig.5.20. shows a series of images taken at the same angle but with some delay to capture the whole phenomena, from the beginning to its end. In Fig.5.21. , holograms were captured for relative delays of $2[ms]$ each ($0[ms], 2[ms], \dots, 66[ms]$) for angles of $0[°], 10[°], 20[°], \dots, 160[°]$. The tomographic reconstruction looks as shown in Fig.5.21. From these results, it can be seen that digital holographic interferometry is a powerful technique to visualize fast occurring phenomena with a simple non-invasive technique.

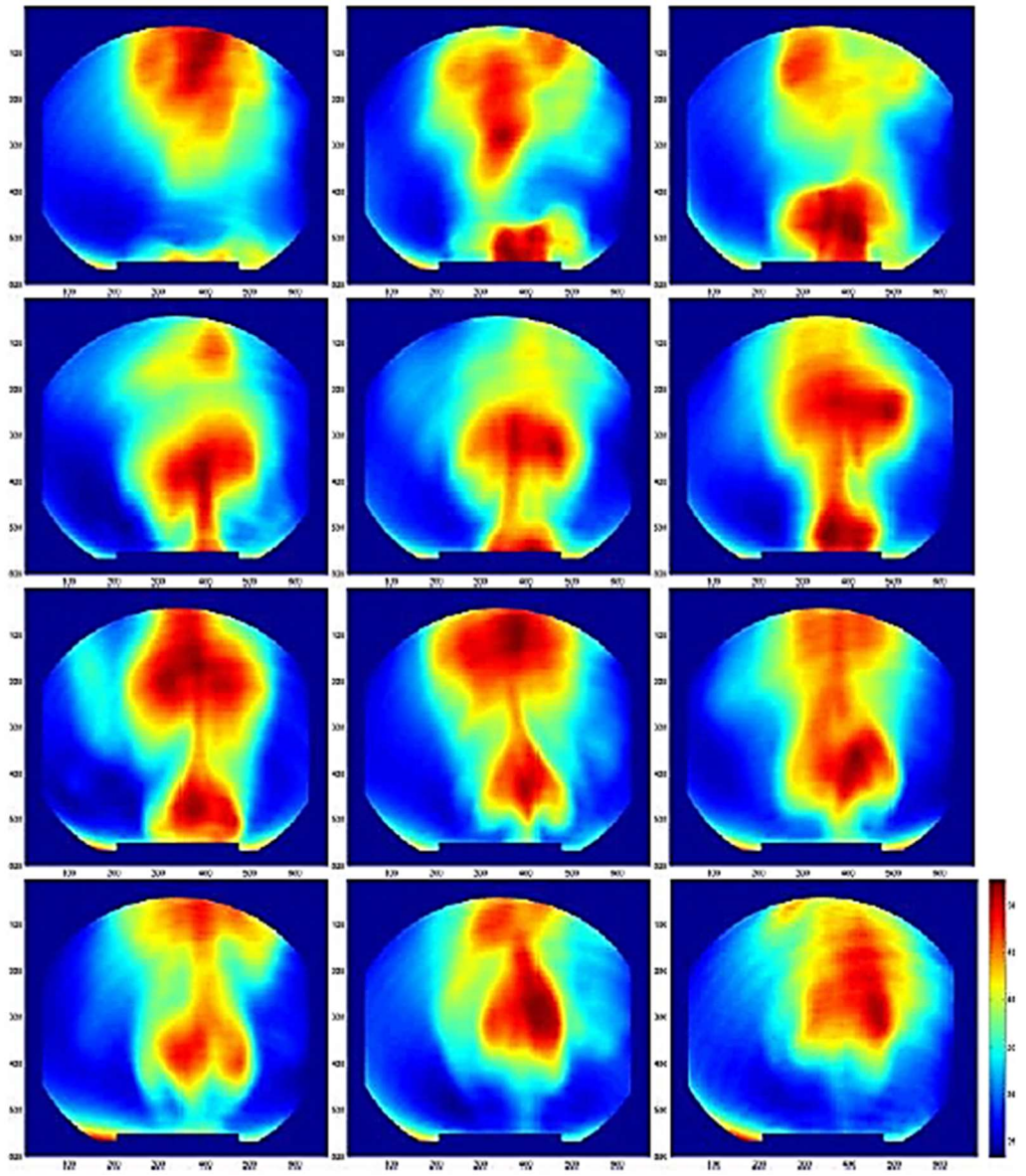

Fig.5.20. *Evaluated dynamic temperature fields at angle of view of 50[°] and relative time delays starting from 0[ms], 3.2[ms], 6.4[ms], …, 38.4[ms]*.[76]

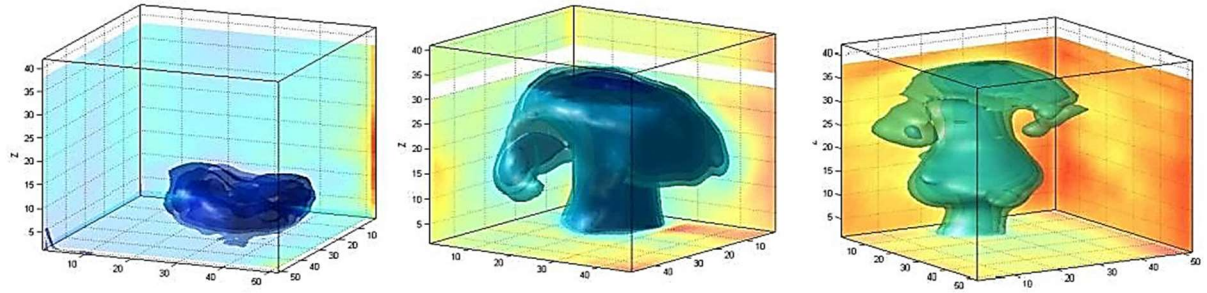

Fig.5.21. *3D reconstructing of the asymmetric temperature profile for the time delay of 3.2[ms], 9.6[ms] and 19.2[ms]*.[76]

5.2.6. Temperature measurement of temperature field in fluid

The aim of this experiment was to visualize the temperature field in a moving fluid. The experiment, setup and data processing are similar to the experiment in *section-5.2.1*. A Twyman-Green setup with double sensitivity was employed. The asymmetrical distribution of the temperature field is shown. The setup employed for this experiment is shown in Fig.5.22.

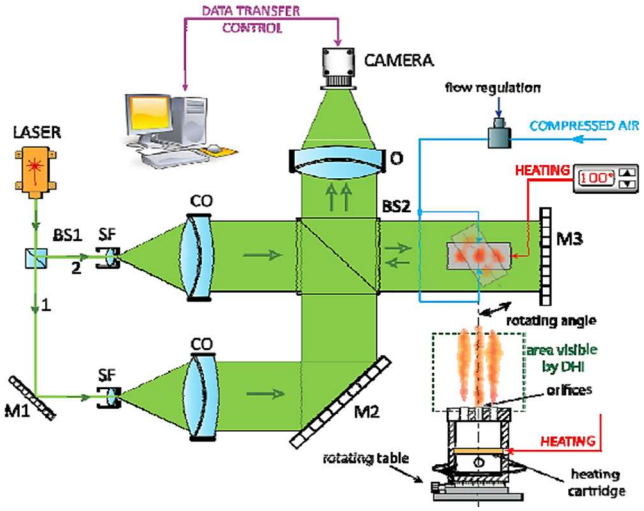

Fig.5.22. *Setup based on the Twyman-Green type of interferometry used for this experiment.*[36]

The same principle of using a single camera synchronized to a jet was used. Data were collected as well through the technique of hot-wire method (constant-temperature anemometry) for comparison. One of the limiting factor of using constant-temperature anemometry in moving fluids is the frequency of temperature change that shouldn't pass $1[kHz]$, and this is where digital holographic interferometry steps in as a powerful technique.

The visualization was performed using the tomographic approach, with a camera mounted in a rotational stage which was remotely controlled. The back-projection method was used for reconstruction. Same principle and mathematical formulation were used. Same process of averaging random fluctuation was performed as well, as in *section-5.2.1.* and *section-5.2.5.* In this experiment, a jet with a nozzle of three orifice system was used, with a diameter of $1[mm]$ each. The jet has a heat cartridge to heat the air before being blown, with a frequency of $8[Hz]$.

The tomographic reconstruction of the 3D temperature field is shown in Fig.5.23. and was performed with the same procedure of slice-by-slice stacking along the rotational axis, via the inverse Radon Transform.

The temperature's field dynamic evolution in time is shown in Fig.5.24.

Comparison with constant-current anemometry measurements is shown in Fig.5.25.

As it is shown from Fig.5.25. , both measurement are in a very good accordance. The agreement is in the range of 10% and digital holographic interferometry resulted 20 times faster as a technique compared to constant temperature anemometry.[36]

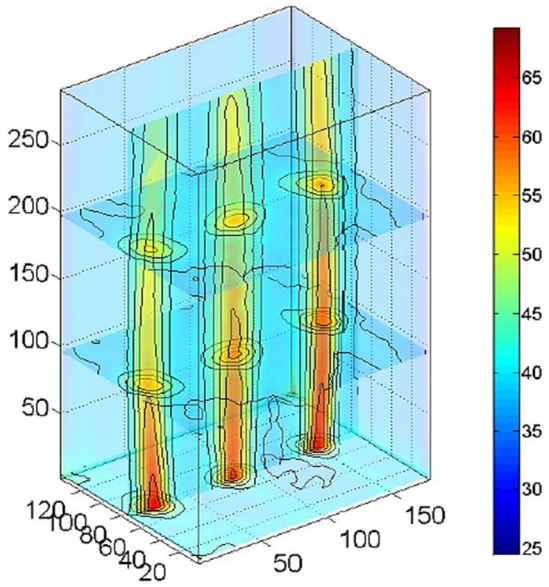

Fig.5.23. *Tomographic reconstruction of the hot air blown by the jet.*[36]

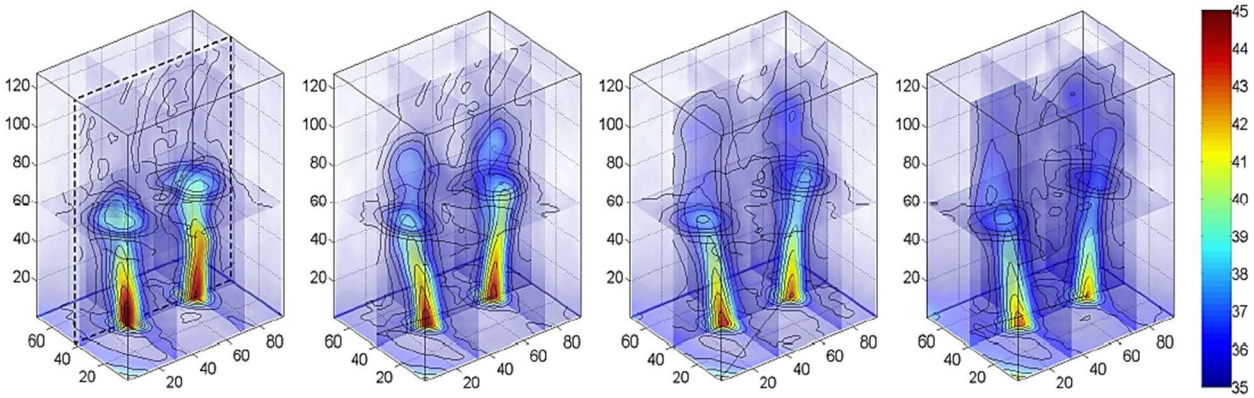

Fig.5.24. *3D tomographic reconstruction at 0.21[ms], 0.24[ms], 0.27[ms] and 0.3[ms].*[36]

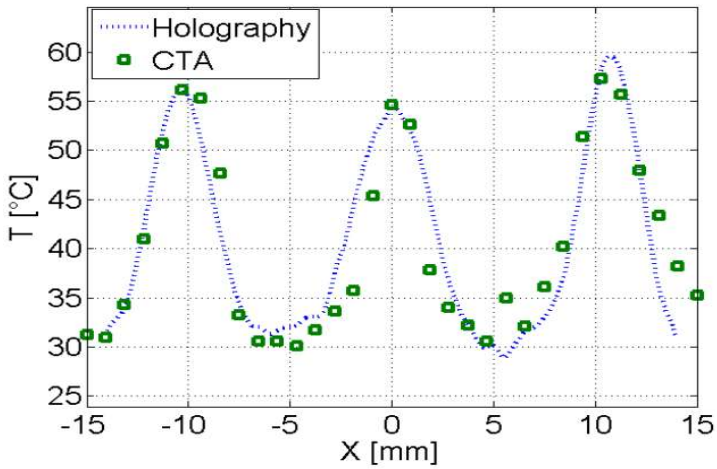

Fig.5.25. *Comparison of measurements between digital holographic interferometry and constant temperature anemometry at 20[mm] height above the nozzle.*[36]

5.2.7. Measuring temperature distribution

The aim of this experiment was to measure the temperature distribution over a heat source. A laser of wavelength $\lambda = 532[nm]$, and maximal power $P_{max} = 5[W]$ was used. The region of interest is the region above the heat source. The radiator is a device that can control the temperature of its surface, hence a good comparison with the DHI data can be made. Thermocouples were placed near the surface at several points in order to compare to DHI. The setup and the results are shown in Fig.5.26 and Fig.5.27.

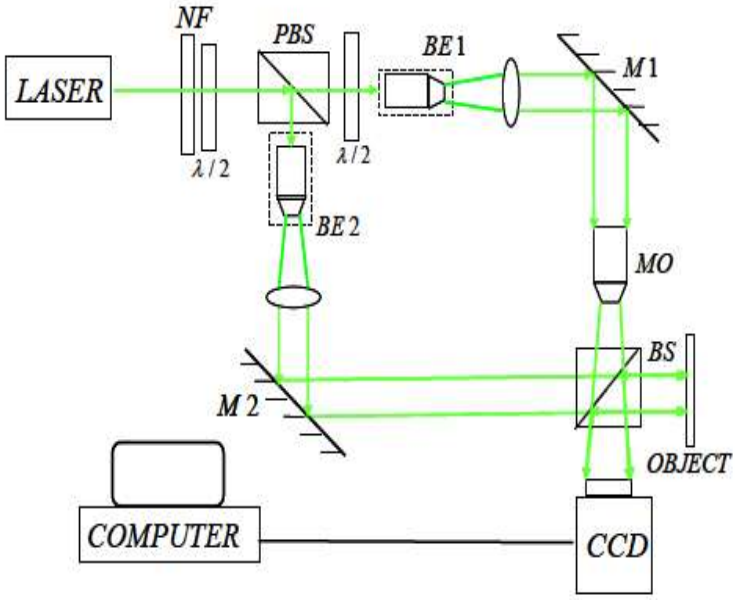

Fig.5.26. *Optical setup.*[95]

From Fig.5.27., it can be seen that data obtained by digital holographic interferometry and thermocouples are in great agreements. The average deviation in the range from the $302.70[K]$ to the $338.01[K]$ is $0.1811[K]$. Thus, it can be said that the data shown in Fig.5.27. represent the value of temperatures in the corresponding location in space and time.

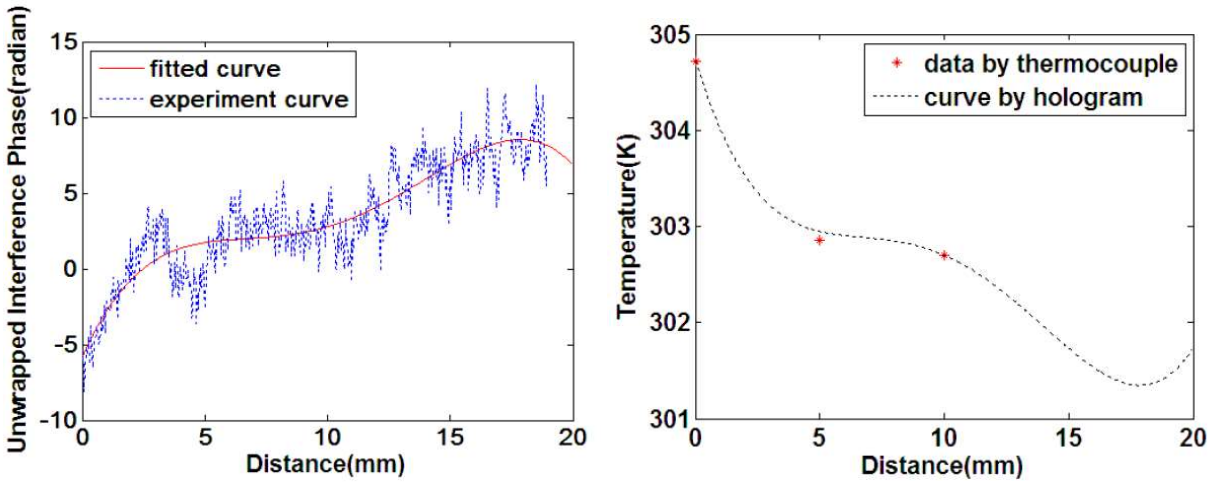

a) b)

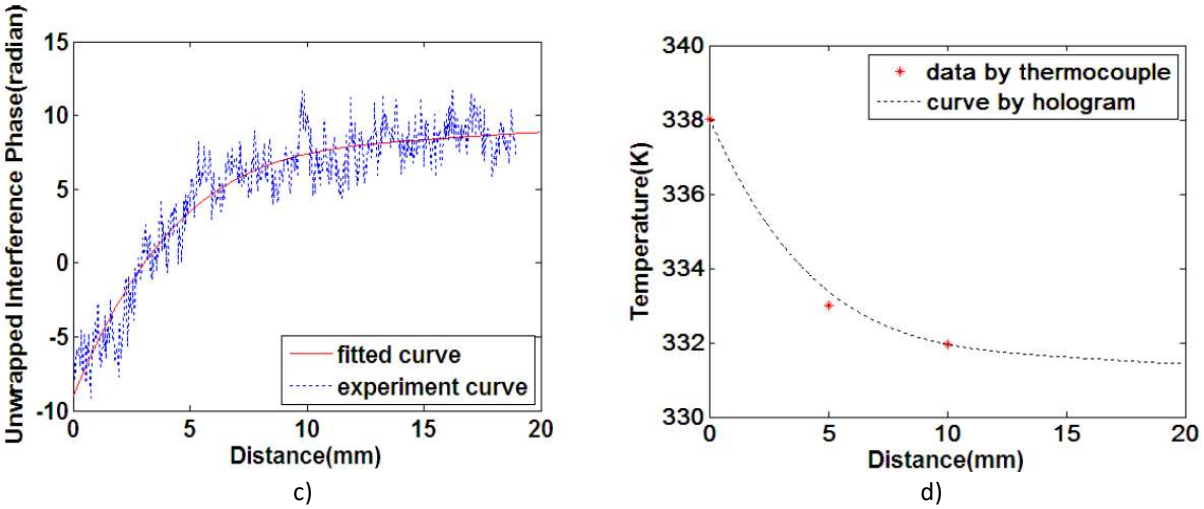

Fig.5.27. *a) Unwrapped phase distribution after 1[min] of heating, b) temperature values after 1[min], c) unwrapped phase distribution after 6[min] of heating, d) temperature values after 6[min].*[95]

5.2.8. Other works of DHI in air

Other works that concern generally measurement of air temperature or temperature fields in air can be found in the following references[35,76,103,104,95–102].

Other works that concern generally measurements with flames can be found in the following references [105–112]. Other works about DHI's applications in different sectors can be found in the following references[66,113,114].

5.3. Digital holographic interferometry for liquids

The principle of using Digital holographic interferometry for liquids remains generally the same as for air/gases. It is through the interference fringes that we obtain any change of the phase, which results from the time development of the temperature profile. In fluids, concentration can be measured as well, always based on the change of the index of refraction.

Digital holographic interferometry is an important tool in investigating temperature distribution through a volume. Using thermocouples or other devices/techniques to measure temperature distribution might disrupt the field under investigation, especially if the phenomena is on low-scale motions and is susceptible to instabilities. Laminar flow is important in liquid-metal-type nuclear reactors for example.

Phenomena that can be investigated by means of digital holographic interferometry are diffusion, dissolution, Soret effect, and temperature among others.

5.3.1. Possibilities of using digital holographic interferometry in liquids

Diffusion can be measured in various ways. The following way was done through interdiffusion. In order to measure the diffusion coefficient D of an aqueous protein solution, firstly half of the optical cell was filled with the solution at a slightly lower concentration. Here the reference hologram was captured. Secondly, the second half was filled with a solution with a slightly larger concentration. When introduced the second half of the solution, interdiffusion occurred, which caused a change in concentration. This

change of concentration caused a refractive index change, which resulted in a change on the fringe pattern. The concentration evolution in space and time is given by[115]:

$$c(z,t) = c_0 + \frac{\Delta c}{2} \cdot \frac{1}{\sqrt{\pi}} \int_{-\frac{cz}{2\sqrt{Dt}}}^{\frac{cz}{2\sqrt{Dt}}} e^{-t^2}\, dt \tag{5.5.}$$

, where z is the vertical coordinate ($z = 0$ is the interface between the two solutions) and Δc is the amount of concentration change from the initial value at which we start. Remember that the first solution has a concentration of $c_0 - \frac{\Delta c}{2}$ while the second one of $c_0 + \frac{\Delta c}{2}$. More details can be found in [20] and [115].

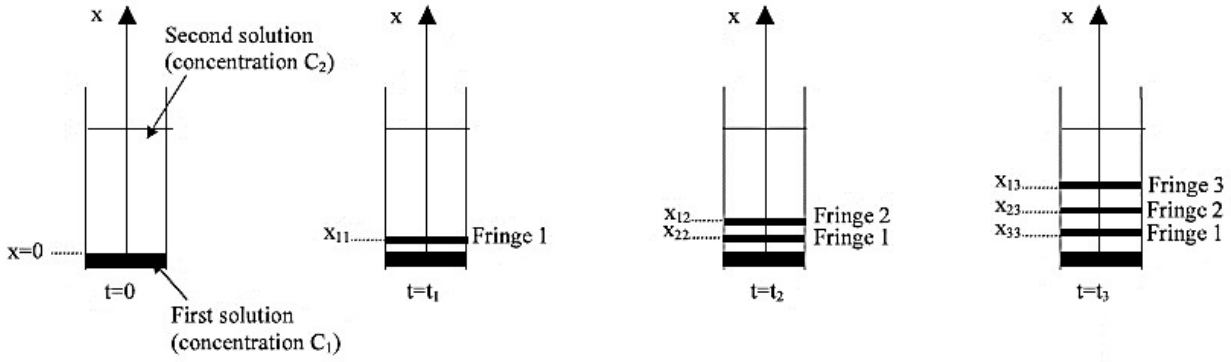

Fig.5.28. *Fringe pattern evolution with time during the diffusion process.*[115]

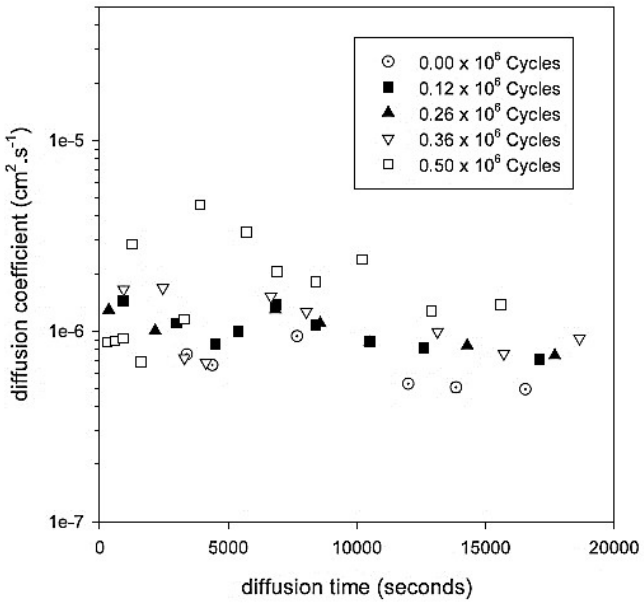

Fig.5.29. *Example from the results of the variation of the diffusion coefficient with time. Evolution of D with the number of constraints cycles during the tribological test.*[115]

The Soret effect or thermal diffusion can also be measured by means of digital holographic interferometry. Firstly, a reference of a homogenous sample of the liquid mixture under investigation is taken. By introducing a thermal gradient in the vertical direction, fringe pattern will change accordingly. After, the concentration fringes slowly will settle because of the Soret effect.[115]

Knowing that the concentration difference between the top and the bottom of the cell can be calculated by[115]:

$$\Delta c = \frac{N_c \lambda}{e \frac{\partial n}{\partial c}} \tag{5.6.}$$

, then the evolution of the concentration gradient between the top and the bottom of the cell in regard with time can be drawn.

More details on digital holographic interferometry application for the study of the Soret effect can be found in [20],[116] and [117]. Application for the study of convection during thermotransport and microgravity experiment can be found in [118].

5.3.2. Real-time measurement of the average temperature profiles in liquid cooling

The aim of this experiment was to measure and visualize the cooling process of transparent, nonscattering liquid samples by means of digital holographic interferometry.

Different digital holographic interferometry techniques obtain the useful data by means of phase differences, using the entire wrapped phase map difference, or a part of it, and also an unwrapping algorithm. A physical model was used to link the phase difference and the temperature variation of a certain time of sample, from which the temperature value at any point of the liquid could be determined.

Fourier transform was used to calculate the wrapped phase map between the reference and the object holograms. Using the whole phase map wasn't necessary, but instead, from the phase variation in a single pixel in the wrapped phase, temperature values could be determined.

The setup used for this experiment is shown in Fig.5.30.

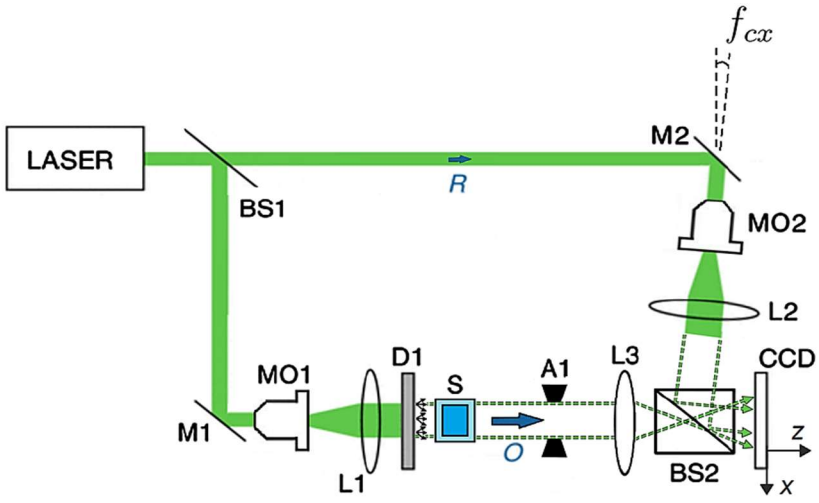

Fig.5.30. *Experimental setup with an off-axis geometry.*[77]

Light reflected from the beam splitter, passes through a 10X microscope MO1 and continues through a lens expander to collimate the beam. The reason why a diffuser (D1) was used, was to create diffused illumination to avoid concentric ring patterns arising from dust particles or scratching of the optical elements.[77]

The sample is a $10x10x50[mm]$ transparent quartz cell filled with the hot liquid. The aperture A1 is used to modulate the light coming from the sample S. The reason of this rectangular aperture is the improvement of light collection and the obtention of higher spatial frequencies, which gives better spatial resolution.[77]

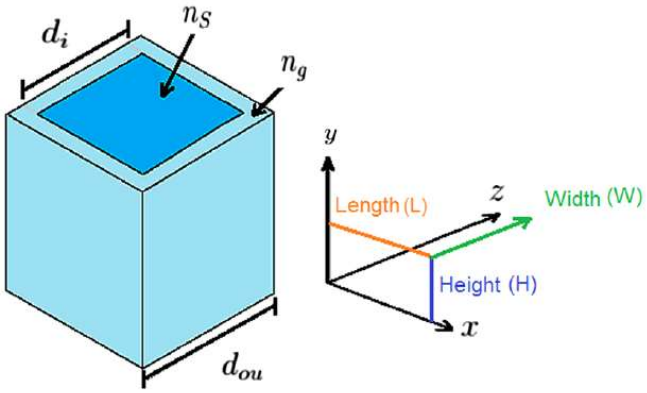

Fig.5.31. *Dimension of the cell*.[77]

The cell's refractive index and the liquid's one were taken in account in calculations. The phase variation is expressed as[77]:

$$\Delta\theta_{t-0}(x,y) = \frac{2\pi}{\lambda}\Delta OPL = \frac{2\pi}{\lambda}\int_0^{d_i}\left(n_{S_t}(x,y,t) - n_{S_0}\right)dz = \frac{2\pi}{\lambda}d_i(x,y)\Delta n_{S_{t-0}}(x,y) \tag{5.7.}$$

While the relation of the refractive index to the variation of temperature and concentration of the liquid sample is[77]:

$$\Delta n_{S_{t-0}}(x,y) = \left[\frac{\partial n_S}{\partial T}\right]_{Conc.}\left(T_t(x,y) - T_0(x,y)\right) + \left[\frac{\partial n_S}{\partial Conc.}\right]_{Conc.}\left(Conc_t(x,y) - Conc_0(x,y)\right) \tag{5.8.}$$

For $Conc_t(x,y) = Conc_0(x,y) = const.$, we obtain[77]:

$$\Delta n_{S_{t-0}}(x,y) = \left[\frac{\partial n_s}{\partial T}\right]_{Conc.}\cdot\left(T_t(x,y) - T_0(x,y)\right) \tag{5.9.}$$

, where $T_t(x,y)$ is the temperature at time t, $T_0(x,y)$ at $t = 0$, $Conc_t(x,y)$ is the concentration at time t and $Conc_0(x,y)$ at time $t = 0$. By combining these identities, the final equation is[77]:

$$T_t(x,y) = T_0(x,y) + \frac{\lambda\Delta\theta_{t-0}(x,y)}{2\pi d_i(x,y)\left[\frac{\partial n_s}{\partial T}\right]_{Conc.}} \tag{5.10.}$$

By using the reference temperature $T_0(x,y)$ and a small region of the wrapped phase difference, the temperature was determined in that small region. The cell was filled with $0.66[ml]$ of hot distilled water at $22[°C]$. Monitorization was done by taking 1460 holograms at $12[fps]$. Some 2D wrapped phase are shown in Fig.5.32. Three measuring points near the thermometer were set, to compare the data acquired and verify the phase variations. The points were set as $p1(4.1X2.8[mm])$, $p2(8.3X6.7[mm])$ and $p3(6.8X4.8[mm])$ on the 2D wrapped phase difference. Note also that the temperature measurement can be done over the full field of the phase variation over the entire liquid sample.[77]

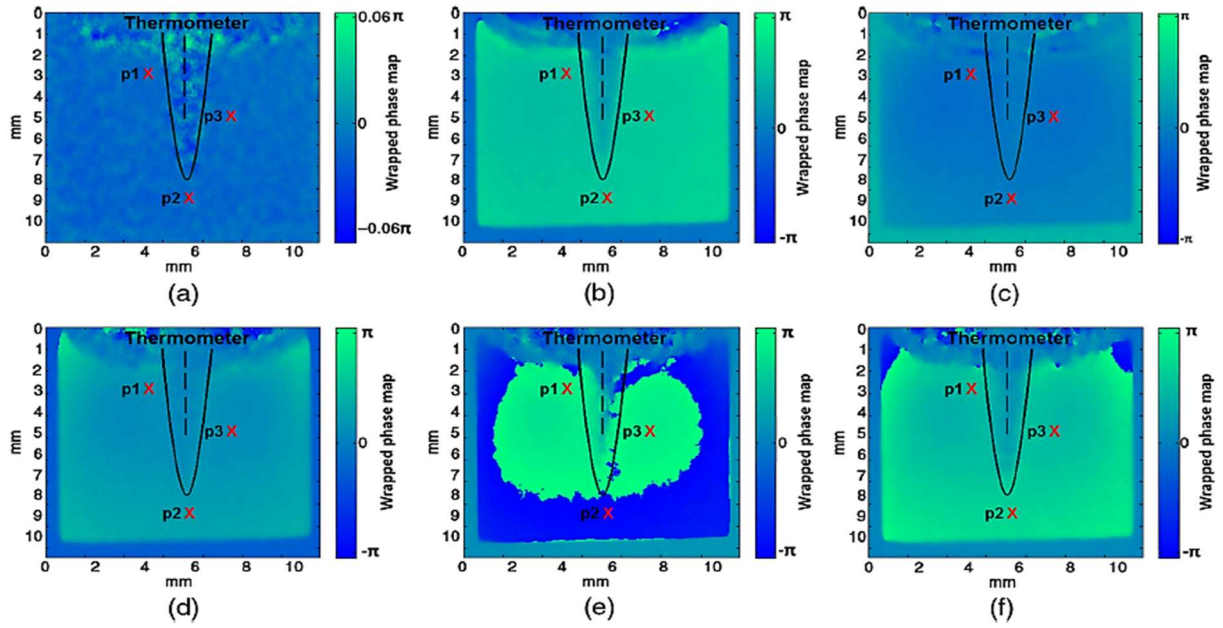

Fig.5.32. *Wrapped phase maps obtained from eq.(4.15) showing temperature variation at (a) t=1[s], (b) t=21[s], (c) t=43[s], (d) t=64[s], (e) t=85[s] and (f) t=108[s].*[77]

Fig.5.33. shows in (a) a 1D wrapped phase graph generated from the equation of the phase modulo 2π substraction at each of the three points at different time of cooling and in (b) the temperature at each point by using the reference temperature value and every phase increment during a certain time t.[77]

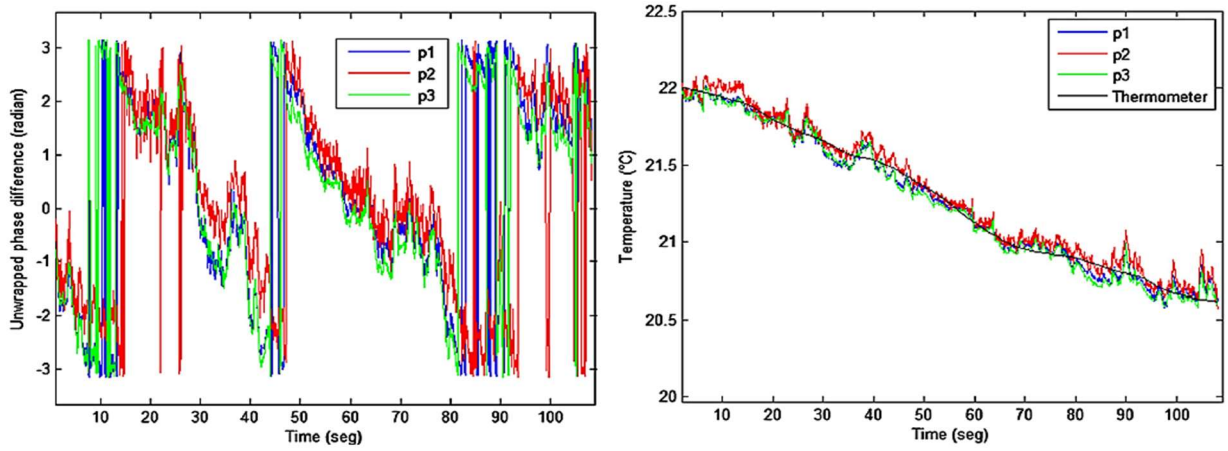

Fig.5.33. *(a) 1D wrapped phase, (b) the temperature at each point.*[77]

It was concluded that the magnitude of the temperature variation decreases while the final temperature approach the environment's temperature. Digital holographic interferometry detected small changes in temperature of the order of $\pm\, 0.2[°C]$. It was also concluded that the temperature can be determined only by using a single pixel in the 2D wrapped phase difference map without the need to use the entire phase difference map.[77]

The measurements done by using both technique were consistent, as it can be conclude from Fig.5.33. This experiment puts digital holographic interferometry in the list of easy, fast and reliable techniques to visualize heat loss from liquids.

5.3.3. Temperature measurement in laminar free convective flow

The aim of this experiment was to measure the temperature in laminar free convection flow, where the fluid being used was water. To ensure a free laminar convection, the heating plate was kept at constant temperature and low rate and the size of the heater was selected as such not to trigger any turbulence.

This method used the lensless Fourier transform digital holography which makes it rather fast and simple. Other DHI methods suffer from having problems with the angle between the reference and object beam, speckle effects and involving several Fourier Transforms in its algorithm, thus slowing down the processing, difficulties that are effectively handled by the lensless Fourier Transform DH.[42]

This technique uses only one Fourier transform. The off-axis geometry was used, in order to separate the real and twin images (to avoid the overlap of the DC component, the twin image and the real image), thus an angle is introduced between the reference and object wave. The angle was sufficiently large to make sure that those components are separated.

Because in its initial state there are no movement of the fluid in regard to the wall, the first process happening is conduction. A density gradient will be generated when a temperature gradient appears, forcing the liquid to move and be replaced under gravitational force, thus establishing buoyancy forces, which is when the convection forces play in.

A $He-Ne$ laser of approx. power of $30[mW]$, a test section of $6x3x6.5[cm]$ with inner wall thickness of $8.5[mm]$ and a flat squared $2x2[cm]$ electric heater were used. The initial temperature room was $297.7[K]$. A set of thermocouples were also used for comparison. The relationship between water and its refractive index was expressed by the Tilton and Taylor formula[42]:

$$n(y) = 1.33711 - 9.3784 \cdot 10^{-6} T(y) - 2.71726 \cdot 10^{-6} T(y)^2 \qquad (5.11.)$$

, where y is the vertical coordinate perpendicular to the plate and the direction of propagation of the laser light, $T(y)$ is the temperature at y distance from the plate given in $[K]$. From Fig.5.34., it can be seen that the temperature development is one dimensional, in the y direction. The experimentally measured temperature values differ for $0.58[°K]$ from those of the thermocouples.[42]

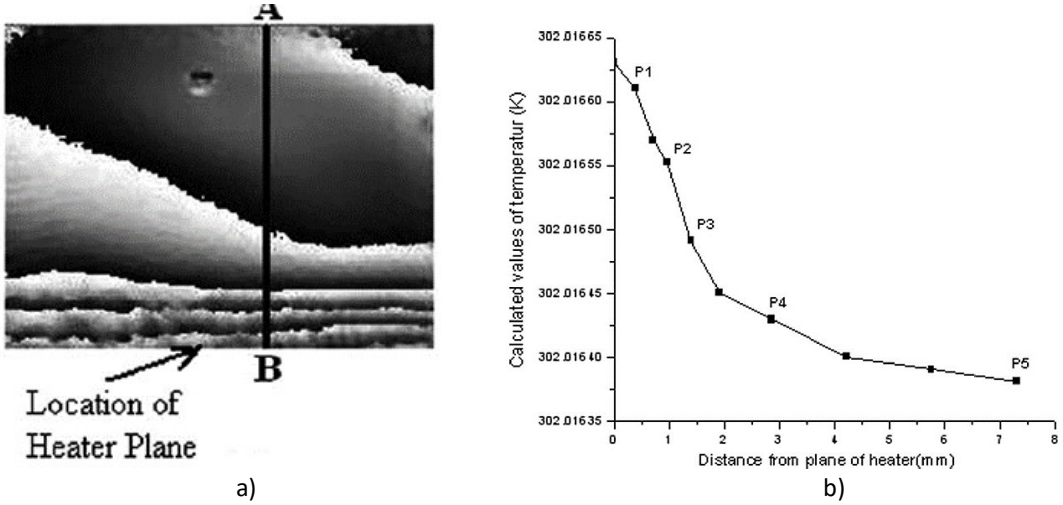

a) b)

Fig.5.34. *a) Real phase map in steady laminar free convection flow and b) Calculated temperature with distance from the plate on the AB line traced in a).*[42]

The accuracy depends on the optoelectronics that are used. Phase accuracy depends on phase evaluation from the speckle noise, the signal discretization and the unwrapping process.[42]

Another measurement was done for a turbulent flow, by increasing the heat rate from the heater. It can be seen from Fig.5.35. that the cold water replaces the newly heated water from the vicinity of the plate by the downward direction of the phase fringes in the center line, while the heated water travels upwards which can be seen from the upward orientation of the phase fringes on the sides. More details can be found in the paper in the reference [42].

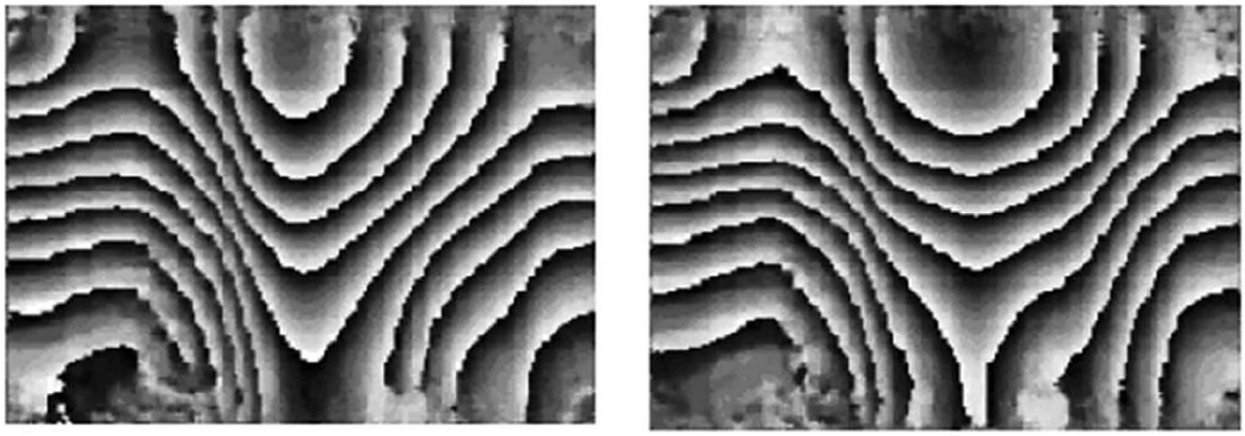

Fig.5.35. *Phase fringes of turbulent free convection flow fields at two different times*.[42]

5.3.4. Measuring concentration

Concentration difference between liquid mixtures can be measured using DHI. Sensitivity of the technique was reported as up to $0.001[mol]$ which is equivalent of $0.003[g]$ of sodium chloride in solutions.[119]

In this experiment, the Fourier method was used to retrieve the phase. It used a $He-Ne$ laser of $\lambda = 543[nm]$, an ordinary glass tube with unknown inner wall dimensions, where the solution was inserted at a rate of approximatively $36\left[\frac{mL}{s}\right]$ with a temperature of $T = 20[°C]$. Liquid samples were prepared by mixing distilled water and $NaCl$ at various concentrations (see [119] for more details on the whole experiment).

They obtained very accurate results as shown in the table in Fig.5.36.

Solutions compared	$\Delta CON_{S_2-S_1}$ (value in Ref. 20) [mol]	$\Delta CON_{S_2-S_1}$ (with DHI) [mol]	Deviation
$S_{mol_1} - S_{H_2O}$	0.083	0.083	0.0
$S_{mol_2} - S_{mol_1}$	0.086	0.086	0.0
$S_{mol_3} - S_{mol_2}$	0.086	0.088	+0.002
$S_{mol_4} - S_{mol_3}$	0.086	0.081	−0.005
$S_{mol_5} - S_{mol_4}$	0.086	0.082	−0.004
$S_{mol_6} - S_{mol_5}$	0.086	0.085	−0.001

Fig.5.36. *Comparison of values obtained through DHI and those in* [120] and [121].[119]

According to the experimentally obtained data, the technique can distinguish changes in salt concentration of $6 \cdot 10^{-5}$ by weight.[119]

5.3.5. Dynamic visualization of complex flow fields and other works

A group performed many different experiments by means of digital holographic interferometry. Some of their results are shown below.

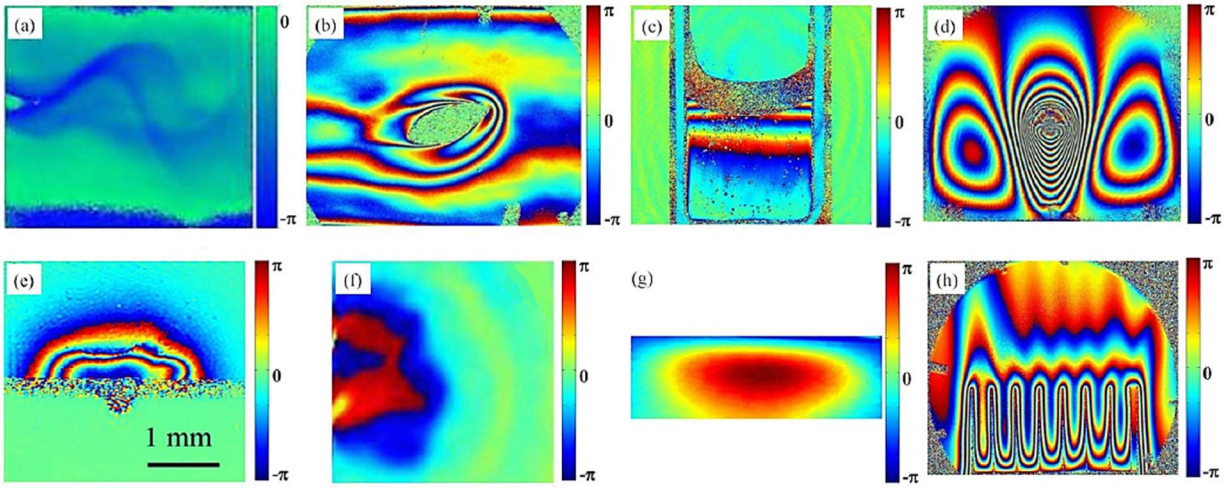

Fig.5.37. *Reconstructed phase maps (in radians) for: (a) Karman vortex street, (b) an airflow field, (c) a protein-lysozyme solution crystallization process, (d) thermocapillary motion of a droplet, (e) laser ablation process on the surface of deionized water, (f) a shockwave on a solid surface, (g) an acoustic sounding wave and (h) the heat dissipation process of a heat sink.*[78]

Other publications that deal with temperature measurements in liquids can be found in the references [99] and [122], [123] offers an interesting review on some development of DHI for various applications, PIV and temperature fields are explained in [53], [124] deals both with liquid and solids, [125] deals with DHI and its application for vapor concentration measurements, [126] deals with temperature field near condensing bubble. Other works of DHI's application in fluids can be found in[112,127–130].

5.4. Digital holographic interferometry for solids

Not many experiments have been performing using DHI in solids. This is probably due to the fact that the object under investigation must be transparent or semitransparent to some degree in order to allow the laser beam to pass through. Some experiments have been performed using thin films for different application, especially to detect some conformational changes etc.

5.4.1. Temperature measurement with infrared interferometry

The aim of this experiment was to determine the temperature variation of two substrates by using the existing relation with the refractive index. Two substrates, made of $GaAs$ of thickness $500[\mu m]$ or InP of thickness $300[\mu m]$, both double-sided and polished, were investigated. An infrared laser of $\lambda = 115[nm]$ was used.

In MBE (molecular beam epitaxy) growth chamber, in order to create the thin film, the substrate must rotate in order to achieve the uniformity of the film's thickness. Since the pyrometer registers the absolute infrared radiation intensity, any other radiation source in the chamber decreases the accuracy of the temperature measurement. Thermocouples were mounted so as to be $2[mm]$ from the laser spot. Starting temperature was set to $25[°C]$.

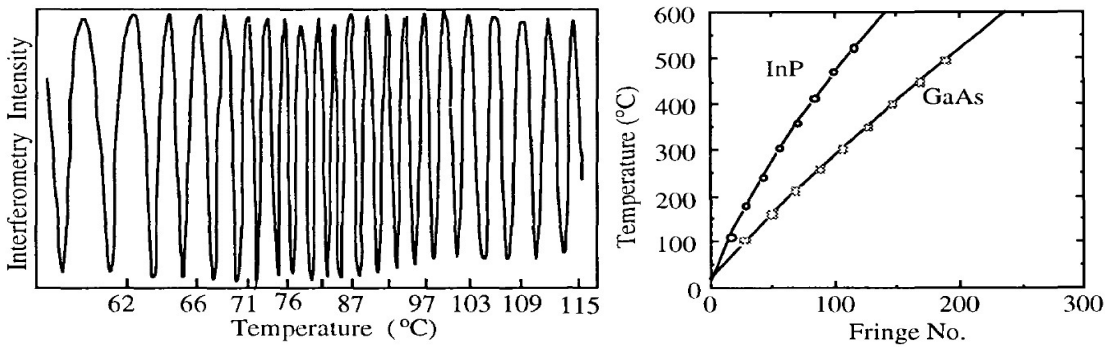

Fig.5.38. *a) Interferogram of GaAs substrate while heated and b) Wafer temperature as a function of fringe number.*[131]

Some drawbacks of the infrared interferometry in this experiment were the requirement of a good knowledge of the starting temperature, a uniform temperature of the material during detection-hence a very controlled temperature increment, and that a decrease/increase of temperature would be hard to detect, but this could be solved (by detecting phase differences in periodic signal intensity from two regions with slightly different thickness). More information can be found in [131].

5.4.2. Temperature measurement of an inclined elliptical cylinder

The aim of this experiment was to determine the temperature measurement of an inclined elliptical aluminium cylinder, with dimensions $350x36x24[mm](Lx2ax2b)$ with its major axis inclined by $30°$.

A $He-Ne$ laser with $\lambda = 632.8[nm]$ was used. The cylinder was heated up to $T_s = 335.15[K]$ with hot water, while thermocouples placed at a distance of $100[cm]$ measured a constant ambient temperature of $T_{ref} = 295.25[K]$ as a reference.

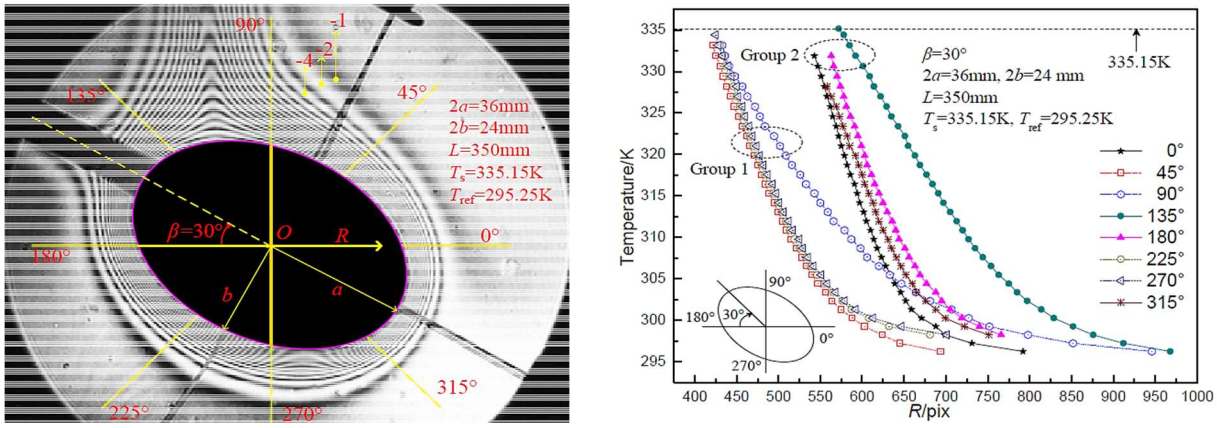

Fig.5.39. *a) Interferograms, b) temperature variation for different inclination angles.*[132]

From Fig.5.39.b) the values obtained from the thermocouples positioned around the cylinder at different angles can be seen. It can be seen that the values for angles of $90°$ and $135°$ are set apart from the others. This is because of the plum shape of the heat formed around the elliptical cylinder, which points upwards as it can be seen in Fig.5.39.a). The others can be regrouped into two groups. The x axis represents the positon of the center of fringes for which the temperature was evaluated. The maximal value obtained as seen from b) is $335.16[K]$ for the angle of $135°$ which is $0.008[K]$ different from $T_s = 335.15[K]$.[132]

5.4.3. Digital holographic interferometry for measuring polymerization shrinkage of composite materials

Polymerization shrinkage is the dimensional instability of composite materials, a chemical reaction characteristic for the resins, caused by the polymerization of the organic matrix.[133]

The importance of the polymerization shrinkage is connected to the fact that the quality and durability of tooth composite restoration is influenced by it and different techniques are used in order to quantify it in order to compensate or reduce it. There exist different methods for measuring this shrinkage, as the direct methods (dilatometric methods, linometer, "strain-gauge", etc.) and the indirect methods (determining depth of bacterial penetration, use of radioisotopes, etc.).[133]

A red laser light of wavelength $\lambda = 633[nm]$ was used to measure the shrinkage. Samples' thickness used for the measurements were $0.65[mm]$, and 10 samples were prepared.

Samples of the composite material Spectrum TPH were polymerized using a low intensity program of $400\ \left[\frac{mW}{cm^2}\right]$ with an halogen lamp. For the first $10[s]$, a light of intensity of $50\ \left[\frac{mW}{cm^2}\right]$ was emitted and for the $30[s]$ left with an intensity of $150\ \left[\frac{mW}{cm^2}\right]$.

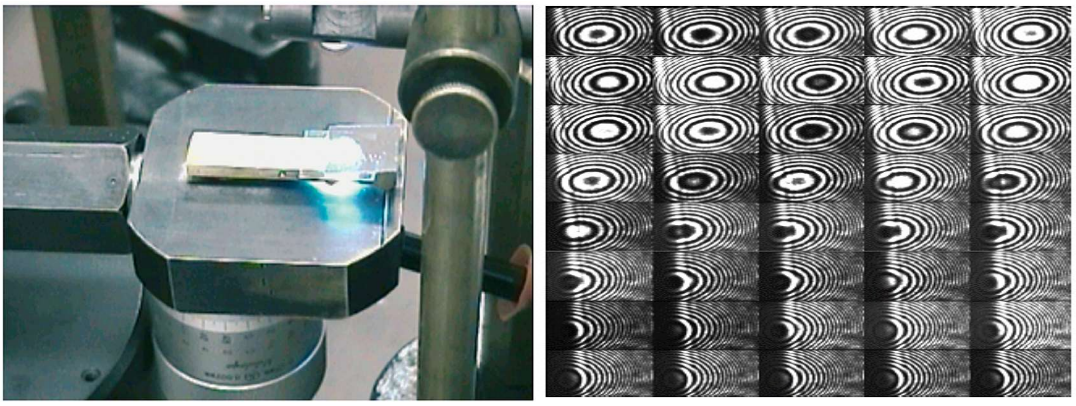

a) b)

Izvor svjetla / Source illumination	POLIMERIZACIJSKO SKUPLJANJE / POLYMERISATION SHRINKAGE Spectrum TPH kompozitnoga materijala / Spectrum TPH composite material			
	Rezultati dobiveni programom za obradbu interferometrije (% linearno skupljanje) (x ± sd) / Results of the program for processing the interferogram (% linear shrinkage) (x ± sd)			Rezultati dobiveni mikrometarskim vijkom (µm) (x ± sd) / Results with micrometer serew (µm) (x ± sd)
	10 sekundi / 10 second	20 sekundi / 20 second	40 sekundi / 40 second	40 sekundi / 40 second
Program "niskog intenziteta" Astralis 7 halogenog uređaja / "Low intensity" program Astralis 7 halogen lamps	0.23±0.32	0.58±0.71	0.83±0.39	53.2±1.08
Lux-o-Max uređaj / Lux-o-Max diode device	-0.01±0.29	0.21±0.42	0.78±0.98	42.6±0.98

c)

Fig.5.40. *a) Sample holder with the sample, b) Polymerization shrinkage of Spectrum TPH composite material during $40[s]$ of illumination with "low intensity" program of the Astralis 7 halogen curing unit), c) Polymerization shrinkage of Spectrum TPH composite material polymerized with "low intensity" program of the Astralis 7 and Lux-o-Max curing unit.*[133]

5.4.4. Temperature measurement of human hand skin

The aim of this study was the surface temperature measurement of human body skin. In general, contact type temperature sensors are used for temperature monitoring. This study is important in the field of health management and diagnostics, especially in time of COVID19 pandemic. The reconstructed temperature near to the surface of palm skin and along the lines can be considered as the skin temperature.

A He-Ne laser with wavelength $\lambda = 632.8[\mathrm{nm}]$ was used. The optical system is shown in Fig.5.41. and consists of a laser, a volume phase holographic grating (VPHG), a mirror (M), microscope objectives (M01 and M02), collimator (CL), diffuser (D) and a recording camera. The theory behind the data processing remains the same as in *section-3.5.* The ambient temperature was measured with K-type (Chromel–Alumel) thermocouple with multilogger. Three test subjects (healthy persons) were chosen. Measurements in finger and palm region were conducted. The temperature of the index finger was also measured with the commercially available digital thermometer (Model: PHX-01, Make: Phoenix Healthcare Solutions, LLC) and with an infrared thermometer (Model: TG8818C, Make: Microtek).[134]

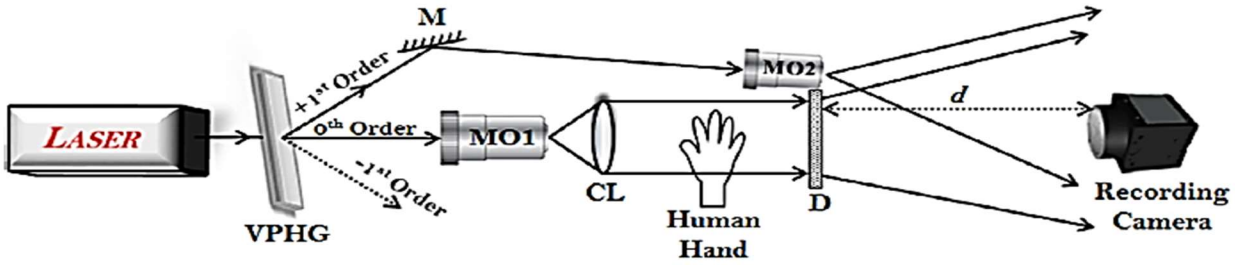

Fig.5.41. *Optical setup for human skin temperature measurement*.[134]

Fig.5.42. shows the map of the unwrapped phase difference around the index finger of Subject '2' with its unwrapped profile and the final estimated temperature value. Here, only the results for Subject'2' are shown. More can be found in [134]. Data shown in Fig.5.43. in the form of a table show that temperature values obtained using the proposed volume phase holographic optical element based DHI system are well within the range as compared to temperature values obtained by the digital thermometer and the infrared thermometer. Lower values from the digital thermometer come from the fact that an adhesive tape was used to bring the digital thermometer in contact with the skin and since the sensor was not always in equilibrium with the skin surface, values are greatly affected by environmental conditions.[134]

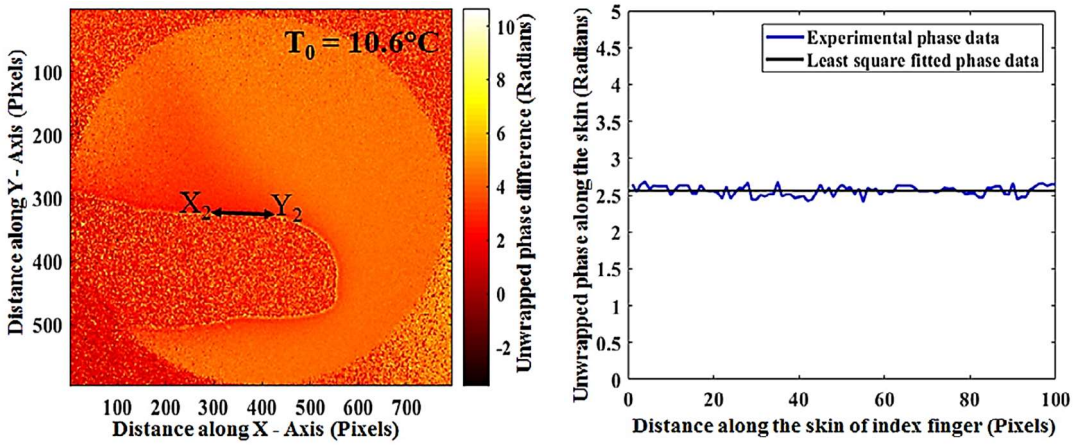

a) b)

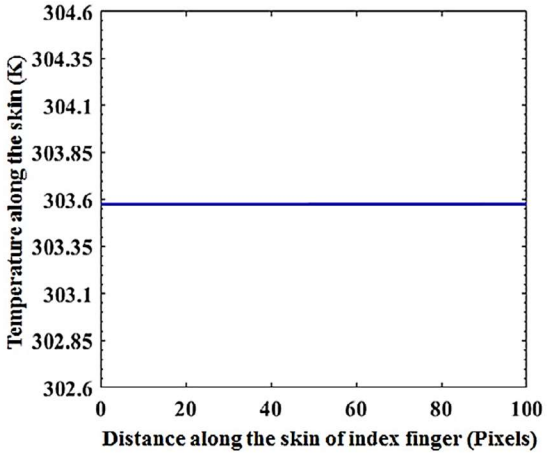

c)

Fig.5.42. *a) Map of the unwrapped phase difference around the index finger of Subject '2', b) profile of the unwrapped phase difference of air along the designated measuring line "X_2Y_2" and c) the temperature profile along the line*.[134]

Method	Subject '1'		Subject '2'		Subject '3'	
	Index Finger	Palm Skin	Index Finger	Palm Skin	Index Finger	Palm Skin
Experimental	33.7 °C	33.8 °C	32.6 °C	32.7 °C	30.6 °C	30.7 °C
Digital Thermometer	33.4 °C	33.6 °C	32.3 °C	32.5 °C	30.5 °C	30.4 °C
Infrared Thermometer	33.6 °C	33.8 °C	32.6 °C	32.6 °C	30.6 °C	30.7 °C

Fig.5.43. *Comparison of the temperature of human hand skin (index finger and palm skin) from all three subjects obtained using the optical setup in Fig.5.41., digital thermometer and infrared thermometer*.[134]

5.4.5. Other works of DHI in solids

Other works on solids include two-wavelength holographic measurement of temperature and concentration during alloy solidification[135], evaluation of thermal exposure on absorbing objects[136], determination of the thermal lens effect of a $Nd{:}YAG$ laser crystal[137], detection of welding failures on ribbed iron structures[138] and off-axis electron holography for studying changes in electrostatic potential in ultrathin solid oxide fuel cells[139].

6. Digital holographic interferometry for whole-field temperature measurement in liquid media

This thesis is aimed at developing a holographic setup based on digital holographic interferometry for the study of gases and liquids, more precisely to measure and visualize temperature fields in flowing gases and liquids. The first step was to develop and test the technique for liquids. It was started initially with an off-axis configuration by making use of spatial-carrier interferometry.

6.1. Introduction

There are different methods for the direct interference phase calculation, for example those based on the inversion of the cosine function or skeletonizing[140], but they have low accuracy. Another drawback is that they can't be fully automated. This is one of the reasons that phase shifting interferometry is used for the quantitative phase evaluation of the interference phase map $\varphi(x,y)$.[141] The problem with phase shifting interferometry is the fact that three interferograms in different times must be recorded in order to solve the system of equations. This means that this technique is not suitable to be used for measuring dynamic phenomena. Spatial-carrier interferometry bases its analysis on a single interferogram, making it a suitable technique for dynamic phenomena.

6.2. Spatial-carrier interferometry

The superposition of two interfering waves generates an interference patter that can be written as[141]:

$$I(x,y) = A(x,y) + B(x,y)\cos\big(\varphi(x,y)\big) \tag{6.1}$$

, where $A(x,y)$ is the additional component, $B(x,y)$ is the multiplicative component and $\varphi(x,y)$ the interference phase which is coded in a cosine modulate fringe pattern. If we write the term $B(x,y)$ in term of a complex exponential of the form:

$$C(x,y) = \frac{1}{2}B(x,y)e^{j\varphi(x,y)} \tag{6.2}$$

, then the previous equation can be written as:

$$I(x,y) = A(x,y) + B(x,y)\left(\frac{e^{j\varphi(x,y)} + e^{-j\varphi(x,y)}}{2}\right) = A(x,y) + C(x,y) + C^*(x,y) \tag{6.3}$$

Applying a Fourier Transform on both sides yields:

$$\hat{I}\big(\vartheta_x,\vartheta_y\big) = \hat{A}\big(\vartheta_x,\vartheta_y\big) + \hat{C}\big(\vartheta_x,\vartheta_y\big) + \hat{C}^*\big(\vartheta_x,\vartheta_y\big) \tag{6.4}$$

, with $\hat{I}\big(\vartheta_x,\vartheta_y\big) = \hat{I}\big(-\vartheta_x,-\vartheta_y\big)$ since it is a Hermitean matrix in the spatial frequency domain. This means that $\big|\hat{I}\big(\vartheta_x,\vartheta_y\big)\big|$ will look symmetrical to the DC term $\hat{I}(0,0)$. Low frequency variations of the background are in the first term $\hat{A}\big(\vartheta_x,\vartheta_y\big)$. Both terms $\hat{A}\big(\vartheta_x,\vartheta_y\big)$ and $\hat{C}^*\big(\vartheta_x,\vartheta_y\big)$ can be eliminated by bandpass filtering. In that case, the remaining spectrum won't be Hermitean, which means that by applying an inverse Fourier Transform, a complex field $C(x,y)$ where both the real and imaginary part will not cancel out will remain. The wrapped phase then is directly calculated as[141]:

$$\varphi^{W}(x,y) = \arctan\left(\frac{Im\{C(x,y)\}}{Re\{C(x,y)\}}\right) \tag{6.5}$$

For the proper separation and filtering of the terms in the frequency domain, carrier frequencies must be introduced. This yields the followings:

$$I(x,y) = A(x,y) + B(x,y)\left(\frac{e^{j\{2\pi\vartheta_{Cx}x+2\pi\vartheta_{Cy}y+\varphi(x,y)\}} + e^{-j\{2\pi\vartheta_{Cx}x+2\pi\vartheta_{Cy}y+\varphi(x,y)\}}}{2}\right) = \tag{6.6}$$
$$= A(x,y) + C(x,y)e^{j\{2\pi\vartheta_{Cx}x+2\pi\vartheta_{Cy}y\}} + C^{*}(x,y)e^{-j\{2\pi\vartheta_{Cx}x+2\pi\vartheta_{Cy}y\}}$$

$$\hat{I}(\vartheta_x,\vartheta_y) = \hat{A}(\vartheta_x,\vartheta_y) + \hat{C}(\vartheta_x-\vartheta_{Cx},\vartheta_y-\vartheta_{Cy}) + C^{*}(\vartheta_x,+\vartheta_{Cx},\vartheta_y+\vartheta_{Cy}) \tag{6.7}$$

On one hand, the Nyquist sampling criteria sets also some limits to the maximum value those carrier frequencies can have, which is given by the digital sensor pixel extension ξ as ϑ_N=$\frac{1}{2\xi}$. On the other hand, in order for the terms not to overlap, values of carrier frequencies must be sufficiently high. The spectral bandwidth ϑ_B of $C(\vartheta_x,\vartheta_y)$ or $C^{*}(\vartheta_x,\vartheta_y)$ reflects the slope of the interference phase $\vartheta_B \approx \nabla\varphi$ and it influences the size of the applied filtering window and optimal values of carrier frequencies.[141]

High density interferogram associated to the spatial-carrier interferometry can also be viewed as digital hologram (''diffraction grating''), where $A(\vartheta_x,\vartheta_y), C(\vartheta_x,\vartheta_y), C^{*}(\vartheta_x,\vartheta_y)$ represent different diffraction orders, making this technique a special case of off-axis holography. In general, this technique applies imaging lens and no wavefront propagation from a hologram plane to an image plane during the data processing.[141]

Temporal change of the temperature field is the difference of temperature at time t with respect to a reference state at $t = 0$:

$$\Delta T(t) = T(t) - T(0) \tag{6.8}$$

When light passes into media with different densities, its speed changes. The speed of light is related to the density and the wavelength of the light, and the density is related to the change of refractive index. The relation between them is:

$$\Delta\varphi(x,y) = \frac{2\pi}{\lambda}\int_{L_1}^{L_2}(\Delta n(x,y,z) - n_{\infty})dz \tag{6.9}$$

The change of the refractive index with temperature for $\lambda = 632.8[nm]$ is given by[29]:

$$-\frac{dn}{dT} = 0.985\cdot 10^{-4} \tag{6.10}$$

Thus, the temperature change is computed as:

$$\Delta T = \frac{\lambda}{2\pi}\frac{\Delta\varphi}{-\frac{dn}{dT}L} \tag{6.11}$$

6.3. Optical setup and method

The optical setup used for this experiment is shown in Fig.6.1. and represents a Mach-Zehnder interferometer. A cw laser of wavelength $\lambda = 632.8[nm]$ has been used, with a maximal output power of $50[mW]$. The beam coming from the laser is split by a beamsplitter, equipped with half-wave plates with $10[mm]$ of diameter in order to equalize the power and intensity of both beams in the objective and reference arm of the interferometer. Both beams are filtered and collimated. The object beam passes through the testing unit, a non-polarizing splitter and an imaging lens before being sent into the camera. The imaging lens made possible to reduce the beam size and image the object plane. The reference beam is reflected by a mirror to the non-polarizing splitter where it combines with the object beam. The intensity interference pattern is captured by a digital camera (IDS UI-1490LE) with a CMOS sensor being composed of 3840×2748 pixels with each pixel having dimensions of $1.67 \times 1.67[\mu m^2]$.[141]

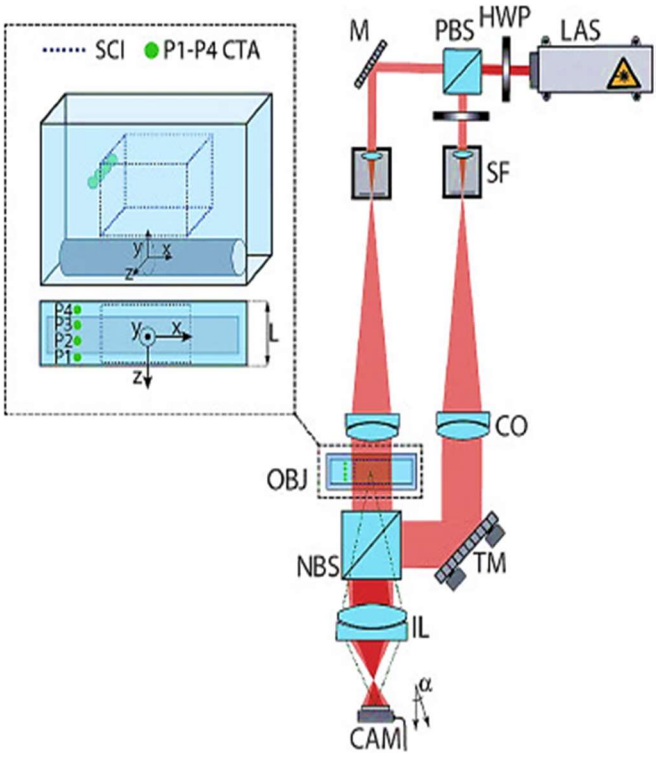

Fig.6.1. *Experimental setup employing a laser (LAS), a half-wave plate (HWP), polarizing and non-polarizing beam splitters (PBS, NBS), spatial filters (SF), collimating objectives (CO), a mirror and tip–tilt mirror (M, TM), a camera (CAM), and an object (OBJ).* [141]

The object under investigation is a glass water tank with inner dimensions of $(x \times y \times z)130 \times 143 \times 59[mm^3]$. Light propagates through the glass tank in a path that is $L = 59[mm]$. Heat was provided by a cylindrical stainless-steel heater (from MALAPA), $14[mm]$ in diameter and $67[mm]$ long. The heater is placed at the bottom of the glass tank and the center of the coordinate system was chosen to be the center of the heater. The heater operated at $20.4[V]$ with a power of $28.9[W]$.

Dimensions	14x85[mm] (14x67[mm] without the upper part)
Operating voltage	0-24[V](max.27[V]) 20.4 [V] for our experiment
Power	40[W](1.6[A])
Power distribution	1.2[W/cm²]
Diameter	14[mm]
Screw-thread	G 1/2''
Beginning of the screw-thread	14/'' [foot]
Length of the cable	Approx.1[m]
Insulation of the inner cord	Silicon
Coating	Stainless steal
Surface treatment	Electrolytic polishing
Heating element	Resistive semiconductor allow
Working temperatures	-40[°C] to 200[°C]
Shell temperature	Max. 750[°C]
Max. temperature	For short times up to 1000[° C]
Cover	IP67
Total weight	165[g]

Fig.6.2. *Properties of the cylindrical heater from the producer.*

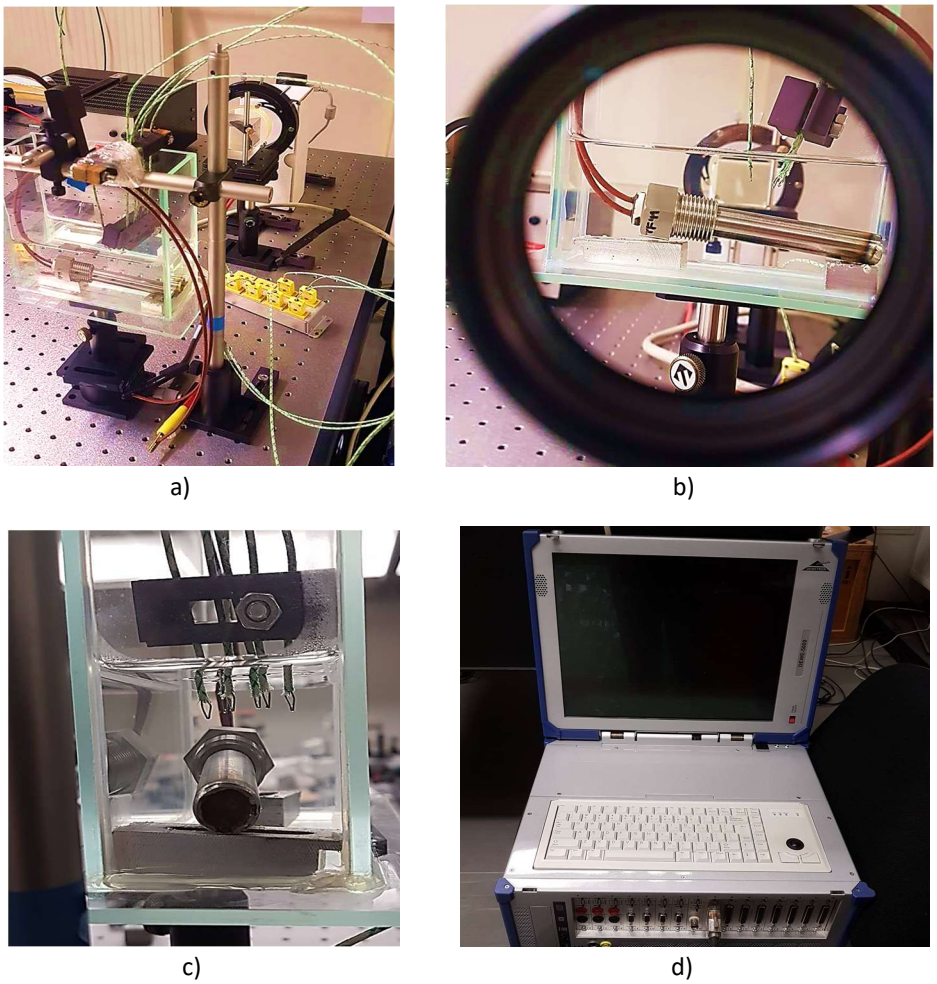

a) b) c) d)

Fig.6.3. a) Testing unit, b) glass tank containing the heater seen from one side where the thermocouples can be seen, c) heater position seen from the other side and d) device used to obtain simultaneous data from all the thermocouples used in this experiment from DEWETRON.

A reference hologram was firstly captured before running the experiment. In this experiment, the field of view of the measured area is $24 \times 16[mm^2]$. There are $N + 1 = 599$ captured interferograms (including the reference one as the first one), with a framerate of $2.65[fps]$ and time sampling $\Delta t = 0.38[s]$.[141]

Phase maps $\varphi^w(n\Delta t)$ were captured at different times and were retrieved by the procedure explained before. An example of the first hologram that was captured for referencing is shown in Fig.6.4.

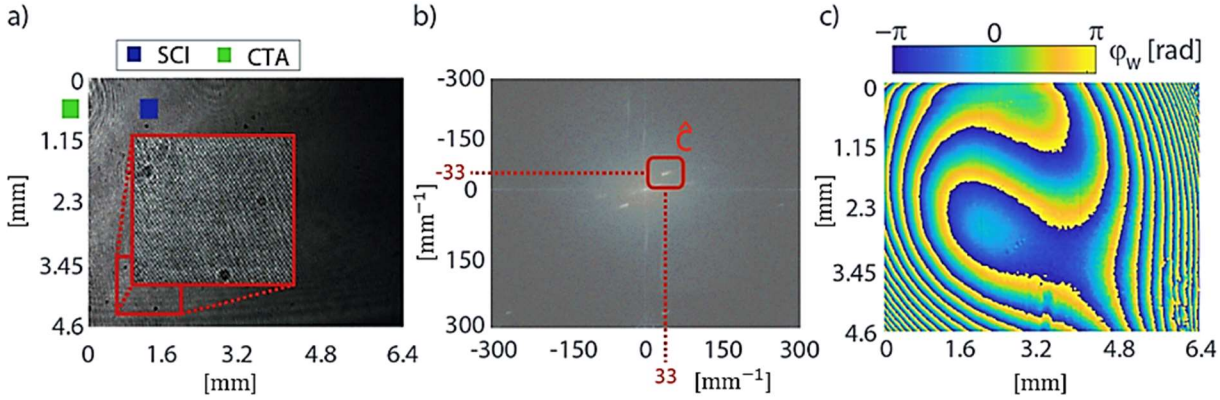

Fig.6.4. *a) Interferogram at t=0[s] (reference state), b) its magnitude in logarithmic scale of the Fourier Transform and c) wrapped phase computed from* $C(\vartheta_x, \vartheta_y)$.[141]

Carrier frequencies that made it possible for the separation of $A(\vartheta_x, \vartheta_y)$ and $C^*(\vartheta_x, \vartheta_y)$ from $C(\vartheta_x, \vartheta_y)$ are $\vartheta_{Cx} = 33[mm^{-1}]$ and $\vartheta_{Cy} = 33[mm^{-1}]$. The angles between the reference and the object beam on the x and y axis with respect to the z axis are $\alpha_x \approx \lambda\vartheta_x = 1.2°$ and $\alpha_y \approx \lambda\vartheta_y = 1.2°$.[141]

The proper choice of spatial-carrier frequencies ϑ_{Cx} and ϑ_{Cy} defined by the reference beam tilt and the frequency bandwidth use for filtering the term $C(\vartheta_x, \vartheta_y)$ depends on the gradient of the phase φ. They have to be greater than the maximum slopes of the object wavefront in both directions. If the phase has no significant slopes, the reference beam tilt can be almost anything between a relatively small value and the Nyquist limit. In this experiment, the spatial-carrier frequencies were used based on real time observation of the interferograms in the spectral domain. This means that the tilt of the tilting mirror was set up to when the term $C(\vartheta_x, \vartheta_y)$ was clearly separated from the zero-order term $A(\vartheta_x, \vartheta_y)$. A slightly greater tilt was added in order to avoid phase errors due to diffraction effects.[141]

A 2D Hanning window with spatial frequency bandwidth $\vartheta_B = 60[mm^{-1}]$ was applied in order to filter the term $C(\vartheta_x, \vartheta_y)$. This restricted the spatial resolution in image (camera) plane to $\Delta d_{cam} = \frac{1}{\vartheta_B} = 17[\mu m]$. With a magnification factor $M = \frac{1}{4}$, the resolution related to the object plane dimensions is $\Delta d = \frac{\Delta d_{cam}}{M} = 67[\mu m]$.[141]

Wavefront aberrations integrated along the whole optical path in both arms of the interferometer must be taken in account. They usually come from imperfect optical elements or when the optomechanical elements are not well adjusted. Stationary aberration can also come from the improper selection of spatial frequency carriers. For example, the phase map in Fig.6.4.c) shows strong aberrations such as tilt, defocus, astigmatism, coma and also higher order optical aberrations. Wavefront aberrations can be eliminated by subtraction.[141]

These aberration don't affect our results when done through interferometry, but if conventional spatial-carrier interferometry is performed, they would play a role.[141,142]

One advantage of this interferometric optical setup is that imperfections of optical elements don't pose a problem. This also means that carrier frequencies don't have to be set very precisely.

The reference state is captured shortly before the experiment is run. This makes possible to reassure that the same conditions of the surrounding environment and arrangement of optical elements exist. This also makes possible to remove from the equation the fact that phase aberrations could be time variant. But perspective distortion caused from the imaging lens can still be present, which is numerically compensated.[29,141]

Instead of using direct subtraction in the form of[141]:

$$\Delta\varphi^w(n\Delta t) = \varphi^w(n\Delta t) - \varphi^w(0) \tag{6.12}$$

, here the cumulative sum of differences is made us of, expressed as[141]:

$$\Delta\varphi^w(n\Delta t) = \sum_{n=1}^{N} \varphi^w(n\Delta t) - \varphi^w((n-1)\Delta t) \tag{6.13}$$

, which leads to digital spatial-carrier interferometry. The real phase change $\Delta\varphi$ is related to the measured wrapped phase change by including integer multiple of 2π as explained before. Since the integer is not known a priori, supplementary information can be obtained by using one more wavelength[143] or using a single point measurement by another method. Since the phase change $\varphi^w(n\Delta t) - \varphi^w((n-1)\Delta t)$ from two successive phase maps is small, then we can consider that the multiple integer is zero. This means that $\varphi(n\Delta t) = \varphi^w(n\Delta t)$. Therefore, this way of calculating the phase map is free of ambiguity and doesn't need to be spatially unwrapped, which is time consuming[29].[141]

At the end, *eq.(6.11)* was used to calculate temperature maps from the phase maps.

It is worth noting that in the case of rapid phenomena (turbulent flows or forced convection) that present large local magnitudes of variation, adding the low frame rate from the camera, the phase map difference obtained by digital spatial-carrier interferometry could still contain wrapped regions. In the case of high-density fringe maps obtained by conventional spatial-carrier interferometry, spatial unwrapping is more vulnerable to fail, and in the case of when the density of fringes exceeds spatial sampling criteria it would be impossible to further evaluate the value of the multiple integer. Further, the starting point to calculate the integer multiple must be known for a successful spatial unwrapping.[141]

The fact that here spatial unwrapping is used in combination with temporal unwrapping makes digital spatial-carrier interferometry suitable even for rapid and high-gradient phenomena.[141]

In order to avoid spatial unwrapping, temporal sampling condition for maximum phase change $\varphi^w(x, y, n\Delta t) - \varphi^w(x, y, (n-1)\Delta t) < \pi[rad]$ between two consecutive frames must be fulfilled. The allowed temperature change between the two frames for a given camera frame rate must be $T_{max} < \frac{\lambda}{1.97 \cdot 10^{-4} L}$[fps].[141]

In order to verify the technique, $0.05[mm]$ diameter $K - type$ thermocouples were used to measure the temperature inside the glass tank. Digital spatial-carrier interferometry integrates the phase along the

propagation path, which means that it measures the average temperature, while thermocouples measure at single points and represent the temperature values at those positions. Position coordinate of the thermocouples are: $P1(-13.5,22,24), P2(-13.5,22,8), P3(-13.5,22,-8)$ and $P4(-13.5,22,-24)$. In order to verify the results, the thermocouples were places along the propagation axis and the final temperature value was obtained as an average of them.[141]

6.4. Results

Digital spatial-carrier interferometry is a technique that offers relative measurements. This means that only the temperature change $\Delta T(x,y,t)$ can be mapped. To determine the absolute temperature distribution $T(x,y,t)$, temperature at the reference steady-state $T_0(t=0)$ must be evaluated by other means. The reason why the x and y dimensions aren't added in this case in the formula for the steady-state temperature T_0 is because it is assumed that the system is in thermodynamic equilibrium with the environment when the experiment starts, which means that the temperature is uniform in all the volume. The final temperature can be written as[141]:

$$T(x,y,t) = T_0 + \Delta T(x,y,t) \tag{6.14}$$

Fig.6.5. shows temperature fields measured at different times. It reveals convective process happening but layer convection due to high dynamic range of temperature values are not seen.

In order to see heat layer movement, a decrease in dynamic range of temperatures must be made. This is possible by making use of temporal finite difference of temperature[141]:

$$T_t(n\Delta t) = \frac{T(n\Delta t + \Delta t) - T(n\Delta t)}{\Delta t} \tag{6.15}$$

This also makes it possible to observe phenomena such as heat wave travel and material mixing. The temporal temperature difference can be calculated as[141]:

$$T_t(x,y,n\Delta t) = \frac{\lambda}{2\pi}\frac{\varphi^w(x,y,n\Delta t) - (x,y,(n-1)\Delta t)}{0.985\cdot 10^{-4}\cdot L}\frac{1}{\Delta t} \tag{6.16}$$

Fig.6.6. below shows the temporal difference of the temperature T_t at various times. It shows the thermal convection layer along the heater length.

Fig.6.7. shows the temporal difference temperature starting at $t = 153.6[s]$. Here the layer movement was much faster due to stronger gradient fields. For comparison, the convection velocity at $t = 3.8[s]$ is around $1.3\left[\frac{mm}{s}\right]$, while at $t = 153.6[s]$ it is $18.6\left[\frac{mm}{s}\right]$. The increase in velocity is consistent with the idea that the layers will move faster with higher temperature gradients.[141]

The point for evaluation of temperature from digital spatial-carrier interferometry is selected to be near the thermocouples, and considering the diffraction and shadowing effects coordinates of $x = -9.5[mm]$ and $y = 22[mm]$ are chosen. Both points, the one of the thermocouple and the one for evaluation with digital spatial-carrier interferometry are shown in Fig.6.4. and Fig.6.5. as small squares on the first figures. Comparison of both methods is shown in Fig.6.8.[141]

The fact that the position for digital calculation doesn't match the true position of thermocouples is a source of mismatch between both techniques. Also, the fact that our optical technique integrates along the propagation path and the fact that thermocouples represent point measurements, which we have four, meaning they represent four discrete points, also contribute in the mismatch. This is particularly seen for rapid phenomena.[141]

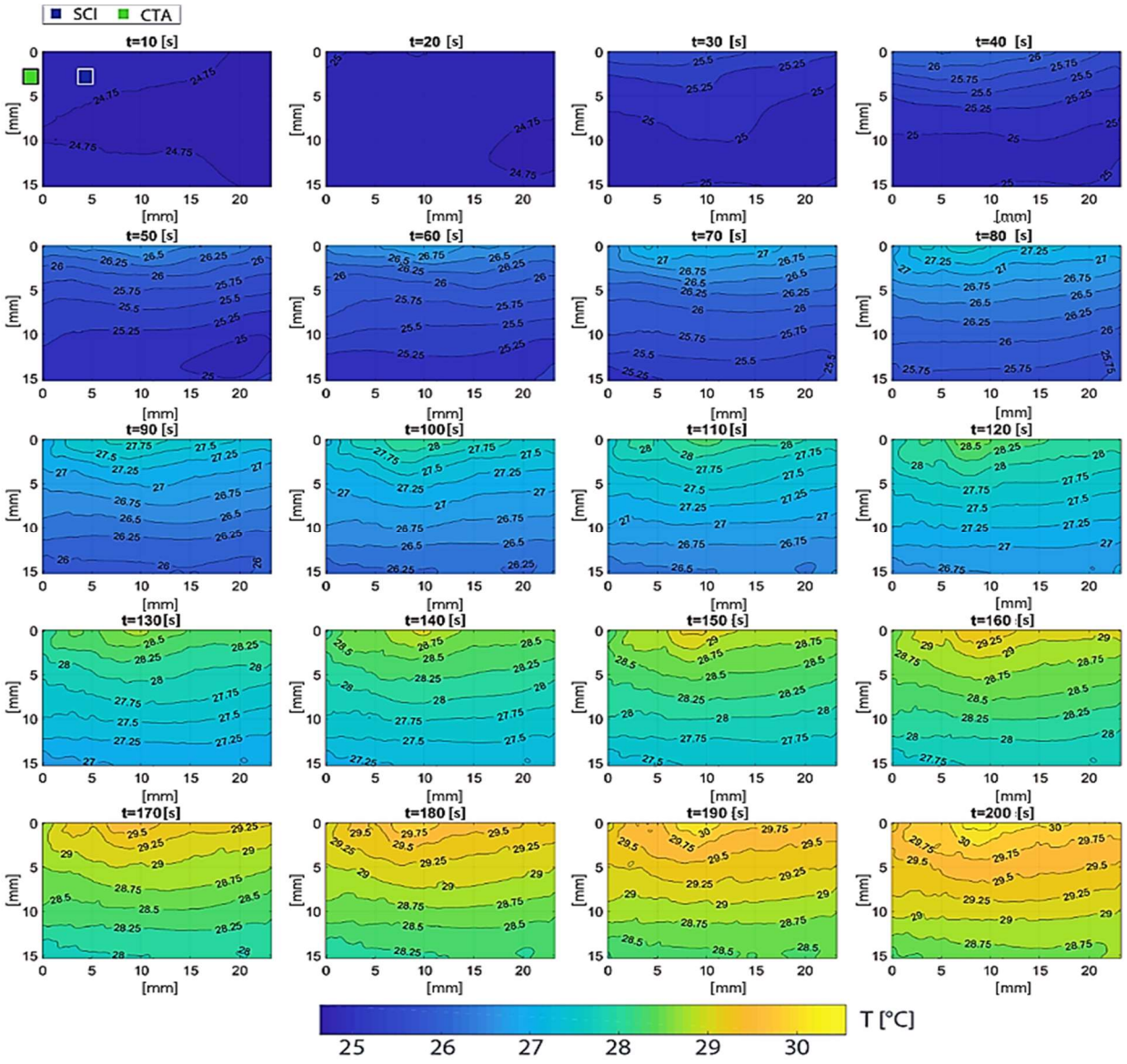

Fig.6.5. *Absolute values of temperature at different time after the heater was turned on.*[141]

The standard deviation between the temperature registered by the thermocouples and the one evaluated by the optical method is $\sigma(\delta T) = 0.08[°C]$. The graph of the difference between both methods for the whole range of measurements can be seen in Fig.6.8.b). Since δT show to have a Gaussian distribution, then the confidence level of deviation for up to 99% is $3\sigma(\delta T) = 0.24[°C]$. The temperature range here is $T_{range} = 4.98[°C]$ and the deviation falls within $100 \cdot \frac{3\sigma(\delta T)}{T_{range}} \approx 5\%$.[141]

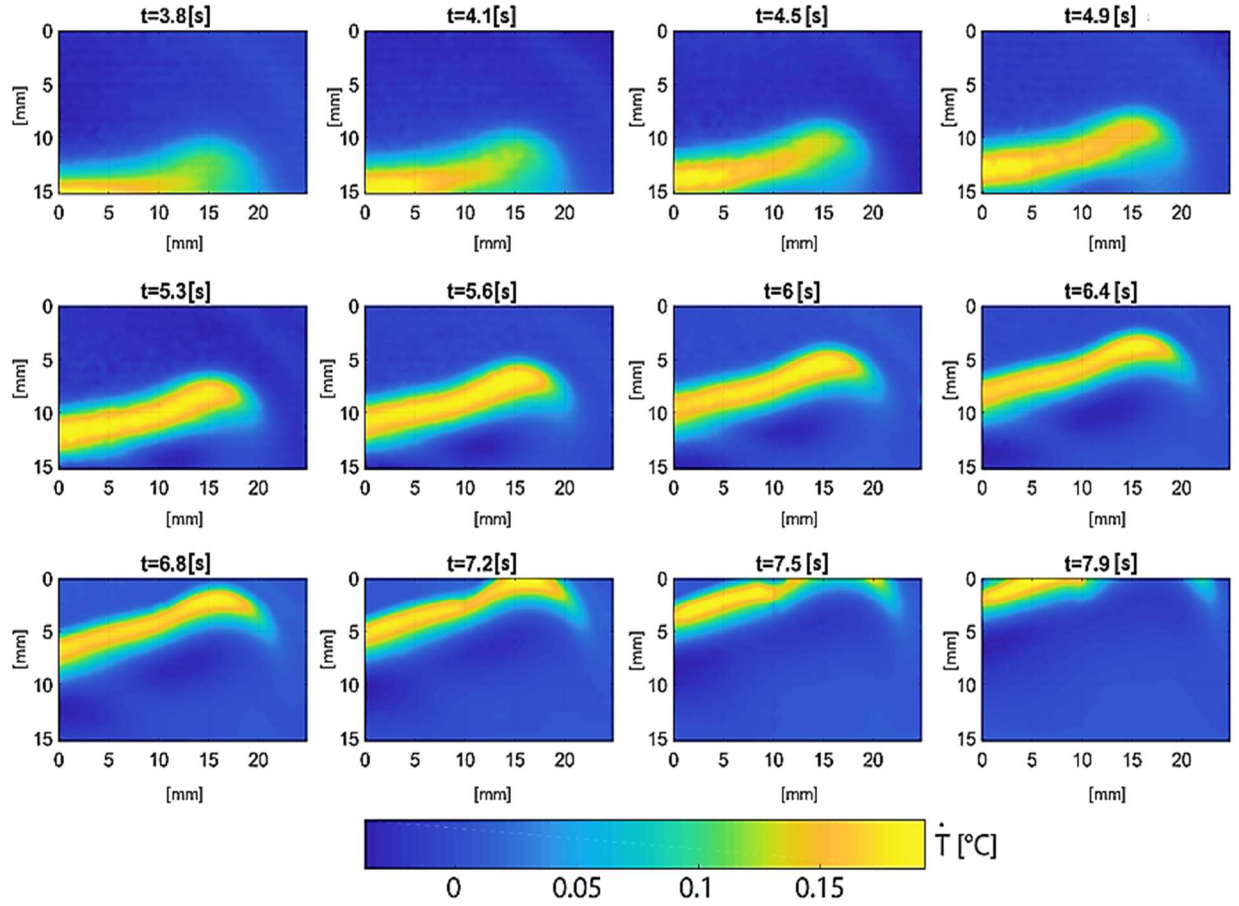

Fig.6.6. *Temporal difference of temperature field within 3.8[s] and 7.9[s] interval. The phenomena of convection is clearly seen.*[141]

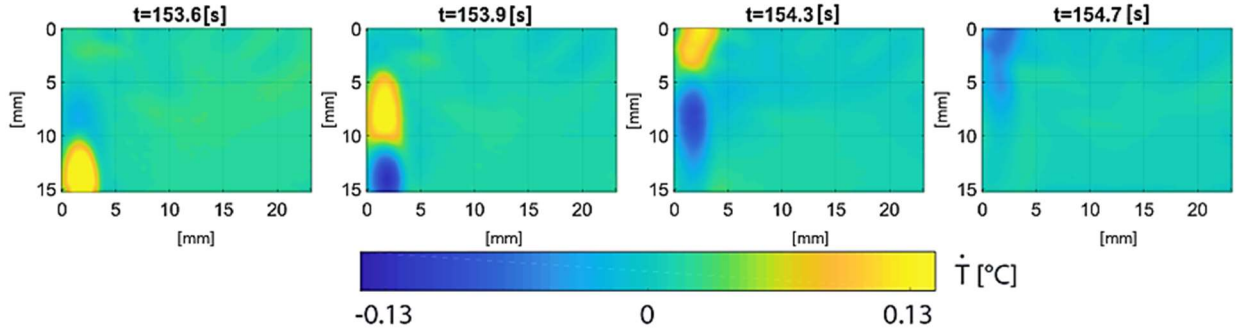

Fig.6.7. *Temporal difference of temperature field within 153.6[s] and 154.7[s] interval. The phenomena of convection is faster and more local when compared to Fig. 6.6.*[141]

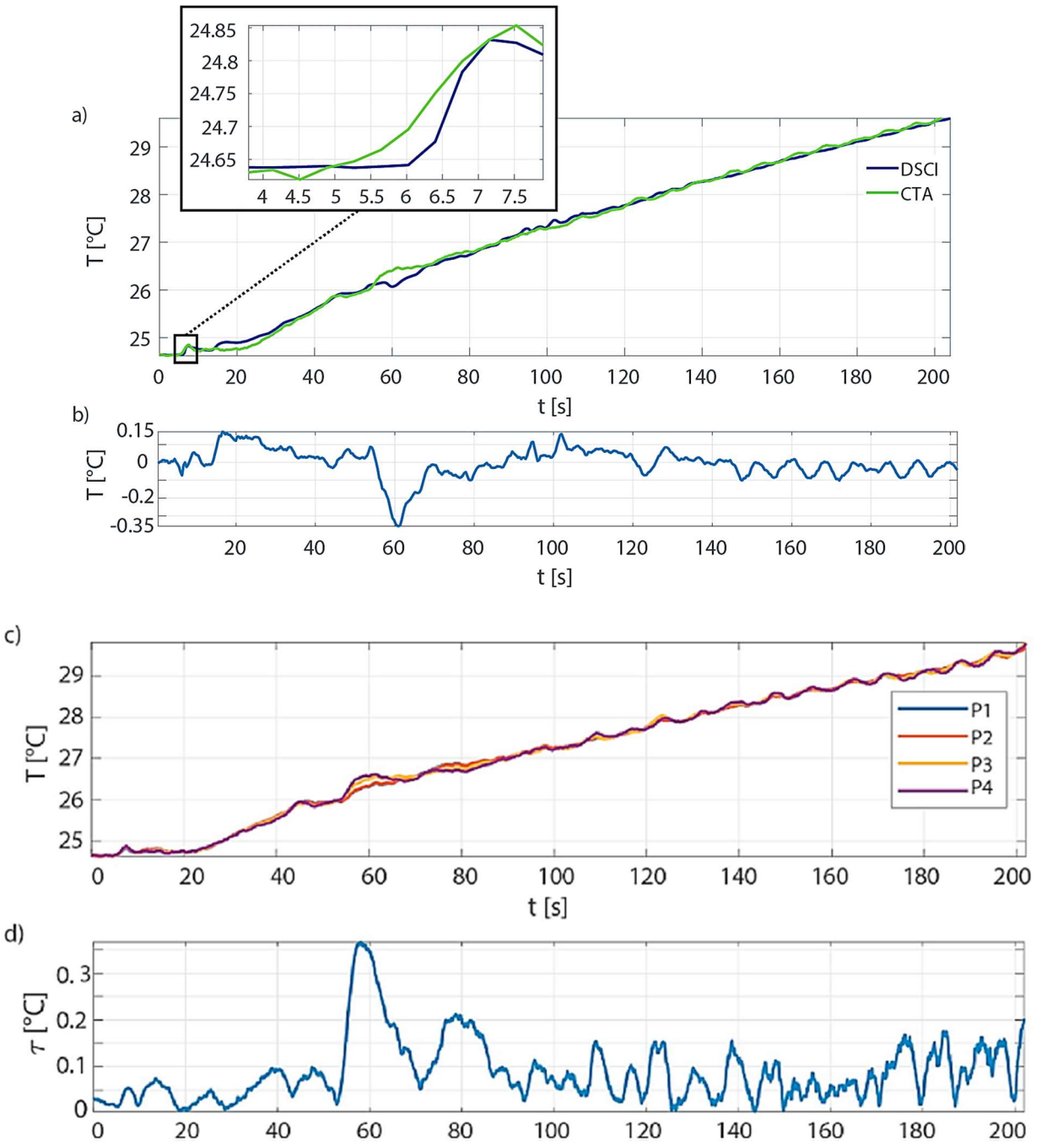

Fig.6. 8. *a) Results obtained by the thermocouples and our optical approach, b) the difference between measurement methods, c) measured values by the thermocouples and d) a peak-to-valley deviation plot between the results obtained for the thermocouples.*[141]

As said before, it is supposed that the variation of the refractive index is constant along the optical path of propagation. But this is not completely true[39]. Fig.6.8.c) shows the temperature values obtained from all the thermocouples. In an ideal case, all of those should match. But the fact that there is a slight variation of the refractive index, not precise alignment of the thermocouples along a single path, uncertainty in values obtained make these value to differ from each other.

Fig.6.8.d) represents a peak-to-valley deviation that regroups all the factors mentioned previously and is calculated by[141]:

$$\tau(t) = Max\{T_{th-i}(t)\} - Min\{T_{th-i}(t)\} \tag{6.17}$$

, where $i = 1,2,3,4$ representing the thermocouples. Considering 95% percentile, the temperature variation along z-axis that represents deviation from the field two-dimensionality is $0.2[°C]$. This value may vary with x, y coordinates being probably higher when approaching the heater.[141]

6.4.1. Limits and errors of interferometry in liquids

These kind of measurements in water are challenging compared to measurements done in water. This comes from the fact that the dependence of the refractive index with temperature in water is two order more sensitive than the one for air: $\left(-\frac{dn}{dT}\right)_{air} \approx 1 \cdot 10^{-4}$, $\left(-\frac{dn}{dT}\right)_{water} \approx 1 \cdot 10^{-6}$. For the same temperature change, the phase change in water is steeper than the one in air, thus causing denser fringes, which can cause problem in determining phase jumps and can violate the criteria for sampling which is given by the pixel pitch of the camera.[141]

The allowed phase difference between two neighbouring pixels is given by[141]:

$$\Delta\varphi = \varphi^w(y) - \varphi^w(y-1) \leq \pi\ [rad] \tag{6.18}$$

From this , the temperature change per image plane pixel extension for $\Delta y = 67[\mu m]$ is given as[141]:

$$\left(\frac{\Delta T}{\Delta y}\right)_{experiment} = \frac{\lambda}{2\pi\Delta y}\frac{\Delta\varphi(y)}{-\frac{dn}{dT}L} \approx \frac{\lambda}{0.985 \cdot 10^{-4} \cdot L} \approx 0.1\left[\frac{℃}{mm}\right] \leq \frac{\Delta T}{\Delta y} = 0.8\left[\frac{℃}{mm}\right] \tag{6.19}$$

The deflection of the propagation wave is not taken in consideration in previous calculations. This also brings some uncertainties in the measurements. For the convection cases, water layers get stratified. The temperature increases on the vertical direction. In these cases, the temperature distribution can be approximated by a linear model involving the refractive index in the form of[141]:

$$n(y) = n_0 - dn \cdot y = n_0 + dT \cdot y \cdot 10^{-4} \tag{6.20}$$

$$dT = \frac{\Delta T_{max} - \Delta T_{min}}{y_{max}} \approx 0.2\left[\frac{℃}{mm}\right] \tag{6.21}$$

and $n_o = 1.33$.

By making use of the ray propagation equation:

$$\frac{d}{ds}\left(n(x,y,z)\frac{d\vec{r}}{ds}\right) = \nabla n(x,y,z) \tag{6.22}$$

where $\vec{r} = (x,y,z)$, $ds = \sqrt{1 + \left(\frac{dy}{dz}\right)^2}$, s is the length of the ray propagation path, the deflection is calculated by[102,141]:

$$d = \frac{1}{2}\left(\frac{dT \cdot 10^{-4}}{n_0}\right)L^2 \tag{6.23}$$

This means that the ray will travel in a parabolic route inside the glass tank with water, and upon hitting the wall again it will travel deflected from its initial route by a distance of d. Also, the optical path of the deflected beam is longer than the one that we suppose that travels straight. The phase along such path can be calculated by[141]:

$$\varphi_{deflected} = \frac{2\pi}{\lambda}\int_{L} n(y)\sqrt{1+\left(\frac{dy}{dz}\right)^2}\,dz = \frac{2\pi}{\lambda}n_o L^2 \tag{6.24}$$

The phase deviation is:

$$\varphi_{error} = \varphi_{deflected} - \varphi \tag{6.25}$$

, which yields[141]:

$$T_{error} = \frac{1}{3}\left(\frac{dT\cdot 10^{-4}}{n_0}\right)^2 \cdot \frac{L^2}{10^{-4}} \approx 0.03[℃] \tag{6.26}$$

Also, in time, the place where the ray hits the digital camera changes as the gradient of temperature increases, meaning that temperature values at (x, y) can be blurred. For the case when the deflection is bigger than half of the image plane pixel extension, then the spatial resolution decreases. In this experiment, the maximal deflection is lower than half of the effective resolution. One way to reduce this side effect is to shorten the path of light into the glass tank L, or correct this mathematically.[141]

Other kind of noises to be taken in account are the electronic noise, noise coming from the environment, wavelength stability, uncertainty of measurement and interference signal modulation.

The relation between the phase gradient and the spectral bandwidth is given by[141]:

$$\vartheta_B = \frac{\nabla\varphi}{2\pi} \tag{6.27}$$

At the initial state $t = 0[s]$, $C(\vartheta_x, \vartheta_y)$ covers a bandwidth of $\vartheta_B \approx 55[mm^{-1}]$ which yields $\nabla\varphi \approx 314\left[\frac{rad}{mm}\right]$ which comes from the stationary deviation between the reference and object beam and the location of the filtering window.[141]

Temperature stratification makes the phase gradient to increase, which brings the value of the phase gradient at the end of the measurement $t = 288[s]$ to[141]:

$$\nabla\varphi_T \approx \frac{2\pi}{\lambda}\cdot 10^{-4}\cdot L\nabla T = 30\left[\frac{rad}{mm}\right] \tag{6.28}$$

, where $\nabla T \approx \frac{\Delta T}{\xi} \approx 0.5\left[\frac{°C}{mm}\right]$ which represents the temperature gradient related to the camera pixel ξ. The final phase gradient is[141]:

$$\nabla\varphi(t = 288[s]) = \nabla\varphi(t = 0[s] + \nabla\varphi_T \approx 344\left[\frac{rad}{mm}\right] \tag{6.29}$$

This corresponds to a spectral bandwidth of $\vartheta_B \approx 55[mm^{-1}]$ and in this experiment a spatial bandiwth filter with $\vartheta_B \approx 60[mm^{-1}]$ was used.[141]

6.5. Conclusions

This chapter presents a whole-field interferometric method for measuring dynamic phenomena in transparent media. The developed method allows for quantitative and fully automatic measurement. It is based on differential spatial-carrier interferometry which provides interesting features for research in the field of experimental fluid mechanics.[141]

Specifically, the presented method is[141]:

- A comparative measurement with respect to a reference state, i.e., measurement results are unaffected by the optomechanical imperfections of the arrangements, thus, inexpensive optics can be used;
- The measurand (i.e., temperature field here) is evaluated from a single interferogram, so the measurement can conduct in almost real time;
- Due to the differential approach, the dynamic range of the measurement is smaller, thus, no spatial phase unwrapping or spatial unwrapping of low density fringe maps is needed;
- The method is an unambiguous interferometric measurement.

Although the method is suitable for measuring any quantity affecting the refractive index of the medium, and consequently, the optical phase of the transmitting laser beam, it was experimentally tested for measuring the temperature field of water. The experimental arrangement was a Mach-Zehnder interferometer enabling tip and tilt of its reference arm in order to introduce carrier frequencies. The inspected phenomenon was a convection of water layers within a glass tank caused by a heater placed at the bottom. The average temperature along the optical axis was measured interferometrically and simultaneously by four thermocouples to verify the developed interferometric method. The results of both measurements are within 5% agreement. The deviation between the results of the two techniques is mainly due to the slightly different measuring locations and the fact that the interferometric results are average temperatures over the entire optical path, whereas the results of the measured thermocouple represent an average of only four discrete points. It was also demonstrated that in addition to measurement of absolute temperature, differential spatial-carrier interferometry inherently measures temporal temperature differences that show the temperature fields in a reduced dynamic range, thus, revealing heat layer movement, and heat wave travel.[141]

Interferometric measurement in water is challenging due to high sensitivity of the refractive index change to temperature change. Nonhomogenieties of a temperature distribution deflect rays so the optical path is slightly extended and the deflection causes mismatch in the positions where the ray hits the digital camera. Those two effects were analytically analyzed assuming linearly stratified temperature distribution.[141]

It was inferred (for the particular experiment) that the error due to the optical path extension is approximately $0.03\ [°C]$. The value of maximal deflection, $30\ [\mu m]$, is lower than half of effective lateral resolution $(67\ [\mu m])$ of the measurement so the results were not affected by the deflection.[141]

7. Simulations of temperature fields by CFD and its comparison with digital holographic interferometry (DHI) and thermocouples.

Previously, in *Chapter 6* we have introduced a digital holographic interferometric technique to measure and visualize temperature fields in liquids. In this chapter, through simulations conducted by CFD means, we compare our findings in *Chapter 6* to simulated data in order to validate our findings.

7.1. Numerical analysis

In this experiment, the main purpose of study is only the natural convection caused by the cylindrical heater rod submerged in water with temperature of $26.45[°C]$.

The wall materials and the effects of the solid walls are taken in account, which does not always happen in analysis of convection processes. Heat losses from the walls to the outside air are taken in account as well, but unfortunately the value of such coefficient is not given by the producer. Thus, a simplification is made by taking the coefficient of such losses from normal glass heat conduction value.[144]

Taking in account these changes can significantly affect the results, especially in the case of buoyant flows. Defining the walls as solid structures influences the mixing of the fluid and fluid circulations, thus for high quality results, walls must be taken in account.[63,144]

In this simulation, boiling and evaporation are not taken in account, since this is not the purpose of the real experiment.[144]

The numerical study is accomplished using Fluent software in *ANSYS* workbench 18.1. In order to achieve full physical insight of the process, two different cases of three-dimensional models are used. The first model has both heater and water domain with 458352 mesh elements. The second model has only the water domain with 498419 mesh elements using more refined mesh at the walls. The real gas model is implemented to represent the thermophysical properties of water by using the integration of National Institute of Standards and Technology (NIST) Refrigerants Database (REFPROP v9.0) in order to get more consistent and accurate results and probe the physical understanding.[144,145]

Since the temperature range is rather small, the option of double precision for more precise solution is selected. In the modeling, pressure based-segregated solver with transient time is used for viscous laminar model. The governing equations in this solver are solved sequentially. The simple algorithm is used for pressure-velocity coupling with second order upwind scheme for momentum and energy equations. Boussinesq approximation method for the density and pressure interpolation provided by PRESTO scheme is selected because of the buoyancy-driven flow, which is recommended for natural convection flows when the temperatures difference is quite low.[144]

Measurement points were selected as those in the real measurement (see Fig.6.3.c and *section-6.3.*)). They were spread equally along the thickness of the aquarium.

7.2. Results and discussion

7.2.1. First numerical analysis results

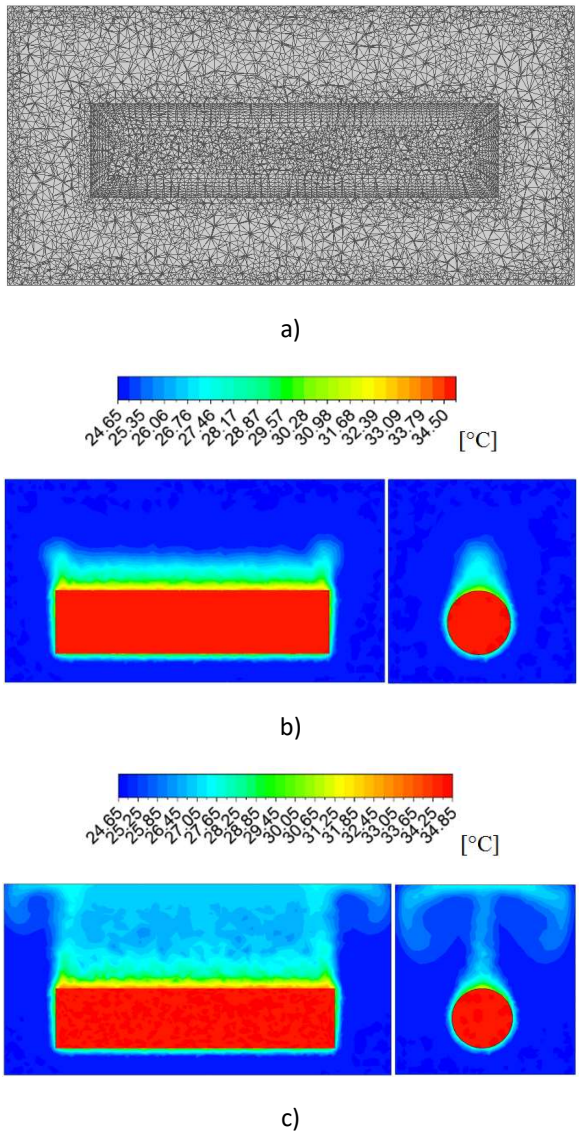

Fig.7.1. *a) Meshing, and temperature profile at b) t=6[s] and c) t=16[s].*[144]

As already explained earlier, the case of natural convection from a cylindrical heater rod submerged into water in a tank is simulated using *ANSYS Fluent*. The results of the numerical simulations are presented in a graph, where they are compared to data from the thermocouple and the DHI technique (see Fig.7.3.). From this plot, it can be seen that the CFD simulations predicts overall good values of temperature for the simulation time.[144]

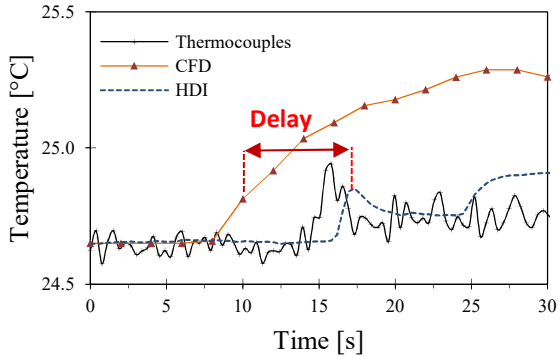

Fig.7.2. *Delay introduced between the CFD results and the data obtained by the thermocouple/DHI.*[144]

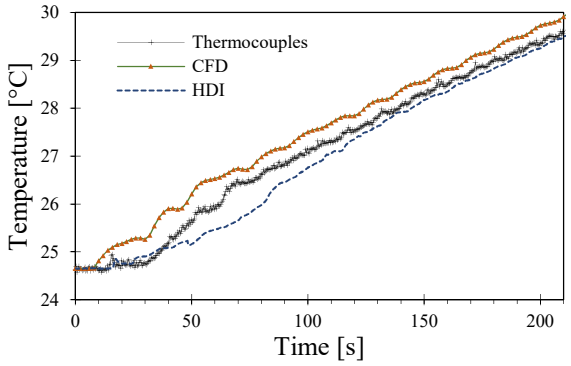

Fig.7.3. *Comparison of data obtained from CFD, thermocouple and DHI for the whole time of measurement.*[144]

As can be seen from Fig.7.2., there has been a time delay between the experimental data/DHI and the simulated ones. The small delay between the data from the thermocouple and DHI can be attributed to the fact that DHI integrates along the pathway while the thermocouple is a point measurement, so the thermocouple ”feels” the temperature a bit earlier than DHI depending on its location. In the first simulation, data from only one thermocouple *(P3, section-6.3.)* is used. Averaging values of thermocouples are used in the second simulation.[144]

In the simulation, the heater starts to heat almost immediately when starting the simulation, while in the real experiment it takes some times. The time delay is believed to come from the fact that not all parameters were set (exact knowledge of heat loss coefficients etc.).[63,144]

Another possibility of such time delay is the real exact composition of the materials composing the cylindrical heater and their thicknesses, which are unknown. We believe that there are three different layers (two were mentioned in the data from the producer, but without any details): the first part consisting of the resistor delivering the heat and its first insulating coating, the second part is the silica material filling the heater and used for heat transfer, and the third part consisting of the stainless steel coating against rust.[144]

Source of error coming from the comparison of the CDF results and the ones obtained from the DHI technique are[144]:

- CFD point locations are exact points in 3D, which means that each point of measurement will provide the temperature value at the specific (x, y, z) coordinate, while the DHI technique integrates along the path of the light propagation. We suppose a constant refractive index along the path of optical propagation. This means that DHI provides with the average temperature value along the optical path.
- Temperature variations along the optical path is reported to be $0.2[°C]$ from the work done previously.[141]
- Uncertainty measurement of DHI also provide with a range of errors. Adding the fact that DHI measurement in water are highly sensitive and can be cause of error addition into the processing values.[141]
- Deflection caused by the ray travelling into the medium, resulting in a curve path (and not straight path as supposed in the DHI experiment) could theoretically cause some errors, but it was reported (see *section-6.4.*) to cause negligible variations of temperature $(0.03[°C])$.[141]
- Missing of the real data for the wall heat transfer coefficients from the producer of the glass tank.
- Missing exact heat transfer coefficients and geometrical data for the cylindrical heater composing materials and layers.
- While the DHI technique measures true physical values, CFD results remain results obtained with a simulation. Not all conditions can be recreated nor have been recreated in our model faithfully.

Error calculation was done using the following formula[144]:

$$error = \frac{T_{DHI/CFD} - T_{Thermocouple}}{T_{Thermocouple}} \cdot 100 \tag{6.30}$$

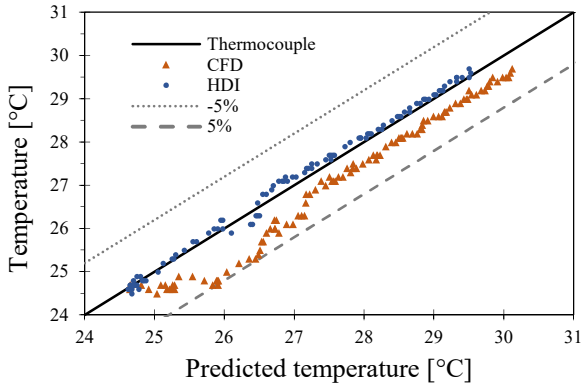

Fig.7.4. *Error plot of data obtained by CFD and DHI in comparison to the data obtained by the thermocouple.*[144]

By calculating the error by the previous equation for both DHI and CFD values with respect to values obtained by the thermocouple, Fig.7.4. is obtained. As it can be seen, DHI faithfully reproduces the data obtained by the thermocouple, and is much lower than the error limit of 5% in this graph (upper part of the graph from the diagonal). On the other hand, CFD data give a higher rate of error than DHI but at the limit of 5% error for the whole range of temperatures.[144]

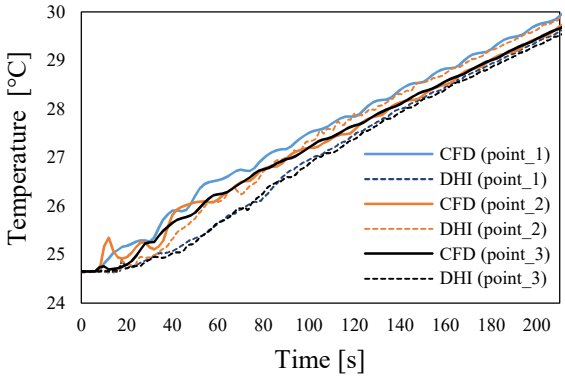

Fig.7.5. *Comparison of CFD results with DHI for three different point positions above the heater.*[144]

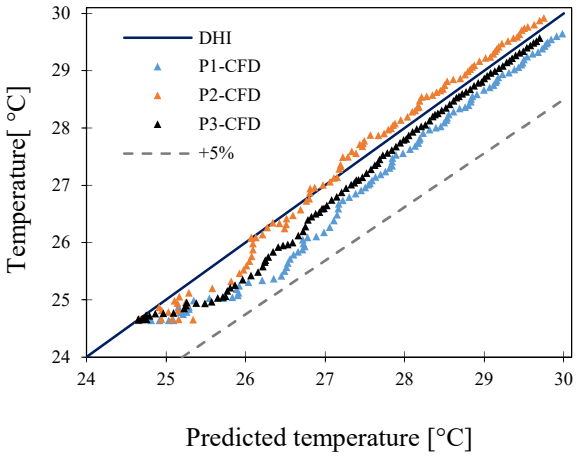

Fig.7.6. *Error plot of data obtained by CFD in comparison to the data obtained by DHI.*[144]

In Fig.7.5., data obtained from the simulation are compared with the ones from DHI in various points inside the field of view (*z* axis). As can be seen, results obtained by the simulation show to be in a good agreement with the data obtained by DHI. The CFD reproduces the general increasing trend of the temperature which can be seen in the plot, but produces somewhat different initial temperature values of the first heat wave. All variations and mismatching of temperature values are due to the causes mentioned previously.[144]

Due to the process of heat transfer from the cylindrical heater, water starts heating up around it. It can be seen that hot water propagates in the upward direction through natural convection (see Fig.7.1.), while colder water stratifies in the bottom of the tank. There is no flow of water under the cylindrical heater for this range of heat supply and time.[144]

Flow under the cylindrical heater is reported only to happen once the water reaches saturation temperature (which is not the case in this experiment, since the experiment and simulation are performed for low heat supply and not long enough for such process to take place).[144,146]

Together with the rising of the temperature, the natural convection phenomenon takes place. It is expected that the water to only mix for larger heat transfer, or eventually waiting long enough that

enough energy would be transferred to the water. With increasing heat, turbulence and the speed of flow of water increase as well which can be seen in Fig.7.3. , where the data obtained from DHI, the thermocouple and CFD don't necessarily match even at higher temperatures.[144]

From the results (see Fig.7.1.), the "puff" shape that is expected in such cases can be seen. Upon arriving at the surface, water starts travelling horizontally in all directions. After starting to mix a bit, it starts to flow downward, but the heat supply is too small to cause massive water displacement for such effect to be clearly seen.[144]

The top part is opened to air, but since the experiment is limited to a small range of temperatures and for a short time (around $200[s]$), air convection isn't expected and doesn't happen. That could be expected if boiling process was under study.[144]

At the time when the phenomenon is more rapid, in this case when the first heat wave arrives to the location measured by the thermocouples and the DHI, the standard deviation is reported as $T = 0.08[°C]$. The deviation relative to the measurement range is reported as being 5% of the measured temperature.[141,144]

7.2.2. Second numerical analysis results

The simulation is redone with a finer meshing, keeping all the other parameters unchanged. The new meshing can be seen in the figure below.

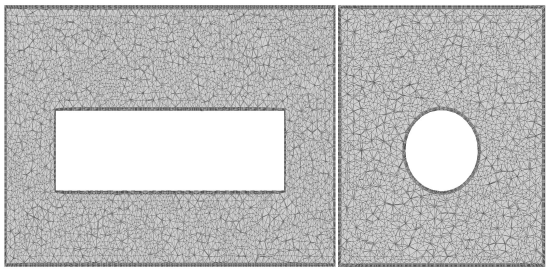

Fig.7.7. *Meshing of the water domain in the tank seen from two sides.*[144]

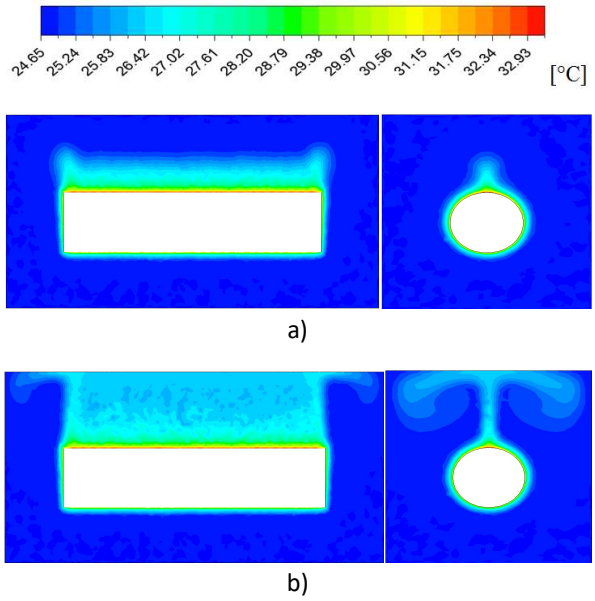

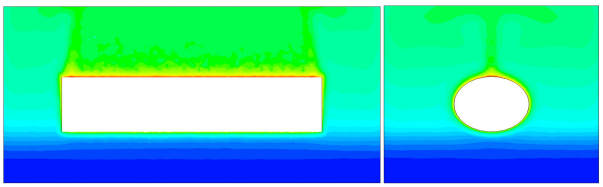

c)

Fig.7.8. *Temperature profile a) t=7[s], b) t=17[s] and c) t=120[s].*[144]

From Fig.7.8. it can be seen that the heat profile was faithfully reproduced as well for the case of finer meshing. In the c) part of Fig.7.8. the stratification of the water below the heater at $t = 120[s]$ can clearly be seen. It can be concluded that no much happens below the heater for these heating parameters and time of measurement.[144]

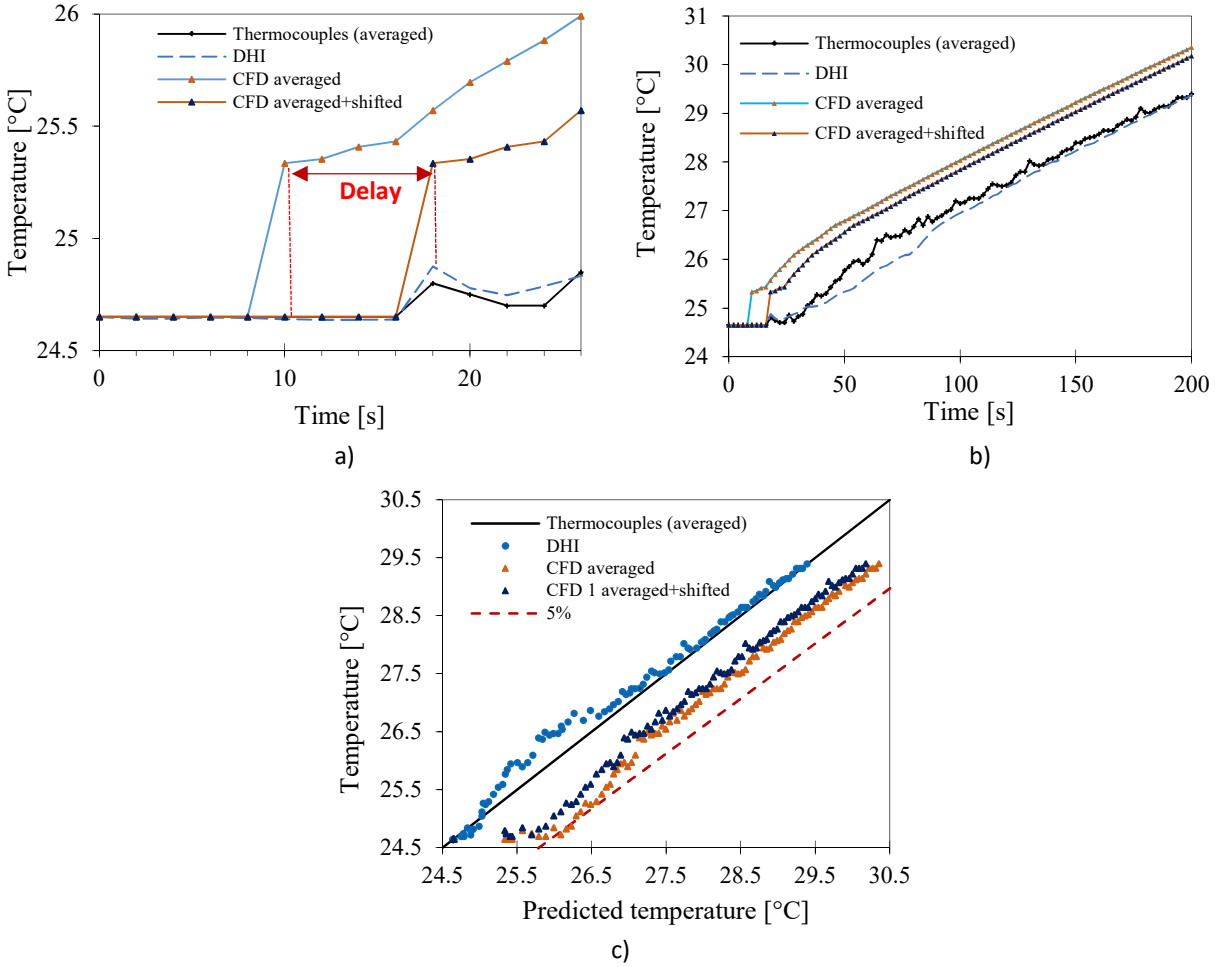

Fig.7.9. *a) Delay introduced between the CFD results and the data obtained by the averaged value of thermocouples and DHI, b) comparison for the whole time of measurement and c) the error plot with respect to the data obtained by the thermocouples.*[144]

Fig.7.9.a) shows the expected delay between the CFD results and the DHI/thermocouples. Here data obtained from DHI are already averaged along the axis of light propagation but data obtained by thermocouples at this point are averaged and represented in the graph. Since the delay is expected and

is caused for the same reasons as mentioned before, the graph has been shifted to the times where DHI/thermocouples show the first sign of heat, in order to have a better insight on the values obtained from the CFD measurement. The non-shifted and shifted ones are represented with different colors. Fig.7.9.c) shows that the simulation data, before and after shift still remain within the error margin of 5% as in the first simulation.[144]

Here more than one point of measurement are taken. Following Fig.7.10 and Fig.7.11. represent the graphs obtained from the CFD in comparison with DHI and their respective error plots for two other points of measurement. From these it can be seen that the margin of error still remains within 5%.[144]

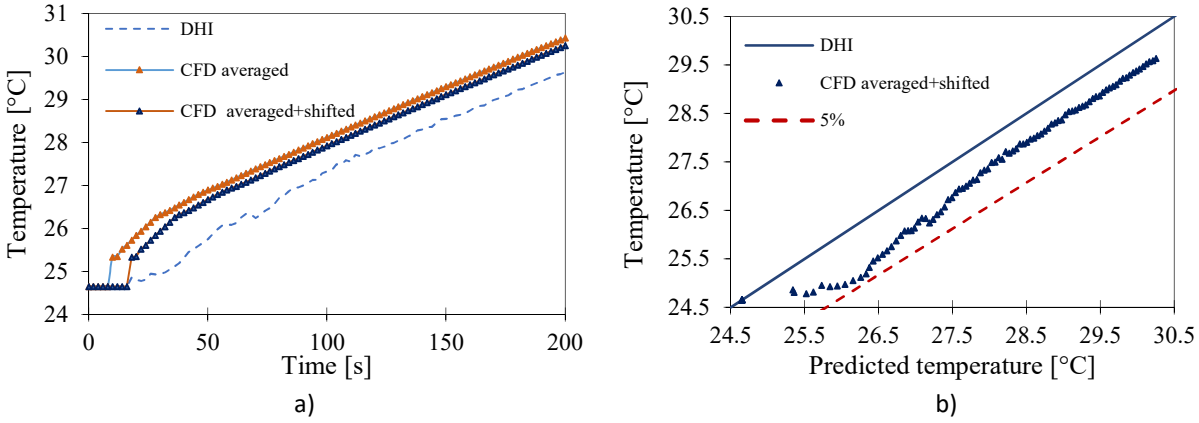

Fig.7.10. *a) Comparison of CFD results with DHI for another point and b) its error plot.*[144]

Fig.7.10.

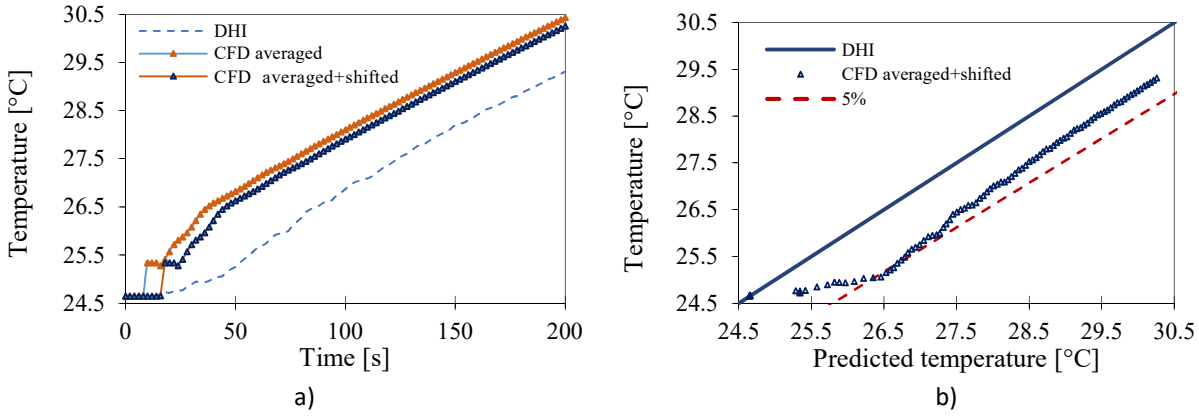

Fig.7.11. *a) Comparison of CFD results with DHI for another point and b) its error plot.*[144]

7.3. Conclusions

This chapter compares data obtained by CFD simulations with data obtained by DHI and thermocouples from *Chapter 6* to assess the validity of using DHI as an optical technique for the study of flowing gases and liquids. It also validates DHI as a whole-field interferometric method for measuring the temperature profile and other phenomena in a glass tank filled with water. This has been done through the simulation of natural convection coming from a cylindrical heater submerged in water in a glass tank and the estimation of the temperature of water. At the same time it validates the model used in this chapter to predict temperature values for such studies.

This chapter reports the precision and reliability, hence the advantages, of using digital spatial-carrier interferometry for temperature measurements and visualizing heat fields in liquids (in this case water).

From figures shown in this chapter, it can be seen that data from the CFD simulations agree generally and follow the same trend as with the ones from DHI and the thermocouple(s). The CFD data, as the DHI ones, show a convective heat transfer process happening. It can also be concluded that the estimation of the coefficients for heat transfer through walls, heat coefficient of the materials and layers' thicknesses composing the cylindrical heater are good enough.[144]

Since real data from the producer are missing, discrepancies between estimated temperature by the CFD simulations and data obtained by the thermocouple(s) and DHI technique are expected. These deviations arise also for a number of other reasons explained previously. Taking into account the fact that the process is quite slow, exact heat losses are impossible to be predicted, thus discrepancies arise as well.[144]

Generally, the comparison of data obtained from the CFD simulations, digital holographic interferometry and thermocouples showing the evolution of heat diffusion in water and the temperature values, put DHI in scene as a tool that can be used as a trustful technique to map, compute and visualize heat fields in gases/liquids without the need of using devices that would interact with the flow. It shows to be a fast, precise and easy technique for such purposes and can offer much more data in real time without the need of complicated measurements using many thermocouples or any other devices for such purposes. Therefore, it is an excellent technique to detect small changes of refractive index, density, pressure and temperature.[144]

It can finally be concluded in short words that data from both simulations are in good agreement with both data collected by thermocouple(s) and the DHI technique. The results indicate that the model can be used to estimate natural convection by a cylindrical heater above it, and can be used not only for temperature measurements, but also velocity profiles and other parameters.[144]

These simulations and results reveal the power of CFD simulations and its abilities to reproduce such phenomena and predict the desired variables. Yet, more has to be done. Further task would be to refine the model in order to take in account missing data from the producer (measuring exact heat loss coefficients for our glass tank, detailed list of composing materials for the heater and their coefficients, etc.).[144]

8. Two-wavelength digital holographic interferometry for unambiguous range extended measurements in fluid mechanics

When the phenomena under study expresses big changes that surpass the range of measurement limited by the wavelength of the laser in use, a phase ambiguity arises. If this ambiguity isn't solved in the phase unwrapping process, it will give faulty result, not mapping the true profile of the phenomenon we are looking at.[147]

In this chapter, a two-wavelength off-axis digital holographic interferometric optical setup for resolving the issue of phase unwrap ambiguity for three different study cases is presented. It presents an interesting way of by-passing the range limit, while still keeping noise values low, by introducing a second laser with a close value wavelength, giving rise to a new interferometric pattern with an extended unambiguous range of measurement where the image acquisition is done simultaneously for both wavelengths and all reconstructions are digitally performed.

8.1. Introduction

The phase of the light hitting the camera is proportional to the surface profile (when trying to image surface profiles from reflection), to the integral refractive index for transparent media when it passes through, otherwise it is linked to the wavelength via respective formula[147]. If the phase profile exceeds 2π $[rad]$, the phase is wrapped yielding in phase ambiguities. Two-wavelength interferometry offers an alternative solution to solve the phase ambiguity problem[147]. This method enables a fast and efficient way of imaging the phase profile for a multitude of applications. It enables to measure in real time phenomena that cause large phase changes without ambiguity. Thus, by using two lasers or more, the range of unambiguity can be increased compared to using a single laser[148]. For quickly evolving phenomena (like flow measurements), the two wavelengths can be captured simultaneously, resulting in a multiplexed hologram. In order to separate information from both wavelengths, off-axis optical configuration can be used. The off-axis configuration also spatially separates the holographic images away from the undiffracted zero order.[149,150]

Two-wavelength interferometry can be used in many areas of optical metrology, for the measurement of the thickness and surface profile/inspections of objects[147]. It can be used in research dealing with samples having large topography changes and biological samples[151]. In interferometry, specifically phase-shifting interferometry, at least three intensity maps are needed to resolve the phase map, while in two-wavelength interferometry it is six but can be decreased to two[152].

8.2. Principle of two-wavelength interferometry

In single-wavelength technique, when the object of investigation is thicker than the laser wavelength (in our case the temperature range that can be mapped surpasses the range of measurement) used for research, the phase gets wrapped and suffers from 2π ambiguities. The range of measurement is directly connected to the wavelength. For smaller wavelength, the range decreases, while for longer wavelength it increases. Longer wavelengths produce fewer fringes, reducing the number of 2π ambiguities[153].

Phase has a periodicity of $2\pi[radians]$ and the phase of light can be expressed as a multiple of this 2π periodicity. The repetitive nature of light propagation as wave in the form of a sinusoidal wave makes the range of clear unambiguous measurement to be limited to one cycle of repetition, i.e. one wavelength. Due to Nyquist criteria, the real range of unambiguity is limited to a half-wavelength[154]. In other words, the wrapping is a direct consequence of the 2π periodicity of the $arctan$ function used to extract the phase profile from the light that is being measured[33,155]. During the phase unwrapping process, the absolute phase difference between points of measurement in time and space must be less than the value of $\pi[radians]$, for a better unwrapping[156]. There are cases when the difference is much higher, causing multiple wrapping simultaneously. Care must be taken when dealing with such situations.[157]

The sole idea of using a two-wavelength technique comes from the limitation mentioned above. In two-wavelength or multiple-wavelength interferometry, the unambiguous range of measurements gets extended by what is called the synthetic wavelength (see below)[33,148]. The general graphical concept representation is shown in Fig.8.1.[157]

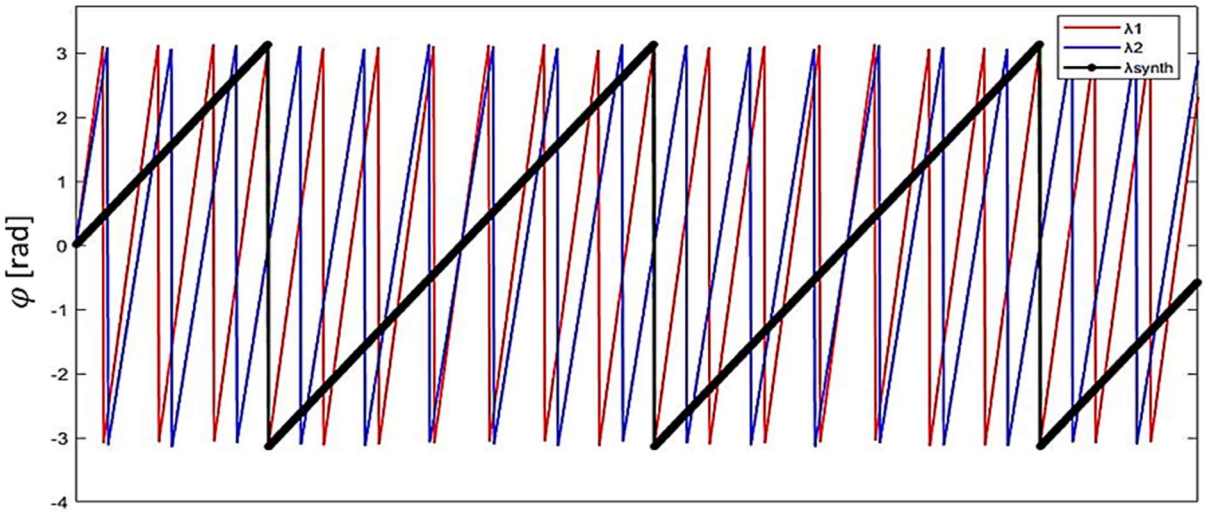

Fig.8.1. *Graphical representation of the difference of the measurement range covered by smaller (λ_1, λ_2) and larger (λ_{syn}) wavelength.*[153,157]

A requirement that must be fulfilled for such optical technique is that the optical path from all beams must be the same. This condition can create some difficulties in the building of the optical setup, and sometimes it can turn out to be expensive[158]. Hence, appropriate geometrical setup must be found in order to accommodate this condition.[157]

A disadvantage of this technique is that, despite ambiguity being solved (reduced), the range of unambiguous measurement can be extended at the cost of increasing noise by the factor of the ratio between the synthetic/equivalent wavelength and the shortest wavelength Λ_{eq}/λ_1, thus decreasing the sensitivity of the technique for the same factor. In length measurement, this is reflected as increase of uncertainty measurement.[148,155,157]

Another disadvantage could be the complexity of some unwrapping phase algorithms, reflecting in time consumption, thus making live observation of fast flow challenging. But in general, multiwavelength phase unwrapping is rather fast.

If $\xi(x,y)$ is the phase of the wave emitted from the laser and $\varphi(x,y)$ is the change in refractive index that the waves experience by passing through the phase object, then the superposition of waves leads to[29]:

$$E_{total1}(x,y) = e^{\frac{2\pi j}{\lambda_1}\xi(x,y)} + e^{\frac{2\pi j}{\lambda_1}\{\xi(x,y)+\varphi(x,y)\}} \tag{8.1}$$

$$E_{total2}(x,y) = e^{\frac{2\pi j}{\lambda_2}\xi(x,y)} + e^{\frac{2\pi j}{\lambda_2}\{\xi(x,y)+\varphi(x,y)\}} \tag{8.2}$$

The intensities are[29]:

$$I_1(x,y) = E_{total1}(x,y)\cdot E^*_{total1}(x,y) = 2 + e^{\frac{2\pi j}{\lambda_1}\varphi(x,y)} + e^{\frac{-2\pi j}{\lambda_1}\varphi(x,y)} \tag{8.3}$$

$$I_2(x,y) = E_{total2}(x,y)\cdot E^*_{total2}(x,y) = 2 + e^{\frac{2\pi j}{\lambda_2}\varphi(x,y)} + e^{\frac{-2\pi j}{\lambda_2}\varphi(x,y)} \tag{8.4}$$

The Moiré is defined as[29]:

$$\begin{aligned} I(x,y) = I_1(x,y)\cdot I_2(x,y) = 4 + 4\cos\left(\frac{2\pi}{\lambda_1}\varphi(x,y)\right) + 4\cos\left(\frac{2\pi}{\lambda_2}\varphi(x,y)\right) + \\ +2\cos\left(2\pi\varphi(x,y)\left(\frac{1}{\lambda_1}+\frac{1}{\lambda_2}\right)\right) + 2\cos\left(2\pi\varphi(x,y)\left(\frac{1}{\lambda_1}-\frac{1}{\lambda_2}\right)\right) \end{aligned} \tag{8.5}$$

This leads to the intensity being proportional to[29,157]:

$$I(x,y) \sim cos\left[2\pi\varphi(x,y)\left(\frac{1}{\lambda_1}-\frac{1}{\lambda_2}\right)\right] \tag{8.6}$$

, which is called the synthetic wavelength (or equivalent/beat wavelength)[29,157,159,160]:

$$\frac{1}{\Lambda_{eq}} = \frac{1}{\lambda_1} - \frac{1}{\lambda_2} = \frac{\lambda_2-\lambda_1}{\lambda_1\lambda_2} \Rightarrow \Lambda_{eq} = \frac{\lambda_1\lambda_2}{|\lambda_2-\lambda_1|} \tag{8.7}$$

For the case of multiple wavelength interferometry, the synthetic wavelength is defined as[29,150,157]:

$$\Lambda_{eq} = \frac{\lambda_1\lambda_n}{|\lambda_n-\lambda_1|} \tag{8.8}$$

, where n represents the number of lasers used and λ_n the wavelength of the laser for which the wavelength is the largest. The respective phase that the camera would see if such wavelength would have been employed is[159]:

$$\Phi_{eq} = \varphi_2 - \varphi_1 = \frac{2\pi L}{\Lambda_{eq}}\Delta n \tag{8.9}$$

In order for the technique to work, it is a must that both lasers are illuminating at the same time. Using both lasers projected from opposite sides will create a pair of interference fringe that are orthogonal with eachother (in the reference state). This will be reflected in the power spectrum by having a set pair of images. By making use of the off-axis configuration, the diffraction order of interests can be filtered out, as explained in *section-6.2*. From *eq.(8.7)*, it can be seen that the smaller the difference in the dominator, the larger the synthetic wavelength will be. This implies that, if the two lasers have a smaller difference in wavelengths, then the new range of unambiguous measurement will increase, thus the range of unambiguity and its extension are directly dependent to the set of wavelengths that are chosen.[149,153]

8.2. Unwrap

8.2.1. Introduction to unwrapping

Phase unwrapping has been extensively studied and adapted for many different applications. Different techniques that require phase unwrapping process are magnetic resonance[161], x-ray crystallography[162], synthetic aperture radar (SAR)[163] etc.[157]

There exist many different techniques to extract the phase distribution from the fringe pattern, such as phase-shifting profilometry, Fourier transform profilometry, windowed Fourier transform profilometry etc. Highest resolution and accuracy are provided through the first technique, phase-shifting profilometry[164]. Phase-shifting interferometry is not suitable for measuring dynamic phenomena because it requires at least three holograms to be recorded in order to solve the equations to retrieve the coefficients[33].[157]

Phase unwrapping process has some requirements when it comes to the noise and the discontinuity the phase might have. The easiest way is usually to use one of the 2π phase unwrapping algorithms, but in certain cases not the same algorithms are valid for different kinds of wrappings. Unwrapping algorithms usually are heavy computational wise and can be subject of failure where the object or phenomena under study has large irregularities.[157]

In the cases when the phenomena is restricted to a small confinement in the image, the edge of the image where no change has occurred can be chosen as the starting point for phase unwrapping, since interferometric measurement require at least one point where the phase change is known.[33,157]

The basic idea of phase unwrapping consists on dividing the phase image into horizontal line, which are then unwrapped pixel by pixel by adding or subtracting the offset ($2\pi\ radians$) when necessary. This is done separately for each of the lines. Once this is done, the same process happens, but vertically. At the end the phase image will be unwrapped in 2D[156].[157]

By having the difference of the two wrapped phase profiles created from both wavelengths, a new wrapped phase profile arises. This new phase profile ''belongs'' to a much greater wavelength, which we called previously as the synthetic wavelength. The synthetic wavelength is used to resolve the ambiguity by detecting the average phase shift (by calculating the fringe order) while using the lower laser wavelength to measure the temperature.[157]

Based on the dependence of the path, there are path dependent and path independent phase unwrapping techniques. In path dependent techniques, image processing is used to detect the edges and the phase ambiguities, and from that to calculate the offset that must be added or subtracted, while in path independent techniques the regions where error could be caused are eliminated before the phase unwrap process starts.[153,157]

Spatial phase unwrapping, from its name, uses the relationship between the phase information of the spatial neighboring pixels[165,166]. There exist different kinds of spatial unwrapping algorithms, notably the Goldstein's method, Flynns' method etc.[157]

Determining the fringe order from spatial neighboring pixels is not possible in the spatial phase unwrapping since it is based on the information that neighboring pixels have.[157]

The necessity of temporal phase unwrapping plays in when we need to unwrap a general phase map with large discontinuities. The fact that each pixel is unwrapped independently from its neighbor makes that any present noise in one of the pixels not to spread to other pixels during the process of unwrapping. There are also different kinds of temporal phase unwrapping algorithms, and the advantage of using temporal unwrapping stands from the fact that phenomena with large phase changes (in the case of profile measurements coming from high discontinuities) can be studied. The simplest one is the Gray-code temporal phase unwrapping. Other techniques, for example that use additional wrapped phase maps that differ from their fringe order to unwrap temporally the phase map, can be categorized into three groups: multiwavelength (heterodyne), multifrequency (hierarchical) and number-theoretical approach. A detailed review over these three techniques has been published, according to which, this group outperforms the Gray-code algorithm in accuracy, pattern efficiency and unambiguous range.[152,157]

The interference pattern on the CCD camera can also be expressed as[33,154,157]:

$$I(x,y) = A(x,y) + \sum_{l=1}^{2} B_i(x,y)\, cos\{\varphi_l(x,y) + 2\pi f_l x\} = \tag{8.10}$$

$$= A(x,y) + B_1(x,y)\, cos\{\varphi_1(x,y) + 2\pi f_1 x + 2\pi f_1 y\} + B_2(x,y)\, cos\{\varphi_2(x,y) + 2\pi f_2 x + 2\pi f_2 y\}$$

, where $A(x,y)$ is the background intensity and pattern brightness, $B(x,y)$ is the intensity modulation and f_1, f_2 are the carrier frequencies. The relation between the interference phase and the refractive index variation is given in *eq.(3.40)* by assuming no variation of the refractive index in the direction of propagation.

The basic idea of unwrapping consists of shifting back to its place each phase jump by adding or subtracting integer multiples of $2\pi\ radians$, in order to draw the phase as a continuous function (without the jumps, causing this characteristic sawtooth/triangle form of the phase) as given in *eq.(3.56)*, by retrieving as fast and accurately possible the fringe order term $N(x,y)$ for each of the pixels of the camera. We can make of use the extended range of unambiguous measurement from the synthetic wavelength and the accurate measurement of single wavelength phase that doesn't suffer from noise amplification to unwrap the original phase profile. There are several ways of how to do it and different technique corresponding to different applications. The most straightforward way of unwrapping is to make use of the synthetic phase profile in order to extract the average phase shift (fringe order). By making use of the average operator ⟨ ⟩ the procedure can be mathematically represented as[157,159]:

$$N = round\left(\frac{\langle \Phi_{eq} \frac{\Lambda_{eq}}{\lambda_2} \rangle - \langle \varphi_2 \rangle}{2\pi}\right) \tag{8.11}$$

Other unwrapping procedures are for example the hierarchical temporal phase unwrapping which uses one of the wavelength's phase map, usually the one with the shortest wavelength. It unwraps the phase map with the help of additional wrapped phase maps which have different fringe orders. Temporal processing is for relatively slowly developing phenomena.[157]

It is worth saying that, for any kind of phase unwrapping algorithm, if the process is successful, the final accuracy will be identical. The difference between hierarchical and multiwavelength unwrapping lays in

that that the first uses one of the wavelengths for the process of unwrap, while the later uses the synthetic wavelength to start the process of unwrapping.[157,160]

The information that was measured from both wavelengths is retrieved in the reconstructed phase field. Both phase information have different dimensions in the Fourier spectrum, thus they must be cropped and resized in order to be used for the obtention of the synthetic phase field. This means that the size of pixels in both fields must be the same. This is achieved by resizing one of the phase fields, using the equation below[157,159]:

$$\Delta\xi_2' = \frac{\lambda_1}{\lambda_2}\Delta\xi_2 \tag{8.12}$$

, where $\Delta\xi_2$ denotes the sampling interval before compensation. Linear interpolation between neighbouring pixel values is adopted to determine the value of the compensated pixel.[157]

8.2.2. Unwrapping for two-wavelength interferometry

When measuring profiles, the height of the profile is expressed as integer multiples of λ while the last part that is left is denoted as h'. The angle φ that corresponds to the height h' can be expressed as[155,167]:

$$h'(x,y) = \frac{\lambda}{2\pi} \cdot \varphi(x,y) \tag{8.13}$$

If the light passes through a medium where the refractive index changes, we obtain[167]:

$$h'(x,y) = \frac{\lambda}{2\pi\Delta n} \cdot \varphi(x,y) = \frac{\lambda}{2\pi(n-n_o)} \cdot \varphi(x,y) \tag{8.14}$$

The total height of the profile in terms of integers can be expressed as[167]:

$$h(x,y) = m(x,y) \cdot \lambda + \frac{\lambda}{2\pi(n-n_o)} \cdot \varphi(x,y) \tag{8.15}$$

, where $m(x,y)$ is the nonnegative multiple integer at (x,y) coordinate. When using both lasers, we can describe $h(x,y)$ as[167]:

$$h(x,y) = m_1(x,y) \cdot \lambda_1 + \frac{\lambda_1}{2\pi(n-n_o)} \cdot \varphi_1(x,y) \tag{8.16}$$

$$h(x,y) = m_2(x,y) \cdot \lambda_2 + \frac{\lambda_2}{2\pi(n-n_o)} \cdot \varphi_2(x,y) \tag{8.17}$$

Because $\lambda_1 \neq \lambda_2$, then λ_1 and λ_2 should "see" $h(x,y)$ by a different multiple integer, which leads having $m_1(x,y)$ and $m_2(x,y)$ in the equation above. We can express the equations as[167]:

$$\begin{cases} \dfrac{h(x,y)}{\lambda_1} = m_1(x,y) + \dfrac{1}{2\pi(n-n_o)} \cdot \varphi_1(x,y) \\ \dfrac{h(x,y)}{\lambda_2} = m_2(x,y) + \dfrac{1}{2\pi(n-n_o)} \cdot \varphi_2(x,y) \end{cases} \tag{8.18}$$

By subtracting the equations above, mathematically manipulating and arranging them, at the final stage the following is obtained[167]:

$$h(x,y) = \frac{\lambda_1\lambda_2}{\lambda_1 - \lambda_2}\left[\{m_1(x,y) - m_2(x,y)\} + \frac{1}{2\pi(n-n_o)}\{\varphi_1(x,y) - \varphi_2(x,y)\}\right] = \\ = \Lambda_{eq}\left[\Delta m(x,y) + \frac{1}{2\pi(n-n_o)}\Delta\varphi(x,y)\right] \tag{8.19}$$

Since $\lambda_2 > \lambda_1$, then logically it can be concluded that $m_1 \geq m_2$, thus $\Delta m(x,y) \geq 0$. Also, supposing that $h(x,y) \ll \Lambda_{eq}$, then[167]:

$$0 \leq \left[\Delta m(x,y) + \frac{1}{2\pi(n-n_o)}\Delta\varphi(x,y)\right] < 1 \tag{8.20}$$

Since $0 \leq \varphi_1(x,y) \leq 2\pi$ and $0 \leq \varphi_2(x,y) \leq 2\pi$, then the second term in the equation above results to be in the interval[167]:

$$-1 \leq \frac{1}{2\pi(n-n_o)}\Delta\varphi(x,y) \leq 1 \tag{8.21}$$

Depending on *eq.(8.20)*, then[167]:

$$\Delta m(x,y) = 0 \; or \; \Delta m(x,y) = 1 \tag{8.22}$$

Since $\Delta m(x,y)$ is nonnegative and is a small multiple integer, we can go further by saying the following[167]:

$$If \;\; \frac{1}{2\pi(n-n_o)}\Delta\varphi(x,y) < 0 \Rightarrow \;\; \Delta m(x,y) = 1 \tag{8.23}$$

, in order to keep the term in bracket in *eq.(8.19)* in the interval $[0,1)$.

$$If \;\; \frac{1}{2\pi(n-n_o)}\Delta\varphi(x,y) > 0 \Rightarrow \;\; \Delta m(x,y) = 0 \tag{8.24}$$

, for the same reason as previously.

As it can be seen, by taking the difference of the phase profiles of both lasers and adding a multiple integer to the additional factor 2π whenever the phase difference is negative, a new phase profile which corresponds to the synthetic wavelengths will be obtained and represents what the camera would have "seen" if such laser wavelength would have been used.

8.3. Study case: glass

8.3.1. Optical setup and method

In order to demonstrate the extended dynamic range of the measurement, two stacked coverslips (thickness defined by the manufacturer between $127 - 152[\mu m]$) were used as the measured object. It is obvious, that the thickness of the coverslips is much greater than wavelength of the light being used for measurements and thus cannot be measured by a single wavelength approach. Such object can simulate shock-waves causing large pressure changes in a small area while keeping handy manipulation during the development and testing stage. Wavelengths being used for the measurements are $\lambda_1 = 779.1\ [nm]$ and $\lambda_2 = 780[nm]$ yield in synthetic wavelength of $\Lambda_{eq} = 675[\mu m]$.[159]

The experimental lensless Fourier arrangement is introduced in Fig.8.2. Two fiber-coupled DFB (distributed feedback) laser diodes having different wavelengths are used as coherent light sources. When measuring high speed phenomena, the light can be chopped using acoustooptical modulators (AOM). Camera trigger (TRIG) controlled by an electronic unit (EL) and the AOMs are synchronized in order to avoid blurring of the interference pattern. Fibersplitters (FS1, FS2) split the light from the lasers into two beams called reference (RB1, RB2) and object beam (OB1, OB2). The ends of the reference beam fibers (ferrules) generate the spherical reference waves. The object beams from the two different lasers are combined in FS3 and illuminate a ground glass (DIF). Scattered light propagates through the measured area (MA) and impinges the sensor of a digital camera (CAM) where the reference and the object beams are superposed. Note angles between OB12 and RB1, RB2, respectively, introducing the required spatial-carrier frequencies in order to separate phase information from the two wavelengths. Superposition of reference and object waves yields in digital hologram, see Fig. 8.3.a).[159]

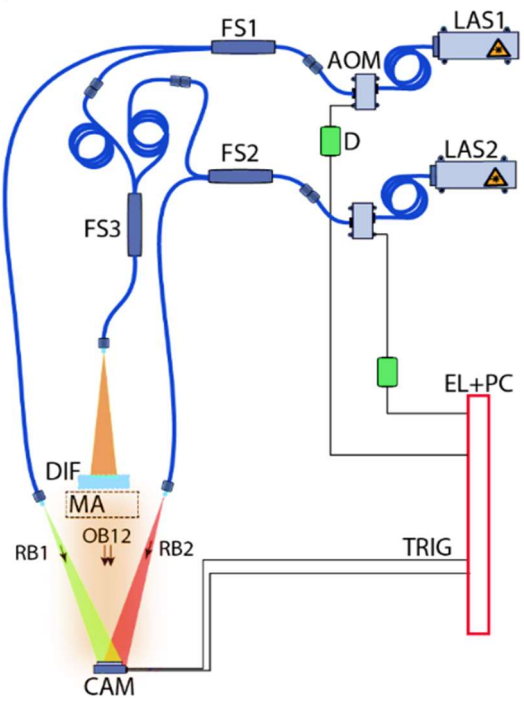

Fig.8.2. *The two-wavelength lensless measuring systems: DIF - diffuser, FS - fiber splitter, LAS - laser, AOM - acoustooptical modulator, D - driver, CAM - camera (synchronized with AOM), MA - measured area, EL+PC - electronics and computer.*[159]

The reconstructed phase field contains information measured by the two different wavelengths, see Fig.8.3.b). The two different phase fields can be cropped and processed separately. However, for correct phase difference calculations by *eq.(8.9)* it is required that the reconstructed fields U_1, U_1 are superposed i.e. $\Delta x_1 = \Delta x_2$ and $\Delta y_1 = \Delta y_2$. From *eq.(3.35)* and *eq.(3.36)* it follows that the pixel size Δx_2 and Δy_2 of the reconstructed fields in image plane do not agree with Δx_1, Δy_1 due to $\lambda_1 \neq \lambda_2$. To equalize Δx (same holds for Δy) at the both wavelengths, one of the parameters in *eq.(3.35)* or *eq.(3.36)* has to be changed. The method used in our measurement changes the pixel size $\Delta\xi_2$ (sampling interval) of the digital hologram H_2. Using *eq.(3.35)* and *eq.(3.36)*, the compensated sampling interval $\Delta\xi_2'$ can be written as in *eq.(8.12)*. Base on the compensation, the pixel value (intensity) of the hologram H_2 should be changed. Linear interpolation between neighbor pixel values is adopted to determine the value of the compensated pixel.[159]

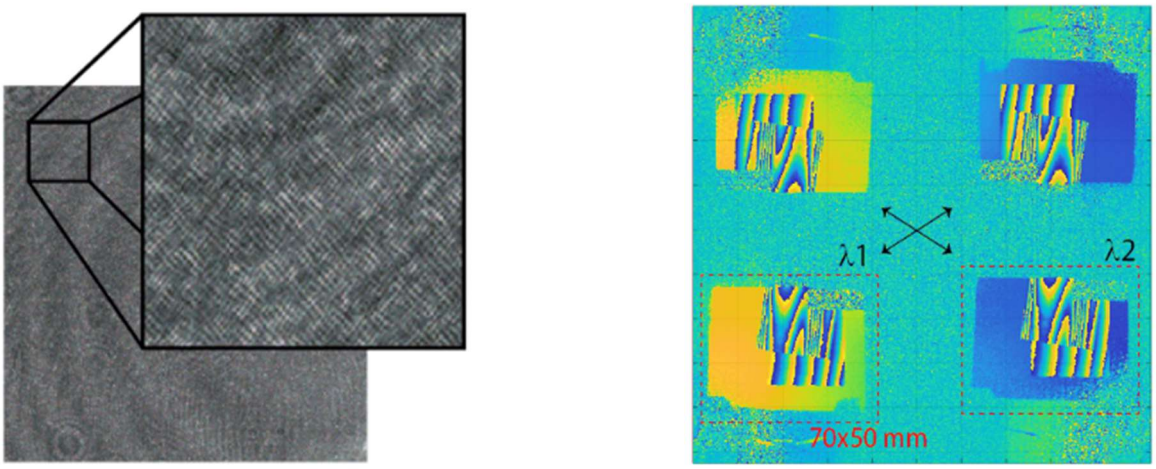

a) b)

Fig.8.3. *a) Digital hologram and b) reconstructed phase map.*[159]

Naturally, as the noise in the phase field is directly proportional to the wavelength, the synthetic phase map suffers much more with noise than the phase field computed from single wavelength measurement[33]. Several procedures can be used to refine the synthetic phase map in order to gain advantage from the both approaches: large measurement unambiguity of synthetic phase and accurate measurement of single wavelength phase. The easiest and most straightforward procedure is to use the synthetic phase to detect the average phase shift (in terms of fringe order N) across the field of view by *eq.(8.11).*[159]

The unwrapped phase φ_2 providing relative information can be adjusted in order to have absolute measurement (within $\Lambda_{eq}/2$) by[159]:

$$\varphi_2{}^{ABS} = \varphi_2 + 2\pi N \tag{8.25}$$

There are also other procedures, which can be used for the combination of the synthetic and the single wavelength phase maps[102,168].[159]

8.3.2. Results

The captured digital hologram was reconstructed using[159]:

$$\Gamma(x_D, y_D) = F^{-1}\{h(x,y)E_R{}^*(x,y)\} \tag{8.26}$$

and the reconstructed phase fields φ_1, φ_2 within one frame are shown in Fig. 8.3.b). In the next step, only the phase field corresponding to first wavelength was cropped, see Fig.8.4.a). The same digital hologram was then treated using *eq.(8.12)* and reconstructed using *eq.(8.26)* in order to get the same pixel extension for the second wavelength phase field, see Fig.8.4.b). The two phase fields were aligned using image registration and the synthetic phase was computed using *eq.(8.9)*, see Fig.8.4.c). As the synthetic wavelength is sufficiently large, three significant layers corresponding to "free space" w/o coverslip, one coverslip layer and two coverslips layers are recognizable. Reversely, measured values of the synthetic phase can be used to calculate the coverslips thickness. The synthetic phase change between layer 0 and layer 1 is $\phi_{01} = 1.85[rad]$, while the difference between layer 2 and layer 1 is $\phi_{01} = 1.91[rad]$, see Fig.8.4.c). Assuming refractive index of the coverslip glass to be 1.5 and using *eq.(*8.9), the computed (measured) thicknesses are $L_{01} = 133[\mu m]$ and $L_{12} = 137[\mu m]$, and thus in the manufacturer tolerances. This experiment was not to demonstrate thickness measurement but to verify the extended range of the method so even large phase jump can be detected and measured.[159]

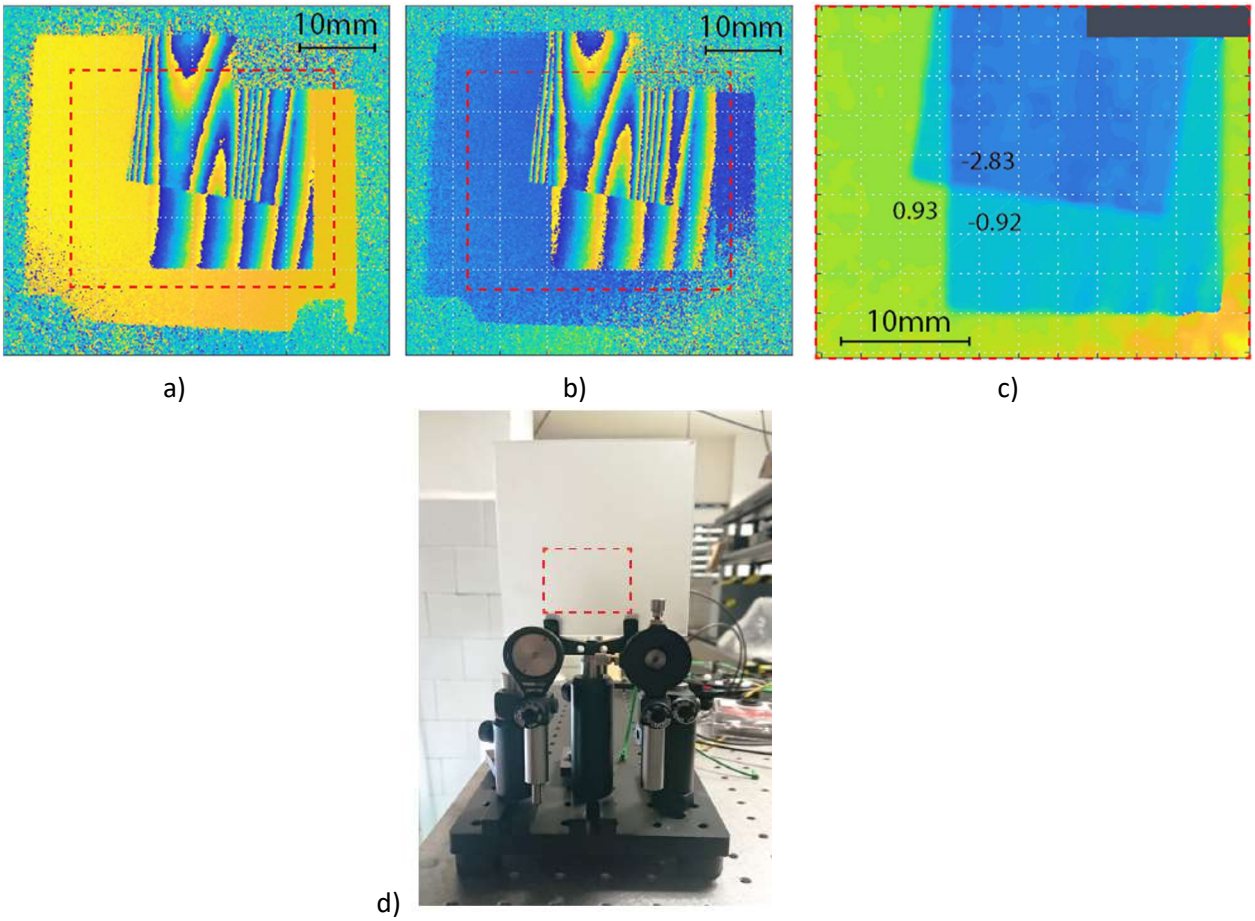

Fig.8.4. *a) Phase map of two stacked coverslips measured at λ_1, b) phase map of two stacked coverslips measured at λ_2, c) synthetic phase and average values within 100 squared pixels from different layers and d) measured area as seen from camera direction including the red rectangle defining the region of interest.*[159]

8.4. Study case: nozzle

8.4.1. Optical setup

In the next step, using the same optical setup as in *section-8.3.*, we measured the surroundings of a nozzle (diameter $0.25[mm]$), denoted as the black rectangle in Fig.8.5. when blowing with compressed *1,3,3,3-Tetrafluoropropene* using wavelengths $\lambda_1 = 779.1[nm]$ and $\lambda_2 = 852[nm]$. Such wavelengths yield a synthetic wavelength of $\Lambda_{eq} \approx 9[\mu m]$. Results from the single wavelengths are shown in Fig. 8.5.a)-b) while the synthetic phase is in Fig. 8.5.c). For such small phase gradients, single wavelength measurements together with the spatial unwrapping in *eq.(8.26)* would be sufficient, however, the aim of this experiment was to demonstrate the ability of the technique to measure fast phenomena occurring in fluid mechanics and therefore the following analysis is rather illustrative.[159]

8.4.2. Results

Assuming measured phase value $\varphi = 1.8\ [rad]$ within the position denoted by the red circle in Fig.8.5.c), thickness of the air jet layer $L = 5[mm]$ and the synthetic wavelength $\Lambda_{eq} \approx 9[\mu m]$, the refractive index change can be calculated using *eq.(3.40),* yelding a value of $\Delta n = 5 \times 10^{-4}$. It is important to note that we assumed the refractive index distribution to be a two dimensional field which brings some error in the calculations. The refractive index is related to pressure P and temperature T using the Gladstone-Dale equation as in *eq.(3.42)* and assuming the ideal gas equation.[159]

In our measurement, the temperature change ΔT as well as pressure change ΔP due to the air flow took place and thus the measured refractive index change refers to equation[159]:

$$\Delta n = \frac{kM}{RT}\Delta P - \frac{kMP}{RT^2}\Delta T \tag{8.27}$$

The temperature change can be estimated to be $\Delta T \approx 10[K]$, and using *eq.(8.27)*, $\Delta P = 17[kPa]$.[159]

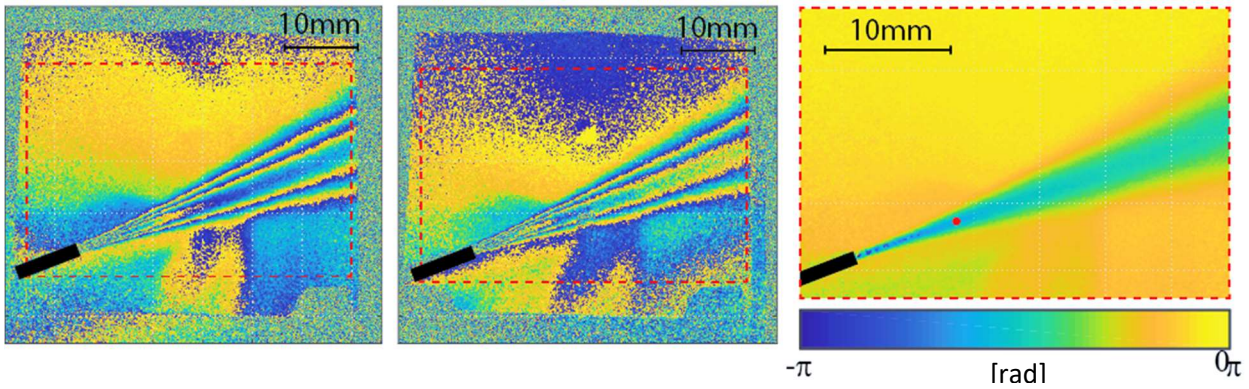

Fig.8.5. *a) Phase map of two stacked coverslips measured at λ_1, b) phase map of two stacked coverslips measured at λ_2, c) synthetic phase and average values within 100 squared pixels from different layers, d) phase map of nozzle air flow measured at λ_1, e) phase map of nozzle air flow measured at λ_2, f) synthetic phase of the nozzle air flow and g) measured area as seen from camera direction including the red rectangle defining the region of interest.*[159]

8.5. Study case: resistor

8.5.1. Optical setup

The phase object under study is the temperature field generated by a resistor. By being connected to a voltage supply, the resistor will release heat, which will be measured and mapped using both lasers simultaneously.

Two lasers of wavelengths $\lambda_1 = 773[nm]$ and $\lambda_2 = 780[nm]$ were employed for the measurement. This gives rise to a synthetic wavelength of $\Lambda_{eq} = 86134.28[nm]$.[157]

Fig.8.6. represents the experimental lensless Fourier optical setup used to conduct this experiment. Two fiber-coupled DFB (distributed feedback) laser diodes having different wavelengths are used. Light is split into the reference (RB1, RB2) and object beams (OB1, OB2) by means of fibersplitters. The object beams are combined and are collimated by a lens to then fall onto the diffuser. Scattered light from the diffuser passes through the measured area (MA) to combine with reference beams and be recorded by the camera (CAM). Both reference beams form angles with respect to the axis of propagation. It is these angles that introduce the spatial-carrier frequencies that make it possible to separate phase information.[157]

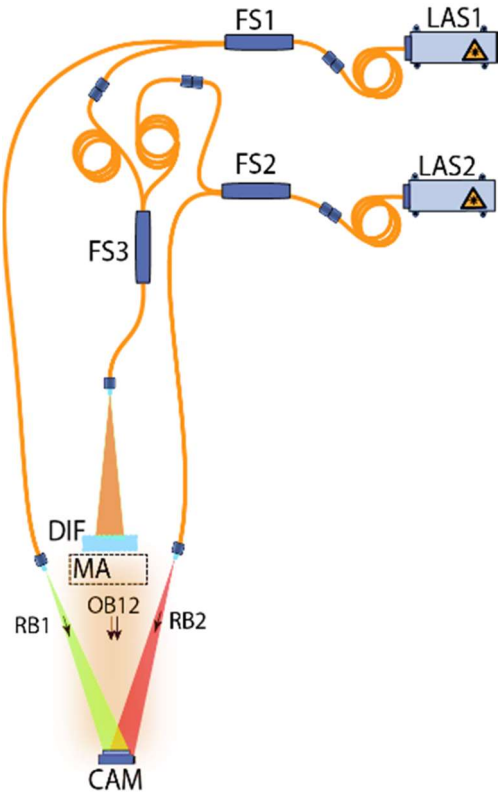

Fig.8.6. *The two-wavelength lensless measuring system: LAS-laser, FS-fiber splitter, DIF-diffuser, MA-measured area, OB-object of investigation, RB-reference beam, CAM-camera.*[157]

8.5.2. Results

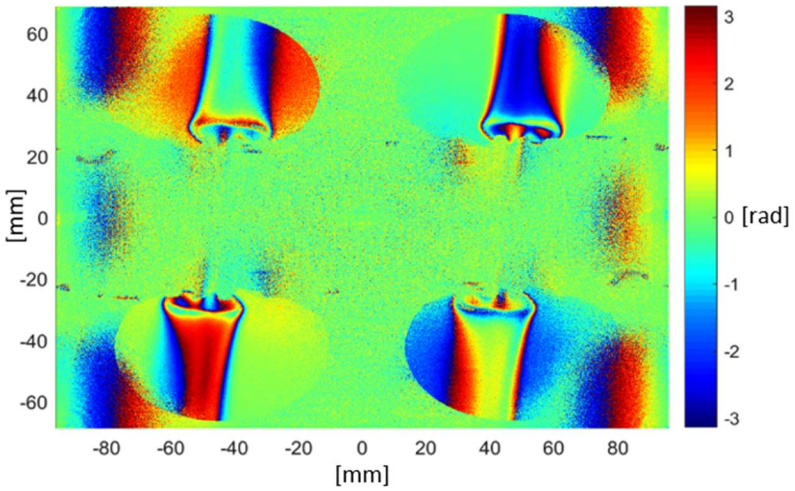

Fig.8.7. *Reconstructed phase field map at some time instant.*[157]

Fig.8.7. represents the reconstructed phase field map recorded by the CCD camera at some time instant. Each recorded phase field is represented in a conjugated pair. The introduction of spatial-carriers through the introduction of the angle between each of the reference wave and the axis of propagation has introduced enough separation so that the set of conjugated phase pairs don't overlap and can be filtered out confidently (i.e. off-axis arrangement). Any of the identical but conjugated pair carries the same valuable phase information used for further analysis. Any sudden change of the color red-blue indicates a 2π jump.[157]

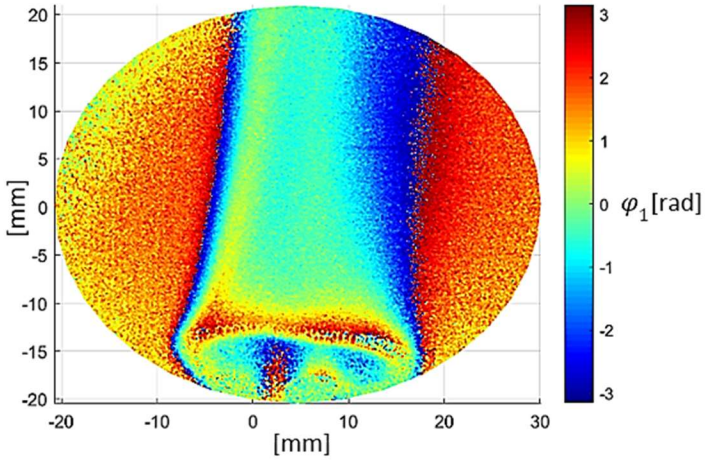

a)

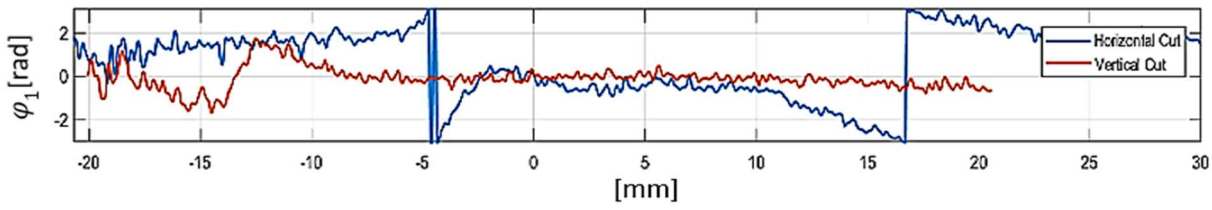

b)

Fig.8.8. *a) Reconstructed phase field map at some time instant from λ_1 and b) plot of the phase profile run across the phase field horizontally and vertically through the origin axis*.[157]

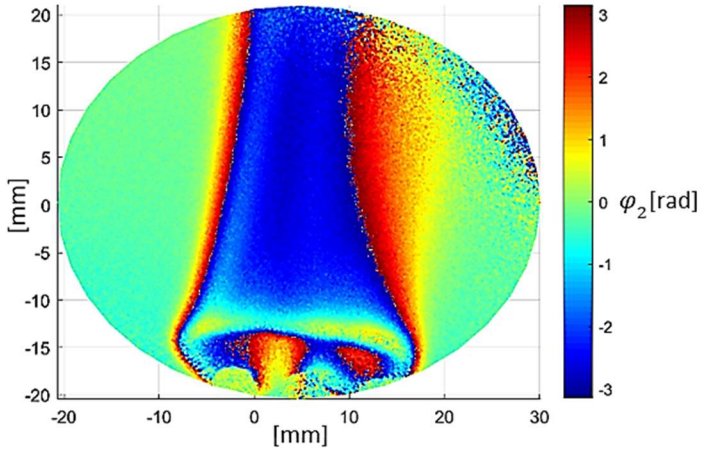

a)

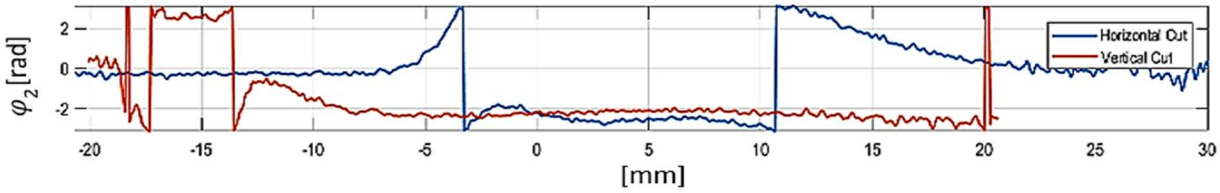

b)

Fig.8.9. *a) Reconstructed phase field map at some time instant from λ_2 and b) plot of the phase profile run across the phase field horizontally and vertically through the origin axis.*[157]

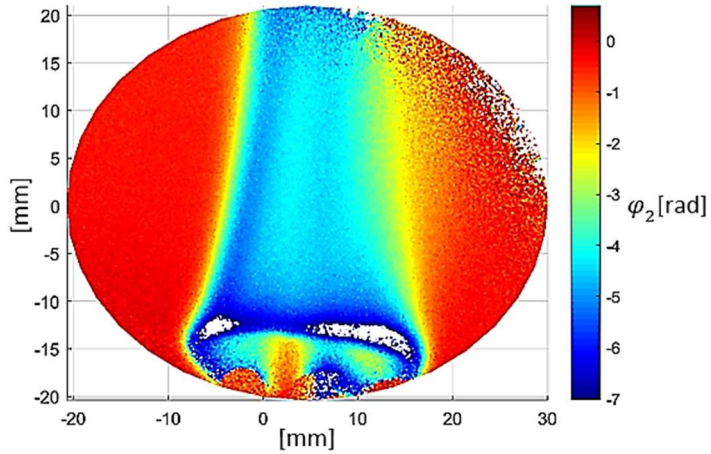

a)

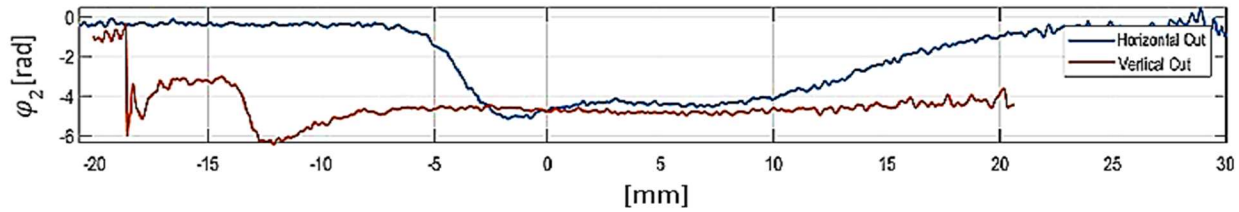

b)

Fig.8.10. *a) Corrected phase field map at some time instant from λ_2 and b) plot of the phase profile run across the phase field horizontally and vertically through the origin axis.*[157]

Fig.8.8. and Fig.8.9. represent the reconstructed phase field map for each of the wavelengths. The background is masked out and only the physical field of view is shown. For different wavelengths, the camera "sees" different phase values, thus making the profile look different as what is seen from the other wavelength. The phase profile was plotted for both phase field maps, passing by the origin axis for both horizontal and vertical profiles. Clear phase jumps can be seen in the horizontal cut of Fig.8.8. as indicated in Fig.8.8.b), while the phase profile across the vertical cut of the phase field is smoother and no noticeable jump can be observed.[157]

Fig.8.10. represents the corrected phase map coming from λ_2 based on *eq.(3.56)*. The phase field that had 2π jumps is now corrected and represents visually a continuous phase map.[157]

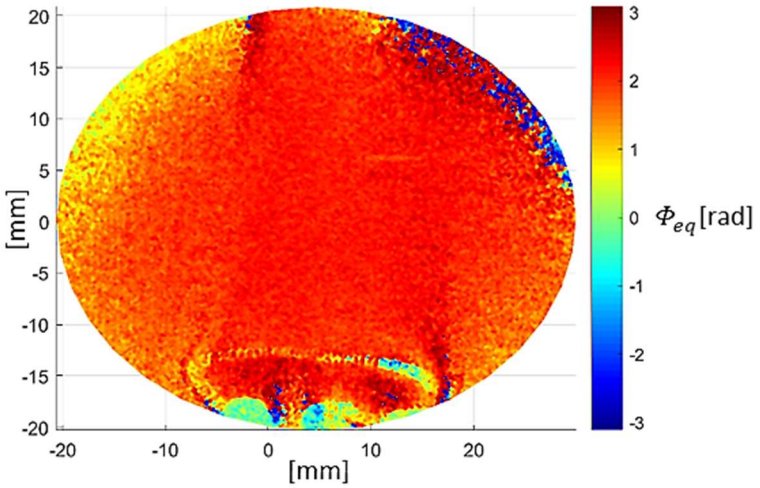

a)

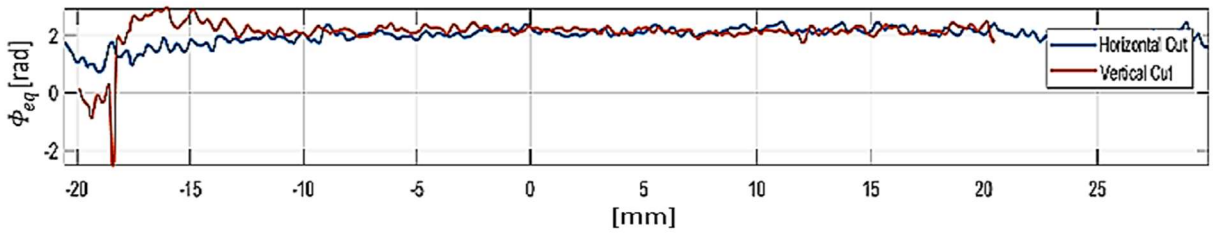

b)

Fig.8.11. *a) Synthetic phase field map at some time instant and b) phase profile run across the phase field.*[157]

Fig.8.11. represents the fictional synthetic phase map which the CCD camera would have "seen" if a laser with wavelength Λ_{eq} would have been used. In our case, since the heat gradient wasn't high, the synthetic phase map manifests itself with relatively smooth flat profile. It is worth noting that even the synthetic phase map can present phase jumps if the range of measurement is exceeded. The synthetic phase map however obscures phenomena that cause relatively small phase changes.[157]

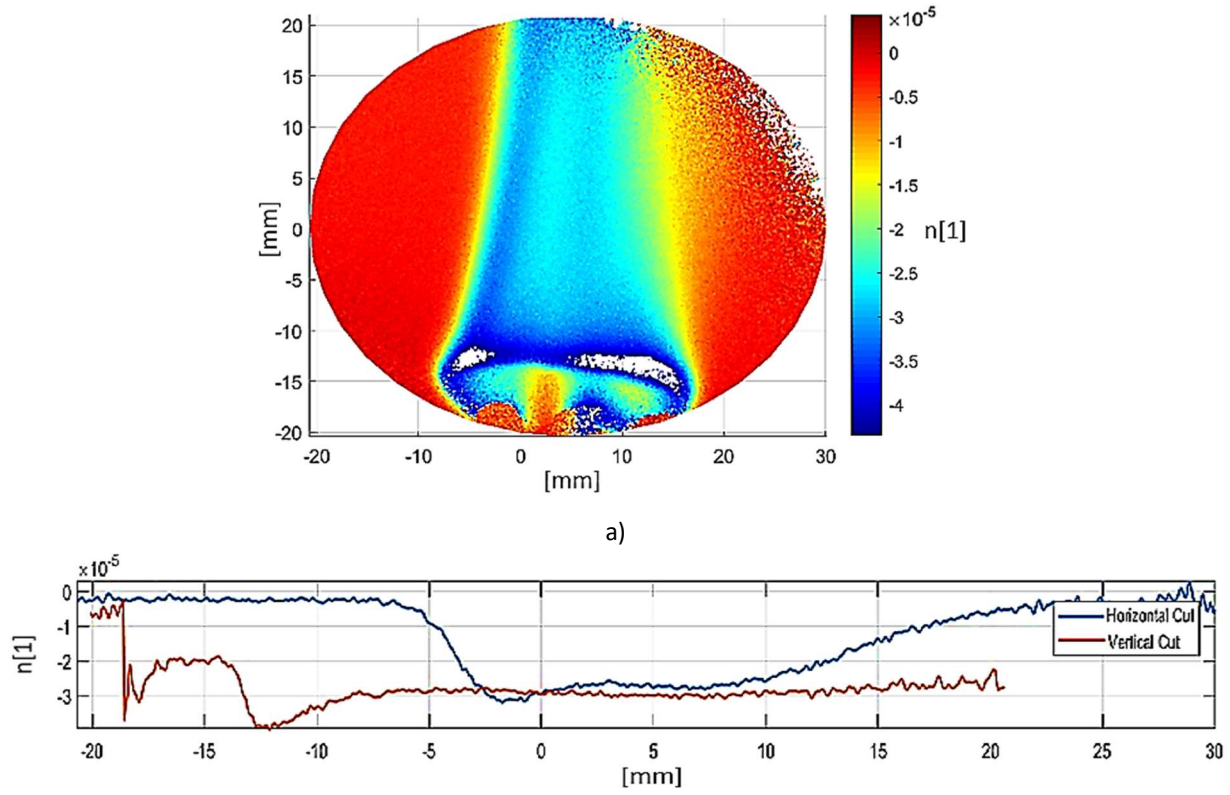

Fig.8.12. *a) Refractive index field map at some time instant and b) refractive index profile run across the field.*[157]

Through the phase field map of either λ_1 or λ_2, the refrative index distribution can be obtained via *eq.(3.40)* assuming a 2D distribution field of the refractive index. A distribution of the refractive index at some instant is shown in Fig.8.12. Notice that digital holographic interferometry is able to detect very small changes in the refractive index cause by external influence (in this case heat gradient).[157]

Through the determination of the refractive index, many other important parameters such as the temperature, density, fluid velocity etc. can be determined. This allows for the study of fluid and gases and phenomena related to. An interesting application of such technique could prove useful for the study of shockwaves around blade cascade in wind tunnels. Flow in wind tunnels are supersonic and demonstrate high levels of pressure and velocities. Such high gradients cause many fold wrapping of the phase. The use of a two-wavelength technique could therefore help in studying e.g. dynamic events during transonic and supersonic blade flutter.[157]

Fig.8.13. represents the temperature change field calculated by making use of λ_2. It was calculated using the following mathematical relation[157]:

$$\Delta T(x,y) = \frac{\lambda_2 \cdot \varphi_2(x,y)}{2\pi L \frac{dn}{dT}} \tag{8.28}$$

, where $L = 20[mm]$ is the estimated object length and $\frac{dn}{dT}$ as in *eq.(3.55)*. But, this temperature was measured as a reference to the starting temperature T_0. Thus, the absolute temperature can be calculated from *eq.(6.14)*, where $T_0 = 20[℃]$ in our case.[157]

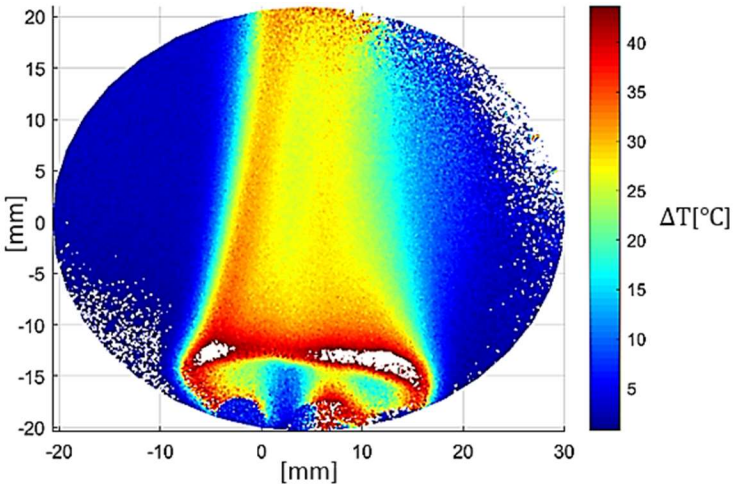

a)

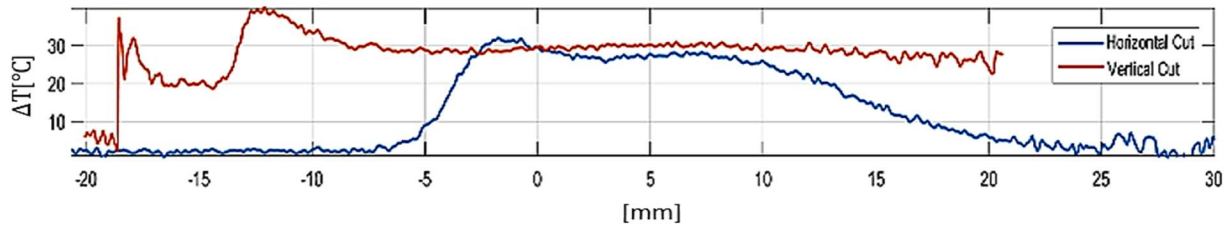

b)

Fig.8.13. *a) Reconstructed temperature field map* $\Delta T(x, y)$ *at some time instant and b) temperature profile run across the field.*[157]

8.6. Conclusions

This chapter introduces a new approach to measure dynamic processes in fluid mechanics using lensless Fourier digital holographic interferometry with extended dynamic range. A key factor is the use of two wavelengths and the recording of digital holograms from both wavelengths in one shot.[157,159]

We showed that the spectral separation of the phase information from both wavelengths can be achieved when the hardware of the experimental arrangement (angles of the reference waves) is properly adjusted[33]. The difference between the measured phase fields yields in a synthetic phase that has significantly larger dynamic range of measurement[169]. Such range covers large changes of the measured quantity as it was demonstrated in our three experiments (glass, nozzle and resistor).[157,159]

However, the synthetic phase is more influenced by noise. By combining the synthetic phase and the phase obtained from the single wavelength, we can achieve the same accuracy as single wavelength technique but with a significantly higher range of measurement. This method is applicable to dynamic processes in fluid mechanics, which was verified by measuring the air flow from the nozzle.[157,159]

The influence of the ratio of chosen laser wavelengths and aberrations haven't been taken in account here.

9. Digital holographic interferometry for the measurement of symmetrical temperature fields in liquids

Previous study cases dealt with 2D temperature field in fluids and gases. The problem of ambiguity has been treated and resolved in the previous chapter. However, in many real cases we deal with temperature fields that are complex and can't be treated as having a 2D distribution of the refractive index. Those cases, having symmetrical refractive index distribution or not, require the use of a tomographic approach in order to be evaluated and visualized. They can be found in many real applications in fluid mechanics and other disciplines. Fortunately, many applications exhibit a symmetrical profile.

This chapter aims at investigating temperature fields that are symmetrical, more specifically the case of a pulsatile jet with water as its working fluid.

9.1. Introduction

The amplitude of the propagating object wave through the transparent media is not significantly affected, while the phase of an optical wave is[34]. Digital holographic interferometry is sensitive to the optical phase change and thus can be advantageously used for investigation of this kind of problem. However, as the optical phase is integrated along the optical path, the calculation of the quantity under investigation must be performed with regard to the nature of the physical field that we measure. Three categories of physical fields can be considered[170]:

1. Two-dimensional temperature field (temperature varies only in one direction);
2. Symmetrical temperature field (temperature is a function of radius only);
3. Asymmetrical temperature field (general temperature distribution);

Two-dimensional[34,86,92,171,172] and purely symmetrical[74,173,174] fields can be measured by one arm interferometer, only the data processing differs for each category.[170]

Examination of asymmetric fields[103,175,176] could not be generally done without the use of cumbersome tomographic approach. The tomographic approach requires a large number of different projections of the measured field. It is either necessary to use many interferometer arms and many digital sensors in the measurement setup to obtain digital holograms for different viewing directions or the problem could be solved having only one digital sensor and a rotating stage. Rotation of the object is applicable only for steady or periodical coherent (self-similar in each cycle) phenomenon. Very often the tomographic approach cannot be realized due to the mentioned physical limits or technical issues as rotating of the object (particularly for heavy system in liquids) or building multiple-arm interferometer might be very challenging. However, in practice, we often encounter quasi-symmetric fields. Pulsatile jets (PJ) with symmetrical openings are a good example. Such a stream of fluid is represented by the time-mean, periodic (symmetrical) and fluctuating random part, of which the periodic part is of the main interest. Moreover, so far, little effort has been made into the pulsatile jets (PJ) study in liquids, which is more challenging than PJ investigation in gases. Some other phenomena in fluids using DHI have been investigated[20,42,77]. In this chapter, we present a single-shot DHI technique suitable for the investigation of quasi-symmetric PJ in fluids, including uncertainty analysis.[170]

9.2. Pulsatile jets

In fluid dynamics, a jet is defined as a stream of fluid that is projected through an opening under pressure into a surrounding medium[177].

When a fluid flows out of the free openings or other outlets into free space, a free jet forms. Based on viscosity, the particles from the surroundings are entrained into the main stream. By absorbing a portion of the jet's power, the particles play a role in slowing it. With distance, the velocity of the fluid decreases and the jet expands[178].[170]

A pulsatile jet in the other hand, is a fluid jet generated from fluid oscillations during a periodical fluid exchange between an actuator cavity and surrounding fluid[179]. Pulsatile jets have a zero-net-mass-flux. This is due to the fact that pulsatile jets suck in the working fluid from the environment and eject it at the end. On the other hand, they allow momentum transfer to the flow. This comes from the asymmetry of the flow conditions across the orifice. By generating vortices in some operational conditions, flow dynamics of the external flow far from the orifice can be affected. Pulsatile jets are inherently pulsatile and periodic, and they can be produced in a number of ways through the use of piezoelectric, electromagnetic (e.g., solenoids), acoustic (e.g., speakers), or mechanical (piston) drivers[180,181].[170]

A meaningful advantage of PJs is a relative simplicity of an arrangement: neither blower nor fluid supply piping is required, and only a small electrical power input is needed. This makes jets efficient and attractive [179–181]. Applications of pulsatile jets are numerous: improved fluid mixing and higher heat transfer coefficients have been demonstrated in electronic cooling applications using pulsatile jets[182], applications in flow control in external aerodynamics[183], in supersonic aircraft[184], drag reduction improvement in space aircraft[185], for cooling[186,187], etc. A typical PJ actuator consists of a cavity with an oscillating wall (diaphragm or piston) as shown in Fig.9.1. Mechanical energy is transferred from a transducer via oscillating wall to the fluid. The transducer can be arranged either separately from the actuator or it can be integrated into the cavity[179].[170]

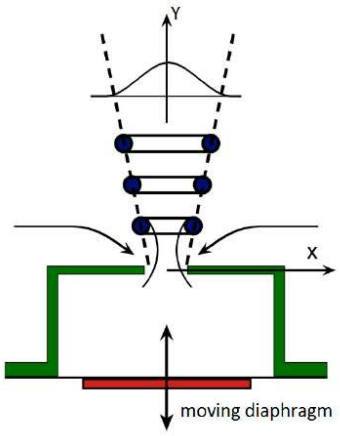

Fig.9.1. *Schematic of a pulsatile jet.*[188]

The jet profile after ejections consists of mainly three regions[189]:

- The initial region;
- The transition region;
- The region of the fully developed jet.

9.3. Theoretical tool

For axially symmetric distribution of the refractive index, the relation between the refractive index and the phase can be estimated by making use of *eq.(3.44)*. The link between the temporal change of temperature ΔT and the phase change $\Delta\varphi$ is given by *eq. (3.45)*. The temperature can finally be computed by *eq.(6.14).* The hologram is recorded by a camera and the reconstruction is done by numerical methods as in *section-3.4*.The maximum angle θ_{max} between the two interfering waves is expressed as[170]:

$$\theta_{max} = 2arcsin\left(\frac{\lambda}{4\Delta\xi}\right) \approx \frac{\lambda}{2\Delta\xi} \tag{9.1}$$

, while the maximum frequency is limited by the Nyquist frequency υ_N, which is defined by the digital sensor pixel extension $\Delta\xi$ as $\upsilon_N = 1/2\Delta\xi$. By limiting the value of spatial-carrier frequencies, we limit the angle between the two interfering waves, thus influencing the distance and size the object must have in regard to the detector. All this makes it possible to directly access the needed information without having to obtain multiple holograms. This makes this technique suitable for rapid developing phenomena.

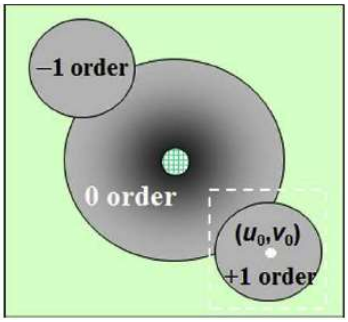

Fig.9.2. *Example of a structure of a diffracted field with off-axis digital holography.*[190]

The complex field $c(x, y)$ in *eq.(6.5)* represents an optical field at a certain initial plane. In the case of lensless DHI, the optical field c is associated to the object plane while for image plane DH (using lens to image the object), $c(x, y)$ stands for the image plane. Using diffraction theory, one can propagate optical fields from object to image plane (lensless DHI) or focus around the image plane (image plane DHI). Diffraction theory describes the propagation of optical fields and allows for the numerical reconstruction of images which are each described by its intensity and phase. Complex optical fields in the image plane U_i are calculated using the Sommerfeld formula, which describes the diffraction of light at distance d from the initial plane. The Sommerfeld integral can be solved by Fresnel approximation which in the discrete finite form is expressed as[29,170]:

$$U_i(n\Delta x, m\Delta y) = \frac{e^{-j\frac{2\pi}{\lambda}d}}{\lambda d}\sum_{k=1}^{N}\sum_{l=1}^{M} c(k\Delta\xi, l\Delta\eta)\cdot r^*(k\Delta\xi, l\Delta\eta) \cdot e^{j\frac{\pi}{\lambda d}[(k\Delta\xi)^2+(l\Delta\eta)^2]}\, e^{-j2\pi\left(\frac{kn}{N}+\frac{lm}{M}\right)} \tag{9.2}$$

, where $j = \sqrt{-1}$, $n = 1, \dots, N$ and $m = 1, \dots, M$ represents the pixels of the camera, and d is the distance of the phase object from the sensor of the camera. The stored holograms have $N \times M$ discrete values, with pixel distances $\Delta\xi$ and $\Delta\eta$, with physical size of the recording area of the camera to be $N\Delta\xi \times M\Delta\eta$. r^* represents the conjugated of discrete numerical reference wave, which is used for the reconstruction of the sharp real image at distance d.

9.4. Tomographic reconstruction

Tomography is generally a non-invasive imaging technique. It allows for visualization of internal structures without the superposition of over- and under-lying structures[172]. As said previously, the refractive index distribution can be generally classified into three groups in regard of its distribution: flat, symmetrical and asymmetrical. The first two represent the simplest case and the easiest to reconstruct the temperature fields.[170]

Tomography in general involves two steps: the recording of the projection data and the reconstruction of the original data that was projected. Projections from many angles in order to be able to faithfully reconstruct the real temperature field are required. The more projections there are, the more exact and reliable the reconstruction will be. This undoubtedly makes the setup more complex and the need of a superfast camera is a must. The recording is done by digital cameras and the captured images represent the projection of the 3D object into 2D images. Although for the case of periodically self-similar repetitive phenomena, only one superfast camera can be used, by changing the angle of recording for each period of the phenomena (by a rotating stage) and synchronizing the recording with the period of repetition. Noise and errors are suppressed by averaging the images with the same phase in different periods.[170]

Naming z the direction of propagation through the water tank, and since the phase is the variable of interest, from the interference pattern we can define the Radon Transform in general in its polar mathematical form by[191,192]:

$$g(s,\theta) = \int_{-\infty}^{+\infty} \int_{-\infty}^{+\infty} f(x,y)\delta(xcos\theta + ysin\theta - s)dxdy \tag{9.3}$$

where s is the shift distance from the origin of the coordinate system, θ the angle of projection, δ the Dirac pulse and $f(x,y)$ represents the temperature distribution, which in our case is actually the distribution of the refractive index difference, since temperature values are dependent on it. Thus, the previous integral can be rewritten as:

$$\Delta\varphi(s,\theta) = \frac{2\pi}{\lambda} \int_{-\infty}^{+\infty} \int_{0}^{2\pi} \Delta n(x,y)\delta(xcos\theta + ysin\theta - s)dxdy \tag{9.4}$$

The Radon Transform is a linear operator. The representation of the data obtained by Radon Transform as a function of the angle of projection is called a sinogram. It contains the data from the projection for different angles stored as columns. The name comes from the fact that, since each object can be mathematically described as a linear combination of infinite delta functions δ, the projection will be the sum of sine waves, giving the special characteristic shape, hence the name sinogram. Since we deal with the case of a symmetrical phase distribution, data on all columns will be similar.[191,192]

The *Fourier slice theorem* states that taking the Fourier transform of a projected function into a line is the same as taking a parallel slice in the form of a line passing through the 2D Fourier Transform of that same function. So, by measuring a single projection, a single line passing through the center of the 2D Fourier Transform is filled. By doing this for all angles, the whole Fourier representation of that object can be reconstructed. This theorem comes in hand in data processing when dealing with tomographic reconstruction.[191,192]

The passing from the projection domain which contains the projection data from all direction on one axis and the pixel coordinate on the other, into the volume domain which represents the real scanned object, is called the back-projection. Because the Fourier Transform will sample more frequently low frequencies in the center and less higher frequencies at the periphery of the domain, it will lead in a blurred reconstructed object. The solution to this problem is to apply a filter to suppress some range of frequencies and a window in order to prevent possible numerical Fourier Transform issues. By applying a filter, we obtain what is known as the filtered back-projection.[191,192]

The inverse Radon Transform is in general expressed as[191,192]:

$$f(x,y) = \int_0^{\pi} \int_{-\infty}^{\infty} g(s,\theta) \cdot b(xcos\theta + ysin\theta - s) ds\, d\theta \tag{9.5}$$

, where b represents a filter and a window. It expresses the filtered back-projected image for all angles which are smeared out in space. The filtered back-projection is an analytical method that propagates the sinograms into space for all angles along specific projection paths in order to reconstruct the 3D profile. For our case, we can rewrite the inverse Radon Transform as:

$$\Delta n(x,y) = \frac{\lambda}{2\pi} \int_0^{\pi} \int_{-\infty}^{\infty} \Delta\varphi(s,\theta) \cdot b(xcos\theta + ysin\theta - s) ds d\theta \tag{9.6}$$

The Abel Transform is a specific case of the Radon Transform, with symmetrical distribution of the refractive index.

Overall, the filtered back-projection includes the following steps[191,192]:

- Computing the 1D Fourier Transform of each projection;
- Multiplying each Fourier Transform by a filtering function;
- Evaluating the inverse Fourier Transform;
- Integrate results from all angles to reconstruct the phase distribution.

9.5. Optical setup and method

Fig.9.3. shows a schematic of the holographic setup that was implemented for this study. The setup consists of two portable parts, made for easier transportation and a more compact setup. It is based on the Mach-Zehnder interferometer, which gives as output the interference pattern that is dependent on the refractive index change occurring in the phase object (OBJ). A Mach-Zehnder interferometer consists of two interferometric arms, the object arm and the reference arm. After passing through a fibre-beamsplitter (FS), the laser beam is split into two. The first beam acts as the object wave that passes through the phase object under investigation, while the other beam acts as the reference wave. The object beam is collimated into a parallel beam by a collimator (L) before passing through the water tank containing the pulsatile jet. Before impinging the camera, the object wave passes through lenses L1 and L2, which act as a 0.12X beam expander in order to reduce the beam diameter to fit the digital sensor size. Both waves are recombined and superimposed by a non-polarizing beamsplitter (NBS), collimated by a lens (L2) and redirected to the digital camera (CAM) where the microinterference pattern is

electronically recorded for further processing. The reference wave was aligned with the object wave by positioning of the fiber output aiming to NBS. The angle between both waves was set by analyzing the Fourier spectrum in real time. The adjustment of both waves intensities has been made for the highest fringe contrast value possible. A highly coherent helium-neon laser (LAS) of wavelength $\lambda = 633[\mathrm{nm}]$ with maximal output optical power of $50[mW]$ has been employed for this study. Since holographic interferometry is very sensitive, the optical setup has been put on a vibration-isolated optical table.[170]

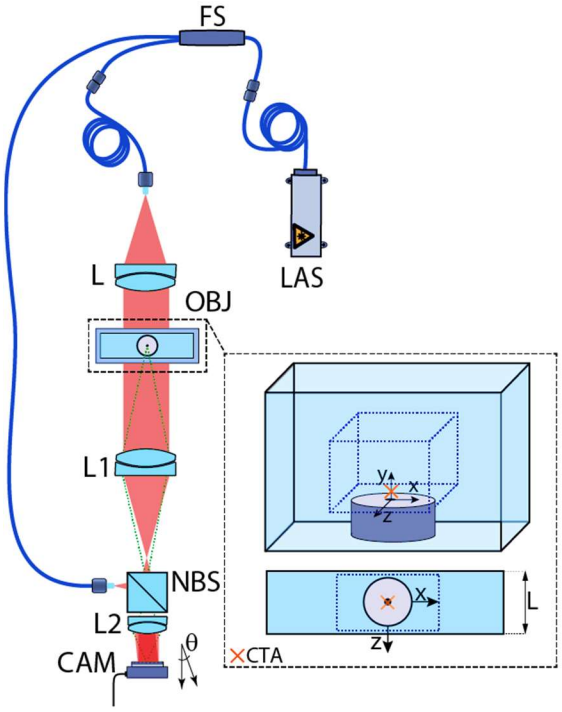

Fig.9.3. *Schematic of the Mach-Zehnder optical setup.*[170]

The used camera is a UI-3370CP Rev. 2, 2048×2048 pixel, $5.50[\mu\mathrm{m}]$ pixel size CMOS camera. The field of view of the measured area was $92.1 \times 92.1[mm^2]$.[170]

The object under study is a pulsatile jet (PJ) with a circular opening of $4[\mathrm{mm}]$, submerged in a water tank containing water at temperature of $T_0 = 17[°\mathrm{C}]$. The pulsatile jet is fed with prewarmed water, the temperature of which was predetermined to be around $33[°\mathrm{C}]$. The warm water passes through the orifice to create the jet profile. Time period of the PJ is $5[\mathrm{s}]$, i.e., long enough for the flow to get steady. The PJ period therefore consists of the initial transient stage, steady stage, and final transient stage. The long period phenomenon with a steady flow was chosen on purpose in order to separate random and steady component of the PJ. The inner dimensions of the glass water tank are (x, y, z) $31[cm] \times 31[cm] \times 11[cm]$ with wall thickness of $5[\mathrm{mm}]$ and has been filled with water up to the height of $h = 24$ cm.[170]

In the first step, all holograms have been recorded and reconstructed by *eq.(9.2)*. In total, 314 holograms have been recorded, with some being captured when the system was off and later used as the reference. Example of a hologram is shown in Fig.9.4. They have been captured with framerate of $8.67[\mathrm{fps}]$ and sampling time of $0.1304[\mathrm{s}]$.[170]

Fig.9.4.b) shows the Fourier domain of the reference hologram. Here, the term $\hat{C}(\upsilon_x - \upsilon_{Cx}, \upsilon_y - \upsilon_{Cy})$ can clearly be seen separated from the terms $\hat{A}(\upsilon_x, \upsilon_y)$ and $\hat{C}^*(\upsilon_x + \upsilon_{Cx}, \upsilon_y + \upsilon_{Cy})$ due to the tilt between the reference wave and the object wave, from which the carrier frequencies υ_{Cx} and υ_{Cy} were introduced by real time observation of the Fourier spectrum while adjusting the reference arm of the interferometer. In order to avoid phase errors from diffraction effects, the angle has been selected to be slightly greater. The choice of the carrier frequencies depends on various factors, as the Nyquist criteria, distance from the detector and its size, and importantly the gradient of phase $\nabla\varphi$. The gradient of phase $\nabla\varphi$, i.e., object wavefront curvature, is high due to the "lensing" effect of the water tank. The digital sensor's spatial-frequency bandwidth was sufficient in order to cover the spectral bandwidth υ_B of $\hat{C}$ and the spatial-carrier frequencies were adjusted in order to avoid overlapping in the Fourier spectrum. The carrier frequencies were determined to be $\upsilon_{Cx} = 123[\,\mathrm{mm}^{-1}]$ and $\upsilon_{Cy} = -157[\,\mathrm{mm}^{-1}]$. This allows for the determination of the tilt angle between both waves with respect to the direction of propagation z to be $\alpha_x \approx \lambda\upsilon_{Cx} = 4.45[°]$ and $\alpha_y \approx \lambda\upsilon_{Cy} = 5.68[°]$. A 2D Hanning window with a bandwidth of $\upsilon_B = 200[\mathrm{mm}^{-1}]$ and centers $\upsilon_{Cx} = 123[\mathrm{mm}^{-1}]$, $\upsilon_{Cy} = -157[\mathrm{mm}^{-1}]$, corresponding to the carrier frequencies that have been applied in order to filter the term out, was used in order to retrieve the complex field $F^{-1}\{\hat{C}(\upsilon_x - \upsilon_{Cx}, \upsilon_y - \upsilon_{Cy})\} = C(x,y)e^{j(2\pi\upsilon_x x + 2\pi\upsilon_y y)}$.[170]

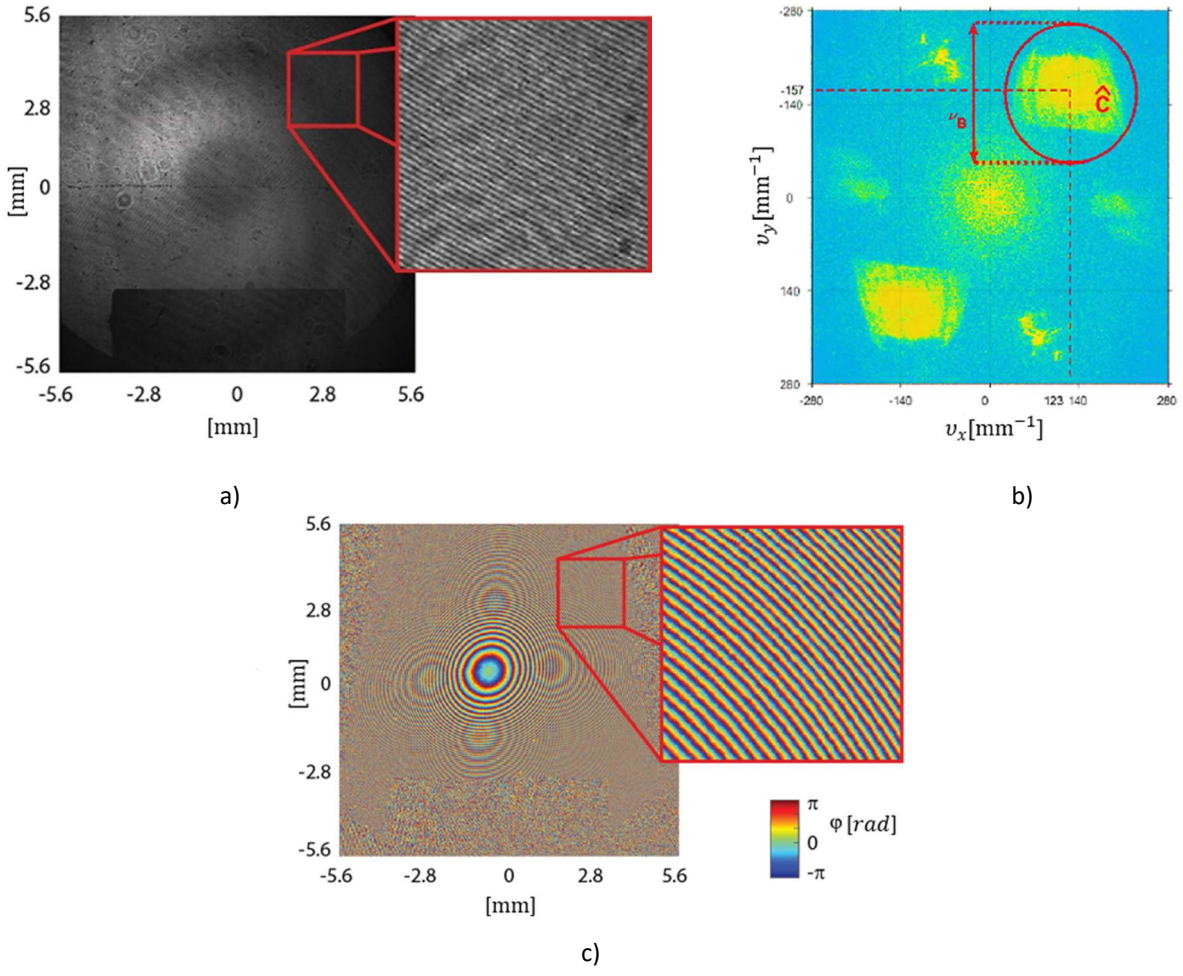

Fig.9.4. *a) Interferogram at t=0[s] (reference state), b) magnitude in logarithmic scale of the interferogram's FT spectra with the denoted term $\hat{C}(\upsilon_x, \upsilon_y)$ and c) the wrapped phase computed from $\hat{C}(\upsilon_x, \upsilon_y)$.*[170]

The same procedure is applied to all digital holograms. It is important to note that the filtering window remains unchanged for all holograms. The interference phase between a hologram captured at time t with respect of the reference hologram has been calculated as modulo of 2π. The wrapped interference phase distributions were free of undersampled areas and therefore has been successfully unwrapped through the Goldstein algorithm[193]. The process of unwrapping introduces itself error uncertainty. Mostly, these uncertainties are too small to be taken in consideration. Phase aberrations are present, apart from the dynamic phase change from the measured phenomena, in both the reference and the object beam along the whole optical path. Phase aberrations can come from different contributors, such as the improper selection of carrier frequencies, tilt between the reference and object wave, imperfections in the optical components or the misalignment of the optomechanical components of the interferometers. The filled water tank in steady state introduces significant wavefront error. Fig.9.3.c) illustrates the phase aberration from the combined wavefront hitting the sensor of the camera. Since these aberrations are stationary (time invariant) and come from the optical system, in case of digital holographic interferometry where the phase fields are compared to the reference state that carries the same phase field aberration, these aberrations vanish from calculation. This is one advantage of this technique, since all imperfections in the optomechanical elements become less relevant and carrier frequencies do not have to be precisely set. Therefore, the state reference has been captured shortly before the exhibition of the phenomena of interest.[170]

Since we deal with the case of symmetrical orifice, we assume the development of a symmetric temperature field. Based on this assumption, only capturing one projection for the analysis is supposed to be sufficient in order to retrieve the refractive index field in *eq.(3.44.).* The temperature field has been retrieved by using the inverse Abel Transform. This was done by taking one row of the phase data and reconstructing the slice. The reconstruction of the 2D plan sliced has been done by the filtered back-projection method, which later were all stacked on top of each other to form the 3D temperature profile.[170]
In real experiment, steady (symmetrical) and random components of the flow occur. Within the middle stage of the PJ period when the PJ flow is laminar, we separated the steady (symmetrical) and random flow components using averaging of phase maps at different time instants. This reveals how valid the assumption about the symmetrical flow is.[170]

9.6. Results

The results from the interferometry-based visualization of temperature fields from a jet with warm water have been discussed in this chapter. Some of the illustrated results are restricted only to the relevant regions for study and are a projection of the testing subject, hence they are predominantly two-dimensional and averaged along the optical path. Three dimensional reconstructions are also presented.[170]
Temperature values measured through off-axis digital holographic interferometry are relative, meaning that a starting point must be a priori known. The temperature of the water in the tank has been measured right before the experiment started with a thermometer and is assumed to be only slowly varying at the edge of the digital camera field of view. The temperature has been computed using *eq.(6.14)*.[170] Phase and temperature values are displayed according to the color bar legends located on the side of the results. In the case of 2D visualization, displayed values must be understood as averaged values along the optical propagation path. Fig.9.5. shows the symmetrical whole-field interference phase profile of warm

water flowing out from a single circular orifice with a diameter of $4[\mathrm{mm}]$ from the orifice at two different instants of time. Three cross sections were drawn for analysis. It shows the effect of temperature on the refractive index of water at the three cross sections, which are plotted in the graphs right next to them. As expected, the phase is lower at the vicinity of the orifice where the warm water comes out and the phase change is less at the distance where the warm water mixes with the colder water. The time instants were chosen when the jet profile was the most stable.[170]

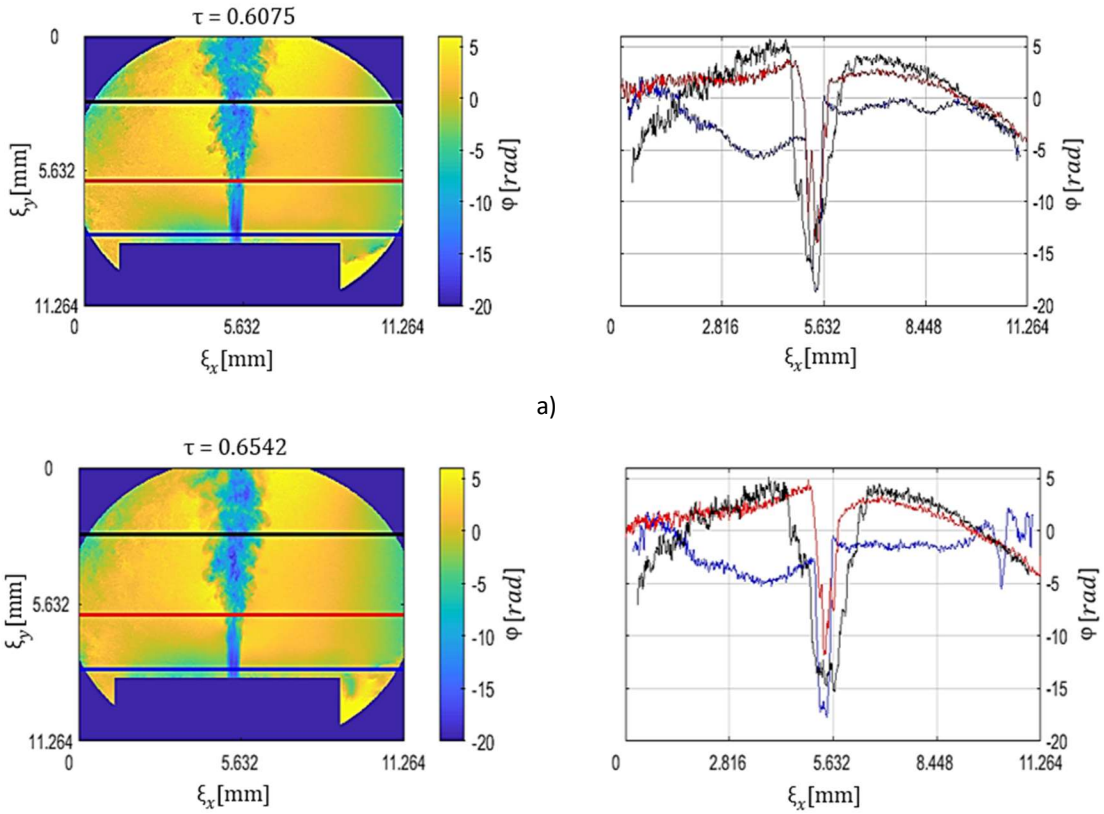

Fig.9.5. *a)-b) Whole–field interference phase profile of warm water flowing out from a single circular orifice and its plot at two different relative instants in [rad].*[170]

Fig.9.6. shows the time development of the phase profile of the jet stream coming out of the orifice. Several points in time have been selected to show the formation of the characteristic jet profile and its development in time. The first row shows the beginning when warm water starts flowing under pressure. The jet profile can be seen clearly established on the second row. On the last row, after stopping the incoming warmer water, a small pocket of warm water can be seen moving upwards. Digital holographic interferometry can clearly visualize the PJ position and evolution and track its movement in space and time. Retrieved phase distributions and characteristics of PJs deduced from them are valid regardless of the kind of measured phenomenon. However, in order to quantitatively retrieve refractive index distribution and hence temperature field distribution, the phase fields are assumed to be symmetrical. This assumption introduces some uncertainty, as discussed further in the text. Fig.9.7. shows the 3D reconstruction using inverse Abel transform of the jet profile at three different instants in time. The first one depicts the 3D reconstruction of the jet profile, while the two consecutive ones depict the reconstruction of the small warm water pocket. Tracking can be done from frame to frame.[170]

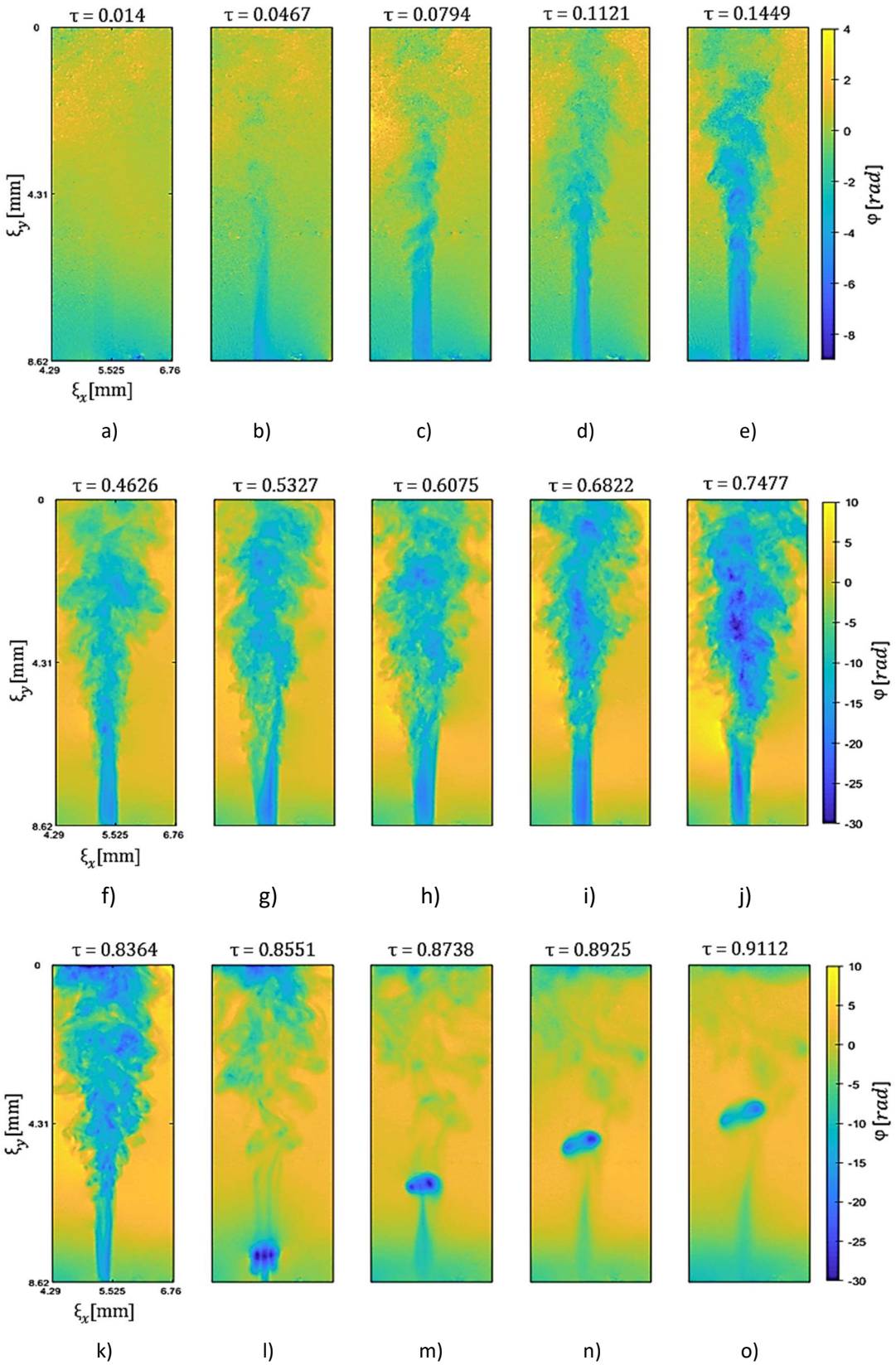

Fig.9.6. *a)-o) Time evolution of the jet phase profile in [rad].*[170]

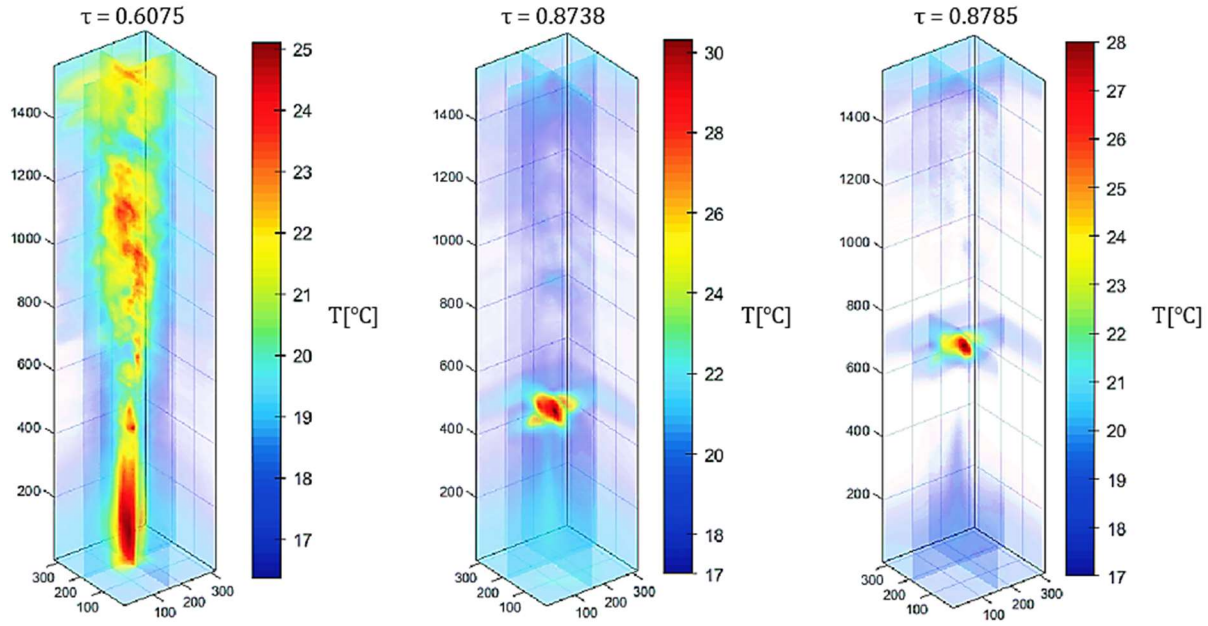

a) b) c)

Fig.9.7. *a)-c) Tomographic reconstruction at three different instants.*[170]

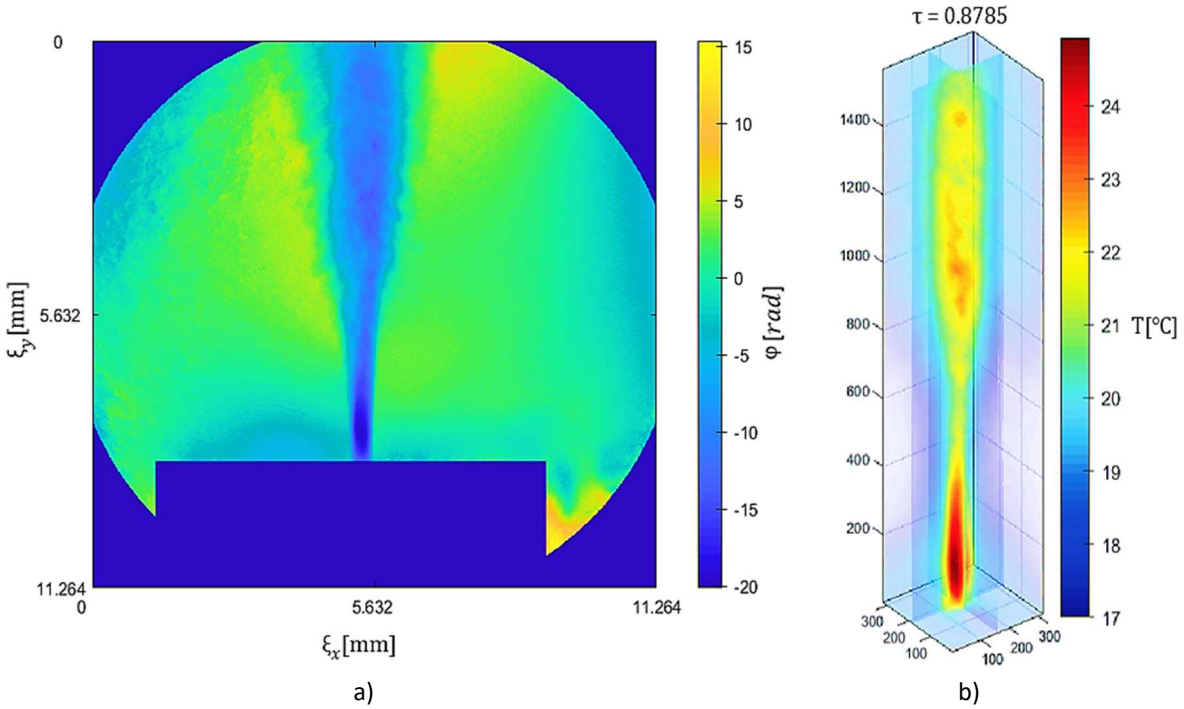

a) b)

Fig.9.8. a) *Averaged whole−field phase profile and b) its tomographic temperature profile reconstruction.*[170]

However, the condition on symmetry is not fully met. The averaging of many phase fields during the steady flow stage, results in the suppression of the signal fluctuation (random) component. The averaged phase profile over 15 consecutive frames is shown in Fig.9.8.a). The averaging time is $1.47[s]$ and thus faster random components are suppressed. Fig.9.8.b) shows the tomographic reconstruction from the averaged phase values (see Fig.9.7.a)) for comparison).[170]

In order to observe the thermal phenomena happening in the liquid in more detail, the dynamic range of the temperature values must be reduced. Therefore, temporal finite difference temperature $\dot{T}(n\Delta t)$ is computed. It has been computed as[170]:

$$\dot{T}(x,y,n\Delta t) = \frac{T(x,y,n\Delta t) - T(x,y,(n-1)\Delta t)}{\Delta t} \tag{9.7}$$

Fluid mixing can be seen on the first row of images of Fig.9.9., where colder water from the tank is shown in blue color being pulled and mixed with warmer water, shown with yellowish color. The second row depicts the small warm water pocket traveling upward once the flow through the circular orifice was stopped. As seen, if the speed of the camera is high enough, this technique allows for its tracking.[170]

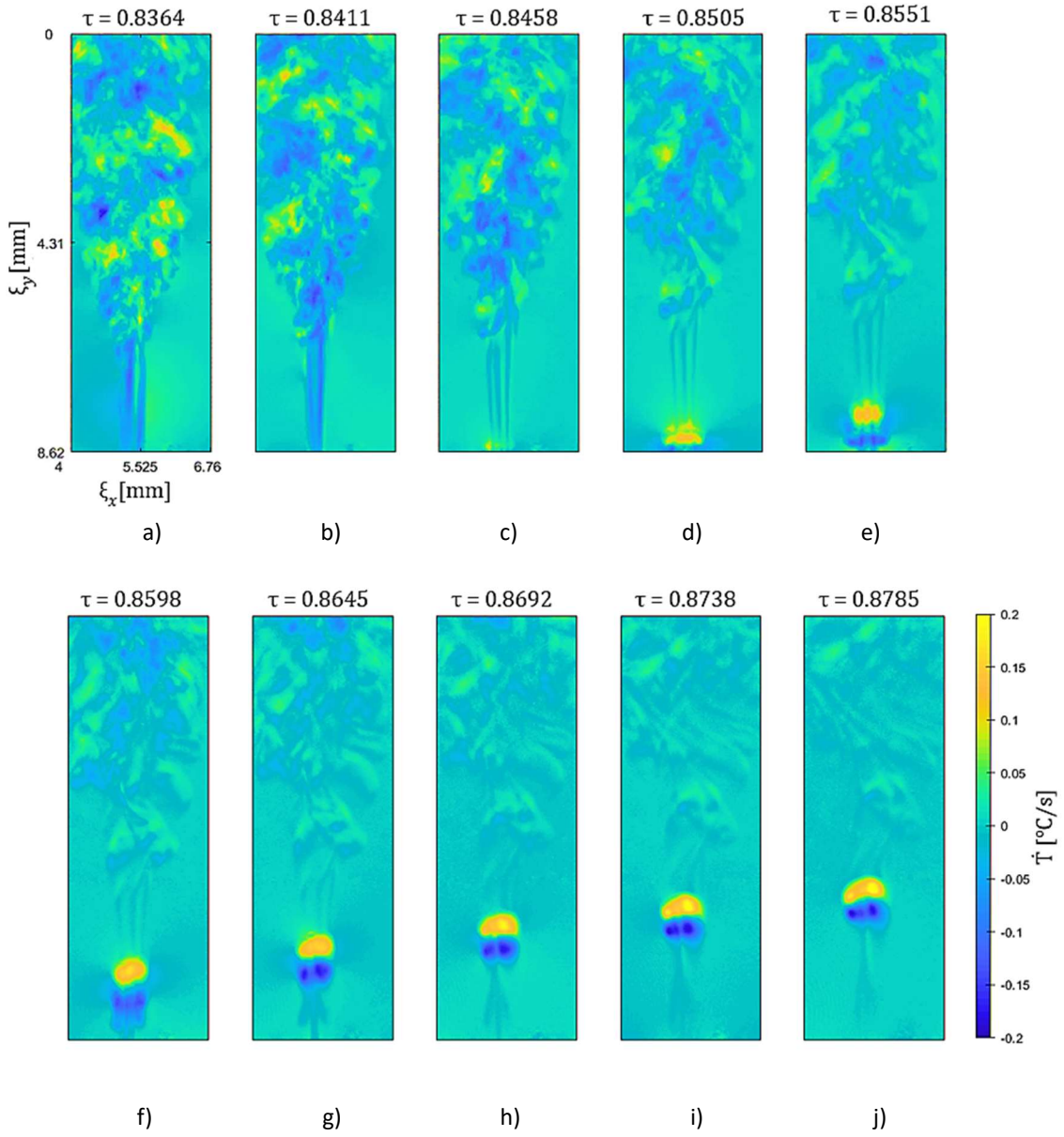

Fig.9.9. *a)-j) Temporal finite difference temperature for different instants in* [°C/s].[170]

9.6.1. Limits and errors of interferometry in liquids-symmetrical fields

Several sources of error that are influencing our measurement are considered. Fundamentally, DHI measures interference phase $\Delta\varphi$, which is further converted into refractive index variation and in the last step the temperature change is determined, assuming $\left(-\frac{dn}{dT}\right)_{water} \approx 1 \cdot 10^{-6}$. Each of these steps suffer from some uncertainties. The uncertainty of interference phase measurement comes from factors such as misalignment and settling of optical components , fluctuation of laser wavelength , electronic noise, and external unstable environment conditions[39]. The phase noise for our measurement is estimated to be $0.05[\mathrm{rad}]$. The value was determined from experimental data (without the phenomenon) as the peak-to-valley value of an unwrapped phase map after low order polynomial subtraction (i.e., high spatial frequency components were considered as the noise). Such phase error contributes to temperature measurement uncertainty $\sim 0.01[°\mathrm{C}]$. However, the major uncertainty source is in the second step, i.e., the refractive index distribution calculation using inverse Abel transform.[170]

We assumed weakly-varying refractive index with the approximation of straight rays. Analysis[89,194] revealed that even if a diffraction of light is considered, the refractive index uncertainty is always about one order lower than the measured variation of refractive index. However, this is valid for purely symmetrical fields or asymmetrical fields using many projections. Hence, the major source of uncertainty in our case is the assumption of symmetrical field even though the physical field evinces some random fluctuations. In order to estimate validity of the assumption, standard deviation of phase fields during the steady stage of the PJ was calculated as[170]:

$$\sigma(n,m) = \sqrt{\frac{1}{N}\sum_{i=1}^{N}(\Delta\varphi_i(n,m) - \overline{\Delta\varphi_\iota}(n,m)^2)} \tag{9.8}$$

, where $\overline{\Delta\varphi_\iota}$ is the averaged phase, and $N = 13$ is the number of phase maps.

The standard deviation map of interference phase maps has been calculated and shown in Fig.9.10.b), where a) shows the averaged phase map and b) shows the standard deviation map. Two regions for evaluation have been selected: one further away in the developed area where the random flow fluctuations are more obvious and one near the opening where almost laminar flow is predicted. The estimated error in the region of the developed puff is $u_{\Delta\varphi} = 1.56[\mathrm{rad}]$ while in the region near the orifice the standard deviation is $u_{\Delta\varphi} = 0.7[\mathrm{rad}]$.[170]

From Fig.9.10., it follows that the assumption on symmetry is the main uncertainty source (one order higher than the aforementioned sources). Assuming flat (2D) field for simplification, the temperature uncertainty can be estimated as $u_T = \frac{\lambda}{2\pi}\frac{u_{\Delta\varphi}}{L \cdot 1\times10^{-4}}$, where $L = 4\,mm$ is the orifice diameter. The uncertainty u_T near the PJ opening is $0.03[°C]$, which is relatively below 5%. On the other hand, further from the opening, where the random fluctuations play a more significant role $u_T \sim 0.6[°\mathrm{C}]$, it is relatively about 15%.[170]

In case of steady flow, averaging of phase maps can filter out the random fluctuations and hence decrease the uncertainty. On the other hand, many phenomena are rapidly time varying, averaging cannot be applied, and the uncertainty ranges are deduced in the range $5\% - 20\%$.[170]

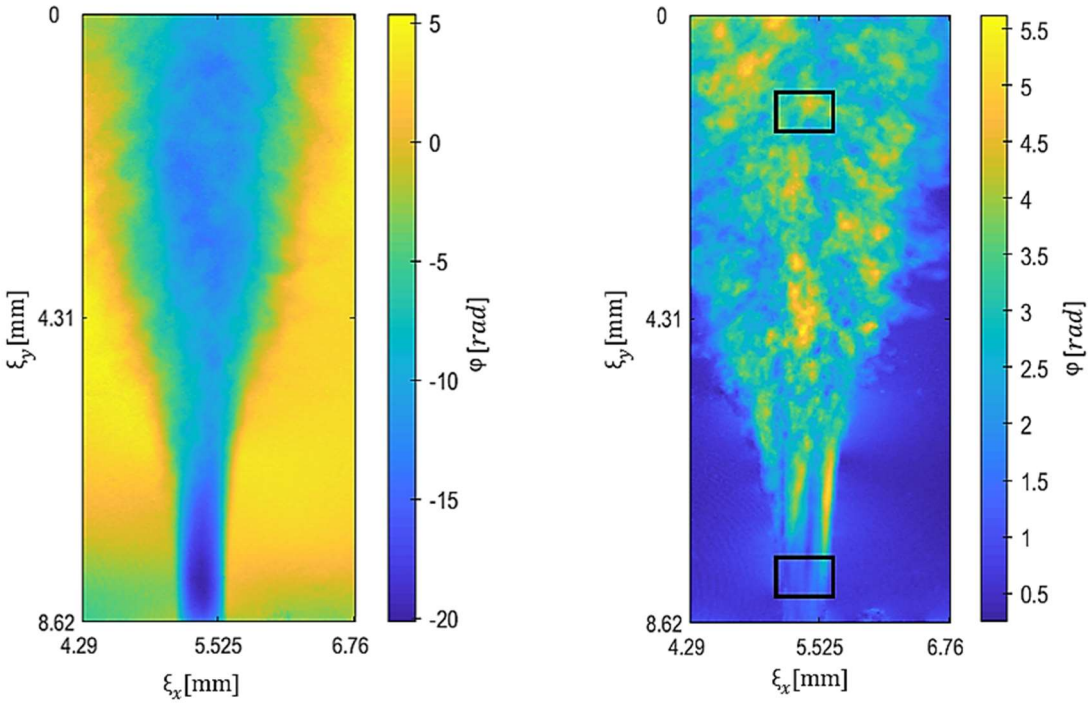

a) b)

Fig.9.10. *a) Averaged phase map and b) standard deviation.*[170]

To verify the reliability of DHI we compared the results to results of well-established CTA (Constant Temperature Anemometry). CTA is single point method and therefore we chose one representative point within the measured area that was located on the axis of the orifice approximately $2[mm]$ above the opening. Location of the CTA sensor is illustrated as a red cross in Fig.9.3. DHI is a full-field method and therefore we had to pick voxels of the measured temperature distribution corresponding to those values measured by CTA. Results showing a good agreement are plotted in Fig.9.11. The red color stands for DHI while blue represents values obtained by CTA. A significant source of the discrepancies in results between DHI and CTA is the fact that both measurements (DHI and CTA) had to be performed separately at different time due to invasive feature of CTA. Although the initial experimental parameters were set as similar as possible, the environmental conditions as well as behavior of the phenomenon itself could slightly vary between both measurements.[170]

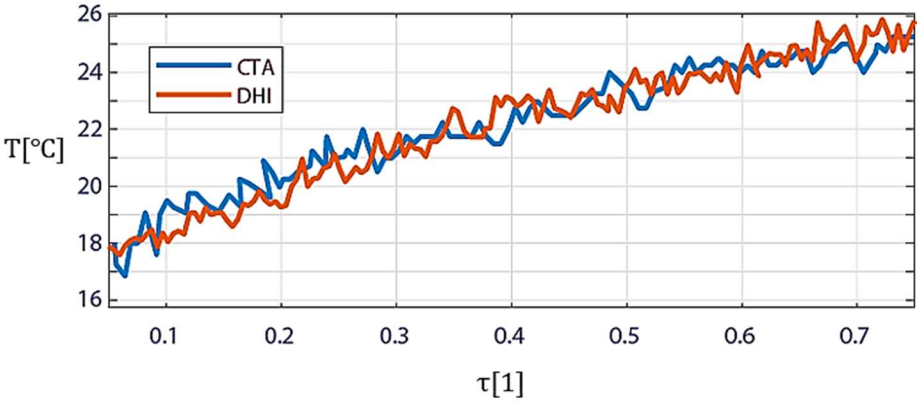

Fig.9.11. *Comparison of DHI and CTA within one representative point within the measured area.*[170]

9.7. Conclusions

A digital holographic interferometric methodology for the measurement of temperature fields through the analysis of the refractive index variation has been implemented. Real-time dynamic temperature field change and visualization of volumetric temperature fields generated by a heated fluid from a pulsatile jet in a water tank through off-axis digital holographic interferometry have been reported. This chapter, through the conducted experiment and results, presents and puts off-axis digital holographic interferometry as a powerful technique to visualize symmetrical temperature fields in water created by a periodic pulsatile jet.[170]

The pulsatile jet generator was placed in a water tank filled with water at room temperature. A pulsatile jet with higher temperature was coming out of the orifice with a circular diameter of $4[\mathrm{mm}]$. A portable Mach-Zehnder interferometer has been used in order to record the holograms with a digital camera. Digital holograms have been evaluated and symmetrical temperature fields have been retrieved using inverse Abel transform.[170]

The main source of uncertainty was the assumption of a symmetric field, although the flow shows turbulence and other asymmetries. Due to the steady flow behavior during the middle part of the period, we estimated that the relative uncertainty of the temperature field measurement near the orifice is below 5%. On the other hand, further from the orifice, where random fluctuations play a more significant role, the relative uncertainty increases up to 15%. This must be considered when using single-shot DHI for symmetrical pulsatile jets investigation.[170]

Results obtained through this study demonstrate a successful appliance of this approach for temperature field measurement in pulsatile jets with water as the working fluid. Our study indicates that digital holographic interferometry can be used to visualize temperature fields, study flows and evaluate their characteristic quantities, and is superior to other conventional methods since it is a non-invasive whole-field technique that can be automated and deliver real time results with high temporal and spatial resolution.[170]

10. Conclusions

10.1. General conclusions

This dissertation thesis presents a thorough work on visualizing and measuring temperature fields in flowing gases and liquids. Through each of its chapters, it sheds light onto different aspects of using digital holographic interferometry for specific study cases.

The necessity and importance of non-contact optical methods that do not interact with the phenomena under study in the field of research and industry, as well as the lack of such research for flowing gases and liquids, created the foundation of work intended in this dissertation thesis. The aim of this work was to push the limits of exploring the application and effectivity of digital holographic interferometry for interesting study cases that haven't been tackled before in the field of applied fluid mechanics.

I have greatly benefited from the expertise on this topic of the collaborative team that constituted the head of this research (supervisors and specialist supervisor), coming from both the *Faculty of Mechanical Engineering* and the *Faculty of Mechatronics, Informatics and Multidisciplinary studies,* specifically the *Laboratory of Optical Measurements, at the Technical University of Liberec*. All this teaming made it possible to plan and bring to table the experiments intended for this dissertation thesis. This collaboration had already expertise in using digital holographic interferometry for investigation in applied fluid mechanics with many previous publications in journals and conferences. This dissertation thesis somehow represents a continuation in the work of using optical techniques for flow studies.

In *Chapter 6, t*hrough a Mach-Zehnder interferometer, a simple case of 2D refractive index distribution coming from heat generated by a rod heater in a water tank through convection was studied. Carrier frequencies were introduced through the tilting of the reference arm. Four thermocouples placed in the tank were used to assess the validity of interferometrically measured average temperature along the optical axis. Results of both measurements were within 5% agreement.[141]

In *Chapter 7*, through simulations conducted by *ANSYS*, data obtained in *Chapter 6* were compared to simulated results. Data from both simulations have shown to be in good agreement with data collected by thermocouple(s) and those estimated through digital holographic interferometry at the limit of 5% error for the whole range of temperatures.[144]

In *Chapter 8*, a two-wavelength off-axis digital holographic interferometric optical setup for resolving the issue of phase unwrap ambiguity for three different study cases was presented. By combining the synthetic phase and the phase obtained from the single wavelength, a significantly higher range of measurement has been achieved with the accuracy of a single wavelength, avoiding the amplified noise in the synthetic phase.[157,159]

In *Chapter 9*, through a portable Mach-Zehnder interferometer, symmetrical temperature field from a pulsatile jet with water as its working fluid was studied. Data were reconstructed using a tomographic approach. It was estimated that the relative uncertainty of temperature field measurement near the orifice to be below 5% and for the regions further from the orifice to be up to 15%.[170]

Through all these experiments, we provide solid experimental data and results that indeed highlight the advantages and possibilities that digital holographic interferometry offers, not only for research but also for industry, with possible future applications that go beyond the scope of this dissertation thesis.

Based on all conclusions drawn at the end of each chapters, we can faithfully conclude that digital holographic interferometry can be used as a tool for temperature field visualization and measuring, to study different kinds of flows and determine important quantities that are relevant for the process under study.

Through this work we can also state that digital holographic interferometry stands as an exquisite optical technique for non-contact, whole-field, high precision techniques where a change in refractive index induced by a phenomena can be detected and is superior to other conventional methods since it is a non-invasive whole-field technique.

10.2. Fulfillment of objectives

Clear objectives in regards of the content and research constituting the dissertation thesis have been set in the beginning as explained in the section *Objectives*. All predetermined objectives have been fulfilled, that is:

- A comprehensive introduction to all aspects in regard of this thesis have been presented, starting from general theoretical introduction dealing with light, its nature and properties, general and more specific details on holography and optics, and a brief introduction to heat;
- An extensive literature review on experiments dealing with temperature fields in gases, liquids and solids has been presented, through which the reader can have a general image on the vast domain of possible applications of digital holographic interferometry, mostly related to the work in this dissertation thesis;
- Initial research on temperature fields generated by a rod heater in a tank filled with water with digital holographic interferometry has been successfully accomplished and opened the pavement for further research;
- CFD simulations with *ANSYS* for the case of the rod heater in water have shown to be in good agreement with the estimated values of digital holographic interferometry and the actual measured values with thermocouples, thus giving green light to continue with further research;
- The concept of two-wavelength optical measurement for range extension has been successfully applied and shown very satisfying results for three different study cases;
- And finally, a tomographic approach was successfully implemented for the visualization and temperature measurements for the case of a 3D temperature profile coming from a pulsatile jet with water as its working fluid.

10.3. Future work

Through the work implemented in this dissertation thesis, many possible interesting ideas arose, but due time limitation for such work and applications going beyond the scope of this dissertation thesis, they remain to be implemented by researchers who will pick up where this work left and explore different options.

Digital holographic interferometry through the two-wavelength optical configuration could be used to explore the analysis of phenomena that exceed their range measurement and where other techniques fail to provide realistic and undisturbed flow data. It could be expanded to the case of flowing water with higher temperature gradients.

Other interesting experiments that could be conducted would be temperature measurements and visualization for the case of jets with multiple orifices, even for the case of non-symmetric shape of the orifices and their arrangements. Other working fluids could also be considered, keeping in mind that the fluid must be at least semi-transparent and exhibit a change of refractive index when an external force is applied to it.

Generally, the range of possibilities of using digital holographic interferometry for applied fluid mechanics is immense.

References

[1] K. Simonyi and D. Kramer, *A cultural history of physics*. Boca Raton, Fla. : CRC Press, 2012.

[2] A. M. Smith, *From sight to light : the passage from ancient to modern optics*. The University of Chicago Press, Ltd., London, 2017.

[3] O. Darrigol, *A history of optics : from Greek antiquity to the nineteenth century*. Oxford University Press, 2012.

[4] H. Varvoglis, *History and evolution of concepts in physics*. Springer International Publishing, 2014.

[5] A. Zajonc, *Catching the light : the entwined history of light and mind*. Bantam Books, 1993.

[6] B. Vohnsen, "A Short History of Optics," *Phys. Scr.*, vol. 2004, no. T109, p. 75, Jan. 2004, doi: 10.1238/PHYSICA.TOPICAL.109A00075.

[7] M. Bertolotti, *The history of the laser*. Institute of Physics Publishing, 2005.

[8] M. D. Al-Amri, M. M. El-Gomati, and M. S. Zubairy, *Optics in our time*. Springer International Publishing, 2016.

[9] K. Iizuka, *Engineering Optics*. Springer International Publishing, 2019.

[10] H. F. Buckley, *A Short History of Physics*. Methuen & Co. Ltd., 1927.

[11] E. Hecht, *Optics*, 5th ed. Reading, Mass. : Addison-Wesley Pub. Co., 2017.

[12] F. Cajori, *A History Of Physics*. Dover Publications, Inc., 1969.

[13] Alhazen and F. Risner, *Opticae thesaurus : Alhazeni Arabis libri septem, nuncprimum editi*. Basileae : Per Episcopios, 1572.

[14] R. Descartes, *Discours de la méthode pour bien conduire sa raison, et chercher la vérité dans les sciences ...* . Leyden, 1637.

[15] N. Kipnis, *History of the Principle of Interference of Light*. Birkhäuser Basel, 1991.

[16] M. Von Laue, *Geschichte der Physik*. Berlin: Ullstein Bucher, 1959.

[17] I. Sir Newton, *Opticks: or a treatise of the reflexions, refractions, inflexions and colours of light. Also two treatises of the species and magnitude of curvilinear figures*. London: Printed for S. Smith, and B. Walford, 1704.

[18] A. Robinson, *The Scientists: An Epic of Discovery*. New York: Thames and Hudson USA, 2011.

[19] C. Huygens, *Traité de la lumière : où sont expliquées les causes de ce qui luy arrive dans la reflexion, & dans la refraction et particulierement dans l'etrange refraction du cristal d'Islande*. Leyde : Pierre vander Aa, 1690.

[20] J. Colombani and J. Bert, "Holographic interferometry for the study of liquids," *J. Mol. Liq.*, vol. 134, no. 1-3 SPEC. ISS., pp. 8–14, May 2007, doi: 10.1016/j.molliq.2006.12.013.

[21] J. Bajer, *Optika 2*. Univerzita Palackého. Přírodovědecká fakulta, Vladimir Chlup, 2018.

[22] A. Einstein, “Über einen die Erzeugung und Verwandlung des Lichtes betreffenden heuristischen Gesichtspunkt,” *Ann. Phys.*, vol. 322, no. 6, pp. 132–148, Jan. 1905, doi: 10.1002/andp.19053220607.

[23] S. F. W Dyson, P. A. S Eddington, and M. C. Davidson On A, “IX. A determination of the deflection of light by the sun’s gravitational field, from observations made at the total eclipse of May 29, 1919,” *Philos. Trans. R. Soc. London. Ser. A, Contain. Pap. a Math. or Phys. Character*, vol. 220, no. 571–581, pp. 291–333, Jan. 1920, doi: 10.1098/rsta.1920.0009.

[24] B. Saleh, *Fundamentals of photonics*, Third edition. Hoboken NJ: Wiley, 2019.

[25] M. Born and E. Wolf, *Principles of Optics*. Cambridge University Press, 2019.

[26] P. Malý, *Optika*. Karolinum, 2013.

[27] R. P. Feynman, R. B. Leighton, and M. Sands, *The Feynman lectures on physics : Volume I: Mainly mechanics, radiation and heat*, vol. I. Addison-Wesley, 1965.

[28] U. Schnars and W. Jueptner, *Digital holography: Digital hologram recording, numerical reconstruction, and related techniques*. Springer Berlin Heidelberg, 2005.

[29] T. Kreis, *Handbook of Holographic Interferometry: Optical and Digital Methods*. Wiley, 2004.

[30] H. Gross, *Handbook of Optical Systems*, vol. 1. Wiley-VCH, 2005.

[31] A. Štrba, V. Mesároš, and D. Senderáková, *Svetlo-vlny, lúče, fotóny*. Žilina: Enigma Publishing, 2011.

[32] P. Psota, “ADVANCED TIME AVERAGE DIGITAL HOLOGRAPHY BY MEANS OF FREQUENCY AND ___ PHASE MODULATION PhD dissertation,” Technical University of Liberec, 2015.

[33] P. Psota, R. Doleček, V. Lédl, and T. Vít, “Dynamic interferometric measurement with extended unambiguity range in flow measurement,” *EPJ Web Conf.*, vol. 180, p. 02087, 2018, doi: 10.1051/EPJCONF/201818002087.

[34] V. Lédl, P. Psota, R. Doleček, and T. Vít, “Digital holographic setups for phase object measurements in micro and macro scale,” in *EPJ Web of Conferences*, May 2015, vol. 92, doi: 10.1051/epjconf/20159201001.

[35] Y. Hamamoto, E. Tomita, and T. Okada, “Measurement of the transient temperature of gas by laser interferometry,” *JSME Int. Journal, Ser. B Fluids Therm. Eng.*, vol. 32, no. 2, pp. 247–251, 1989, doi: 10.1299/JSMEB1988.32.2_247.

[36] R. Doleček, P. Psota, V. Lédl, T. Vít, P. Dančová, and V. Kopecký, “Comparison of digital holographic interferometry and constant temperature anemometry for measurement of temperature field in fluid,” *Hologr. Adv. Mod. Trends IV*, vol. 9508, p. 95080P, May 2015, doi: 10.1117/12.2185056.

[37] A. H. Ali, “Measurement of air temperature using laser interferometry,” *J. Appl. Sci.*, vol. 11, no. 7, pp. 1431–1435, 2011, doi: 10.3923/JAS.2011.1431.1435.

[38] V. Lédl, P. Psota, P. Vojtíšek, and R. Doleček, *Digitální holografická interferometrie (Digital holographic interferometry)*, 1st ed. Liberec: ReproArt Liberec s.r.o., 2015.

[39] S. Narayan, A. K. Singh, and A. Srivastava, “Interferometric study of natural convection heat transfer phenomena around array of heated cylinders,” *Int. J. Heat Mass Transf.*, vol. 109, pp. 278–292, Jun. 2017, doi: 10.1016/j.ijheatmasstransfer.2017.01.106.

[40] P. E. Ciddor, “Refractive index of air: new equations for the visible and near infrared,” *Appl. Opt. Vol. 35, Issue 9, pp. 1566-1573*, vol. 35, no. 9, pp. 1566–1573, Mar. 1996, doi: 10.1364/AO.35.001566.

[41] R. J. Mathar, “Refractive index of humid air in the infrared: model fits,” *J. Opt. A Pure Appl. Opt.*, vol. 9, no. 5, p. 470, Apr. 2007, doi: 10.1088/1464-4258/9/5/008.

[42] M. M. Hossain and C. Shakher, “Temperature measurement in laminar free convective flow using digital holography,” *Appl. Opt.*, vol. 48, no. 10, pp. 1869–1877, Apr. 2009, doi: 10.1364/AO.48.001869.

[43] K. H. Chen, S. L. Yang, and K. C. Chang, “Measurement of small differences in refractive indices of solutions with interferometric optical method,” *Opt. Lasers Eng.*, vol. 45, no. 11, pp. 1071–1076, Nov. 2007, doi: 10.1016/J.OPTLASENG.2007.05.004.

[44] A. Mialdun and V. M. Shevtsova, “Development of optical digital interferometry technique for measurement of thermodiffusion coefficients,” *Int. J. Heat Mass Transf.*, vol. 51, no. 11–12, pp. 3164–3178, Jun. 2008, doi: 10.1016/J.IJHEATMASSTRANSFER.2007.08.020.

[45] B. Nilsson and T. E. Carlsson, “Direct three-dimensional shape measurement by digital light-in-flight holography,” *Appl. Opt. Vol. 37, Issue 34, pp. 7954-7959*, vol. 37, no. 34, pp. 7954–7959, Dec. 1998, doi: 10.1364/AO.37.007954.

[46] I. Yamaguchi, S. Ohta, and J. I. Kato, “Surface contouring by phase-shifting digital holography,” *Opt. Lasers Eng.*, vol. 36, no. 5, pp. 417–428, Nov. 2001, doi: 10.1016/S0143-8166(01)00069-0.

[47] M. M. Hossain, G. Sheoran, D. S. Mehta, and C. Shakher, “Contouring of diffused objects by using digital holography,” *Opt. Lasers Eng.*, vol. 45, no. 6, pp. 684–689, Jun. 2007, doi: 10.1016/J.OPTLASENG.2006.11.004.

[48] C. Shakher, M. M. Hossain, D. S. Mehta, and G. Sheoran, “Measurement of temperature field in steady laminar free convection flow using digital holography,” *Ninth Int. Symp. Laser Metrol.*, vol. 7155, p. 71551X, Sep. 2008, doi: 10.1117/12.814570.

[49] G. Pedrini, P. H. Fröning, H. Fessler, and H. J. Tiziani, “Transient vibration measurements using multi-pulse digital holography,” *Opt. Laser Technol.*, vol. 29, no. 8, pp. 505–511, Apr. 1998, doi: 10.1016/S0030-3992(97)00048-0.

[50] P. Picart *et al.*, “2D full field vibration analysis with multiplexed digital holograms,” *Opt. Express*, vol. 13, no. 22, p. 8882, Oct. 2005, doi: 10.1364/OPEX.13.008882.

[51] M. De La Torre-Ibarra, F. Mendoza-Santoyo, C. Pérez-López, and T. Saucedo-A, “Detection of surface strain by three-dimensional digital holography,” *Appl. Opt.*, vol. 44, no. 1, pp. 27–31, Jan. 2005, doi: 10.1364/AO.44.000027.

[52] B. Skarman, K. Wozniak, and J. Becker, “Digital in-line holography for the analysis of Benard-convection,” *Flow Meas. Instrum.*, vol. 10, no. 2, pp. 91–97, 1999, doi: 10.1016/S0955-5986(98)00046-6.

[53] B. Skarman, J. Becker, and K. Wozniak, “Simultaneous 3D-PIV and temperature measurements using a new CCD-based holographic interferometer,” *Flow Meas. Instrum.*, vol. 7, no. 1, pp. 1–6, Mar. 1996, doi: 10.1016/0955-5986(96)00006-4.

[54] C. Wagner, S. Seebacher, W. Osten, and W. Jüptner, “Digital recording and numerical reconstruction of lensless Fourier holograms in optical metrology,” *Appl. Opt.*, vol. 38, no. 22, p. 4812, Aug. 1999, doi: 10.1364/AO.38.004812.

[55] F. Montel, J. Bickert, J. Hy-Billiot, and M. Royer, “Pressure and compositional gradients in reservoirs,” *Soc. Pet. Eng. - Niger. Annu. Int. Conf. Exhib. 2003, NAICE 2003*, 2003, doi: 10.2118/85668-MS.

[56] J. P. Severinghaus, T. Sowers, E. J. Brook, R. B. Alley, and M. L. Bender, “Timing of abrupt climate change at the end of the younger dryas interval from thermally fractionated gases in polar ice,” *Nature*, vol. 391, no. 6663, pp. 141–146, Jan. 1998, doi: 10.1038/34346.

[57] B. Culshaw, “Optical Fiber Sensor Technologies: Opportunities and - Perhaps - Pitfalls,” *J. Light. Technol.*, vol. 22, no. 1, pp. 39–50, Jan. 2004, doi: 10.1109/JLT.2003.822139.

[58] R. KOCHOLATY, “MICROBIOLOGICAL OXIDATION OF ETHANOL IN VOLATILE FRUIT CONCENTRATES,” *J. Food Sci.*, vol. 15, no. 5, pp. 347–354, 1950, doi: 10.1111/J.1365-2621.1950.TB16484.X.

[59] W. Lukosz and C. Stamm, “Integrated optical interferometer as relative humidity sensor and differential refractometer,” *Sensors Actuators A. Phys.*, vol. 25, no. 1–3, pp. 185–188, 1990, doi: 10.1016/0924-4247(90)87029-I.

[60] D. Schlatter *et al.*, “The difference interferometer: application as a direct affinity sensor,” *Biosens. Bioelectron.*, vol. 8, no. 2, pp. 109–116, 1993, doi: 10.1016/0956-5663(93)80059-X.

[61] S. Kato and N. Maruyama, “Holographic interferometric measurements of the three-dimensional temperature field with thermally developing flow in the measuring-beam direction,” *Exp. Therm. Fluid Sci.*, vol. 2, no. 3, pp. 333–340, 1989, doi: 10.1016/0894-1777(89)90022-8.

[62] R. Escalona, “Study of axial absorption in liquids by interferometry,” *J. Opt. A Pure Appl. Opt.*, vol. 5, no. 5, p. S355, Aug. 2003, doi: 10.1088/1464-4258/5/5/391.

[63] A. Graževičius, A. Kaliatka, and E. Uškuras, “Numerical investigation of two-phase natural convection and temperature stratification phenomena in a rectangular enclosure with conjugate heat transfer,” *Nucl. Eng. Technol.*, vol. 52, no. 1, Jan. 2019, doi: 10.1016/J.NET.2019.06.022.

[64] A. Ito, K. Saito, and T. Inamura, “Holographic interferometry temperature measurements in liquids for pool fires supported on water,” *J. Heat Transfer*, vol. 114, no. 4, pp. 944–949, 1992, doi: 10.1115/1.2911905.

[65] M. Wetzel and C. Herman, “Accurate measurement of high-speed, unsteady temperature fields by holographic interferometry in the presence of periodic pressure variations,” *Meas. Sci. Technol.*, vol. 9, no. 6, pp. 939–951, 1998, doi: 10.1088/0957-0233/9/6/011.

[66] M. Wetzel and C. Herman, “Limitations of temperature measurements with holographic interferometry in the presence of pressure variations,” *Exp. Therm. Fluid Sci.*, vol. 17, no. 4, pp. 294–308, Aug. 1998, doi: 10.1016/S0894-1777(98)10001-8.

[67] B. J. de Gans, R. Kita, S. Wiegand, and J. Luettmer-Strathmann, “Unusual thermal diffusion in polymer solutions,” *Phys. Rev. Lett.*, vol. 91, no. 24, 2003, doi: 10.1103/PHYSREVLETT.91.245501.

[68] S. Wiegand and W. Köhler, “Measurement of Transport Coefficients by an Optical Grating

Technique," pp. 189–210, 2002, doi: 10.1007/3-540-45791-7_10.

[69] V. Korman, D. A. Gregory, and R. M. Banish, "Phase transition thermal expansion measurement technique using a modified Michelson interferometer," *J. Opt. A Pure Appl. Opt.*, vol. 6, no. 8, pp. 781–786, Aug. 2004, doi: 10.1088/1464-4258/6/8/007.

[70] D. C. Yin, Y. Inatomi, N. I. Wakayama, and W. D. Huang, "Measurement of temperature and concentration dependences of refractive index of hen-egg-white lysozyme solution," *Cryst. Res. Technol.*, vol. 38, no. 9, pp. 785–792, Sep. 2003, doi: 10.1002/CRAT.200310096.

[71] J. H. Lienhard IV and J. H. Lienhard V, *A heat transfer textbook*. Phlogiston Press, 2008.

[72] T. L. Bergman and A. Lavine, *Fundamentals of heat and mass transfer*, 8th ed. Hoboken, NJ : John Wiley & Sons, Inc., 2017.

[73] T. Vít, V. Lédl, R. Dolecek, and P. Psota, "The Possibility of Visualizing Temperature Fields Using Digital Holographic Interferometry," *Appl. Mech. Mater.*, vol. 284–287, pp. 988–995, 2013, doi: 10.4028/WWW.SCIENTIFIC.NET/AMM.284-287.988.

[74] S. Sharma, G. Sheoran, and C. Shakher, "Digital holographic interferometry for measurement of temperature in axisymmetric flames," *Appl. Opt.*, vol. 51, no. 16, pp. 3228–3235, Jun. 2012, doi: 10.1364/AO.51.003228.

[75] C. Chen and K. Chang, "Application of laser holographic interferometry to temperature measurements in premixed flames with different flame structures," *http://dx.doi.org/10.1080/02533839.1991.9677379*, vol. 14, no. 6, pp. 633–638, 2011, doi: 10.1080/02533839.1991.9677379.

[76] R. Doleček, V. Kopecký, P. Psota, and V. Lédl, "Digital holographic setup for measurement of asymmetric temperature field and tomographic reconstruction," *EPJ Web Conf.*, vol. 48, 2013, doi: 10.1051/EPJCONF/20134800003.

[77] C. Guerrero-Mendez *et al.*, "Real-time measurement of the average temperature profiles in liquid cooling using digital holographic interferometry," *Opt. Eng.*, vol. 55, no. 12, p. 121730, Oct. 2016, doi: 10.1117/1.OE.55.12.121730.

[78] J. Zhao and J. Di, "Dynamic visualization of complex flow fields using digital holographic interferometry," *SPIE Newsroom*, Aug. 2015, doi: 10.1117/2.1201507.006052.

[79] S. Aurisicchio, A. Finizio, and G. Pierattini, "Real-Time Holographic Interferometry for Painting Conservation and Restoration," *Bull. Assoc. Preserv. Technol.*, vol. 15, no. 2, p. 11, 1983, doi: 10.2307/1494009.

[80] V. Tornari, "Optical and digital holographic interferometry applied in art conservation structural diagnosis," *e-Preservation Sci. Morana RTD d.o.o.*, vol. 3, pp. 51–57, Dec. 2006, Accessed: Aug. 07, 2021.[Online].Available:https://www.researchgate.net/publication/26449230_Optical_and_digital_holographic_interferometry_applied_in_art_conservation_structural_diagnosis.

[81] D. A. Russell, D. E. Parker, and R. S. Hughes, "Analysis of standing sound waves using holographic interferometry," *Am. J. Phys.*, vol. 77, no. 8, p. 678, Jul. 2009, doi: 10.1119/1.3147683.

[82] S. N. Maina *et al.*, "Thermal Stress Monitoring on Piston Rings by Real Time Holographic Interferometry," *Opt. Photonics J.*, vol. 3, no. 8, pp. 379–384, Dec. 2013,

doi: 10.4236/OPJ.2013.38059.

[83] C. S. Seelamantula, N. Pavillon, C. Depeursinge, and M. Unser, “Zero-order-free image reconstruction in digital holographic microscopy,” *Proc. - 2009 IEEE Int. Symp. Biomed. Imaging From Nano to Macro, ISBI 2009*, pp. 201–204, 2009, doi: 10.1109/ISBI.2009.5193018.

[84] B. Zheng *et al.*, “An effective configuration for interferometric measurement of pulsed laser-induced plasma densities,” *Optik (Stuttg).*, vol. 119, no. 15, pp. 733–737, Nov. 2008, doi: 10.1016/J.IJLEO.2007.05.003.

[85] H. Wahba and M. S. El-Din, “Digital Holographic Interferometric Characterization of Optical Waveguides,” *Adv. Hologr. - Metrol. Imaging*, Nov. 2011, doi: 10.5772/22311.

[86] T. Vít and V. Lédl, “Identification of the temperature field in pulsatile impinging flow,” in *AIP Conference Proceedings*, Sep. 2010, vol. 1281, no. 1, pp. 135–138, doi: 10.1063/1.3497977.

[87] C. Shakher and A. K. Nirala, “A review on refractive index and temperature profile measurements using laser-based interferometric techniques,” *OptLE*, vol. 31, no. 6, pp. 455–491, 1999, doi: 10.1016/S0143-8166(99)00037-8.

[88] R. E. Brooks and L. O. Heflinger, “Holographic instrumentation studies,” 1970.

[89] D. Wilkie and S. A. Fisher, “Measurement of Temperature by Mach-Zehnder Interferometry,” *Proc. Inst. Mech. Eng.*, vol. 178, no. 1, pp. 461–470, Jun. 1963, doi: 10.1177/002034836317800166.

[90] M. Atlan and N. Verrier, “Off-axis digital hologram reconstruction: some practical considerations,” *Appl. Opt. Vol. 50, Issue 34, pp. H136-H146*, vol. 50, no. 34, pp. H136–H146, Dec. 2011, doi: 10.1364/AO.50.00H136.

[91] I. Yamaguchi, “Phase-Shifting Digital Holography,” *Opt. Photonics News*, vol. 19, no. 7, p. 48, Jul. 2008, doi: 10.1364/OPN.19.7.000048.

[92] P. Dančová, T. Vít, V. Lédl, Z. Trávníček, and R. Doleček, “Holographic Interferometry as a tool for visualization of temperature fields in air,” *Eng. Mech.*, vol. 20, no. 4, pp. 205–212, 2013.

[93] V. Lédl, T. Vít, R. Doleček, and P. Psota, “Digital holografic interferometry used for identification of 2D temperature field,” *EPJ Web Conf.*, vol. 25, 2012, doi: 10.1051/epjconf/20122502014.

[94] C. C. Chen, K. C. Chang, and H. F. Yuan, “Studies of premixed laminar flame structure: Concentration measurement,” *J. Chinese Inst. Eng. Trans. Chinese Inst. Eng. A/Chung-kuo K. Ch’eng Hsuch K’an*, vol. 14, no. 4, pp. 431–436, 1991, doi: 10.1080/02533839.1991.9677355.

[95] G. Wang, Y. Li, D. Wang, and J. Zhao, “Application of digital holography in temperature distribution measurement,” *Hologr. Diffractive Opt. Appl. IV, Proceeding SPIE*, vol. 7848, p. 78482V, 2010, doi: 10.1117/12.870490.

[96] D. Wu, W. Yao, Z. Wang, and A. He, “Three-dimensional tomography for asymmetric field containing opaque object,” *Opt. Eng.*, vol. 37, no. 8, pp. 2255–2257, Aug. 1998, doi: 10.1117/1.601744.

[97] J. Zhu, S. Huang, W. Lv, and H. Zhou, “Study on the measurement of temperature field using laser holographic interferometry,” *Front. Energy*, vol. 5, no. 1, pp. 120–124, Jun. 2010, doi: 10.1007/S11708-010-0107-9.

[98] K.-C. Chang, J.-M. Huang, and S.-M. Tieng, “Application of laser holographic interferometry to temperature measurements in buoyant air jets,” *https://doi.org/10.2514/3.370*, vol. 6, no. 2, pp. 377–379, May 2012, doi: 10.2514/3.370.

[99] D. W. Sweeney and C. M. Vest, “Measurement of three-dimensional temperature fields above heated surfaces by holographic interferometry,” *Int. J. Heat Mass Transf.*, vol. 17, no. 12, pp. 1443–1454, Dec. 1974, doi: 10.1016/0017-9310(74)90054-4.

[100] C. Shakher, M. Kumar, and V. Kumar, “Measurement of natural convective heat transfer coefficient along the surface of a heated wire using digital holographic interferometry,” *Appl. Opt. Vol. 53, Issue 27, pp. G74-G83*, vol. 53, no. 27, pp. G74–G83, Sep. 2014, doi: 10.1364/AO.53.000G74.

[101] J. Marn, “The Use of Holographic Interferometry for Measurements of Temperature in a Rectangular Heat Pipe,” 1989. Accessed: Aug. 17, 2021. [Online]. Available: https://hclib.bibliocommons.com/v2/record/S109C4041238.

[102] R. Doleček, P. Psota, V. Lédl, T. Vít, J. Václavík, and V. Kopecký, “General temperature field measurement by digital holography,” *Appl. Opt.*, vol. 52, no. 1, pp. A319–A325, Jan. 2013, doi: 10.1364/AO.52.00A319.

[103] P. Psota, R. Doleček, V. Lédl, T. Vít, P. Mokrý, and P. Dančová, “Validation of digital holographic tomography in flow measurement,” in *EPJ Web of Conferences*, May 2017, vol. 143, doi: 10.1051/epjconf/201714302097.

[104] D. Mishra, k. Muralidhar, and P. Munshi, “Measurements of Three Dimensional Temperature Field in Fluids using Laser Interferometry,” *Def. Sci. J.*, vol. 49, no. 3, pp. 243–255, 1999, doi: 10.14429/DSJ.49.3836.

[105] A. Ito and T. Kashiwagi, “Characterization of flame spread over PMMA using holographic interferometry sample orientation effects,” *Combust. Flame*, vol. 71, no. 2, pp. 189–204, Feb. 1988, doi: 10.1016/0010-2180(88)90007-7.

[106] C. Ma, J. Di, J. Zhao, S. Dai, T. Xi, and Y. Li, “Measurement of ultrafast combustion process of premixed ethylene/oxygen flames in narrow channel with digital holographic interferometry,” *Opt. Express, Vol. 26, Issue 22, pp. 28497-28504*, vol. 26, no. 22, pp. 28497–28504, Oct. 2018, doi: 10.1364/OE.26.028497.

[107] C. Qi, S. Zheng, and H. Zhou, “Experimental investigation on gas-phase temperature of axisymmetric ethylene flames by large lateral shearing interferometry,” *Int. J. Therm. Sci.*, vol. C, no. 115, pp. 104–111, May 2017, doi: 10.1016/J.IJTHERMALSCI.2017.01.026.

[108] S. Agarwal, V. Kumar, and C. Shakher, “Temperature measurement of wick stabilized micro diffusion flame under the influence of magnetic field using digital holographic interferometry,” *Opt. Lasers Eng.*, vol. 102, pp. 161–169, Mar. 2018, doi: 10.1016/J.OPTLASENG.2017.10.019.

[109] J. C. Aguilar, L. R. Berriel-Valdos, and J. F. Aguilar, “Measuring of temperatures of a candle flame using four multidirectional point-diffraction interferometers,” *Opt. Eng.*, vol. 52, no. 10, p. 104103, Oct. 2013, doi: 10.1117/1.OE.52.10.104103.

[110] B. Zhou, S. Wang, C. Xu, and J. Zhang, “3-D flame temperature reconstruction in optical sectioning tomography,” *2009 IEEE Int. Work. Imaging Syst. Tech. IST 2009 - Proc.*, pp. 313–318, 2009, doi: 10.1109/IST.2009.5071656.

[111] B. Zhang *et al.*, “Three-dimensional temperature field measurement of flame using a single light field camera,” *Opt. Express, Vol. 24, Issue 2, pp. 1118-1132*, vol. 24, no. 2, pp. 1118–1132, Jan. 2016, doi: 10.1364/OE.24.001118.

[112] S. M. Tieng and W. Z. Lai, “Temperature measurements of reacting flowfield by phase-shifting holographic interferometry,” *J. Thermophys. Heat Transf.*, vol. 6, no. 3, pp. 445–451, Jul. 1992, doi: 10.2514/3.381.

[113] B. Saucedo-Orozco, D. Ariza-Flores, I. Moreno, J. S. Pérez-Huerta, and T. Saucedo-Anaya, “Digital holographic interferometry applied to the investigation of ignition process,” *Opt. Express, Vol. 25, Issue 12, pp. 13190-13198*, vol. 25, no. 12, pp. 13190–13198, Jun. 2017, doi: 10.1364/OE.25.013190.

[114] C. LI, W. LIU, X. PENG, L. SHAO, and S. FENG, “Measurement of mass diffusion coefficients of O2 in aviation fuel through digital holographic interferometry,” *Chinese J. Aeronaut.*, vol. 32, no. 5, pp. 1184–1189, May 2019, doi: 10.1016/J.CJA.2019.01.012.

[115] L. Reyes, J. Bert, J. Fornazero, R. Cohen, and L. Heinrich, “Influence of conformational changes on diffusion properties of bovine serum albumin: a holographic interferometry study,” *Colloids Surfaces B Biointerfaces*, vol. 25, no. 2, pp. 99–108, Jun. 2002, doi: 10.1016/S0927-7765(01)00288-0.

[116] J. Colombani, H. Dez, J. Bert, and J. Dupuy-Philon, “Hydrodynamic instabilities and soret effect in an aqueous electrolyte,” *Phys. Rev. E - Stat. Physics, Plasmas, Fluids, Relat. Interdiscip. Top.*, vol. 58, no. 3, pp. 3202–3208, 1998, doi: 10.1103/PHYSREVE.58.3202.

[117] J. Colombani, J. Bert, and J. Dupuy-Philon, “Thermal diffusion in (LiCl, RH2O),” *J. Chem. Phys.*, vol. 110, no. 17, p. 8622, Apr. 1999, doi: 10.1063/1.478769.

[118] J. Colombani and J. Bert, “Holographic visualization of convection during thermotransport: application to microgravity experiments,” *Meas. Sci. Technol.*, vol. 10, no. 10, p. 886, Oct. 1999, doi: 10.1088/0957-0233/10/10/308.

[119] C. Guerrero-Méndez, T. Saucedo-Anaya, M. Araiza-Esquivel, R. E. Balderas-Navarro, A. López-Martínez, and C. Olvera-Olvera, “Measurements of concentration differences between liquid mixtures using digital holographic interferometry,” *Metrol. Meas. Syst.*, vol. 24, no. 1, pp. 19–26, 2017, doi: 10.1515/MMS-2017-0002.

[120] F. Lee Rodkey, “Aqueous Solutions and Body Fluids. Their Concentrative Properties and Conversion Tables. A. V. Wolf. Hoeber Medical Division, Harper & Row, Publishers, New York, 1966, 182 pp., 8 illus., $7.50,” *Clin. Chem.*, vol. 12, no. 8, pp. 517–518, Aug. 1966, doi: 10.1093/CLINCHEM/12.8.517.

[121] J. Barthel and Gores, “Densities of Aqueous Solutions of Inorganic Substances,” *Berichte der Bunsengesellschaft für Phys. Chemie*, vol. 89, no. 6, pp. 722–723, Jun. 1985, doi: 10.1002/BBPC.19850890633.

[122] D. Naylor and A. D. Machin, “THE ACCURACY OF BEAM-AVERAGED INTERFEROMETRIC TEMPERATURE MEASUREMENTS IN A THREE-DIMENSIONAL FIELD,” *Exp. Heat Transf.*, vol. 14, no. 3, 2010, doi: 10.1080/089161501301419614.

[123] D. Naylor, “Recent developments in the measurement of convective heat transfer rates by laser interferometry,” *Int. J. Heat Fluid Flow*, vol. 24, no. 3, pp. 345–355, 2003,

doi: 10.1016/S0142-727X(03)00021-3.

[124] V. V Bat'kovich, O. N. Budenkova, V. B. Konstantinov, O. L. Sadov, and E. A. Smirnova, "Determination of the temperature distribution in liquids and solids using holographic interferometry," *Tech. Phys.*, vol. 44, no. 6, 1999.

[125] S. Dehaeck, A. Rednikov, and P. Colinet, "Vapor-Based Interferometric Measurement of Local Evaporation Rate and Interfacial Temperature of Evaporating Droplets," *Langmuir*, vol. 30, no. 8, pp. 2002–2008, Mar. 2014, doi: 10.1021/LA404999Z.

[126] Y. M. Chen and F. Mayinger, "HOLOGRAPHIC INTERFEROMETRY STUDIES OF THE TEMPERATURE FIELD NEAR A CONDENSING BUBBLE.," *Mater. Sci.*, pp. 13–20, 1985, doi: 10.1007/978-3-642-82459-3_3.

[127] S. Venkatesh, A. Ito, K. Saito, and I. S. Wichman, "FLAME BASE STRUCTURE OF SMALL-SCALE POOL FIRES," in *International Symposium on Combustion 26(1)*, 1996, pp. 1437–1443.

[128] J. Colombani and J. Bert, "Holographic interferometry study of the dissolution and diffusion of gypsum in water," *Geochim. Cosmochim. Acta*, vol. 71, no. 8, pp. 1913–1920, Apr. 2007, doi: 10.1016/J.GCA.2007.01.012.

[129] D.-J. Cha and H. S. Hwang, "Measurement of convective heat transfer from an isothermal cube using holographic interferometric tomography," *Opt. Diagnostics Fluids/Heat/Combustion Photomech. Solids*, vol. 3783, pp. 165–174, Oct. 1999, doi: 10.1117/12.365737.

[130] E. Tomita, N. Kawahara, and Y. Toda, "A New Sensor for Temperature Measurement of Water by Laser Interferometry Technique," Jun. 2006.

[131] S. C. H. Hung, H. K. Dong, and C. W. Tu, "Non-Contact Temperature Measurement with Infrared Interferometry," *MRS Online Proc. Libr. 1994 3401*, vol. 340, no. 1, pp. 35–40, Mar. 1994, doi: 10.1557/PROC-340-35.

[132] J. R. Zhu, J. M. Dai, X. M. Cheng, and Y. Y. Li, "Temperature Measurement of An Inclined Cylinder Using Optical Interferometry," *Proc. 2015 Int. Conf. Artif. Intell. Ind. Eng.*, vol. 123, pp. 82–84, Jul. 2015, doi: 10.2991/AIIE-15.2015.23.

[133] R. Cilli, A. Prakki, and M. A. J. de Araújo, "Measuring polymerization shrinkage of composites utilizing a gas pycnometer," *Brazilian Dent. Sci.*, vol. 6, no. 3, Aug. 2010, doi: 10.14295/BDS.2003.V6I3.595.

[134] V. Rastogi, V. Kumar, S. K. Dubey, G. S. Khan, and C. Shakher, "Noncontact temperature measurement of human hand skin using volume phase holographic optical element based digital holographic interferometer," *Opt. Lasers Eng.*, vol. 151, p. 106886, 2022, doi: 10.1016/J.OPTLASENG.2021.106886.

[135] A. Ecker, "Two-wavelength holographic measurement of temperature and concentration during alloy solidification," *https://doi.org/10.2514/3.87*, vol. 2, no. 3, pp. 193–196, May 2012, doi: 10.2514/3.87.

[136] P. S. Bodienkov, B. G. Manukhin, N. V. Andreeva, and O. V. Andreeva, "Evaluation of thermal exposure on absorbing objects with digital holographic interferometry method," *Opt. Sens. Detect. III, Proceeding SPIE*, vol. 9141, 2014, doi: 10.1117/12.2057498.

[137] A. Asundi, J. Di, W. Qu, and Y. Yu, “Measurement of thermal effects of diode-pumped solid-state laser by using digital holography,” *Appl. Opt.*, vol. 57, no. 19, pp. 5385–5391, Jul. 2018, doi: 10.1364/AO.57.005385.

[138] F. M. Vincitorio *et al.*, “Holographic interferometry as a method to detect welding failures on ribbed iron structures,” *8th Iberoam. Opt. Meet. 11th Lat. Am. Meet. Opt. Lasers, Appl.*, vol. 8785, p. 87852M, Nov. 2013, doi: 10.1117/12.2025549.

[139] T. AH, A. S, M. S, T. T, and D.-B. RE, “In situ transmission electron microscopy of ionic conductivity and reaction mechanisms in ultrathin solid oxide fuel cells,” *Microsc. Microanal.*, vol. 20, no. 6, pp. 1817–1825, Sep. 2014, doi: 10.1017/S143192761401349X.

[140] J. D. (Jonathan D. Ellis and Society of Photo-optical Instrumentation Engineers, *Field guide to displacement measuring interferometry*. .

[141] P. Psota *et al.*, “Development and application of spatial carrier interferometry for whole field real-time investigation of temperatures in liquid media,” *Int. J. Therm. Sci.*, vol. 145, p. 106029, Nov. 2019, doi: 10.1016/j.ijthermalsci.2019.106029.

[142] Z. Malacara and M. Servín, *Interferogram analysis for optical testing*. CRC Press, 2005.

[143] D. Malacara, *Optical Shop Testing*. Hoboken, NJ, USA: John Wiley & Sons, Inc., 2007.

[144] G. Cubreli, A. Elbarghthi, P. Dancova, and A. Kouta, “Temperature measurement by CFD simulations, Digital Holographic Interferometry, thermocouples and their comparison,” 2019.

[145] E. W. Lemmon, M. L. Huber, and M. O. McLinden, “Reference Fluid Thermodynamic and Transport Properties - REFPROP 9.0,” 2010. Accessed: Jul. 26, 2021. [Online]. Available: https://www.bibsonomy.org/bibtex/2ae369b98c7cc721f7e4eb576d6dee1e7/thorade.

[146] S. Kim, D. E. Kim, S. U. Ryu, S. T. Lee, and D. J. Euh, “Experimental investigation on the natural convection flow in pool boiling,” *Nucl. Eng. Des.*, vol. 280, pp. 349–361, Aug. 2015, doi: 10.1016/J.NUCENGDES.2014.09.040.

[147] N. A. Turko, P. J. Eravuchira, I. Barnea, and N. T. Shaked, “Simultaneous three-wavelength unwrapping using external digital holographic multiplexing module,” *Opt. Lett. Vol. 43, Issue 9, pp. 1943-1946*, vol. 43, no. 9, pp. 1943–1946, May 2018, doi: 10.1364/OL.43.001943.

[148] K. Meiners-Hagen, R. Schödel, F. Pollinger, and A. Abou-Zeid, “Multi-wavelength interferometry for length measurements using diode lasers,” *Meas. Sci. Rev.*, vol. 9, no. 1, pp. 16–26, Jan. 2009, doi: 10.2478/V10048-009-0001-Y.

[149] D. Parshall and M. K. Kim, “Digital holographic microscopy with dual-wavelength phase unwrapping,” *Appl. Opt. Vol. 45, Issue 3, pp. 451-459*, vol. 45, no. 3, pp. 451–459, Jan. 2006, doi: 10.1364/AO.45.000451.

[150] V. Jaedicke, S. Goebel, N. Koukourakis, N. C. Gerhardt, H. Welp, and M. R. Hofmann, “Multiwavelength phase unwrapping and aberration correction using depth filtered digital holography,” *Opt. Lett.*, vol. 39, no. 14, pp. 4160–4163, Jul. 2014, doi: 10.1364/OL.39.004160.

[151] A. Khmaladze, M. Kim, and C.-M. Lo, “Phase imaging of cells by simultaneous dual-wavelength reflection digital holography,” *Opt. Express*, vol. 16, no. 15, p. 10900, Jul. 2008, doi: 10.1364/OE.16.010900.

[152] C. Zuo, L. Huang, M. Zhang, Q. Chen, and A. Asundi, “Temporal phase unwrapping algorithms for fringe projection profilometry: A comparative review,” *Opt. Lasers Eng.*, vol. 85, pp. 84–103, Oct. 2016, doi: 10.1016/J.OPTLASENG.2016.04.022.

[153] N. Warnasooriya and M. K. Kim, “Quantitative Phase Imaging Using Multi-Wavelength Optical Phase Unwrapping,” *Adv. Lasers Electro Opt.*, Apr. 2010, doi: 10.5772/8668.

[154] R. Onodera and Y. Ishii, “Two-wavelength interferometry that uses a Fourier-transform method,” *Appl. Opt.*, vol. 37, no. 34, pp. 7988–7994, Dec. 1998, doi: 10.1364/AO.37.007988.

[155] N. A. Turko and N. T. Shaked, “Simultaneous two-wavelength phase unwrapping using an external module for multiplexing off-axis holography,” *Opt. Lett.*, vol. 42, no. 1, pp. 73–76, Jan. 2017, doi: 10.1364/OL.42.000073.

[156] Y.-Y. Cheng and J. C. Wyant, “Two-wavelength phase shifting interferometry,” *Appl. Opt.*, vol. 23, no. 24, pp. 4539–4543, Dec. 1984, doi: 10.1364/AO.23.004539.

[157] G. Çubreli, P. Psota, A. Kouta, and P. Dančová, “Two-wavelength digital holographic interferometry for unambiguous range extended measurements in fluid mechanics,” in *International Conference Experimental Fluid Mechanics 2021*, 2021, pp. 238–244.

[158] T. Guo, F. Li, J. Chen, X. Fu, and X. Hu, “Multi-wavelength phase-shifting interferometry for micro-structures measurement based on color image processing in white light interference,” *Opt. Lasers Eng.*, vol. 82, pp. 41–47, Jul. 2016, doi: 10.1016/J.OPTLASENG.2016.02.003.

[159] P. Psota, G. Cubreli, J. Kredba, M. Stasik, and V. Ledl, “Two wavelength digital holographic interferometry for investigation of dynamic processes in fluid mechanics,” May 2021, Accessed: Aug. 01, 2021. [Online]. Available: https://dl.astfe.org/conferences/tfec2021,586fceb86446aa50,35eb4e3178980f3c.html.

[160] C. Wagner, W. Osten, and S. Seebacher, “Direct shape measurement by digital wavefront reconstruction and multi-wavelength contouring,” *Opt. Eng.*, vol. 39, no. 1, pp. 79–85, Jan. 2000, doi: 10.1117/1.602338.

[161] S. Chavez, Q. S. Xiang, and L. An, “Understanding phase maps in MRI: a new cutline phase unwrapping method,” *IEEE Trans. Med. Imaging*, vol. 21, no. 8, pp. 966–977, Aug. 2002, doi: 10.1109/TMI.2002.803106.

[162] A. Momose, “Recent Advances in X-ray Phase Imaging,” *Jpn. J. Appl. Phys.*, vol. 44, no. 9A, pp. 6355–6367, 2005, doi: 10.1143/JJAP.44.6355.

[163] M. D. Pritt, “Phase unwrapping by means of multigrid techniques for interferometric SAR,” *IEEE Trans. Geosci. Remote Sens.*, vol. 34, no. 3, p. 728738, 1996, doi: 10.1109/36.499752.

[164] W. Yin *et al.*, “High-speed three-dimensional shape measurement using geometry-constraint-based number-theoretical phase unwrapping,” *Opt. Lasers Eng.*, vol. 115, pp. 21–31, Apr. 2019, doi: 10.1016/J.OPTLASENG.2018.11.006.

[165] W. Yin *et al.*, “High-speed three-dimensional shape measurement using geometry-constraint-based number-theoretical phase unwrapping,” *Opt. Lasers Eng.*, vol. 115, pp. 21–31, Apr. 2019, doi: 10.1016/J.OPTLASENG.2018.11.006.

[166] L. Lu, Z. Jia, Y. Luan, and J. Xi, “Reconstruction of isolated moving objects with high 3D frame rate

based on phase shifting profilometry," *Opt. Commun.*, vol. 438, pp. 61–66, May 2019, doi: 10.1016/J.OPTCOM.2018.12.092.

[167] A. Khmaladze, R. L. Matz, C. Zhang, T. Wang, M. M. B. Holl, and Z. Chen, "Dual-wavelength linear regression phase unwrapping in three-dimensional microscopic images of cancer cells," *Opt. Lett.*, vol. 36, no. 6, pp. 912–914, Mar. 2011, doi: 10.1364/OL.36.000912.

[168] M. Peca, P. Psota, P. Vojtíšek, and V. Lédl, "Absolute and relative surface profile interferometry using multiple frequency-scanned lasers," in *Optics and Measurement International Conference*, 2016, doi: 10.1117/12.2263656.

[169] H. K and C. F, "Two-wavelength interferometry: extended range and accurate optical path difference analytical estimator," *J. Opt. Soc. Am. A. Opt. Image Sci. Vis.*, vol. 26, no. 12, p. 2503, Dec. 2009, doi: 10.1364/JOSAA.26.002503.

[170] G. Cubreli, P. Psota, P. Dančová, V. Lédl, and T. Vít, "Digital Holographic Interferometry for the Measurement of Symmetrical Temperature Fields in Liquids," *Photonics*, vol. 8, 2020, doi: 10.3390/photonics8060200.

[171] C. Herman and E. Kang, "Experimental visualization of temperature fields and study of heat transfer enhancement in oscillatory flow in a grooved channel," *Heat Mass Transf. und Stoffuebertragung*, vol. 37, no. 1, pp. 87–99, Jan. 2001, doi: 10.1007/s002310000101.

[172] T. Vit, R. Doleček, P. Psota, and Z. Travniček, "Perspectives in holographic interferometry," 2013, Accessed: Mar. 31, 2021. [Online]. Available: https://scholar.google.com/citations?user=ZBgL234AAAAJ&hl=en.

[173] M. Kumar and C. Shakher, "Measurement of temperature and temperature distribution in gaseous flames by digital speckle pattern shearing interferometry using holographic optical element," *Opt. Lasers Eng.*, vol. 73, pp. 33–39, Oct. 2015, doi: 10.1016/j.optlaseng.2015.04.002.

[174] S. Sharma, G. Sheoran, and C. Shakher, "Temperature measurement of axisymmetric flame under the influence of magnetic field using lensless Fourier transform digital holography," *Appl. Opt.*, vol. 51, no. 19, p. 4554, Jul. 2012, doi: 10.1364/ao.51.004554.

[175] F. Olchewsky, Z. Essaïdi, J. Desse, and F. Champagnat, "3D reconstructions of jets by multidirectional digital holographic tomography," *Proc. 18th Int. Symp. Flow Vis.*, Oct. 2018, doi: 10.3929/ethz-b-000279142.

[176] K. A. Sallam, K. C. Lin, and C. D. Carter, "Spray structure of aerated liquid jets using double-view digital holography," 2010, doi: 10.2514/6.2010-194.

[177] Z. Alaswad, "Experimental and Numerical Study of a Synthetic Jet Ejector," University of Windsor, 2019.

[178] E. Janotkova and M. Pavelek, "Determination of air outlet C-values by means of interferometry," *Int. J. Vent.*, vol. 4, no. 4, pp. 311–321, Mar. 2006, doi: 10.1080/14733315.2005.11683711.

[179] Z. Broučková, S. S. Hsu, A. B. Wang, and Z. Trávníček, "Water Synthetic Jet Driven by a Piezoelectric Actuator – LIF and PIV Experiments," *Adv. Mater. Res.*, vol. 1104, pp. 45–50, May 2015, doi: 10.4028/www.scientific.net/amr.1104.45.

[180] K. Mohseni and R. Mittal, Eds., *Synthetic Jets: Fundamentals and Applications*, First edition. Boca

Raton: CRC Press, 2014.

[181] M. Amitay, “Synthetic jets and their applications for fluid/thermal systems,” in *Solid Mechanics and its Applications*, 2008, vol. 7, pp. 77–93, doi: 10.1007/978-1-4020-6858-4_9.

[182] S. Li, “A Numerical Study of Micro Synthetic Jet and Its Applications in Thermal Management,” Georgia Institute of Technology, 2005.

[183] J. Tensi, I. Boué, F. Paillé, and G. Dury, “Modification of the wake behind a circular cylinder by using synthetic jets,” *J. Vis.*, vol. 5, no. 1, pp. 37–44, 2002, doi: 10.1007/BF03182601.

[184] J. Li and X. Zhang, “Active flow control for supersonic aircraft: A novel hybrid synthetic jet actuator,” *Sensors Actuators, A Phys.*, vol. 302, p. 111770, Feb. 2020, doi: 10.1016/j.sna.2019.111770.

[185] K. D. Weltmann *et al.*, “The future for plasma science and technology,” *Plasma Process. Polym.*, vol. 16, no. 1, p. 1800118, Jan. 2019, doi: 10.1002/ppap.201800118.

[186] M. B. Gillespie, W. Z. Black, C. Rinehart, and A. Glezer, “Local Convective Heat Transfer From a Constant Heat Flux Flat Plate Cooled by Synthetic Air Jets,” *J. Heat Transfer*, vol. 128, no. 10, pp. 990–1000, Oct. 2006, doi: 10.1115/1.2345423.

[187] Z. Trávníček, V. Tesař, Z. Broučková, and K. Peszyński, “Annular impinging jet controlled by radial synthetic jets,” *Heat Transf. Eng.*, vol. 35, no. 16–17, pp. 1450–1461, Nov. 2014, doi: 10.1080/01457632.2014.889467.

[188] P. Dancova, P. Psota, and T. Vit, “Measurement of a temperature field generated by a synthetic jet actuator using digital holographic interferometry,” *Actuators*, vol. 8, no. 1, p. 27, Mar. 2019, doi: 10.3390/act8010027.

[189] Z. Broučková, “Synthetic and continuous jets impinging on a circular cylinder: Flow field and heat transfer experimental study,” CZECH TECHNICAL UNIVERSITY IN PRAGUE, Prague.

[190] P. A. Blanche, *Optical holography: Materials, theory and applications*. Elsevier, 2019.

[191] R. J. Radke, “DIP Lecture 18: Reconstruction from parallel projections and the Radon transform - YouTube,” *DIP Lecture 18: Reconstruction from parallel projections and the Radon transform*. Apr. 13, 2015, Accessed: Jan. 24, 2022. [Online]. Available: https://www.youtube.com/watch?v=ZgcD4C-4u0Q&ab_channel=RichRadke.

[192] R. C. Gonzalez and Woods; Richard E., *Digital image processing*, 3. ed. New Jersey: Parson, 2008.

[193] T. M. Venema and J. D. Schmidt, “Optical phase unwrapping in the presence of branch points,” *Opt. Express*, vol. 16, no. 10, p. 6985, May 2008, doi: 10.1364/oe.16.006985.

[194] W. Gorski, “Tomographic microinterferometry of optical fibers,” *Opt. Eng.*, vol. 45, no. 12, p. 125002, Dec. 2006, doi: 10.1117/1.2405351.

List of publications by the author

1. Pavel Psota, Gramoz Çubreli, Jindřich Hála, David Šimurda, Petr Šidlof, Jan Kredba, Marek Stašík, et al. 2021. "Characterization of Supersonic Compressible Fluid Flow Using High-Speed Interferometry." Sensors 2021, Vol. 21, Page 8158 21 (23): 8158. https://doi.org/10.3390/S21238158
2. Gramoz Cubreli, Pavel Psota, Ahmad Kouta and Petra Dančová. 2021. "Two-wavelength digital holographic interferometry for unambiguous range extended measurements in fluid mechanics" In International Conference of Experimental Fluid Mechanics 2021 EFM'21. Liberec, Czechia: Technical University of Liberec.
   https://efm.kez.tul.cz/
3. Pavel Psota, Gramoz Cubreli, Jan Kredba, Marek Stasik, and Vit Ledl. 2021. "Two Wavelength Digital Holographic Interferometry for Investigation of Dynamic Processes in Fluid Mechanics." In 5-6th Thermal and Fluids Engineering Conference (TFEC) -American Society of Thermal and Fluids Engineers. Begell House Publishers, Inc.
   https://dl.astfe.org/conferences/tfec2021,586fceb86446aa50,35eb4e3178980f3c.html
4. Gramoz Cubreli, Pavel Psota, Petra Dančová, Vít Lédl, and Tomáš Vít. 2021. "Digital Holographic Interferometry for the Measurement of Symmetrical Temperature Fields in Liquids." Photonics 2021, Vol. 8, Page 200.
   https://doi.org/10.3390/photonics8060200 .
5. Gramoz Cubreli, Anas Elbarghthi, Petra Dančová, and Ahmad Kouta. 2019. "Temperature Measurement by CFD Simulations, Digital Holographic Interferometry, Thermocouples and Their Comparison." In International Conference of Experimental Fluid Mechanics 2019 EFM'19. Franzensbad, Czechia: Technical University of Liberec.
   https://efm.kez.tul.cz/
6. Ahmad Kouta, Tomáš Vít and Gramoz Cubreli. 2019. "Gas Mixture Separation by Thermoacoustic Waves" In International Conference of Experimental Fluid Mechanics 2019 EFM'19. Franzensbad, Czechia: Technical University of Liberec.
   https://efm.kez.tul.cz/
7. Pavel Psota, Petra Dančová, Gramoz Cubreli, Vít Lédl, Tomáš Vít, Roman Doleček, and Ondřej Matoušek. 2019. "Development and Application of Spatial Carrier Interferometry for Whole Field Real-Time Investigation of Temperatures in Liquid Media." International Journal of Thermal Sciences 145 (November): 106029.
   https://doi.org/10.1016/j.ijthermalsci.2019.106029